

Title	Thermophysical properties of advanced fuels and high-burnup fuels
Author(s)	Adachi, Jun
Citation	大阪大学, 2008, 博士論文
Version Type	VoR
URL	https://hdl.handle.net/11094/23432
rights	
Note	

Osaka University Knowledge Archive : OUKA

<https://ir.library.osaka-u.ac.jp/>

Osaka University

Doctoral Thesis

**Thermophysical properties of advanced fuels and
high-burnup fuels**

Jun Adachi

Division of Sustainable Energy and Environmental Engineering,
Graduate School of Engineering, Osaka University

2008

Doctoral Thesis

**Thermophysical properties of advanced fuels and
high-burnup fuels**

(新型燃料および高燃焼度燃料の熱物理的性質)

Jun Adachi

Division of Sustainable Energy and Environmental Engineering,
Graduate School of Engineering, Osaka University

2008

Abstract

MA (Minor Actinide)-containing MOX (Mixed OXide) fuel and nitride fuel are the candidates of the fuels loaded in the fast neutron system such as FBR (Fast Breeder Reactor) and ADS (Accelerator Driven System). However, there are few data of their thermophysical properties. Therefore, in the present study, their thermophysical properties were evaluated by the simulation method and experimental method. The present study consists of following 6 subjects.

Chapter 1: General introduction

In this chapter, the importance of partitioning and transmutation (P and T) of MA is explained. The fuel form for P and T of MA is not determined yet. When we determine the fuel form, it is very important to evaluate the crystallographic, mechanical, thermal and electrical properties of MA-containing MOX and nitride fuels.

Chapter 2: Experimental evaluation of thermophysical properties of UN, simulated ADS target fuels (UN+TiN (U:Ti=4:6) and $U_{0.4}Zr_{0.6}N$) and inert matrix material (TiN and ZrN)

The thermophysical properties of ZrN and TiN expected as the inert matrix of the nitride fuels were evaluated. In addition, $U_{0.4}Zr_{0.6}N$ and UN+60mol%TiN as the simulated ADS target fuels were also evaluated to understand the interaction between actinide nitrides and inert matrix materials.

In case of $U_{0.4}Zr_{0.6}N$, the mechanical properties were improved by the addition of ZrN. On the other hand, the electrical and thermal conductivities decreased due to the high sintering resistivity of ZrN.

In case of UN+60mol%TiN, the mechanical, electrical and thermal properties were improved by the addition of TiN and were roughly predicted by the theoretical or empirical model. Therefore, it would be easy to predict the thermophysical properties of (Pu,MA)N+TiN with various component. Judging from only these results, TiN is more effective than ZrN as the inert matrix.

In the present study, the newest technique, which are SPS, EBSP and indentation test, and the new concept such as MSA were used in the field of the nuclear fuel engineering for the first time. The author succeeded to precisely evaluate the thermophysical properties of inert matrix materials (ZrN and TiN) and was able to suggest the new methods to evaluate the porosity dependences of the thermophysical properties, which are extremely effective for the

research of MA-containing fuels.

Chapter 3: Molecular dynamics (MD) studies of actinide nitrides, nitride ADS target fuels, actinide dioxides and MA-containing MOX fuels

In this chapter, the thermophysical properties of MA-containing fuels were evaluated by MD (Molecular Dynamics) simulation because it is very difficult to experimentally measure the thermophysical properties of MA-containing fuels.

By fitting the limited experimental data of the thermal expansion and bulk modulus, the potential parameters for the nitrides (ThN, UN, NpN, PuN, AmN and ZrN) and actinide dioxides (UO_2 , NpO_2 , PuO_2 and AmO_2) were semi-empirically determined. Using these parameters, the author evaluated the thermal expansion, bulk modulus, specific heat capacity and thermal conductivity of not only AnO_2 , AnN and ZrN, but also MOX, MA-containing MOX, and nitride fuels with the inert matrix.

It was found that the thermophysical properties of MA-containing MOX fuels are very close to those of MOX fuels. Therefore, it is thought that the fuel behavior of MA-containing MOX fuel in the reactor core could be predicted by the code, which had been used to predict the fuel behavior of MOX fuel. In the present study, it was confirmed that MD simulation is very useful when we evaluate the thermophysical properties of the fuels with the complex component such as MA-containing MOX fuels and nitride fuels with the inert matrix.

Chapter 4: FPs (Pd, Mo and Nd) effects on thermophysical properties of simulated high-burnup nitride fuels

The simulated high-burnup nitride fuel pellets ($\text{UN}+\text{Pd}$, $(\text{U,Nd})\text{N}$, $\text{UN}+\text{Mo}$, $(\text{U,Nd})\text{N}+\text{Mo}$) were prepared and their thermophysical properties were measured to evaluate the thermophysical properties of the high-burnup nitride fuels.

From the result of Chapter 4, it was suggested that the mechanical and thermal properties of the nitride fuels are improved and descended by the addition of FPs, respectively. In addition, the thermophysical properties of the simulated high-burnup nitride fuels were vastly larger than those of the non-irradiated UO_2 .

Chapter 5: Thermodynamics modeling of U-N and Pu-N binary system

U-N and Pu-N binary systems were assessed thermodynamically from the criticism of the available experimental data on both phase diagram and thermodynamics properties.

A consistent set of Gibbs energy parameters for the various phases was obtained. The

agreement between the experimental and calculated phase diagram of thermodynamic properties is quite satisfactory.

Chapter 6: Conclusion

In this chapter, the results of the chapter from 2 to 5 are summed up.

Contents

Chapter 1: General introduction	1
References	4
Tables and figures	7
 Chapter 2: Experimental evaluation of thermophysical properties of UN¹⁾, simulated ADS²⁾ target fuels (UN+60mol%TiN⁵⁾ and U_{0.4}Zr_{0.6}N⁶⁾) and inert matrix materials (TiN³⁾ and ZrN⁴⁾)	 11
2-1 Background	11
2-2 Experimental procedure	12
2-2-1 Sample preparation	12
2-2-2 Sample characterization and crystallographic properties	14
2-2-3 Mechanical properties	16
2-2-4 Electrical properties	19
2-2-5 Thermal properties	20
2-3 Results and discussion	21
2-3-1 Sample characterization and crystallographic properties	21
2-3-2 Mechanical properties	25
2-3-3 Electrical properties	35
2-3-4 Thermal properties	37
2-4 Summary	42
References	47
Tables and figures	53
 Chapter 3: MD⁷⁾ studies of actinide nitrides, nitride ADS target fuels, actinide dioxides and MA⁸⁾-containing MOX⁹⁾ fuels	 85
3-1 Background	85
3-2 Molecular dynamics techniques	85
3-2-1 Simulation algorithm	86
3-2-2 Quantum correction	87
3-2-3 Calculations of thermophysical properties	87
3-2-4 Decision of ionic model	89

3-2-5 Potential function	89
3-2-6 Conditions of calculations	90
3-3 Results and discussions of actinide nitrides and nitride ADS target fuels	90
3-3-1 Potential parameter	90
3-3-2 Thermal expansion	90
3-3-3 Bulk modulus	92
3-3-4 Specific heat capacity	92
3-3-5 Thermal conductivity	93
3-4 Results and Discussions of actinide dioxide and MA-containing oxide fuel	94
3-4-1 Potential parameter	94
3-4-2 Thermal expansion	94
3-4-3 Specific heat capacity	95
3-4-4 Thermal conductivity	97
3-5 Summary	98
References	102
Tables and figures	108
 Chapter 4: FPs¹⁰⁾ (Pd¹¹⁾, Mo¹²⁾, and Nd¹³⁾ effects on thermophysical properties of simulated high-burnup nitride fuels	 129
4-1 Background	129
4-2 Experimental procedure	130
4-2-1 Sample preparation	130
4-2-2 Sample characterization and crystallographic, mechanical, electrical and thermal properties	131
4-3 Results and discussion	131
4-3-1 Sample characteristics and crystallographic properties	131
4-3-2 Mechanical properties	134
4-3-3 Electrical properties	137
4-3-4 Thermal properties	138
4-4 Summary	142
References	146
Tables and figures	150

Chapter 5: Thermodynamics modeling of U–N¹⁴⁾ and Pu–N¹⁵⁾ binary system	177
5–1 Background	177
5–2 Thermodynamics modeling	177
5–3 Assessment method	180
5–4 Optimization results	182
5–5 Summary	182
References	184
Tables and figures	187
 Chapter 6 Conclusion	 195
 Acknowledgment	 200
Research achievements	201

- 1) UN: uranium mononitride
- 2) ADS: accelerator driven system
- 3) TiN: titanium mononitride
- 4) ZrN: zirconium mononitride
- 5) UN+60mol%TiN: Composite of UN and TiN ($Ti/(U+Ti)=0.6$)
- 6) $U_{0.4}Zr_{0.6}N$: solid solution of UN and ZrN ($Zr/(U+Zr)=0.6$)
- 7) MD: molecular dynamics
- 8) MA: minor actinides
- 9) MOX: mixed oxide
- 10) FPs: fission products
- 11) Pd: palladium
- 12) Mo: molybdenum
- 13) Nd: neodymium
- 14) U–N: uranium–nitrogen binary system
- 15) Pu–N: plutonium–nitrogen binary system

Chapter 1: General introduction

The stable supply of the primary energy resource is very important in terms of economy and industry. However, there is a big problem about it in Japan because about 80 % of the primary energy resource is imported from the other countries [1] and their countries are politically unstable. Therefore, it is very difficult to stably supply the primary energy resources such as the petroleum and natural gases. To dissolve this big problem, the nuclear power generation has been promoted in Japan from 1970's [2].

Recently the developing countries such as India and China have rapidly developed on economy and the economic development is causing the environmental disruption such as the global warming, air pollution and resource shortage such as the energy and feed. Such relationship between the economic developments, environmental disruption and resource shortage is called "Trilemma", which means three discrepancies. In particular, the global warming derived from the energy supply has rapidly become a main concern over the world. To resolve such problem, it is necessary to establish the sustainable energy supply.

The power generation method to supply the sustainable and adequate energy is only the nuclear power generation because the nuclear power generation doesn't almost emit carbon dioxide (CO₂) and generates a lot of electric power. Therefore, the nuclear power generation is reconsidered as the excellent power generation method in East Asia, Europe and U.S.A. [3]. The following segment describes the recent streams of the nuclear power generation.

A new nuclear power plant with large power (1600 MWe) has been constructed in Finland, where a new nuclear power plant had not been constructed for more 20 years due to the campaign of the abandon nuclear power generation. In whole of Europe, 11 of the new nuclear power plants are being constructed now. In U.S.A., the new plant was not constructed since the accident in TMI-2 and the spent fuel was directly disposed. However, U.S.A. is laying out the construction of 12-15 of the new nuclear power plants until 2015. In addition, U. S. A. suggested Global Nuclear Energy Partnership (GNEP) project [4] at 2006 and showed the willingness for the fast breeder reactors (FBR) and indirect disposal. In the same way, China and Korea will construct 30 and 14 of the new nuclear power plants until 2020 and 2014, respectively. In Japan, the rate of the nuclear power generation in the total energy is 31 % now. The government and FEPC (Federation of Electric Power Companies of Japan) promote the project that increases the rate of the nuclear power generation to 43 % until 2014. Such movements promoting the nuclear power generation are called the renaissance of the nuclear energy.

Chapter 1: General introduction

In addition to the advantages on CO₂ problems, there are a lot of other advantages in the nuclear energy. One of the advantages is on the economy because the generation cost of the nuclear energy is most cheap and the values is about 9 ¥/kWh [5]. In addition, it is a large advantage that the nuclear energy resource can semi-permanently become available if the fast breeder reactor (FBR) [6] is put into practice and the fissile materials such as plutonium (Pu) is bred in FBR. Namely, in the countries not to have a lot of energy resource such as Japan and France, the domestic resource can be hold by FBR.

Therefore, Japan is lying out the construction of the demonstration reactor of FBR until 2025 and commercial reactor of FBR until 2050. China has the project to construct the prototype reactor of FBR until 2020. In France, the construction of the prototype reactor of Generation IV reactor until 2020 was determined in the law at 2006. Gen IV reactor indicates the GFR (Gas-cooled Fast Reactor), VHTR (Very High Temperature gas-cooled Reactor), SCWR (Super-Critical-Water cooled Reactor), SFR (Sodium-cooled Fast Reactor), LFR (Lead-cooled Fast Reactor) and MSR (Molten Salt Reactor). Like this way, the trend promoting the FBR and Gen IV reactor is intensifying over the world. Therefore, a closed nuclear fuel cycle using the FR must be established, in which new energy resource Pu is effectively utilized with acceptable impact on the environmental caused mainly by disposal of the high level radioactive waste (HLW). At the same time, it is very important to reduce the environmental burden of HLW.

As shown in Fig. 1.1 referred from Ref. 7, the period to immunize the HLW in case of the direct disposal is several hundreds of thousand years, and that in case of P and T (Partitioning and Transmutation) of U and Pu is several thousands years. It is difficult for human to manage the HLW for such long period. In fact, the construction of the final disposal site in Yucca Mountain has been proceeding with difficulty for twenty years. On the other hand, the period in case of T and P of U, Pu and MAs (Minor Actinides: Np, Am, Cm) is about three hundreds years because Pu and MAs have high and lasting radiotoxicity, which cause the lasting environmental burden at the final disposal. It is not difficult to manage the HLW for three hundreds years. In addition, the decay heat is vastly decreased by T and P of Pu and MAs. It is the advantage for the setting area of the high level waste and material deterioration. Therefore, in a closed fuel cycle, management of MAs is a key technology.

The FBR [6] and ADS (Accelerator-Driven System) [8,9] are considered as the method of transmutation of MAs and Pu. To increase the efficiency of transmutation of MAs and Pu, inert matrix fuels not including U are considered as the good candidates of FR fuels. Various

kinds of fuels for the fast neutron system core such FBR and ADS have been proposed and studied in SUPERFACT (1995) [10], FUTURIX-FTA (2005) [11], and so on. Table 1.1 [11-23] lists a part of the candidates of the inert matrix, which dilute MAs and Pu contents instead of U. Table 1.2 shows the fuel form fabricated in SUPERFACT (1995) [10], ECRIX (1999) [16], CAMIX-COCHIX (2003) [15], and FUTURIX-FTA (2005) [11]. However, the fuel form used in FBR and ADS is not clearly determined over the world. In Japan, the oxide and metal fuels are determined as the main and sub concept fuels loaded in FBR [7]. In the oxide fuels, MA-containing MOX fuel is the most promising candidate [24].

In addition, it has been thought that the nitride fuels [25-27] are better than the oxide fuels for FBR due to the superior properties such as high melting temperature, high thermal conductivity, high chemical compatibility with SUS 316L and liquid Na, and so on [28-30]. Table 1.3 summarizes the advantages and disadvantages of nitride fuels. Recently, it was found that Np, Am and Cm form mononitride with NaCl type structure, and that their lattice parameters are close to those of UN and PuN [31]. From these researches, it is thought that actinide nitrides could easily make the solid solutions. Therefore, in case of the nitride fuel, we can flexibly change the composition of the fuel on the design of the reactor core. So, the nitride fuels with the inert matrix are considered as good candidates of the ADS target in Japan and Europe [11, 20-23].

It is very important to evaluate the thermophysical properties such as mechanical and thermal properties, when we evaluate the fuel behavior and design the fuel assembly. However, in case of the MA-containing MOX fuels and nitride fuels with the inert matrix, the thermophysical properties are not adequately studied.

In the present study, the author mainly researched the crystallographic, mechanical, thermal, electric, and thermodynamic properties of MA-containing MOX ((U,Pu, Am, Np)O₂), nitride fuels with inert matrix, and simulated high burnup nitride fuels.

References

- [1] IEA, Energy Balance of OECD Countries, 2002.
- [2] 原子力百科事典 ATOMICA, “なぜわが国は引き続き原子力発電を推進して行こうとしているのですか。” 15-01-01-02.
- [3] 電気新聞・海外原子力取材班, “原子カルネサンスの風,” 日本電気協会新聞部, 東京, 2006.
- [4] 佐賀山 豊, “GNEP 構想の行方,” エネルギーレビュー 27[2] (2007) 42-45.
- [5] 原子力百科事典 ATOMICA, “日本の原子力発電の予測,” 01-03-04-01.
- [6] 安 成弘, “高速増殖炉,” 同文書院, 東京, 1982.
- [7] 日本原子力研究開発機構: 次世代原子力システム研究開発部門, 日本原子力発電株式会社, “高速増殖炉サイクルの実用化戦略調査研究: フェーズ II 最終報告書,” JAEA-Evaluation 2006-002.
- [8] T. Sasa, H. Oigawa, K. Tsujimoto, K. Nishihara, K. Kikuchi, Y. Kurata, S. Saito, M. Futakawa, M. Umeno, N. Ouchi, Y. Arai, K. Minato, H. Takano, “Research and development on accelerator-driven transmutation system at JAERI,” Nucl. Eng. Des. 230[1-3] (2004) 209.
- [9] S. Saito, K. Tsujimoto, K. Kikuchi, Y. Kurata, T. Sasa, M. Umeno, K. Nishihara, M. Mizumoto, N. Ouchi, H. Takei, H. Oigawa, “Design optimization of ADS plant proposed by JAERI,” Nucl. Instrum. Meth. A 562 (2006) 646-649.
- [10] C.T. Walker, G. Nicolaou, “Transmutation of neptunium and americium in a fast neutron flux: EPMA results and KORIGEN predictions for the superact fuels,” J. Nucl. Mater. 218 (1995) 129-138.
- [11] L. Donnet, F. Jorion, N. Drin, S.L. Hayes, J.R. Kennedy, K. Pasamehmetoglu, S.L. Voit, D. Haas, A. Fernandez, “The FUTURIX-FTA experiment in PHENIX: Status of fuel fabrication,” Proc. Int. Conf. GLOBAL2005, Tsukuba, Japan, Oct. 9-13, 2005, Paper No. 258.
- [12] J. Wallenius, “Neutronic aspects of inert matrix fuels for application in ADS,” J. Nucl. Mater. 320 (2003) 142-146.
- [13] V.V. Rondinella, T. Wiss, H. Matzke, R. Mele, F. Bocci, P.G. Lucuta, “Radiation damage and simulated fission product effects on the properties of inert matrix materials,” Prog. Nucl. Energ., 38[3-4] (2001) 291-294.
- [14] N. Boucharat, A. Fernandez, J. Somers, R.J.M. Konings, D. Haas, “Fabrication of zirconia-based targets for transmutation,” Prog. Nucl. Energ., 38[3-4] (2001) 255-258.
- [15] Y. Croixmarie, E. Abonneau, A. Fernandez, R.J.M. Konings, F. Desmouliere, L. Donnet, “Fabrication of transmutation fuels and targets: the ECRIX and CAMIX-COCHIX experience,” J. Nucl. Mater. 320 (2003) 11-17.

Chapter 1: General introduction

- [16] J.C. Garnier, N. Schmidt, N. Chauvin, A. Ravenet, J.M. Esclaine, C. Molin, F. Varaine, C. De Saint Jean, T. Philip, G. Vambenepe, G. Chaigne, "The ECRIX experiments," Proc. Int. Conf. GLOBAL99, Jackson Hole, U.S.A., 1999, paper No. 206.
- [17] E.A.C. Neeft, K. Bakker, R.L. Belvroy, W.J. Tams, R.P.C. Schram, R. Conrad, A. van Veen, "Mechanical behavior of macro-dispersed inert matrix fuels," J. Nucl. Mater. 317 (2003) 217–225.
- [18] 矢野 豊彦, 逢坂 正彦, 滑川 卓志, "Si₃N₄を母材とした Am 含有ターゲット燃料製造プロセスの開発," JNC-TY9400 2004-002.
- [19] D. Haas, A. Fernandez, C. Nastren, D. Staicu, J. Somers, W. Maschek, X. Chen, "Properties of cermet fuels for minor actinides transmutation in ADS," Energ. Convers. Manage. 47 (2006) 2724–2731.
- [20] K. Minato, M. Akabori, M. Takano, Y. Arai, K. Nakajima, A. Itoh, T. Ogawa, "Fabrication of nitride fuels for transmutation of minor actinides," J. Nucl. Mater. 320 (2003) 18–24.
- [21] M. Streit, F. Ingold, M. Pouchon, L.J. Gauckler, J.-P. Ottaviani, "Zirconium nitride as inert matrix for fast systems," J. Nucl. Mater. 319 (2003) 51–58.
- [22] K. Wheeler, P. Peralta, M. Parra, K. McClellan, J. Dunwoody, G. Egeland, "Effect of sintering conditions on the microstructure and mechanical properties of ZrN as a surrogate for actinide nitride fuels," J. Nucl. Mater. 366 (2007) 306–316.
- [23] Y. Arai, K. Nakajima, "Preparation and characterization of PuN pellets containing ZrN and TiN," J. Nucl. Mater. 281 (2000) 244–247.
- [24] T. Namekawa, K. Kawaguchi, K. Koike, S. Haraguchi, S. Ishii, "Conceptual design study and evaluation of advanced fuel fabrication systems in the feasibility study on commercialized FR fuel cycle in Japan," Proc. Int. Conf. GLOBAL2005, Tsukuba, Japan, Oct. 9–13, 2005, paper No. 424.
- [25] H. Matzke, "Science of Advanced LMFBR Fuels: solid state physics, chemistry, and technology of carbides, nitrides, and carbonitrides of uranium and plutonium," Elsevier Science Pub. Co., Amsterdam, North-Holland, 1986.
- [26] D. Brucklacher, W. Dienst, T. Dippel, O. Goetzmann, P. Hofmann, H. Holleck, H. Kleykamp, W. Siebmans, F. Thuemmler, "Basic work on advanced ceramic nuclear fuel," Neue Technik. 13[7] (1971) 299–307.
- [27] 半田宗男, 福島奨, 岩井孝, "高速炉燃料の特性および照射挙動," 日本原子力学会誌 31 (1989) 886–893.
- [28] A.A. Bauer, P. Cybulsis, J.L. Green, "Mixed-nitride fuel performance in EBR-II," Adv. LMFBR Fuels Top. Meet. Proc., 1977, 299–312.

Chapter 1: General introduction

[29] D. Brucklacher, Fak. Maschinenbau, "Examination of the creep behavior of ceramic fuel elements under neutron irradiation," Fed. Rep. Ger. Avail. INIS. Report [INIS-mf-5402] (1978) 101-128.

[30] A.K. Sengupta, C. Ganguly, "Plutonium uranium nitride ($\text{Pu}_{0.7}\text{U}_{0.3}\text{N}$) fuel for fast breeder test reactor – thermal conductivity and chemical compatibility with SS 316 and sodium," T. Indian I. Metals, 43 [1] (1990) 31-35.

[31] R.G. Haire, "Preparation, properties, and some recent studies of actinide metals," J. Less-Common Metals 121 (1986) 379.

Table 1.1 Candidates of inert matrix [11–23]

Chemical form of Pu and MAs	Form	Matrix
Oxide	Solid solution	ZrO ₂ [Wallenius (2003)]
		CeO ₂ [Rondinella (2001)]
		YSZ [Boucharat (2001), Croimarie (2003)]
	Composite	MgO
		[Donnet (2005), Garnier (1999), Croimarie (2003)]
		Y ₂ O ₃ [Neeft (2003)]
		MgAl ₂ O ₄ [Rondinella (2001)]
		ZrSiO ₄ [Rondinella (2001)]
		Y ₃ Al ₄ O ₁₂ [Neeft (2003)]
		Si ₃ N ₄ [Yano (2004)]
		W [Wallenius (2003)]
		Cr [Wallenius (2003)]
		Mo [Donnet (2004), Haas (2006)]
Nitride	Solid solution	ZrN [Wallenius (2003), Minato (2003), Streit (2003), Wheeler (2007)]
		HfN [Wallenius (2003)]
	Composite	TiN [Minato (2003), Arai (2001)]
Metal	Composite	Zr [Donnet (2005)]

Table 1.2 MAs-containing fuels fabricated in MAs transmutation projects [10,11,15,16]

Type	Composition	Program name
Oxide	(U,Pu,Am)O ₂ (U,Pu,Np)O ₂ (U,Am,Np)O ₂ (U,Np)O ₂	SUPERFACT [Walker (1995)]
Metal	U–Pu–Am–Np–Zr	FUTURIX–FTA
Metal without U	Pu–Am–Zr	[Donnet (2004)]
Nitride	(U,Np,Pu,Am)N	FUTURIX–FTA
Nitride without U	(Pu,Am,Zr)N	[Donnet (2004)]
CERMET without U (CERamic & METal)	(Pu,Am)O ₂ +Mo (Pu,Am,Zr)O ₂ +Mo	FUTURIX–FTA [Donnet (2004)]
CERCER without U (CERamic & CERamic)	AmO ₂ +MgO	ECRIX [Garnier (1999)]
	(Am,Zr,Y)O+MgO	CAMIX–COCHIX [Croimarie (2003)]
	(Pu,Am)O ₂ +MgO [Donnet]	FUTURIX–FTA [Donnet (2005)]

Chapter 1: General introduction

Table 1.3 Advantages and disadvantages of nitride fuel

Advantages	Brief meanings
High thermal conductivity	High economical efficiency and safety
High melting point	High safety
High metallic density	High neutron efficiency
Formation of solid solution of actinide nitrides	High flexibility of fuel components
Low fission gas release	High safety
High mechanical property	High economical efficiency and safety
High electrical conductivity	Easiness for electrolysis dry reprocessing
Etc.	

Disadvantage	Solvent method
N-14 changes C-14 by the nuclear reaction.	Development of technique to enrich N-15 with low cost
Shortage of the following data	Fundamental research of
① Physical properties of high-burnup nitride fuel	thermodynamics and
② Physical properties of minor actinide nitrides	thermophysical properties of
③ Physical properties of nitride inert matrix fuels	nitride fuels by experiment and
④ FCI phenomena (Melting fuel and cladding interaction)	simulation

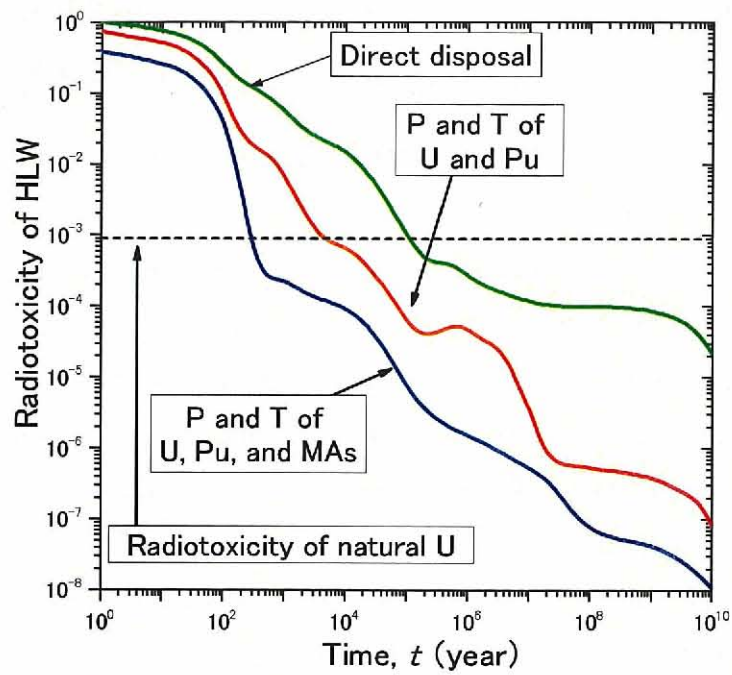


Fig. 1.1 Time dependence of radiotoxicity of HLW referred from Ref. 7

(P and T: Partitioning and Transmutation)

Chapter 2: Experimental evaluation of thermophysical properties of UN, simulated ADS target fuels (UN+TiN (U:Ti=4:6) and $U_{0.4}Zr_{0.6}N$) and inert matrix material (TiN and ZrN)

2-1 Background

The nitride fuel is a good candidate of the fuel used in the fast neutron system. In particular, the nitride fuel has the high potential as the ADS (Accelerator Driven System) target fuels [1, 2]. In case of the ADS target fuel, the inert matrix is needed instead of uranium to prevent the breeding of MAs and Pu from ^{238}U by the nuclear reaction. As the inert matrix of the nitride fuels, it is thought that zirconium nitride (ZrN) [2-4] and titanium nitride (TiN) [3, 4] are the best candidates of the homogeneous mode and heterogeneous, mode respectively. It is because ZrN and TiN have the superior properties such as high chemical stability, high thermal conductivity and so on. However, the thermophysical properties of ZrN and TiN have been scarcely evaluated because it is very difficult to prepare the high-density bulk samples of ZrN and TiN due to their high sintering resistivity. Therefore, most of the researches on the physical properties of ZrN and TiN have been performed on thin films [5-8]. Thus, before we discuss the thermophysical properties of ADS target fuels ((Pu,Np,Am,Zr)N and (Pu,Np,Am)N+TiN), it is necessary to evaluate the thermophysical properties of ZrN and TiN. In addition, it is also necessary to know the porosity dependences of the thermophysical properties because the density of the fuel pellets decreases with increasing the burnup.

In this chapter, the author evaluates the thermophysical properties of ZrN and TiN at first. In case of the properties such as the thermal conductivity and Young's modulus, which are influenced by the porosity, the data of the porosity-free materials were estimated from the porosity dependences. Next, the author evaluates the effect of the inert matrix (= ZrN and TiN) on the thermophysical properties of simulated ADS target fuels. In addition, the thermophysical properties of UN are also evaluated for comparison. ADS target fuels are practically consisted of the solid solution or composite of PuN, NpN, AmN and CmN, and the inert matrix. However, it takes a lot of cost and time to use Pu and MAs. Instead of the actual ADS target fuel [(Pu,Np,Am,Zr)N and (Pu,Np,Am)N+TiN], $U_{0.4}Zr_{0.6}N$ and UN+60mol%TiN are used as the simulated ADS target fuels in the present study to evaluate the interaction between actinide nitrides and inert matrix (ZrN and TiN).

2-2 Experimental procedure

2-2-1 Sample preparation

UN

There are two methods in preparation methods of UN powder. One is nitriding of uranium hydride (UH₃) at high temperature and nitrogen atmosphere after hydriding of metal U. Another is the carbothermic reduction of UO₂. In the former method, the process becomes to be complex because it is not easy to prepare the metal uranium and it is difficult to handle the powder sample of metal uranium and uranium hydride due to their low oxidation resistivity. In case of the latter method, we can easily prepare a lot of UN powder, but must address that the sample prepared by the carbothermic reduction sometimes includes the high impurity oxygen content and carbon content. In the present study, UN pellet was prepared by the carbothermic reduction and atmospheric pressure sintering because their preparation methods are industrially advantageous.

UO₂ powder was obtained from the reduction and roasting of ADU (Ammonium DiUranate: (NH₄)₂U₂O₇) to adjust the specific surface area and ratio of O/M. Table 2.1 summarizes the specific surface area and O/M ratio of UO₂ powder before the carbothermic reduction. UO₂ powder and activated carbon powder with the specific surface area of about 800 m²/g were mixed at a molar ratio of C/U=2.4. Not to remain the oxide phase in the product, the excess activated carbon powder was added to UO₂ powder. The green pellet (T12 mm×φ 12 mm) for the conversion was obtained by the press at 294 MPa at room temperature and 2.5% polyvinyl alcohol (PVA) was used as the binder.

The green pellet of UO₂ and activated carbon were heated at 1773 K under N₂ atmosphere with a flow rate of 10 l/min for 8 hours to convert from UO₂ to UN by the following chemical reaction;



Successively, the green pellet was heated at 1773 K under N₂+5% H₂ atmosphere with a flow rate of 10 l/min for 8 hours to remove the residual carbon as CH₄. After the carbothermic reduction, UN powder was crushed by wet type ball milling used hexane for 40 hours. In the ball milling, the ball and pod made of tungsten carbide (WC) were used.

The green pellet (T10 mm×φ 10 mm) of UN for the sintering was obtained by the press under 196 MPa. As the binder, the author used the solution of polyethyleneglycol 6000 and trichloroethylene. Polyethyleneglycol 6000 was added to UN powder with 0.25 wt.%. The green

pellet was sintered at 2073 K under Ar atmosphere with a flow rate of 3 l/min for 4 hours and UN pellet was obtained. These sample preparation and measurements of oxygen, nitrogen and carbon contents were performed in the high-purity glove box, where O_2 and H_2O contents were below 10 and 40 wt.ppm, respectively.

$U_{0.4}Zr_{0.6}N$

$U_{0.4}Zr_{0.6}N$ pellet was fundamentally made by the same method of UN pellet. There are some different points between the preparation of UN and $U_{0.4}Zr_{0.6}N$. The largest different point is the direct conversion from the mixed powder of UO_2 and ZrO_2 to the solid solution ($U_{0.4}Zr_{0.6}N$) by the carbothermic reduction. The other different points are summarized in Table 2.1.

UN+60mol%TiN

In case of UN+60mol%TiN pellet, UN powder was prepared by the carbothermic reduction in the same way of the preparation of UN and $U_{0.4}Zr_{0.6}N$ powder. On the other hand, TiN powder was prepared by heating of TiH_2 powder at 1673 K under N_2 atmosphere with a flow rate of 3 l/min for 3 hours. TiH_2 powder was prepared by heating of metal Ti at 713 K in Ar+8% H_2 atmosphere with a flow rate of 3 l/min for 30 min. UN and TiN powder was crushed and blended by the ball milling for 40 hr. In this time, the molar ratio of TiN/(UN+TiN) decided to be 0.6. The other different points are summarized in Table 2.1.

ZrN and TiN

The high density samples of TiN and ZrN could not be obtained by the atmospheric pressure sintering used in the sintering of UN, $U_{0.4}Zr_{0.6}N$ and UN+60%TiN. Therefore, in the present study, the spark plasma sintering (SPS) was used to prepare the high density samples of ZrN and TiN. In the SPS, the large pulse current is given to the green pellet. In the grain boundary, the spark plasma, which temperature reaches at 10000 K in a instant, generates from the spark discharge phenomenon. By utilizing the energy of the spark plasma to the thermal and electric field diffusion, the sintering temperature in the SPS process is lower than that in the pressureless sintering process. The schematic of the SPS is shown in Fig. 2.1.

ZrN (99.9%) powder was supplied from Soekawa Chemical Co. Ltd. The powder was placed into a 20 mm diameter graphite die and given a spark plasma sintering (SUMITOMO COAL MINING, Dr Sinter SPS-1020) at 1773, 1873 and 2073 K for 5 min under nitrogen atmosphere.

TiN (99.5%) powder was supplied from Furuuchi Chemical Co. Ltd. In the same way of ZrN, TiN powder was sintered by the SPS at 1648, 1873, 1973, and 2073 K for 5 min under nitrogen atmosphere.

Surface treatment

For all samples of UN, $U_{0.4}Zr_{0.6}N$, UN+60%TiN, ZrN, and TiN, the mechanical polishing was performed using SiC polishing papers with 120, 240, 400, 800 and 1200 grids and Al_2O_3 powders. The grain sizes of Al_2O_3 powder were 1.0, 0.3 and $0.05\mu m$. Finally, the mechano-chemical polishing was performed using Al_2O_3 powder with the grain size of $0.05\mu m$ in alkaline solution (pH=9.0) to remove the surface altered layer such as oxidized surface layer and strain-hardening layer generated from the mechanical polishing.

2-2-2 Sample characterization and crystallographic properties

X-ray diffraction analysis

The crystal structures of all samples were analyzed by a powder and bulk XRD (X-Ray Diffraction) measurements (Rigaku Co. Ltd., RINT2000) using Cu-K α radiation at room temperature. The powder samples before the sintering were mixed with the epoxy resin and mounted on a folder for the XRD measurement in order to keep from oxidation. The bulk samples after sintering were mounted on a folder for the XRD measurement. The lattice parameters were calculated from the obtained XRD patterns using Nelson-Reiley method [9].

Surface observation and crystallographic properties

The surface observations were performed for the mechano-chemical polished samples by the optical microscope (OLYMPUS, BMX51M), SEM (Scanning Electron Microscope) (HITACHI, S-2600H), FE-SEM (Field Emission Scanning Electron Microscope) (JEOL, JSM6500F) SLM (confocal Scanning Laser Microscope) (OLYMPUS, OLS3100). The surface roughness was evaluated by an AFM (Atomic Force Microscope) (JEOL, JSPM-4210). By the EBSP (Electron Backscattering Diffraction Pattern) (JEOL, OIM400), the Kikuchi pattern as shown in Fig. 2.2 is observed at each point in the bulk samples. The crystal direction of each point was revealed from the Kikuchi pattern, and the crystallographic properties such as the grain size and misorientation angle were evaluated. The quantity and distribution of each element (U, Zr, Ti) were evaluated by the EDX (Energy Dispersive X-ray fluorescence spectrometer) (HORIBA, EMAX-7000). The oxygen, nitrogen and carbon contents of the bulk sample were measured by a differential thermal conductivity method (LECO, TC-436 (O_2 and N_2) and LECO IR-412 (C)).

Minimum solid area (MSA)

For the Young's modulus, thermal conductivity, electrical conductivity and so on, various equations to evaluate the porosity (P) influence had been suggested. Eq. 2.2-4 [10]

represent a part of such equations;

$$A_p = A_0 \exp(-\beta P), \quad (2.2)$$

$$A_p = A_0 \frac{1-P}{1+\beta P}, \quad (2.3)$$

$$A_p = A_0 (1-P)^\beta. \quad (2.4)$$

In these equations, A_p and A_0 are the values of the Young's modulus, thermal conductivity with the porosity of P and 0, respectively. β is a constant and the correction factor, which depends on the crystal structure, sintering method and so on.

Fig. 2.3 shows the porosity dependence of Young's modulus of fused silica referred from Ref. 11. In this figure, the differences of the plot colors represent the differences of the preparation method. From this figure, it is understood that the β is changed by the preparation method, and that it is very important to evaluate the β . However, we can't evaluate the β from the results of only one sample because the porosity represents only the quantity of the pores. Therefore, it is effective to consider the porosity parameters, which is independent of the porosity. Rice (1993) [12] suggested that the β could be determined from the MSA (Minimum Solid Area) as shown in Fig. 2.4.

In the present study, the author took notice to the MSA. The reason is described in the following segment.

The β is determined by various porosity parameters. As the porosity parameters, the following properties are considered.

1. Pore size and pore shape
2. Coordination number of pore
3. Distinction of open porosity or closed porosity
4. Distinction of intergranular pore or intragranular pore
5. Pore distribution
6. MSA

To evaluate the porosity dependences, we must choose the porosity parameter. However, 3rd, 4th and 5th candidates strongly depend on the porosity. The details are described in "Porosity of ceramics [10]". So, MSA or the shape and size of pore could be the second parameters. It is very complex to determine the shape and size of pore. As shown in Fig. 2.5 referred from Ref. 10, the shape and size of pore change by the cross section even if the stacking of the grain is very

simple. Therefore, it is very practical and useful to use MSA when we evaluate the porosity dependences of the thermophysical properties. In particular, when the various grains stack in the samples, MSA equals to the average area function of the grain. It is difficult to evaluate the MSA by the SEM and optical microscope because their images don't include the information about the height. Therefore, Rice (1993) [12] only suggested the theory of the MSA and didn't implement its theory. In the present study, the MSA could be evaluated by the SLM observation, which includes the information of the height, and the author related the β to MSA for the first time.

2-2-3 Mechanical properties

Ultrasonic pulse-echo measurement

Ultrasonic pulse-echo measurements were performed for the polished-bulk samples using the echometer (NIHON MATECH, Echometer 1062) to evaluate the longitudinal and shear sound velocities (V_L and V_S). The schematic of this apparatus is shown in Fig.2.6. The sound velocity of the sample was evaluated from the sample length and separation time between ultrasonic echoes obtained from the Echometer. The glue joint between transducer and sample was Sonicoat-SHN13. Using the longitudinal and shear sound velocity, we can evaluate the Poisson's ratio (ν), Young's modulus (E), Shear modulus (G), bulk modulus (B) and Debye temperature (θ_D) by Eq. 2.5-9 [13];

$$\nu = \frac{1}{2} \cdot \frac{V_L^2 - 2V_S^2}{V_L^2 - V_S^2}, \quad (2.5)$$

$$G = \rho V_S^2, \quad (2.6)$$

$$E = G[2(1+\nu)], \quad (2.7)$$

$$B = E/[3(1-2\nu)], \quad (2.8)$$

$$\theta_D = \left(\frac{h}{k_B} \right) \left(\frac{3N}{4\pi V_m} \right)^{\frac{1}{3}} \left(\frac{3}{\frac{1}{V_L^3} + \frac{2}{V_S^3}} \right)^{\frac{1}{3}}, \quad (2.9)$$

where ρ , h , k_B , V_m and N represent the sample density, Planck constant, Boltzmann constant, molar volume and atomic number in the unit cell.

Vickers hardness measurement

Vickers hardness was evaluated by Vickers hardness test (MATSUZAWA SEIKI, MHT-1). Vickers hardness was measured by forcing a Vickers type diamond indenter into the surface of the

specimen and observation of the impression. In the present study, load and unload time were 15 seconds and the load was 9.8 N. Measurements were repeated 16 times, and the average values were obtained from the data excluding the maxima and minima. This measurement method is determined by JIS R 1610 [14]. The Vickers hardness is obtained by the following equation;

$$H_V = 1.854 \frac{F}{d^2}, \quad (2.10)$$

where F and d are the load and length of the diagonal line of the Vickers impression. The impression image by Vickers hardness test is shown in Fig. 2.7, together with the impression of the indentation test.

In case of ceramics, fracture toughness is generally evaluated from an indentation fracture (IF) method using the length of the microcrack generated from the vertex of the Vickers impression because the sample size is very small in IF method and the method is nearly the nondestructive test. However, the fracture toughness of UN had not been evaluated because the microcrack is scarcely generated in Vickers impression and the length is very short in case of UN when the load is lower than 9.8 mN. In the present study, the author could observe the microcrack in UN sample using the high-resolution SLM. The fracture toughness was calculated using Evans & Charles equation (Eq. 2.11) [15] or Niihara equation (Eq. 2.12) [16],

$$K_{IC} = 0.057 \left(\frac{E}{H_V} \right)^{0.4} H_V a^{0.5} \left(\frac{C}{a} \right)^{-1.5} \quad (C > 2.5a), \quad (2.11)$$

$$K_{IC} = 0.0181 E^{0.4} H_V^{0.6} a^{0.5} \left(\frac{C}{a} - 1 \right)^{-0.5} \quad (C < 2.5a), \quad (2.12)$$

where E , H_V , a and C are Young's modulus, Vickers hardness, half of the diagonal length of Vickers impression, and length of the microcrack. As the value of E , the Young's modulus evaluated from the ultrasonic pulse echo method was used.

Indentation measurement

An indentation test suggested by Oliver (1992) [17] to measure the load-displacement curve has been recently developed to evaluate the hardness and Young's modulus. The displacement of the indenter is continuously monitored and a load-displacement history of the indentation is recorded. From the load-displacement curve, we can measure the nanoscale and/or sub-microscale mechanical properties. Therefore, the indentation test allows us to evaluate the mechanical properties at the local point and individual phase in a microstructure.

In order to evaluate the potential of the nitride fuel, a lot of researches have performed

to evaluate the macroscale properties of polycrystalline uranium nitride (UN). However, the inert matrix such as TiN and fission products (FP) such as platinum family elements make the microstructure of the nitride fuel to be complex [3, 18–20]. Thus, it is difficult to estimate the mechanical properties of the high-burnup fuels and inert matrix fuels from the results of the macroscale measurement such as the ultrasonic pulse echo method, Vickers hardness test and so on. Therefore, the author thought that it is very important to evaluate not only macroscale properties, but also the sub-microscale properties. In addition, the values of elastic moduli and Vickers hardness obtained from the ultrasonic pulse-echo measurement and Vickers hardness test depend on the porosity and grain size. So we cannot compare the results obtained from the samples with the different porosity and grain size. On the other hand, the results of the indentation test don't almost depend on the porosity, since the indentation size is sub-micro scale and vastly lower than the grain size as shown in Fig. 2.7(b). In the present study, the indentation tests were performed to evaluate the porosity-free mechanical properties at the sub-microscale of UN, ZrN, TiN, U_{0.4}Zr_{0.6}N and UN+60mol%TiN. In case of UN+60mol%TiN, the author evaluated the mechanical properties of each phase (UN and TiN phases) by the indentation test.

The indentation tests were performed at room temperature using an AFM (JEOL Co., JSPM-4210) with a Triboscope (Hysitron Inc.). Fig. 2.8 shows the appearance of AFM apparatus and nanoindentation system. Fig. 2.9 shows the SEM image and characteristics of the Berkovich type diamond indenter used in the present study. The load range and loading time were from 2.0 to 1960 mN and 15 s. Fused silica with Young's modulus of 72 GPa was used to calibrate the indenter area function using the following equation suggested by Oliver (1992) [17].

$$A_c = 24.5h_c^2 + \sum_{i=1} C_i h_c^{2-i} \quad (2.13)$$

where A_c , h_c and C_i are the contact area, contact depth and correction factor. C_i reflects the misalignment of the indenter used in the present study from the ideal Berkovich indenter.

According to Oliver and Pharr model [17], the load-displacement data was analyzed to determine the reduced Young's modulus (E_r) and the indentation hardness (H_{it}) as followings. After an indentation test, the load-displacement curve is obtained as shown in Fig. 2.10. The indentation hardness is defined by dividing the maximum load (F_{max}) by the contact area (A_c) as the following equation;

$$H_{it} = \frac{F_{max}}{A_c} . \quad (2.14)$$

The stiffness (S) is equal to the slope of the unloading curve (dF/dh) given by;

$$S = \frac{dF}{dh} = \frac{2}{\sqrt{\pi}} E_r \sqrt{A_c} . \quad (2.15)$$

The reduced Young's modulus is described by the following equation;

$$\frac{1}{E_r} = \left(\frac{1-\nu_s^2}{E_s} \right) + \left(\frac{1-\nu_i^2}{E_i} \right) \quad (2.16)$$

where E and ν are the elastic modulus and Poisson's ratio, and subscripts s and i represent the sample and indenter. E_i and ν_i are respectively 1140 GPa and 0.07, and ν_s can be measured by the ultrasonic pulse-echo measurement because ν_s is not almost affected by the porosity [10]. Using this equation and the results of ultrasonic pulse-echo measurement, the author evaluated E_s .

In case of ZrN and TiN, the bulk samples with various porosities are prepared, but the indentation tests were performed for the highest-density samples of ZrN and TiN because the indentation test is almost independent of the porosity.

2-2-4 Electrical properties

The electrical conductivity and thermoelectric power were measured by a direct current four probe method and stationary direct current method using ULVAC ZEM-1, respectively. The electrical conductivity and thermoelectric power were measured from 320 to 1000 K in He atmosphere. In these measurements, two thermocouples (A and B) are attached to the sample, and Ni electrodes with small heaters were mechanically attached to both sides of the sample. In the sample, the small heaters generate the sample temperature gradient (upper and down sides are with low and high temperature). The thermocouples measured not only the temperature of hotter and cooler sides of the sample but also the voltage between A and B. Electrical conductivity (σ) and thermoelectric power ($T.P.$) of the samples were measured by using the following equations;

$$\frac{1}{\sigma} = \frac{1}{\sigma_{Ref}} \frac{V_{Ref}}{V} \frac{s}{L} , \quad (2.17)$$

$$T.P. = \frac{\Delta V}{T_B - T_A} . \quad (2.18)$$

In Eq. 2.17, σ_{Ref} and V_{Ref} is the electrical conductivity and voltage of the reference resistor, and V is the voltage of the sample. s is the area of cross section of the sample and L is the distance between two electrodes. In Eq. 2.18, ΔV is the voltage difference between the thermocouples A with the temperature T_A and B with the temperature T_B .

2-2-5 Thermal properties

Thermal expansion

The thermodilatometry measurement (BRUKER AXS, TD5020SA) was performed to measure the thermal expansion, and carried out in a high purity nitrogen atmosphere with a flow rate of 50 ml/min. The heating rate was 5 K/min. The column-shaped sapphire was used as the reference sample.

Specific heat capacity

The specific heat capacity was measured from 473 to 1273 K by a differential scanning calorimeter (ULVAC-RIKO Inc., Triple-cell DSC). This apparatus developed by Takahashi (1993) [22], has a “triple-cell” system and adiabatic temperature control system. In this apparatus, three cells for sample, reference material and empty pan are used. The temperature differences between sample-empty and reference-empty are detected by thermocouples under the condition of constant heating rate. The specific heat capacity of the sample is determined by comparing each signal.

The specific heat capacity measurement was carried out in a high purity argon (>99.999 %) atmosphere with a flow rate of 100 ml/min. The three cell was heated at 5 K/min. The column-shaped sapphire was used as the reference sample. The specific heat capacity was calculated by a scanning method. The principle of the apparatus is briefly summarized in Ref. 22.

Thermal diffusivity

In the temperature range from room temperature to 1473 K, the thermal diffusivities of the samples were measured by the laser flash method using ULVAC TC-7000 in vacuum (10^{-4} Pa). The technique is based on transiently heating the surface of the sample with an energy pulse from a ruby laser. Subsequently, the temperature change on the opposite surface is monitored with an indium antimonide infrared detector.

In the present study, the thermal diffusivity (D) was determined by a half-time method. In the half time method, D is calculated by the following equation.

$$D = 1.37 \frac{L^2}{\pi^2 t_{1/2}} \quad (2.19)$$

where $t_{1/2}$ is the time to reach at the half of the maximum temperature near the surface of the sample, and L is the thickness of sample.

Thermal conductivity

The thermal conductivity (κ) was calculated by the following equation;

$$\kappa = C_p D \rho / M, \quad (2.20)$$

where ρ is the density of sample, which was calculated from the geometrically method and thermal expansion data.

2-3 Results and discussion

2-3-1 Sample characteristics and crystallographic properties

Sample preparation

From the carbothermic reduction and atmospheric pressure sintering, the high-density bulk samples of UN (92.2 %T.D.), U_{0.4}Zr_{0.6}N (86.8 %T.D.) and UN+60mol%TiN (92.8%T.D.) were obtained. Their oxygen, nitrogen and carbon contents are summarized in Table 2.2. From Table 2.2, it was found that the impurity oxygen and carbon contents of U_{0.4}Zr_{0.6}N is about four times of those of UN and UN+60mol%TiN because the conversion temperature, conversion time, crush time, sintering time of U_{0.4}Zr_{0.6}N were quite higher and longer than those of UN and UN+60mol%TiN (see Table 2.1) due to the high sintering resistivity of ZrN. The high impurity oxygen content may influence the thermophysical properties of U_{0.4}Zr_{0.6}N and the influence is described at later.

Hayes (1990) [23-26], Ross (1988) [27] and so on evaluated the porosity dependences of various thermophysical properties of UN prepared by the atmospheric pressure sintering. If the sintering condition, crystal structure and so on are same, β in Eq. 2.2-2.4 takes the similar values. Therefore, in the present study, it is assumed that β of UN suggested by Hayes (1990) [23-26], Ross (1988) [27] and so on is same to those of U_{0.4}Zr_{0.6}N and UN+60mol%TiN. On the other hand, there are no data of the porosity dependences of the thermophysical properties of the metal nitride such as TiN and ZrN prepared by the SPS. Therefore, some bulk samples of ZrN and TiN with various densities were prepared by the SPS to evaluate the porosity dependences of the thermophysical properties. The densities of the bulk samples of ZrN and TiN were (82.5, 91.1 and 93.5%T.D.) and (71.6, 87.5, 89.8 and 94.0 %T.D.), respectively. Their sample characteristics

were summarized in Table 2.2 and 2.3. In the present study, theoretical densities were determined from the crystal structure and lattice parameters obtained from XRD analysis.

X-ray diffraction

There were no differences between powder XRD patterns and bulk XRD patterns for all samples. The bulk XRD patterns of UN, $U_{0.4}Zr_{0.6}N$, ZrN, UN+60mol%TiN and TiN are shown in Fig. 2.11 and 12, together with the JCPDS (Joint Committee on Powder Diffraction Standards) data [28–33]. In these figures, the peaks of the oxide were not found and the XRD patterns of UN, ZrN and TiN agreed with the JCPDS data. From the XRD pattern of $U_{0.4}Zr_{0.6}N$, it was thought that UN and ZrN make a solid solution. On the other hand, the peaks of UN and TiN were observed in the XRD pattern of UN+60mol%TiN.

From these XRD patterns, the lattice parameters were calculated. The lattice parameter of each sample is shown in Table 2.2 and 2.3 and the lattice parameters of ZrN and TiN were independent of the density of the samples. Zr or Ti content dependences of the lattice parameters of UN, $U_{0.4}Zr_{0.6}N$, ZrN, UN+60mol%TiN and TiN were shown in Fig. 2.13 and 2.14. From these figures, it was found that the lattice parameters of UN, ZrN and TiN are well consistent with the JCPDS data. It was confirmed that $U_{0.4}Zr_{0.6}N$ is the solid solution of UN and ZrN because the lattice parameter of $U_{1-x}Zr_xN$ follows to Vegard's law. The lattice parameters of UN phase and TiN phase in UN+60mol%TiN pellet correspond to those of UN and TiN pellets, respectively. Judging from this result, UN didn't chemically react with TiN at all.

Surface observation and MSA (Minimum Solid Area)

In the SLM, SEM and EDX analysis, the segregations of particular elements and precipitation could not be observed in case of UN, $U_{0.4}Zr_{0.6}N$, ZrN and TiN. On the other hand, in case of UN+60mol%TiN, the segregation of U and Ti elements were clearly observed as shown in Fig. 2.15 and 2.16, in which the dark and light zone in the SEM and SLM image were UN and TiN phase. The SLM, SEM and EDX analysis proved that UN and TiN don't make a solid solution.

Fig. 2.17(a) and (b) show the SLM image and MSA of ZrN with the density of 82.5%T.D. In the present study, the author considered that the zone lower than the average height above 200 nm is the pore. In Fig. 2.17(b), the green zone is the pore and the black zone is MSA. The MSA of each sample was evaluated in the same way. Fig. 2.18 shows the porosity dependences of MSA. For all samples, the values of MSA at $P=0$ equal to 1. As shown in this figure, the value of MSA was evaluated for the first time over the world in the present study. In Fig. 2.18, the data points of UN, $U_{0.4}Zr_{0.6}N$ and UN+60mol%TiN could be fitted by the same equation. Therefore, the

porosity dependences of the thermophysical properties of $U_{0.4}Zr_{0.6}N$ and UN+60mol%TiN would be same to those of UN suggested by Hayes (1990) [20–23], Ross (1988) [24] and so on. On the other hand, the MSA of ZrN and TiN linearly decreased with increasing the porosity along to the different equation from UN, $U_{0.4}Zr_{0.6}N$ and UN+60mol%TiN. These differences are derived from the sintering condition, mechanical properties, and chemical properties and so on. The porosity dependences of the MSA of UN, $U_{0.4}Zr_{0.6}N$, UN+60mol%TiN, ZrN and TiN are represented by the following equations;

$$\text{UN, } U_{0.4}Zr_{0.6}N, \text{ UN+60mol\%TiN: } A' = \exp(-0.90P) \quad (0 < P < 0.2), \quad (2.21)$$

$$\text{ZrN: } A' = \exp(-1.50P) \quad (0 < P < 0.2), \quad (2.22)$$

$$\text{TiN: } A' = \exp(-1.09P) \quad (0 < P < 0.3), \quad (2.23)$$

where A' is the MSA and P is the porosity. In these equations, the constant (β) at the front of P is the coefficient of the porosity dependence of the MSA. In the present study, it is called β_{MSA} . β_{MSA} of UN ($=0.90$) was smaller than those of ZrN ($=1.50$) and TiN (1.09). This phenomenon would be resulted from the differences between the sintering methods. The deformation of TiN grain by the SPS pressure would be smaller than that of ZrN because the mechanical properties and sintering resistivity of TiN are higher and lower than those of ZrN, respectively. This is the reason of the differences between β_{MSA} of ZrN and TiN. The author thinks that β_{MSA} strongly relate to the porosity dependences of the thermophysical properties such as elastic properties, electrical conductivity and thermal conductivity. The relationship is described later.

From the AFM observation, the surface roughness was evaluated as shown in Fig. 2.19. The arithmetic average surface roughness of each sample is summarized in Table 2.2 and 2.3. Their values were lower than 3 nm and are adequately lower than the indentation depth (>50 nm). So, it is thought that the surface roughness doesn't influence the indentation tests.

Crystallographic properties

Fig. 2.20–24 show the SEM image, IQ (Image Quality) map and CD (Crystal Direction) map of each sample. Their IQ and CD map were obtained from the EBSP measurements. In IQ map, the brightness of each grain is proportional to the lattice strain. At the grain boundary, the brightness is near the dark color because the lattice is strongly strained. In CD map, the color of each grain corresponds to the crystal orientation in the inverse pole figure shown at the right size of CD map.

At first, the author thought that the lattice in ZrN and TiN pellets would be orientated for a certain direction because their samples were sintered under 50 MPa in the SPS process. However, from the CD map, it was confirmed that all samples are isotropic. The area function of each grain was evaluated using the CD map. From the area function of each grain, the maximum, minimum and average grain sizes were calculated and summarized in Table 2.2 and 2.3.

The descending order of the average grain sizes were TiN, UN, ZrN, $U_{0.4}Zr_{0.6}N$ and UN+60mol%TiN. In case of UN+60mol%TiN, the diffusion of U, Ti and N would be prevented because UN didn't react with TiN. Therefore, the grain size of UN+60mol%TiN was smallest. In case of $U_{0.4}Zr_{0.6}N$, the grain growth would not finish because the sintering resistivity of ZrN is higher than UN and TiN. In fact, the density of $U_{0.4}Zr_{0.6}N$ sample (86.8%T.D.) is lower than the other samples (>90%T.D.). On the other hand, the grain sizes of ZrN and TiN are larger than those of $U_{0.4}Zr_{0.6}N$ and UN+60mol%TiN. We must use the powder with the small grain size when we want to prepare the high-density samples by the atmospheric pressure sintering. In case of the SPS, we can obtain the high-density samples even if we use the powder with the large grain. Therefore, the author used the powder sample of ZrN and TiN with the large grain (average grain size $\approx 8\mu m$ (ZrN), $11\mu m$ (TiN)) as the starting material in the SPS process. As the results, the grain sizes of ZrN and TiN samples were larger than those of $U_{0.4}Zr_{0.6}N$ and UN+60mol%TiN. In addition, it was confirmed that the grain growth was very small in the SPS process because the grain size of the powder sample before the SPS was very similar to those of each density sample.

From the EBSD analysis, the misorientation angle, which is the differences of between orientation angles of the adjacent grains, was also evaluated. Fig. 2.25(a) and (b) show the number fraction of the misorientation angle of UN, $U_{0.4}Zr_{0.6}N$, UN+60mol%TiN and TiN. In Fig. 2.25(a) and (b), the dot lines represents the average value of the misorientation angle of each sample. The average misorientation angle of UN ($\approx 21.4^\circ$) was similar to that of $U_{0.4}Zr_{0.6}N$ ($\approx 24.3^\circ$), and lower than those of ZrN ($\approx 38.6^\circ$), UN+60mol%TiN ($\approx 30.6^\circ$) and TiN ($\approx 33.2^\circ$). The misorientation angle generally becomes to be low to minimize the surface energy in the sintering process. The misorientation angle of UN+60mol%TiN was larger than that of UN because the binding strength between UN grain and TiN grain is lower than that between UN grains. In case of TiN and ZrN, the green pellets are sintered before the diffusion of molecule reaches at thermal equilibrium in the SPS process. Therefore, the misorientation angle would become to be high. The influence that the differences in the grain sizes give on the thermophysical properties would be small at this grain size level ($3\text{--}10\mu m$) [34]. However, the differences in the misorientation

angles may influence on the thermophysical prosperities, in particular mechanical properties.

2-3-2 Mechanical properties

Elastic properties

The indentation test is usually performed with the AFM observation. In this case, we can't strike the precipitation because the AFM image shows only the surface roughness of the sample and doesn't show the microstructure. In the present study, the indentation tests were performed with the optical microscope and AFM. By this in-situ method, the author succeeded to strike the precipitation such as TiN phase in UN+60mol%TiN shown in Fig. 2.26. From the load-displacement curve obtained in the indentation tests, Young's modulus and indentation hardness were evaluated. Fig. 2.27 shows the indentation depth dependences of Young's modulus. In this figure, Young's moduli of all samples are independent of the depth in the low depth region. On the other hand, Young's moduli rapidly decrease with increasing the depth in the high depth region. The reason would be that the elastic deformation zone shown in Fig. 2.28 referred from Ref. 21 reaches at the grain boundary in the high depth region, and that the expansion of the elastic deformation zone is interfered by the grain boundary. As the result, Young's modulus obtained from the indentation test becomes to be low. In the present study, the author considered the average of Young's modulus obtained in the low depth region as Young's modulus of porosity-free material. Young's modulus of UN obtained from the indentation tests was 276 ± 25 GPa, and this value is well consistent with that of porosity-free UN estimated by Hayes (1990) [24] (≈ 259 GPa). From this result, it was confirmed that Young's modulus obtained by the indentation test shows the value of the porosity-free material.

The values of sound velocities and elastic moduli obtained from the ultrasonic pulse echo measurements are summarized in Table 2.4-6. Fig. 2.29 and 2.30 shows the porosity dependences of the Young's modulus of UN, $U_{0.4}Zr_{0.6}N$, ZrN, UN+60mol%TiN and TiN, together with the literature data of [24, 35-44]. In these figures, Young's modulus obtained from the indentation test of each samples was plotted at $P=0$. The porosity dependence of the Young's modulus of UN was evaluated by Hayes (1990) [24] as the following equation;

$$E_p(\text{GPa}) = 259[(1-P) \times 100]^{3.002} \quad (0 < P < 0.30). \quad (2.24)$$

Generally, the porosity dependence of Young's modulus is represented by Wachtman equation (Eq. 2.2) [45]. In the present study, the author re-evaluated the porosity dependence of the Young's modulus of UN based on the data of Hayes (1990) [24], Padel (1969) [35], Honda (1968) [36],

Whaley (1968) [37] and Speidel (1963) [38] by the following equation;

$$UN: E_p \text{ (GPa)} = 262 \exp(-3.43P) \quad (0 < P < 0.30). \quad (2.25)$$

If the values of β_{MSA} are same, it is assumed that the coefficient of the porosity dependence of Young's modulus (β_E) are also same. In Fig. 2.18, β_{MSA} of UN, $U_{0.4}Zr_{0.6}N$ and UN+60mol%TiN showed the same value each other. From these results and Young's modulus obtained from the ultrasonic pulse echo method, the porosity dependences of $U_{0.4}Zr_{0.6}N$ and UN+60mol%TiN would be estimated by the following equations;

$$U_{0.4}Zr_{0.6}N: E_p \text{ (GPa)} = 371 \exp(-3.43P) \quad (0 < P < 0.30), \quad (2.26)$$

$$UN+60\text{mol}\%TiN: E_p \text{ (GPa)} = 362 \exp(-3.43P) \quad (0 < P < 0.30). \quad (2.27)$$

In case of ZrN and TiN, the porosity dependences of the Young's modulus were evaluated using the results of the ultrasonic pulse echo method obtained from some samples with various porosities, because there are no data of the porosity dependences of the thermophysical properties of the metal nitride prepared by the SPS.

$$ZrN: E_p \text{ (GPa)} = 442 \exp(-5.69P) \quad (0 < P < 0.190), \quad (2.28)$$

$$TiN: E_p \text{ (GPa)} = 575 \exp(-4.11P) \quad (0 < P < 0.284). \quad (2.29)$$

In the same way of UN, Young's modulus of $U_{0.4}Zr_{0.6}N$ ($=370 \pm 27$ GPa) and ZrN ($=452 \pm 38$ GPa) obtained from the indentation tests were well consistent with Young's modulus of porosity-free $U_{0.4}Zr_{0.6}N$ ($=371$ GPa) and ZrN ($=442$ GPa) estimated from Eq. 2.26 and 2.28. Young's moduli of ZrN (Eq. 2.28) and TiN (Eq. 2.29) obtained in the present study are well consistent with the data of Atamanenko (1995) [39] and Kuwahara (2001) [43]. These results are reasonable because ZrN pellets in Ref. 39 and TiN pellets in Ref. 43 were prepared by the hot-press and the porosity dependence of the SPS sample would be similar to that of the hot-pressed sample. Fig. 2.31 shows the relationship between β_E and β_{MSA} . In this figure, the linear relationship between β_E and β_{MSA} could be observed. From this relationship (Eq. 2.30), we would easily estimate the Young's modulus of the porosity-free material from only one data, and predict Young's modulus of the sample with the various microstructures and porosities.

$$\beta_E = 2.78 \times 10^{-2} + 3.78\beta_{MSA} \quad (2.30)$$

There are some models to estimate the Young's modulus of the composite material such as UN+60mol%TiN pellet. However, the interaction between each phase is not taken account into their model. Therefore, we can't precisely estimate the thermophysical properties of the composite material. In the present study, the author succeeded to evaluate the Young's

modulus of each phase in UN+60mol%TiN pellet by the in-situ indentation test. The results should include the interaction between UN phase and TiN phase. Young's modulus of TiN phase in UN+60mol%TiN obtained from the indentation test was higher than that of TiN pellet, although that of UN phase in UN+60mol%TiN was same to that of UN pellet. The author estimated the Young's modulus of UN+60mol%TiN using the Young's modulus of each phases from Fan equation (Eq. 2.31) [46];

$$E_C = E_\alpha f_{\alpha c} + E_\beta f_{\beta c} + E_s f_s \quad (2.31)$$

where E_C , E_α and E_β are the Young's modulus of the composite material, α phase and β phase, and $f_{\alpha c}$, $f_{\beta c}$, E_s and f_s are defined as Eq. 2.32–2.42 in Ref. 46. E_α and E_β were obtained from the indentation tests;

$$f_{\alpha c} = \frac{f_\alpha R}{f_\alpha R + f_\beta} f_\alpha, \quad (2.32)$$

$$f_{\beta c} = \frac{f_\beta}{f_\alpha R + f_\beta} f_\beta, \quad (2.33)$$

$$f_s = \frac{f_\alpha f_\beta (1+R)}{f_\alpha R + f_\beta}, \quad (2.34)$$

$$E_s = 2G_s(1+\nu_s), \quad (2.35)$$

$$\nu_s = f_{\alpha s} \nu_\alpha + f_{\beta s} \nu_\beta, \quad (2.36)$$

$$G_s = \frac{G_\alpha}{1 + \frac{f_{\beta s}}{1 - f_{\beta s} \gamma D}}, \quad (2.37)$$

$$D = \frac{G_\alpha - G_\beta}{(G_\beta - G_\alpha)(1-\gamma) + G_\alpha}, \quad (2.38)$$

$$\gamma = \frac{7 - 5\nu_\alpha}{15(1 - \nu_\alpha)}, \quad (2.39)$$

$$f_{\alpha s} = \frac{f_\alpha R}{f_\alpha R + f_\beta}, \quad (2.40)$$

$$f_{\beta s} = \frac{f_\beta}{f_\alpha R + f_\beta}, \quad (2.41)$$

$$R = d_\alpha / d_\beta, \quad (2.42)$$

where f_i , G_i , ν_i and d_i are the volume fraction, shear modulus, Poisson's ratio and grain size of each phase. In these equations, the grain size and Poisson's ratio were obtained from the EBSP

analysis and ultrasonic pulse echo method, respectively. The shear modulus was calculated using the Young's modulus obtained from the indentation tests and Poisson's ratio obtained from the ultrasonic pulse echo method. In the same way, the upper bound (E_{C-U}) and lower bound (E_{C-L}) of the Young's modulus of UN+60mol%TiN were estimated from Hashin's equation (Eq. 2.43 and 44) [47];

$$E_{C-U} = 2G_{C-U}(1 + \nu_C), \quad (2.43)$$

$$E_{C-L} = 2G_{C-L}(1 + \nu_C), \quad (2.44)$$

where G_{C-L} , G_{C-U} and ν_C are defined by the following equations;

$$B_{C-L} = B_\alpha + \frac{f_\beta}{\frac{1}{B_\beta - B_\alpha} + \frac{3f_\alpha}{3B_\alpha + 4G_\alpha}}, \quad (2.45)$$

$$B_{C-U} = B_\alpha + \frac{f_\alpha}{\frac{1}{B_\alpha - B_\beta} + \frac{3f_\beta}{3B_\beta + 4G_\beta}}, \quad (2.46)$$

$$G_{C-L} = G_\alpha + \frac{f_\beta}{\frac{1}{G_\beta - G_\alpha} + \frac{6(B_\alpha + 2G_\alpha)f_\alpha}{5G_\alpha(3B_\alpha + 4G_\alpha)}}, \quad (2.47)$$

$$G_{C-U} = G_\beta + \frac{f_\alpha}{\frac{1}{G_\alpha - G_\beta} + \frac{6(B_\beta + 2G_\beta)f_\beta}{5G_\beta(3B_\beta + 4G_\beta)}}. \quad (2.48)$$

Fig. 2.32(a) and (b) show ZrN or TiN content dependences of Young's modulus. It was found that the Young's modulus of $U_xZr_{1-x}N$ linearly increase with increasing the ZrN content and Young's modulus of UN+60mol%TiN by the ultrasonic pulse echo method are well consistent with the data estimated from Young's moduli of UN phase and TiN phase in UN+60mol%TiN pellet by the indentation test using Fan's equation and Hashin's equation. On the other hand, Young's modulus of UN+60mol%TiN by the ultrasonic pulse echo method didn't agree with those estimated from Young's moduli of UN pellet and TiN pellet obtained from indentation test or ultrasonic pulse echo method using Fan's equation. This is because Fan's equation and Hashin's equation don't take account into the interaction between UN phase and TiN phase in UN+60mol%TiN. From these results, it was proved that the Young's modulus could be precisely evaluated by the indentation method in both case of the composite and solid solution material. The large samples are required in the general method to measure the Young's modulus such as the ultrasonic pulse echo method ($>T5mm \times \phi 5mm$) and the tensile test ($>100mm \times 1mm \times 5mm$). Therefore, it is

very difficult to evaluate Young's modulus of MA-containing fuels because the sample quantity of MA is strictly regulated. So, this method using the indentation test would be extremely when we evaluate Young's modulus of MA-containing fuels because the sample size is very small in case of the indentation test.

Vickers hardness and fracture toughness

Fig. 2.33 and 2.34 show the porosity dependences of the Vickers hardness at the load of 9.8N of UN, $U_{0.4}Zr_{0.6}N$, ZrN, UN+60mol%TiN and TiN, together with the literature data [24, 39, 43, 44, 48–55]. The porosity dependence of UN were evaluated by Hayes (1990) [24] and Godfrey (1965) [48] as the following equations;

$$\text{Hayes [24]: } H_V (\text{GPa}) = 9.334(1 - 2.1P)\exp(-1.882 \times 10^{-3} T) \\ (0 < P < 0.26, 298 < T < 1673 \text{ K}), \quad (2.49)$$

$$\text{Godfrey [48]: } H_V (\text{GPa}) = 4.778(1 - 2.1P) \quad (0 < P < 0.26). \quad (2.50)$$

The Vickers hardness of UN obtained in the present study agreed with Eq. 2.50. In both case of Hayes (1990) [21] and Godfrey (1965) [44], the coefficients of the porosity dependence of the Vickers hardness of UN were 2.1. Using this value, the author derived the porosity dependences of $U_{0.4}Zr_{0.6}N$ and UN+60mol%TiN as the following equations;

$$U_{0.4}Zr_{0.6}N: H_V (\text{GPa}) = 8.37(1 - 2.1P) \quad (0 < P < 0.26), \quad (2.51)$$

$$\text{UN+60mol\%TiN: } H_V (\text{GPa}) = 10.2(1 - 2.1P) \quad (0 < P < 0.26). \quad (2.52)$$

In the present study, the author used the function with the same form in case of UN and evaluated the porosity dependences of the Vickers hardness of ZrN and TiN as the following equations;

$$\text{ZrN: } H_V (\text{GPa}) = 11.4(1 - 3.8P) \quad (0 < P < 0.20) \quad (2.53)$$

$$\text{TiN: } H_V (\text{GPa}) = 12.0(1 - 2.7P) \quad (0 < P < 0.17) \quad (2.54)$$

Vickers hardness of ZrN pellets with various porosities at load of 4.9N was evaluated by Wheeler (2007) [53]. Using this data, the author derived the following equation;

$$\text{ZrN: } H_V (\text{GPa}) = 12.5(1 - 2.8P) \quad (0 < P < 0.35) \quad (2.55)$$

The Vickers hardness of porosity-free ZrN at 9.8 N estimated in Eq. 2.53 (=11.4 GPa) was slightly lower than that at 4.9 N estimated in Eq. 2.55. The reason is the differences on the load. Fig. 2.35 shows the load dependence of Vickers hardness of porosity-free ZrN. In this figure, the Vickers hardness at the load of 0.98, 2.94 and 9.8 N were obtained in the present study and the Vickers hardness linearly decreased with increasing the load. Therefore, the author considers that the Vickers hardness obtained in the present study is the reasonable data.

Using the Vickers hardness of the porosity-free material obtained in Fig. 2.33 and 2.34, ZrN or TiN content dependences of the Vickers hardness of $U_{1-x}Zr_xN$ and UN+60mol%TiN are shown in Fig. 2.36. In addition, ZrN or TiN content dependences of the fracture toughness of $U_{1-x}Zr_xN$ and UN+60mol%TiN are shown in Fig. 2.37, together with the literature data [42, 43]. In Fig. 2.36, the Vickers hardness of $U_{0.4}Zr_{0.6}N$ and UN+Xmol%TiN simply increased with increasing the ZrN or TiN content. On the other hand, in case of the fracture toughness (Fig. 2.37), the certain trend could not be observed. The author attempted to resolve the crisscross between the Vickers hardness and fracture toughness by the EBSD analysis. Fig. 2.38–42 show the SEM image, IQ map and CD map around the crack generating from the vertex of the Vickers impression of each sample. In case of UN, $U_{0.4}Zr_{0.6}N$ and UN+60mol%, the intragranular crack progresses without stopping at the grain boundary. On the other hand, the intragranular crack of ZrN and TiN stopped at the grain boundary or converted to the intergranular crack. In case of ZrN, Wheeler (2007) [53] reported that the intergranular crack concentrated at the grain boundary with the high misorientation angle. By the EBSD analysis, the misorientation angle of ZrN and TiN prepared by the SPS were higher than those of UN, $U_{0.4}Zr_{0.6}N$, UN+60mol%TiN prepared by the atmospheric pressure sintering. Therefore, the intragranular crack of TiN and ZrN would stop or convert to the intergranular crack at the grain boundary and this is the reason that ZrN or TiN content dependences of the fracture toughness didn't show the certain trend. The fracture toughness ($>2\text{MPam}^{0.5}$) of UN, $U_{0.4}Zr_{0.6}N$, ZrN, UN+60mol%TiN and TiN were vastly larger than that of the porosity-free UO_2 [56: Kutty (1987) ($\approx 0.59\text{MPam}^{0.5}$), 57: Yamada (1998) ($\approx 1.1\text{MPam}^{0.5}$)]. This result indicates that the resistivity of the nitride fuel for the pellet cracking by the thermal stress is higher than that of the oxide fuel.

Indentation hardness

Fig. 2.41 shows the load dependences of the indentation hardness and Vickers hardness of UN, together with the literature data of UO_2 [57–60]. The Vickers hardness of UO_2 was larger than that of UN in the region of $P > 4.9\text{N}$. On the other hand, the indentation hardness of UO_2 was smaller than that of UN in the region of $P < 10\text{mN}$. This phenomenon would be resulted from the indentation size effect (ISE), which detail is described later. The Vickers hardness was larger than the indentation hardness. It is because the indentation hardness indicates the resistivity for only the plastic deformation and the Vickers hardness includes not only the resistivity for the plastic deformation, but also the recovery by the surface tension.

The Vickers hardness and indentation hardness decrease with increasing the load. This

phenomenon is called the indentation size effect (ISE). As the sources of the ISE, the following effects are thought [61].

1. Pile-up or sink-in
2. Surface altered layer such as the strongly strain-hardening surface layer and oxidized surface layer
3. Non-self-similarity in the shape of indenter
4. Strain hardening plasticity in the indentation process

In this segment, each phenomenon is explained and their effects are discussed. Pile-up and sink-in indicate the deformation of the area not contacting with the indenter in the indentation process as shown in Fig. 2.44. If the pile-up or sink-in happens, the hardness and Young's modulus obtained from the indentation test change because the contact area with the pile-up or sink-in is different from that without the pile-up or sink-in. In the present study, it was confirmed that the pile-up or sink-in don't happen in case of the metal nitride with NaCl structure by the AFM observation. The author could observe the clear Kikuchi pattern such as Fig. 2.2 in the EBSD analysis for all samples. If there are surface altered layer such as oxidized surface layer and strain-hardening layer with thickness of several dozen nm, we can't observe the Kikuchi pattern. From these results, it was found that there are almost not surface altered layer in all samples. The self-similarity in the shape of the indenter can be evaluated by the area function defined in Eq. 2.13. In the present study, the area function was evaluated using the fused silica at various load and the area function was independent of the load and depth. From the results described in this segment, it was confirmed that there were no influences of pile-up or sink-in, surface affected layer and non-self-similarity of the indenter shape. Therefore, it was thought that the ISE is resulted from the strain hardening plasticity in the indentation process. Nix and Gao (1998) [62] formulated the ISE by the strain gradient plasticity [63] based on the geometrically necessary dislocations (GNDs) [64]. The GNDs generate to homogenize the strain gradient concentrating at the plastic deformation zone. The strain gradient plasticity is the theory that the material is hardened by the GNDs when the plastic deformation generates in the material. The following sentences briefly explain Nix and Gao model.

For simplicity, Nix and Gao assumed that the indentation was accommodated by circular loops of the GNDs with Burgers vector as shown in Fig. 2.45 referred from Ref. 62. As the indenter is loaded into the surface of a single crystal, the GNDs are required to account for the permanent shape change at the surface. Of course the called statistically stored dislocations

(SSDs) [64], which is the dislocation to exist before the indentation, could contribute to the hardness. Nix and Gao defined the angle between the indenter and the surface of the sample to be θ , the contact radius to be a and the depth of indentation to be h . In this case, the following equation is derived.

$$\tan\theta = \frac{h}{a} = \frac{b}{s} \quad (2.56)$$

where s is the spacing between individual slip steps on the indentation surface.

$$\lambda = \int_0^a d\lambda = \int_0^a 2\pi r \frac{dr}{s} = \int_0^a 2\pi \frac{h}{ba} dr = \frac{\pi ha}{b} \quad (2.57)$$

where λ is the total length of the injected dislocation loops. From Eq. 2.57 and the volume of the plastic deformation zone (V), the density of the GNDs (ρ_G) is represented by the following equation;

$$\rho_G = \frac{\lambda}{V} = \frac{3h}{2ba^2} = \frac{3}{2bh} \tan^2\theta. \quad (2.58)$$

To estimate the deformation resistance, Taylor relation [65] (Eq. 2.59) was used to evaluate the shear strength (τ);

$$\tau = \alpha Gb\sqrt{\rho_T} = \alpha Gb\sqrt{\rho_G + \rho_S}, \quad (2.59)$$

where the ρ_T is the total dislocation density in the indentation, ρ_S is the density of SSDs, G is the shear modulus, α is a constant to be 0.3–0.6. Nix and Gao assumed that the Von Mises flow rule [66] and that Tabor's factor of 3 [65] can be used to convert the equivalent flow stress ($\bar{\sigma}$) to hardness;

$$H = 3\bar{\sigma} = 3\sqrt{3}\tau. \quad (2.60)$$

From Eq. 2.59 and 2.60, the hardness existing the GNDs (H) and not existing the GNDs (H_0) are represented by the following equations;

$$H = 3\sqrt{3}\tau = 3\sqrt{3}\alpha Gb\sqrt{\rho_G + \rho_S}, \quad (2.61)$$

$$H_0 = 3\sqrt{3}\tau = 3\sqrt{3}\alpha Gb\sqrt{\rho_S}. \quad (2.62)$$

H_0 is equal to the hardness at the adequate large depth because the ρ_G is vanishingly small when the depth is close to the infinite value. From Eq. 2.61 and 2.62, Nix and Gao model (Eq. 2.63) was derived.

$$\left(\frac{H}{H_0}\right)^2 = 1 + \frac{\rho_G}{\rho_S} = 1 + \frac{\frac{3}{2b\rho_S} \tan^2\theta}{h} = 1 + \frac{h_0}{h} \quad (2.63)$$

$$h_0 = \frac{3}{2b\rho_s} \tan^2\theta = \frac{3}{2b\left(\frac{H_0}{3\sqrt{3}\alpha Gb}\right)^2} \tan^2\theta = \frac{81}{2} b\alpha^2 \tan^2\theta \left(\frac{G}{H_0}\right)^2 \quad (2.64)$$

H_0 and h_0 are generally obtained by fitting of Eq. 2.63 for the experimental data. Thus, the ISE can't be explained from the load dependent of the hardness and can be explained from the relationship of $1/h$ and H^2 . Therefore, the relationships of $1/h$ and H^2 of UN, U_{0.4}Zr_{0.6}N, ZrN, UN+60mol%TiN and TiN are shown in Fig. 2.46, 2.47, 2.48(a) and 2.48(b). In Fig. 2.46, the experimental data follows to Nix and Gao model in the region of $h > 170$ nm, but Nix and Gao model overestimates the hardness in the region of $h < 170$ nm. In the same way, Swadener (2002) [67] and Feng (2004) [61] evaluated the ISE on Ir and MgO, respectively. In case of Ir and MgO, Nix and Gao model also overestimated the hardness at low h . In Nix and Gao model, it was assumed that all the GNDs are contained within a hemisphere plastic zone, with a radius equal to the contact radius a . Swadener (2002) [67] suggested that this assumption may not be correct at low h and GNDs spreads out from the hemisphere plastic zone with a radius equal to the contact radius. The spread-out effect was experimentally confirmed by Feng (2004) [61]. Feng (2004) [61] suggested the effective plastic zone with a radius of fa to account the spread-out effect, and improved Nix and Gao model as the following equation;

$$\left(\frac{H}{H_0}\right)^2 = 1 + \frac{h_0}{f^3 h} \quad (2.65)$$

Feng (2004) [61] formulated the form of function ($f(h)$) as Eq. 2.66;

$$f = 1 + \alpha e^{-h/h_1} \quad (2.66)$$

where α and h_1 are the fitting parameters. From Eq. 2.65 and Eq. 2.66, Eq. 2.67 was obtained;

$$\left(\frac{H}{H_0}\right)^2 = 1 + \left(1 + \alpha e^{-h/h_1}\right)^3 \frac{h_0}{h} \quad (2.67)$$

The experimental data was adequately fitted by using Eq. 2.67 as shown in Fig. 2.46. However, Feng (2004) did not show the clear ground about Eq. 2.66, but the author think that Eq. 2.67 is not wrong but is not perfect. The reason is described in the following sentences.

It is thought that the GNDs spread out from the plastic zone when the sum of the thermal drift force of dislocations and the repulsive force between GNDs is beyond Peierls stress. Therefore, $f(h)$ should have the threshold value. The relationships described in Eq. 2.68 is suggested on the repulsive force (σ), distance (r) between dislocations, GNDs density (ρ_G), and

indentation depth (h).

$$\sigma \propto 1/r \propto 1/\rho_G \propto h \quad (2.68)$$

So, it is thought that $f(h)$ is strongly relate to σ but the relationship is not clear. Therefore, the relationships between $f(h)$ and h may not be the exponential function (Eq. 2.66) and be the inverse proportional function with the threshold value. However, the dataset of H^2 and $1/h$ is not the continuous data and the precise decision of the threshold is very difficult. In addition, the relationships between $f(h)$ and σ is uncertain. Therefore, the author thought that Eq. 2.67 is reasonable, and the author fitted the experimental data of UN using Eq. 2.67 in the present study. From fitting by Eq. 2.67, the depth dependences of indentation hardness of UN was revealed as the following equation;

$$\text{UN: } \left(\frac{H(\text{GPa})}{4.948} \right)^2 = 1 + [1 + 1.550 \exp(-h(\text{nm})/35.52)]^{-3} \frac{408.7}{h(\text{nm})} \quad (70 < h < 2100 \text{ nm}). \quad (2.69)$$

In the same way, the dependences of the indentation hardness of U_{0.4}Zr_{0.6}N and ZrN were evaluated by using Eq. 2.67 as the following equations.

$$\text{U}_{0.4}\text{Zr}_{0.6}\text{N: } \left(\frac{H(\text{GPa})}{9.103} \right)^2 = 1 + [1 + 1.735 \exp(-h(\text{nm})/22.89)]^{-3} \frac{176.1}{h(\text{nm})} \quad (60 < h < 1000 \text{ nm}) \quad (2.70)$$

$$\text{ZrN: } \left(\frac{H(\text{GPa})}{14.77} \right)^2 = 1 + [1 + 0.3737 \exp(-h(\text{nm})/26.04)]^{-3} \frac{22.89}{h(\text{nm})} \quad (70 < h < 1000 \text{ nm}) \quad (2.71)$$

H_0 of UN (=4.948 GPa), U_{0.4}Zr_{0.6}N(=9.103 GPa) and ZrN (14.77 GPa) in Eq. 2.69–2.71 are close to the Vickers hardness at 9.8N of UN (=4.78GPa), U_{0.4}Zr_{0.6}N (=8.37GPa) and ZrN (=11.4GPa) in Fig. 2.36. In addition, compared with UN, the overestimates by Nix and Gao model could not be almost observed in case of ZrN and U_{0.4}Zr_{0.6}N. Judging from the Debye temperature, the binding force of ZrN and U_{0.4}Zr_{0.6}N are larger than that of UN. Therefore, GNDs in ZrN and U_{0.4}Zr_{0.6}N didn't spread out because the Piers stress of ZrN and U_{0.4}Zr_{0.6}N is larger than that of UN. This is the reason that Nix and Gao model didn't almost overestimate in case of ZrN and U_{0.4}Zr_{0.6}N.

In Fig. 2.48(a), the relationship between H^2 and $1/h$ of UN phase in UN+60mol%TiN pellet agrees with that of UN. In case of Fig. 2.48(b), the overestimates by Nix and Gao model could not be observed and the depth dependences of the indentation hardness of TiN phase in UN+60mol%TiN and TiN were evaluated by the following equations;

$$\text{TiN phase in UN+60mol\%TiN pellet: } \left(\frac{H(\text{GPa})}{15.65} \right)^2 = 1 + \frac{52.95}{h(\text{nm})} \quad (50 < h < 400 \text{ nm}), \quad (2.72)$$

$$\text{TiN: } \left(\frac{H(\text{GPa})}{10.32} \right)^2 = 1 + \frac{151.3}{h(\text{nm})} \quad (50 < h < 700 \text{ nm}), \quad (2.73)$$

From Fig. 2.48(b), it was found that the indentation hardness of TiN phase in UN+60mol%TiN pellet is higher than that of TiN and the h_0 of TiN was about three times of that of TiN phase in UN+60mol%TiN pellet. From Eq. 2.64, these differences were resulted from only the differences of ρ_s . Therefore, it was found that ρ_s of TiN phase in UN+60mol%TiN pellet is about three time of that of TiN. This is also confirmed from the EBSP analysis of UN+60mol%TiN (Fig. 2.23(a) and (b)), too. In the SEM image (Fig. 2.23(a)), UN phase and TiN phase in UN+60mol%TiN pellet represent as the gray and light zone. On the other hand, in the IQ map (Fig. 2.23(b)), the relationship inverted. This inversion indicates that the strain concentrates in TiN phase. This result explains that the indentation hardness of UN phase in UN+60mol%TiN is similar to that of UN and that of TiN phase in UN+60mol%TiN is higher than that of TiN. The author thinks that the strain concentration in TiN phase is resulted from the differences of the oxidation resistivity and the thermal expansion between UN and TiN.

2-3-3 Electrical property

Hayes (1990) [25] evaluated the temperature (T) and porosity (P) dependences of the electrical conductivity (σ) of UN as the following equation;

$$\text{UN: } \sigma(P, T)(10^4 \Omega^{-1} \text{m}^{-1}) = 139.9T^{-0.125} \exp(-2.14 \times P) \quad (298 < T < 1923\text{K}, 0 < P < 0.2). \quad (2.74)$$

In the same way of Young's modulus, the coefficients of the porosity dependences of the electrical properties of $U_{0.4}Zr_{0.6}N$ and UN+60mol%TiN were used with the same value of that of UN (=2.14). Fig. 2.49 shows the porosity dependences of the electrical conductivities at 473K of TiN and ZrN, together with the data of UN (Eq. 2.74). From this figure, the coefficient of the porosity dependences of the electrical conductivity at 473 K of ZrN and TiN were 2.31 and 1.96. In the different way of the Young's modulus, these values (ZrN: 2.31, TiN: 1.96) are similar to that of UN (=2.14). The electrical conductivities of ZrN and TiN were measured along the perpendicular direction of the SPS pressure. On the other hand, the thermophysical properties except for the electrical conductivity were measured along the parallel direction. The MSA of the parallel direction was larger than that of the perpendicular direction because the grains were distorted by the SPS pressure. This is the reason that the coefficients of the porosity dependences of the electrical conductivity of TiN and ZrN took the similar values with that of UN. Fig. 2.50 and 2.51

show the temperature dependences of the electrical conductivities of UN, U_{0.4}Zr_{0.6}N, ZrN, UN+60mol%TiN and TiN, together with the literature data [25, 38, 44, 49, 68–75]. The electrical conductivity of UN obtained in the present study was well consistent with the literature data [25, 38, 49, 68–75]. That of ZrN was within the variation of the literature data [44, 73–76]. The temperature and porosity dependences of the electrical conductivity of U_{0.4}Zr_{0.6}N, ZrN, UN+60mol%TiN and TiN were evaluated as the following equation;

$$\text{U}_{0.4}\text{Zr}_{0.6}\text{N: } \sigma(P, T)(10^4 \Omega^{-1}\text{m}^{-1}) = 54.4 \times 10^{-2} T^{-4.19 \times 10^{-2}} \exp(-2.14 \times P) \quad (333 < T < 873 \text{ K}, 0 < P < 0.20) \quad (2.75)$$

$$\text{UN+60mol\%TiN: } \sigma(P, T)(10^4 \Omega^{-1}\text{m}^{-1}) = 435 \times 10^{-2} T^{-0.237 \times 10^{-2}} \exp(-2.14 \times P) \quad (333 < T < 973 \text{ K}, 0 < P < 0.20) \quad (2.76)$$

$$\text{ZrN: } \sigma(P, T)(10^4 \Omega^{-1}\text{m}^{-1}) = 2.34 \times 10^4 T^{-0.749} \exp(-2.31 \times P) \quad (333 < T < 723 \text{ K}, 0 < P < 0.2) \quad (2.77)$$

$$\text{TiN: } \sigma(P, T)(10^4 \Omega^{-1}\text{m}^{-1}) = 4.99 \times 10^4 T^{-0.833} \exp(-1.96 \times P) \quad (333 < T < 973 \text{ K}, 0 < P < 0.3) \quad (2.78)$$

Fig. 2.52 shows the temperature dependence of the Seebeck coefficient of UN, together with the literature data [49, 77, 78]. In the same way of the electrical conductivity, the Seebeck coefficient of UN obtained in the present study was well consistent with the literature data [49, 76, 77]. The Seebeck coefficient of UN showed the positive value. Therefore, it was found that the main carrier in UN is the hole. In Fig. 2.50, the electrical conductivity of U_{0.4}Zr_{0.6}N was smaller than that of UN nevertheless that of ZrN was vastly larger than that of UN. This is because the hole density of U_{0.4}Zr_{0.6}N would be smaller than those of UN and ZrN due to the high content of the impurity oxygen (Table 2.2). On the other hand, the electrical conductivity of UN+60mol%TiN was vastly larger than that of UN. In Fig. 2.51, the green dash line represents the estimated value of UN+60mol%TiN using the electrical conductivity of UN (Eq. 2.75) and TiN (Eq. 2.79) from Schulz' equation [78] (Eq. 2.79).

$$1 - V_\beta = \left(\frac{\sigma_\alpha}{\sigma_C} \right)^{1/3} \frac{\sigma_\beta - \sigma_C}{\sigma_\beta - \sigma_\alpha} \quad (2.79)$$

In this equation, V and σ are the volume fraction and transport properties such as the thermal conductivity and electrical conductivity, and the subscript of C, α and β shows the composite material, first phase (=UN) and second phase (=TiN). The estimated data of UN+60mol%TiN was higher than the experimental data. Generally speaking, the thermal and electrical resistivity

becomes to be high locally at the grain boundary because there is a large barrier, which the heat flux and current need exceed, at grain boundary due to the high density of the point defect, dislocation at the grain boundary and crystal orientation mismatch between the grains. This phenomenon is called 'grain boundary scattering'. Therefore, it is reasonable that the estimated data is higher than the experimental data. The contribution of the grain boundary scattering decreases with increasing the temperature. So, the differences between the estimated data and experimental data of UN+60mol%TiN decreased with increasing the temperature.

2-3-4 Thermal property

Thermal expansion

The thermal expansion is independent of the porosity [10]. Therefore, in the present study, the author used ZrN pellets with 82.5%T.D. and TiN pellets with 84.1%T.D. as the sample of the thermodilatometry measurement. The thermal expansions of UN, U_{0.4}Zr_{0.6}N, ZrN, UN+60mol%TiN and TiN were shown in Fig. 2.53 and 2.54, together with the literature data [23, 79-87]. The temperature dependences of the lattice parameters of UN, ZrN and TiN were evaluated by Hayes (1990) [23] (Eq. 2.80) and Aigner (1994) [84] (Eq. 2.81 and 2.82).

$$\text{UN (Hayes) [23]: } a(\text{nm}) = 0.4879 + 3.264 \times 10^{-6} T + 6.889 \times 10^{-10} T^2 \quad (298 < T < 2523 \text{ K}) \quad (2.80)$$

$$\text{ZrN (Aigner) [84]: } a(\text{nm}) = 0.45718 + 2.107 \times 10^{-6} T + 8.253 \times 10^{-10} T^2 \quad (298 < T < 1423 \text{ K}) \quad (2.81)$$

$$\text{TiN (Aigner) [84]: } a(\text{nm}) = 0.42313 + 2.338 \times 10^{-6} T + 1.0717 \times 10^{-9} T^2 \quad (298 < T < 1423 \text{ K}) \quad (2.82)$$

Eq. 2.80-82 were obtained from the high temperature XRD analysis. In Fig. 2.53 and 2.54, the thermal expansion of UN, ZrN and TiN obtained in the present study corresponded to Eq. 2.80-2.82. Using Eq. 2.80-82, the thermal expansion of U_{0.4}Zr_{0.6}N and UN+60mol%TiN were evaluated from Vegard's law or Turner's equation [88] (Eq. 2.83).

$$\alpha_{\text{lin},c} = \frac{\alpha_{\text{lin},a} V_a B_a + \alpha_{\text{lin},\beta} V_\beta B_\beta}{V_a B_a + V_\beta B_\beta} \quad (2.83)$$

In this equation, α_{lin} is the linear thermal expansion coefficient (LTEC), B is the bulk modulus, and V is the volume fraction. The thermal expansion of U_{0.4}Zr_{0.6}N and UN+60mol%TiN estimated by Vegard's law or Turner's equation were well consistent with those obtained in the present study. The thermal expansion of each sample obtained in the present study was represented by

the following equations;

$$\text{UN: } \Delta L / L(\%) = 6.745 \times 10^{-4}(T - 298) + 3.350 \times 10^{-7}(T - 298)^2$$

$$(298 < T < 900 \text{ K}), \quad (2.84)$$

$$\text{U}_{0.4}\text{Zr}_{0.6}\text{N: } \Delta L / L(\%) = 5.912 \times 10^{-4}(T - 298) + 3.207 \times 10^{-7}(T - 298)^2$$

$$(298 < T < 1023 \text{ K}), \quad (2.85)$$

$$\text{ZrN: } \Delta L / L(\%) = 6.401 \times 10^{-4}(T - 298) + 1.130 \times 10^{-7}(T - 298)^2$$

$$(298 < T < 1423 \text{ K}), \quad (2.86)$$

$$\text{UN+60mol\%TiN: } \Delta L / L(\%) = 7.843 \times 10^{-4}(T - 298) + 1.945 \times 10^{-7}(T - 298)^2$$

$$(298 < T < 973 \text{ K}), \quad (2.87)$$

$$\text{TiN: } \Delta L / L(\%) = 8.516 \times 10^{-4}(T - 298) + 7.684 \times 10^{-8}(T - 298)^2$$

$$(298 < T < 1473 \text{ K}). \quad (2.88)$$

Specific heat capacity

The specific heat capacity (C_p) of UN, ZrN and TiN could be obtained from the SGTE databases [89] as the following equation;

$$\text{UN: } C_p(\text{Jmol}^{-1}\text{K}^{-1}) = 55.73 + 4.979 \times 10^{-3}T - 8.790 \times 10^{-5}T^2 \quad (298 < T < 1500 \text{ K}) \quad (2.89)$$

$$\text{TiN: } C_p(\text{Jmol}^{-1}\text{K}^{-1}) = 42.66 + 2.922 \times 10^{-2}T - 2.349 \times 10^{-5}T^2 - 1.085 \times 10^{-6}T^3$$

$$(298 < T < 600 \text{ K})$$

$$C_p(\text{Jmol}^{-1}\text{K}^{-1}) = 49.08 + 1.582 \times 10^{-3}T + 2.271 \times 10^{-5}T^2 - 7.658 \times 10^{-5}T^3$$

$$(600 < T < 1600 \text{ K})$$

$$C_p(\text{Jmol}^{-1}\text{K}^{-1}) = 40.89 + 9.615 \times 10^{-3}T + 4.673 \times 10^{-8}T^2 + 1.893 \times 10^{-6}T^3$$

$$(1600 < T < 3200 \text{ K}) \quad (2.90)$$

$$\text{ZrN: } C_p(\text{Jmol}^{-1}\text{K}^{-1}) = 46.42 + 7.056 \times 10^{-2}T - 7.994 \times 10^{-9}T^2 - 7.168 \times 10^{-5}T^3$$

$$(298 < T < 2000 \text{ K})$$

$$C_p(\text{Jmol}^{-1}\text{K}^{-1}) = 9.000 + 2.890 \times 10^{-2}T - 3.474 \times 10^{-6}T^2 + 3.210 \times 10^{-7}T^3$$

$$(2000 < T < 2600 \text{ K})$$

$$C_p(\text{Jmol}^{-1}\text{K}^{-1}) = 41.31 + 9.390 \times 10^{-3}T - 3.049 \times 10^{-7}T^2 + 6.404 \times 10^{-6}T^3$$

$$(2600 < T < 3225 \text{ K}) \quad (2.91)$$

Using these data, the specific capacity of U_{0.4}Zr_{0.6}N and UN+60mol%TiN were estimated from Neuman-Kopp's law and sum of $0.4C_{p,\text{UN}}$ and $0.6C_{p,\text{TiN}}$. Generally, the specific heat capacity at constant pressure (C_p) is the sum of lattice vibrational term (= specific heat capacity at constant

volume) (C_V), lattice dilational term (C_D), electric term (C_{EL}) and other term (C_{OTHER}) such as the effect of the lattice anharmonic and generation of the lattice defect. The C_V can be estimated by Debye model (Eq. 2.92) when we know the Debye temperature (θ_D).

$$C_V = 3NR \left(\frac{T}{\theta_D} \right)^3 \int_0^{\theta_D/T} \frac{x^4 e^x}{(e^x - 1)^2} dx \quad (2.92)$$

In this equation, R , N and T are the molar gas constant, number of the atom in the chemical formula, absolute temperature. The C_D can be also estimated from Eq. 2.93 using the thermal expansion (α_{lin}), bulk modulus (B) and the molar volume (V_m).

$$C_D = (3\alpha_{lin})^2 V_m T B \quad (2.93)$$

The data of α_{lin} , B and V_m was used the data obtained from the thermodilatometry, ultrasonic pulse echo measurement and XRD measurement when the author estimated the C_D . The C_{EL} can be estimated from the C_p at the low temperature (about 0–20K). However, there is no data of the C_p at the low temperature of UN, ZrN and TiN.

The temperature dependences of specific heat capacities of UN, $U_{0.4}Zr_{0.6}N$, ZrN, UN+60mol%TiN and TiN are shown in Fig. 2.55 and 56, together with the literature data [44, 89, 90] and the estimated data from Eq. 2.92 and 2.93. In these figures, the fat solid lines represent the estimated data from Eq. 2.92 and 2.93, and the thin solid lines (Eq. 2.94–98) represent the data obtained in the present study.

$$\text{UN: } C_p (\text{Jmol}^{-1}\text{K}^{-1}) = 48.86 + 1.207 \times 10^{-3} T - 1.422 \times 10^5 T^{-2} \quad (473 < T < 1273 \text{ K}) \quad (2.94)$$

$$U_{0.4}Zr_{0.6}N: C_p (\text{Jmol}^{-1}\text{K}^{-1}) = 45.00 + 1.084 \times 10^{-2} T - 1.2919 \times 10^5 T^{-2} \quad (473 < T < 1273 \text{ K}) \quad (2.95)$$

$$\text{ZrN: } C_p (\text{Jmol}^{-1}\text{K}^{-1}) = 43.78 + 9.992 \times 10^{-3} T - 4.128 \times 10^5 T^{-2} \quad (473 < T < 1273 \text{ K}) \quad (2.96)$$

$$\text{UN+60mol\%TiN: } C_p (\text{Jmol}^{-1}\text{K}^{-1}) = 53.90 + 4.300 \times 10^{-3} T - 1.760 \times 10^6 T^{-2} \quad (473 < T < 1273 \text{ K}) \quad (2.97)$$

$$\text{TiN: } C_p (\text{Jmol}^{-1}\text{K}^{-1}) = 35.25 + 2.477 \times 10^{-2} T - 8.578 \times 10^{-6} T^2 + 5.830 \times 10^5 T^{-2} \quad (473 < T < 1273 \text{ K}) \quad (2.98)$$

From these figures, it was confirmed that the experimental data of UN, ZrN and TiN obtained in the present study agreed with the literature data [44, 89, 90] and the experimental data of $U_{0.4}Zr_{0.6}N$ and UN+60mol%TiN agreed with the estimated data ($0.4C_{p,UN} + 0.6C_{p,ZrN}$ and $0.4C_{p,UN} + 0.6C_{p,TiN}$). From these results, it was found that there are no anomalous effects by the addition of ZrN and

TiN to UN in case of the specific heat capacity and thermal expansion. The experimental data was not consistent with the the sum of C_V and C_D . The subtracts from the C_P to the sum of C_V and C_D at the high temperature (>800K) decreased with the UN, U_{0.4}Zr_{0.6}N, ZrN and TiN. The differences are resulted from the C_{EL} and C_{OTHER} .

Thermal conductivity

Fig. 2.57(a) and (b) show the porosity dependences of the thermal conductivities of ZrN and TiN at each temperature. In these figures, the thermal conductivities of ZrN and TiN exponentially decreased with increasing the porosity. It was thought that the gradient ($=\Delta \ln \kappa / \Delta T$) at each temperature shows the similar value at each temperature. The thermal conductivity of UN was represented by Ross (1988) [24] as the following equation,

$$\text{UN: } \kappa_P (\text{Wm}^{-1}\text{K}^{-1}) = 1.37T^{0.410} \frac{1-P}{1+P} \quad (10 < T < 1923 \text{ K}, 0 < P < 0.2). \quad (2.99)$$

As shown Eq. 2.99, Ross (1988) [27] evaluated the porosity dependences of the thermal conductivity of UN using Maxwell-Eucken's equation (Eq. 2.3). Therefore, in the present study, the author also used Maxwell-Eucken's equation (Eq. 2.3) to evaluate the porosity dependences of ZrN and TiN. The coefficient of the porosity dependences of the thermal conductivity of ZrN and TiN were 5.31 and 2.03. Fig. 2.58 shows the coefficient of the porosity dependence of MSA (β_{MSA}) as the function of the coefficient (β_K) of porosity dependence of thermal conductivity of UN, TiN and ZrN. In the same way of Young's modulus, the linear relationships (Eq. 2.100) could be observed in Fig. 2.58.

$$\beta_K = -5.70 + 7.31 \beta_{MSA} \quad (2.100)$$

Eq. 2.100 allows us to estimate the thermal conductivity at $P = 0$ if MSA and the thermal conductivity of the bulk sample with the porosity of P are known. In the same way of Young's modulus and electrical conductivity, the thermal conductivity of U_{0.4}Zr_{0.6}N (86.8%T.D.) and UN+60mol%TiN (92.8%T.D) were corrected to those of the porosity-free U_{0.4}Zr_{0.6}N and UN+60mol%TiN using the same equation with UN.

Fig. 2.59 and 2.60 show the temperature dependences of the thermal conductivity of porosity-free UN, U_{0.4}Zr_{0.6}N, ZrN, UN+60mol%TiN and TiN, together with the literature data [25, 27, 44, 91–97]. In these figures, the solid lines represent the fitting results (Eq. 2.101–105).

$$\text{UN: } \kappa (\text{Wm}^{-1}\text{K}^{-1}) = 2.08T^{0.342} \frac{1-P}{1+P} \quad (298 < T < 1273 \text{ K}, 0 < P < 0.2), \quad (2.101)$$

$$\text{U}_{0.4}\text{Zr}_{0.6}\text{N: } \kappa (\text{Wm}^{-1}\text{K}^{-1}) = 8.94T^{0.799} \frac{1-P}{1+P} \quad (298 < T < 1273 \text{ K}, 0 < P < 0.2), \quad (2.102)$$

$$\text{ZrN: } \kappa(\text{Wm}^{-1}\text{K}^{-1}) = 21.4T^{0.170} \frac{1-P}{1+5.31P} \quad (298 < T < 1473 \text{ K}, 0 < T < 0.2), \quad (2.103)$$

$$\text{UN+60mol\%TiN: } \kappa(\text{Wm}^{-1}\text{K}^{-1}) = 1.35T^{0.456} \frac{1-P}{1+P} \quad (298 < T < 1473 \text{ K}, 0 < T < 0.2), \quad (2.104)$$

$$\text{TiN: } \kappa(\text{Wm}^{-1}\text{K}^{-1}) = 44.8T^{-1.20 \times 10^{-4}} \frac{1-P}{1+2.03P} \quad (298 < T < 1473 \text{ K}, 0 < T < 0.3). \quad (2.105)$$

The thermal conductivities of ZrN and TiN obtained in the present study were vastly higher than the literature data [92–97]. To discuss about the differences between the data obtained in the present study and literatures, the author noticed the career thermal conductivity. The thermal conductivity (κ_{TOT}) is represented by the sum of the electric contribution (=career thermal conductivity: κ_{EL}), lattice contribution (=lattice thermal conductivity: κ_{LAT}) and the other contribution (κ_{OTHER}). The κ_{EL} can be estimated by Wiedemann–Franz law (Eq. 2.106).

$$\kappa_{\text{EL}} = \frac{1}{3}Cv l = \frac{\pi^2 n k_B^2 T \tau}{3m} \approx \frac{\pi^2}{3} \left(\frac{k_B}{e} \right) \sigma T \equiv L \sigma T \quad (2.106)$$

C : Specific heat at unit volume, l : Mean free path, v : Velocity of electron

n : Density of electron, k_B : Boltzmann constant ($=10^{-23} \text{ JK}^{-1}$),

τ : Mean collision time of electron, m : Atomic weight,

L : Lorenz number ($\doteq 2.45 \times 10^{-8} \text{ WK}^{-2}\Omega$), σ : Electrical conductivity

The κ_{EL} of ZrN and TiN estimated using the σ obtained in the present study were $32.5 \text{ Wm}^{-1}\text{K}^{-1}$ (ZrN) and $38.7 \text{ Wm}^{-1}\text{K}^{-1}$ (TiN) at room temperature and showed the similar value estimated using the literature data of the electrical conductivity [44, 73–75]. These values were higher than the κ_{TOTAL} in Ref. 92–97. In addition, the data evaluated by Nishi [98], which is not published yet, in JAEA shows the similar value of that obtained in the present study. Therefore, the author thinks that in Ref. 92–97 the thermal conductivities of ZrN and TiN was underestimated since the densities of the sample used in Ref. 92–97 were low ($< 82\% \text{ T.D.}$) and the values were below the P_c value, which is the points that the thermal conductivity rapidly decreases with increasing the porosity due to the rapid decreasing of MSA.

The thermal conductivity of UN obtained in the present study was well consistent with the literature data [25, 27, 91]. Nevertheless that of UN was quite lower than that of ZrN, that of U_{0.4}Zr_{0.6}N was lower than that of UN. In case of the solid solution, the thermal conductivity is lower than the simple addition of the thermal conductivity of UN and ZrN because U atoms in U_{0.4}Zr_{0.6}N lattice works as the center of the phonon scattering, which is called impurity scattering.

Even if we take account into this phenomenon, the thermal conductivity of $U_{0.4}Zr_{0.6}N$ is quite low. As the author described above, the electrical conductivity of $U_{0.4}Zr_{0.6}N$ was smaller than those of UN and ZrN due to the high impurity oxygen content in $U_{0.4}Zr_{0.6}N$. So, the κ_{EL} of $U_{0.4}Zr_{0.6}N$ were smaller than that of UN and ZrN. In addition, it was thought that the impurity oxygen and carbon worked as the center of the phonon scattering addition to U atom. At the region of $T < 1100K$, the thermal conductivity of UN+60mol%TiN obtained in the present study was slightly smaller than the value estimated from Schulz's equation. This is resulted from the grain boundary scattering. In fact, the experimental data of UN+60mol%TiN becomes to be close to the estimated data at high temperature, where the contribution of the grain boundary scattering becomes to be low.

2-4 Summary

The thermophysical properties of UN, ZrN and TiN were evaluated, where UN were used as the typical actinide mononitride, and ZrN and TiN were used as the inert matrix. In addition, to understand the interaction between actinide nitrides and inert matrix, the simulated ADS target fuel ($U_{0.4}Zr_{0.6}N$ and UN+60mol%TiN) was measured in terms of the thermophysical properties.

Sample preparation

UN, $U_{0.4}Zr_{0.6}N$ and UN+60mol%TiN were prepared by the carbothermic reduction and atmospheric pressure sintering. The impurity oxygen and carbon contents of $U_{0.4}Zr_{0.6}N$ were about four times of those of UN and UN+60mol%TiN due to the high sintering resistivity of ZrN. In case of ZrN and TiN, the bulk samples with various porosities were prepared by the spark plasma sintering to evaluate the porosity dependences of the thermophysical properties.

Sample characterization and crystallographic properties

The lattice parameters of UN, ZrN and TiN evaluated from the XRD analysis were well consistent with the JCPDS data. The lattice parameter of $U_{1-x}Zr_xN$ followed to Vegard's law, and those of UN phase and TiN phase in UN+60mol%TiN pellet agreed with those of UN and TiN pellets, respectively. From these XRD results and SEM-EDX analysis, it was confirmed that $U_{0.4}Zr_{0.6}N$ pellet is the solid solution of UN and ZrN, and that UN+60mol%TiN pellet is the composite of UN and TiN.

When we evaluate the porosity dependences of the thermophysical properties, it has been suggested by Rice (1999) that the minimum solid area (MSA) is very useful. However, the MSA had been scarcely used because it was very difficult to evaluate the MSA by experimentally method. In the present study, the author succeeded to experimentally evaluate the MSA for the

first time over the world by the confocal scanning laser microscope (SLM) because the SLM analysis includes not only the surface observation, but also the surface roughness. The coefficient (β_{MSA}) of the porosity dependence of MSA of UN agreed with those of $U_{0.4}Zr_{0.6}N$ and UN+60mol%TiN and was lower than those of ZrN and TiN. From these results, it was assumed that the porosity dependences of the thermophysical properties such as the thermal conductivity, electrical conductivity and elastic properties of $U_{0.4}Zr_{0.6}N$ and UN+60mol%TiN are same to that of UN given in the literatures. In addition, some bulk samples of ZrN and TiN with various densities were prepared by the SPS to evaluate the porosity dependences.

From the EBSP measurements, the grain size and misorientation angle were evaluated. The grain sizes and misorientation angles of $U_{0.4}Zr_{0.6}N$ and UN+60mol%TiN were lower and higher than those of UN, respectively. The grain sizes of ZrN and TiN were larger than those of $U_{0.4}Zr_{0.6}N$ and UN+60mol%TiN because the grain size of the starting powder of ZrN and TiN were larger than those of $U_{0.4}Zr_{0.6}N$ and UN+60mol%TiN. On the other hand, the misorientation angle of ZrN and TiN were higher than those of the others because the SPS time is very short. In the present study, the EBSP analysis was used in the field of the nuclear fuel engineering for the first time.

Mechanical properties

(1) Young's modulus

The coefficient of the porosity dependences of Young's modulus of UN, ZrN and TiN were proportional to β_{MSA} . This relationship allows us to easily estimate Young's modulus of the porosity-free material from only one sample. Therefore, since this method vastly decreases the number of times of the experiment and the number of the samples when we evaluate the thermophysical properties, this method would be extremely effective on the research of the thermophysical properties of MA-containing fuels with the strict regulation on the dealing.

By the in-situ indentation test, the author succeeded to strike the precipitation such as UN and TiN phase in UN+60mol%TiN for the first time. Young's modulus of UN, $U_{0.4}Zr_{0.6}N$ and ZrN obtained from the indentation tests were well consistent with those of the porosity-free samples estimated from the results of the ultrasonic pulse echo method using Wachtman equation. It was found that Young's modulus of $U_{1-x}Zr_xN$ linearly increases with increasing the X.

Young's modulus of TiN phase in UN+60mol%TiN obtained from the indentation test was higher than that of TiN pellet. Young's modulus of UN+60mol%TiN obtained by the ultrasonic pulse echo method didn't agree with those estimated from Young's moduli of UN and TiN pellets

obtained from indentation test or ultrasonic pulse echo method using Fan's equation and Hashin's equation, because their equations don't take account into the interaction between UN and TiN phases in UN+60mol%TiN pellet. On the other hand, for the first time, the author succeeded the precise estimation of Young's modulus of UN+60mol%TiN by using Young's modulus of UN phase and TiN phase in UN+60mol%TiN pellet obtained from the in-situ indentation tests. Generally, the large sample is necessary when we evaluate Young's modulus. However, the sample size is very small in case of the method suggested in the present study to estimate the Young's modulus of the composite material. This method would be extremely useful to evaluate the mechanical properties of MA-containing fuels, too.

(2) Vickers hardness and fracture toughness

Vickers hardness of UN and ZrN obtained in the present study agreed with the literature data. Vickers hardness of $U_{1-x}Zr_xN$ and UN+Xmol%TiN at $P = 0$ simply increased with increasing the X. From the EBSD measurements, it was found that the intragranular cracks in UN, $U_{0.4}Zr_{0.6}N$, and UN+60mol% pellets progress without stopping at the grain boundary, but that the intragranular cracks in ZrN and TiN pellets stop at the grain boundary or convert to the intergranular crack due to the high misorientation angle. Therefore, in case of ZrN or TiN content dependences of the fracture toughness of $U_{1-x}Zr_xN$ and UN+Xmol%TiN, the certain trend could not be observed.

(3) Indentation hardness

The indentation hardness of all samples decreased with increasing the load. This phenomenon is called the indentation size effect (ISE), and Nix and Gao suggested that the square of the indentation hardness is proportional to the inverse of the indentation depth. When the author re-plotted the indentation hardness to follow Nix and Gao model, the indentation hardness of UN followed to Nix and Gao model in the region of the high depth. On the other hand, in the region of the low depth, Nix and Gao model overestimated the indentation hardness. By taking account into the spread out effect of the geometrically necessary dislocations, the author could reproduce the indentation hardness in whole region. This model was suggested in the present study to the improved Nix and Gao model.

The indentation hardness of UN phase in UN+60mol%TiN pellet agreed with that of UN pellet. On the other hand, the indentation hardness of TiN phase in UN+60mol%TiN pellet was higher than that of TiN pellet. From this result, it was found that the strain and dislocation concentrate in TiN phase. This was confirmed by the EBSD analysis, too. Like this way, the author evaluated the interaction with each phase by EBSD and indentation test.

Electrical conductivity

The electrical conductivity of UN obtained in the present study was well consistent with the literature data and that of ZrN obtained in the present study was within variations of the literature data. The electrical conductivity of $U_{0.4}Zr_{0.6}N$ was smaller than those of UN and ZrN due to the high content of the impurity oxygen nevertheless that of ZrN was vastly larger than that of UN. The electrical conductivity of UN+60mol%TiN was lower than the data estimated from Schulz's equation due to the grain boundary scattering. The difference between the experimental data and estimated data of the electrical conductivity of UN+60mol%TiN decreased with increasing the temperature.

Thermal properties

(1) Thermal expansion

The thermal expansion of UN, ZrN and TiN obtained in the present study by the thermodilatometry were well consistent with the literature data obtained from the high-temperature XRD measurements. The thermal expansion of $U_{0.4}Zr_{0.6}N$ and UN+60mol%TiN followed to Vegard's law and Turner's equation, respectively.

(2) Specific heat capacity

The specific heat capacity of UN, ZrN and TiN obtained in the present study were well consistent with the literature data and C_p of UN, ZrN and TiN were higher than the sum C_v of C_D estimated from Debye model. Their difference in UN was quit larger than those of ZrN and TiN. Those of $U_{0.4}Zr_{0.6}N$ and UN+60mol%TiN agreed with the data estimated from Neumann-Kopp's law and addition match.

(3) Thermal conductivity

The coefficient of the porosity dependences of the thermal conductivity of UN, TiN and ZrN were 1.0, 2.03 and 5.31 and proportional to β_{MSA} , in the same way of Young's modulus. The thermal conductivity of UN obtained in the present study was well consistent with the literature data. Those of ZrN and TiN obtained in the present study were higher than the literature data, which would underestimate judging from Wiedemann-Franz law. Nevertheless the thermal conductivity of UN is vastly lower than that of ZrN, that of $U_{0.4}Zr_{0.6}N$ was lower than those of UN and ZrN due to the degradation of κ_{EL} by the high oxygen content and impurity scattering from the solution of uranium, oxygen and carbon. The experimental data of the thermal conductivity of UN+60mol%TiN was lower than the data estimated from Schulz's equation at low temperature due to the grain boundary scattering, in the same way of the electrical conductivity. The

experimental data agreed with the estimated data at high temperature.

Judging from the results of Chapter 2, it would be not easy to use $Pu_{x-y}MA_yZr_{1-x}N$ as the actual fuel because the prediction of the thermophysical properties of $Pu_{x-y}MA_yZr_{1-x}N$ is very difficult in the different way of (Pu,MA)N+TiN. In case of UN+60mol%TiN, the mechanical, electrical and thermal properties were improved by the addition of TiN and were roughly predicted by the theoretical or empirical model. Therefore, it is easy to predict the thermophysical properties of (Pu,MA)N+TiN with various component. Judging from only these results, TiN is more effective than ZrN as the inert matrix.

In case of the nitride fuels, it is a problem that the oxidation resistivity of PuN and AmN is very low, and that PuN and AmN vaporize at high temperature due to their high vapor pressure. ZrN may improve this problem because the chemical stability would be improved by the solution of ZrN to PuN and AmN. This effect could not be expected in case of (Pu,MA)N+TiN. Therefore, evaluation of not only the thermophysical properties, but also thermodynamics properties of the nitride fuels would become to be important when we use the nitride fuels as the actual fuels.

When we predict the fuel behavior such as the fuel swelling, temperature distribution, pellet cracking, PCI, FCI and so on, it is very important to evaluate the elastic moduli, hardness, toughness, creep rate, thermal properties and thermodynamic properties. In the present study, the elastic moduli, hardness, toughness and thermal properties were evaluated. If the creep rate and thermodynamics properties of the nitride fuel with inert matrix could be evaluated, we would be able to establish the model of the fuel behavior.

In the present study, the newest techniques, which are SPS, EBSD and indentation test, and the new concept such as MSA were used in the field of the nuclear fuel engineering for the first time. The author succeeded to precisely evaluate the thermophysical properties of inert matrix material (ZrN and TiN) and was able to suggest the new methods to evaluate the porosity dependences of the thermophysical properties, which are extremely effective for the research of MA-containing fuels.

References

- [1] L. Donnet, F. Jorion, N. Drin, S.L. Hayes, J.R. Kennedy, K. Pasamehmetoglu, S.L. Voit, D. Haas, A. Fernandez, "The FUTURIX-FTA experiment in PHENIX: Status of fuel fabrication," Proc. Int. Conf. GLOBAL2005, Tsukuba, Japan, Oct. 9–13, 2005, Paper No. 258.
- [2] K. Minato, M. Akabori, M. Takano, Y. Arai, K. Nakajima, A. Itoh, T. Ogawa, "Fabrication of nitride fuels for transmutation of minor actinides," J. Nucl. Mater. 320 (2003) 18–24.
- [3] Y. Arai, K. Nakajima, "Preparation and characterization of PuN pellets containing ZrN and TiN," J. Nucl. Mater. 281 (2000) 244–247.
- [4] M. Streit, F. Ingold, M. Pouchon, L.J. Gauckler, J.-P. Ottaviani, "Zirconium nitride as inert matrix for fast systems," J. Nucl. Mater. 319 (2003) 51–58.
- [5] A. Mitsuo, T. Mori, Y. Setsuhara, S. Miyake, T. Aizawa, "Mechanical properties of zirconium nitride films prepared by ion-beam assisted deposition," Nucl. Instrum. Meth. B 206 (2003) 366–370.
- [6] E. Atar, C. Sarioglu, U. Demirler, E.S. Kayali, H. Cimenoglu, "Residual stress estimation of ceramic thin films by X-ray diffraction and indentation techniques," Scripta Mater. 48 (2003) 1331–1336.
- [7] M. Chhowalla, H.E. Unalan, "Thin films of hard cubic Zr_3N_4 stabilized by stress," Nat. Mater. 4[4] (2005) 317–322.
- [8] S.Y. Chiou, D. Gan, "Interfacial mechanical properties of TiN coating on steels by indentation," J. Mater. Sci. 42[8] (2007) 2745–2752.
- [9] 理学電機株式会社, "X線回折ハンドブック," 国際文献印刷社, 東京, 1999.
- [10] R.W. Rice, "Porosity of ceramics," Marcel Dekker Inc., New York, U.S.A., 1999.
- [11] G.M. Tomilov, "Changes in the elastic properties of ceramic quartz during sintering," Neorgan. Mater. 13[1] (1977) 117–119.
- [12] R.W. Rice, "Evaluating Porosity Parameters for Porosity-Property Relations," J. Am. Ceram. Soc. 76[7] (1993) 1801–1808.
- [13] 日本材料科学会, "超音波と材料," 裳華房, 東京, 1992.
- [14] JIS R 1610.
- [15] A.G. Evans, E.A. Charles, "Fracture toughness determinations by indentation," J. Am. Ceram. Soc. 59[7–8] (1976) 371–372.
- [16] K. Niihara, R. Morena, D.P.H. Hasselman, "Evaluation of KIC of brittle solids by the indentation method with low crack-to-indent ratios," J. Mater. Sci. Letters 1 (1982) 13–16.

- [17] W.C. Oliver, G.M. Pharr, "An improved technique for determining hardness and elastic modulus using load and displacement sensing indentation experiments," *J. Mater. Res.* 7 (1992) 1564–1583.
- [18] R.B. Matthews, K.M. Chidester, C.W. Hoth, R.R. Mason, R.L. Petty, "Fabrication and testing of uranium nitride fuel for space power reactors," *J. Nucl. Mater.* 151 (1988) 334–344.
- [19] Y. Arai, A. Maeda, K. Shiozawa, T. Ohmichi, "Chemical forms of solid fission products in the irradiated uranium–plutonium mixed nitride fuel," *J. Nucl. Mater.* 210 (1994) 161–166.
- [20] M. Uno, K. Kurosaki, A. Nakamura, "Reactions of uranium nitride with platinum–family metals," *J. Nucl. Mater.* 247 (1997) 322–327.
- [21] A.C. Fisher–Cripps, "Nanoindentation," Springer Co., New York, U.S.A., 2002.
- [22] Y. Takahashi, M. Asou, "Development of a high–temperature differential scanning calorimeter equipped with a triple–cell system," *Thermochim. Acta* 223 (1993) 7–22.
- [23] S.L. Hayes, J.K. Thomas, K.L. Peddicord, "Material property correlations for uranium mononitride; I. Physical properties," *J. Nuclear Mater.* 171 (1990) 262–270.
- [24] S.L. Hayes, J.K. Thomas, K.L. Peddicord, "Material property correlations for uranium mononitride; II Mechanical properties," *J. Nucl. Mater.* 171 (1990) 271–288.
- [25] S.L. Hayes, J.K. Thomas, K.L. Peddicord, "Material property correlations for uranium mononitride; III Transport properties," *J. Nucl. Mater.* 171 (1990) 289–299.
- [26] S.L. Hayes, J.K. Thomas, K.L. Peddicord, "Material property correlations for uranium mononitride; IV Thermodynamic properties," *J. Nucl. Mater.* 171 (1990) 300–318.
- [27] S.B. Ross, M.S. El–Genk, R.B. Matthews, "Thermal conductivity correlation for uranium nitride fuel between 10 and 1923 K," *J. Nucl. Mater.* 151 (1988) 313–317.
- [28] JCPDS 32–1397 (UN).
- [29] JCPDS 41–1422 (UO_2).
- [30] JCPDS 2–956 (ZrN).
- [31] JCPDS 37–1484 (α ZrO_2).
- [32] JCPDS 38–1420 (TiN)
- [33] JCPDS 21–1276 (TiO_2)
- [34] R.W. Rice, C.C. Wu, F. Borchelt, "Hardness–Grain–Size Relations in Ceramics," *J. Am. Ceram. Soc.* 77[10] (1994) 2539–53.
- [35] A. Padel, C.D. Novion, "Constantes elastiques des carbures, nitrures et oxides d'uranium et de plutonium," *J. Nucl. Mater.* 33 (1969) 40–51.
- [36] T. Honda, T. Kikuchi, "Porosity dependence of elastic modulus of uranium nitride," *J. Nucl. Sci.*

Technol. 6 (1968) 221–222.

[37] H.L. Whaley, R.A. Potter, W. Fulerson, “Ultrasonic Velocity Measurements in UN,” U.S. At. Energy Comm. ORNL-4370 (1968) 86.

[38] E.O. Speidel, D.L. Keller, “Fabrication and Properties of Hot-pressed Uranium Mononitride,” U.S. At. Energy Comm. BMI-1633 (1963) 65.

[39] B.A. Atamanenko, “Porosity influence on optical and mechanical properties of zirconium nitride,” *Phy. Chem. Mech. Surfaces* 9 (1995) 281–286.

[40] K.I. Portnoi, A.A. Mulaseev, V.N. Gribkov, Yu.V. Levinskii, “Modulus of normal elasticity of porosity-free titanium and zirconium nitride,” *Soviet Powder Metallurgy and Metal Ceramics* 8[5] (1968) 406–409.

[41] I.N. Frantsevich, E.A. Zhurakovskii, A.B. Lyashchenko, “Elastic constants and electron structure of some refractory compounds obtained by powder metallurgical methods,” *Neorgan. Mat.* 3[1] (1967) 8–16.

[42] J. Russias, S. Cardinal, J. Fontaine, G. Fantozzi, C. Esnouf, K. Bienvenu, “Bulk titanium nitride material obtained from SHS starting powder: Densification, mechanical characterization and tribological approach,” *Int. J. Refract. Met. H* 23 (2005) 344–349.

[43] H. Kuwahara, N. Mazaki, M. Takahashi, T. Watanabe, X. Yang, T. Aizawa, “Mechanical properties of bulk sintered titanium nitride ceramics,” *Mater. Sci. Eng. A* 319–321 (2001) 687–691.

[44] A.G. Alekseev, “高融点化合物物性便覧,” 日ソ通信社, 和歌山, 1994.

[45] J.B. Wachtman Jr, W.E. Tefft, D.G. Lam Jr., C.S. Apstein, “Exponential temperature dependence of Young’s modulus for several oxides,” *Phys. Rev.* 122[6] (1961) 1754–1759.

[46] Z. Fan, P. Tsakiroopoulos, A.P. Miodownik, “Prediction of Young’s modulus of particulate two phase composites,” *Mater. Sci. Tech-Lond.* 8 (1992) 922–929.

[47] Z. Hashin, S. Shtrikman, “A variational approach to the theory of the elastic behavior of polycrystals,” *J. Mech. Phys. Solid.* 10 (1963) 343–352.

[48] T.G. Godfrey, G. Hallerman, O.B. Cavin, “Microhardness Studies on Sintered UN,” U.S. At. Energy Comm. ORNL/TM-1050 (1965) 142.

[49] J.P. Moore, W. Fulkerson, D.L. McElroy, “Thermal conductivity, electrical resistivity, and Seebeck coefficient of uranium mononitride,” *J. Am. Ceram. Soc.* 53 (1970) 76–82.

[50] J.D.L. Harrison, “The hot-hardness of Uranium Carbonitrides,” U.S. At. Energy Comm. ORNL-4330 (1968) 28.

[51] R.W. Endebrook, E.L. Foster, D.L. Keller, “Preparation and Properties of Cast UN,” U.S. At.

Energy Comm. BMI-1690 (1968) 22.

[52] T.G. Godfrey, G. Hallerman, "Microhardness Studies on Sintered UN," U.S. At. Energy Comm. ORNL-3870 (1965) 66.

[53] K. Wheeler, P. Peralta, M. Parra, K. McClellan, J. Dunwoody, G. Egelan, "Effect of sintering conditions on the microstructure and mechanical properties of ZrN as a surrogate for actinide nitride fuels," J. Nucl. Mater. 366 (2007) 306–316

[54] M. Moriyama, K. Kamata, Y. Kobayashi, J. Ceramics Soc. Jpn. 99 (1991) 286.

[55] T. Yamada, M. Shimada, M. Koizumi, "Fabrication and characterization of titanium nitride by high pressure hot pressing," Am. Ceram. Soc. Bull. 59[6] (1980) 611–616.

[56] T.R.G. Kutty, K.N. Chandrasekharan, J.P. Panakkal, J.K. Ghosh, "Fracture toughness and fracture surface energy of sintered uranium dioxide fuel pellets," J. Mater. Sci. Lett. 6 (1987) 260–262.

[57] K. Yamada, S. Yamanaka, M. Katsura, "Mechanical properties of (U,Ce)O₂," J. Alloys Compd. 271–273 (1998) 697–701.

[58] K. Kurosaki, Y. Saito, H. Muta, M. Uno, S. Yamanaka, "Nanoindentation studies of UO₂ and (U,Ce)O₂," J. Alloys Compd. 381 (2004) 240–244.

[59] M.T. Aybers, R. Artir, A.A. Aksit, S. Akbal, "Investigation of some mechanical properties of Ti₂O₃-doped UO₂ fuel pellets," Mater. Charact. 57 (2006) 182–186.

[60] A.K. Sengupta, C.B. Basak, T. Jarvis, R.K. Bhagat, V.D. Pandey, S. Majumdar, "Effect of titania addition on hot hardness of UO₂," J. Nucl. Mater. 325 (2004) 141–147.

[61] G. Feng, W.D. Nix, "Indentation size effect in MgO," Scripta Mater. 51 (2004) 599–603.

[62] W.D. Nix, H. Gao, "Indentation size effects in crystalline materials: a law for strain gradient plasticity," J. Mech. Phys. Solids 46 (1998) 411–425.

[63] N.A. Fleck, J.W. Hutchinson, "A phenomenological theory for strain gradient effects in plasticity," J. Mech. Phys. Solids 41 (1993) 1825–1857.

[64] M.F. Ashby, "The deformation of plastically non-homogeneous alloys," Phil. Mag. 21 (1970) 399–424.

[65] D. Tabor, "The hardness of metal," Clarendon Press, Oxford, 1951, p. 51.

[66] 高橋 幸伯, 町田 進, 角 洋一, "基礎材料力学," 培風館, 東京, 日本, 2004.

[67] J.G. Swadener, E.P. George, G.M. Pharr, "The correlation of the indentation size effect measured with indenters of various shapes," J. Mech. Phys. Solids 50 (2002) 681–694.

[68] W. Fulkerson, T.G. Kollie, S.C. Weaver, J.P. Moore, R.K. Williams, Proc. 4th Int. Conf. On

Plutonium and Other actinides, AIME, Santa Fe, U.S.A., 1970, p.374.

[69] B.A. Hayes, M.A. DeCrescente, "Thermal conductivity and electrical resistivity of uranium mononitride," U.S. At. Energy Comm. PWAC-481 (1965) 28.

[70] T.G. Kollie, J.P. Moore, "Metals and ceramics division annual progress report," U.S. At. Energy Comm. Rep. ORNL-3670 (1964).

[71] R.W. Endebrook, E.L. Foster, D.L. Keller, "Preparation and Properties of Cast UN," U.S. At. Energy Comm. BMI-1690 (1961) 22.

[72] D.L. Keller, "Development of uranium mononitride," U.S. At. Energy Comm. BMI-X-178 (1961).

[73] I.I. Petrova, V.A. Petrov, B.G. Ermakov, V.V. Sokolov, "Specific electrical resistance of zirconium and hafnium nitrides," *Teplofizika Vysokikh Temperature* 10[5] (1972) 1007.

[74] G.V. Samsonov, "Nitrides," Naukova Dumka, Kiev, Russia 1969.

[75] V.S. Neshpor, "Thermal conductivity of cubic monocarbides and mononitrides of transition metals," *Neorgan. Mater.* 4[12] (1968) 2200-2202.

[76] B. Costa, R. Lallement, F. Anselin, D. Rossignol, "Proceedings of the International Symposium on Compounds of Interest in Nuclear Reactor Technology," Metallurgical and Petroleum Engineers, New York, U.S.A., 1964, pp.83-91.

[77] I.H. Warren, C.E. Price, "Thermoelectric properties of cubic uranium monocompounds," *Can. Met. Quart.* 3(2) (1964) 183-196.

[78] B. Schulz, "Thermal conductivity of porous and highly porous materials," *High Temp.-High Press.* 13 (1981) 649-660

[79] Y.S. Touloukian, R.K. Kirby, R.E. Taylor, T.Y.R. Lee, "Thermal expansion: Nonmetallic solids," IFI/Plenum, New York, 1977.

[80] R. Benz, G. Balog, B. H. Baca, "Uranium-uranium dioxide-uranium nitride (UN₂) phase diagram," *High Temp. Sci.* 2[3] (1970) 221-251.

[81] K.M. Taylor, P.A. Smudski, L.N. Halley, T.J. Keaty, "Synthesis and fabrication of refractory uranium compounds," U.S. At. Energy Comm. ORO-248 (1959) 21.

[82] C.P. Kempter, R.O. Elliott, "Thermal expansion of UN, UO₂, (U,Th)O₂, and ThO₂," *J. Chem. Phys.* 30 (1959) 1524-1526.

[83] R. Thetford and M. Mignanelli, "The chemistry and physics of modelling nitride fuels for transmutation," *J. Nucl. Mater.* 320 [1,2] (2003) 44-53.

[84] K. Aigner, W. Lengauer, D. Rafaja, P. Ettmayer, "Lattice parameters and thermal expansion of Ti(C_xN_{1-x}), Zr(C_xN_{1-x}), Hf(C_xN_{1-x}) and TiN_{1-x} from 298 to 1473 K as investigated by high-temperature

X-ray diffraction," J. Alloys Compd. 215 (1994) 121–126

[85] M. Singh, H. Wiedemeier, "Estimation of thermal expansion behavior of some refractory carbides and nitrides," J. Mater. Sci. 32 (1997) 5749–5751.

[86] C.R. Houska, "Thermal expansion and atomic vibration amplitudes for TiC, TiN, ZrC, ZrN, and pure tungsten," Phy. Chem. Solids 25[4] (1964) 359–366.

[87] T.W. Baker, "The coefficient of thermal expansion of zirconium nitride," Acta Crysta. 11 (1958) 300.

[88] R.S. Turner, "Thermal-expansion stresses in reinforced plastics," J. Research Natl. Bur. Standards 37[4] (1946) 239–250.

[89] The SGTE Pure Substance and Solution databases, GTT-DATA SERVICES, 1996.

[90] H. Tagawa, "Phase relations and thermodynamic properties of the uranium–nitrogen system," J. Nucl. Mater. 51 (1974) 78.

[91] Y. Arai, Y. Suzuki, T. Iwai, T. Ohmichi, "Dependence of the thermal conductivity of (U,Pu)N on porosity and plutonium content," J. Nucl. Mater. 195[1–2] (1992) 37–43.

[92] V. Basini, J.P. Ottaviani, J.C. Risharud, M. Streit, F. Ingold, "Experimental assessment of thermophysical properties of (Pu,Zr)N," J. Nucl. Mater. 344 [1–3] (2005) 186–190.

[93] J.C. Hedge, J.W. Kopeck, C. Kostenko, J.L. Lang, "Thermal properties of refractory alloys," U.S. At. Energy Comm. ASD-TDR-63-597, (1963) 128.

[94] D.S. Neel, C.D. Pears, S. Oglesby Jr., "The thermal properties of thirteen solid materials to 5000 °F or their destruction temperatures," NASA Doc. N62-12987 (1962) 216.

[95] R.E. Taylor, J. Morreale, "Thermal conductivity of titanium carbide, zirconium carbide, and titanium nitride at high temperatures," J. Am. Ceram. Soc. 47[2] (1964) 69–73.

[96] T. Vasilos, W.D. Kingery, "Thermal conductivity. XI. Conductivity of some refractory carbides and nitrides," J. Am. Ceram. Soc. 37 (1954) 409–414.

[97] F.H. Norton, W.D. Kingery, G. Economos, M. Humenik Jr., "Metal–ceramic interactions at elevated temperatures," U.S. Atomic Energy Comm. NYO-6144 (1953) 83.

[98] T. Nishi, M. Takano, M. Akabori, K. Minato, Private connection.

Table 2.1 Different point in the preparation conditions of the bulk sample of UN, $U_{0.4}Zr_{0.6}N$ and UN+60mol%TiN

Prepared sample name		UN	$U_{0.4}Zr_{0.6}N$	UN+60mol%TiN
Specific surface area of UO_2	m^2/g	8.0	9.1	8.2
O/M of UO_2 powder	–	2.14	2.08	2.08
Holding temperature in two step of the conversion process ^{a)}	K	1773	1973	1773
Holding temperature in two step of the conversion process	hr	8	24	8
Time of ball milling	hr	40	65	40
Holding temperature in the sintering process	K	2073	2073	2073
Holding time in the sintering process	hr	4	28	8

a) The process to remove the residual carbon as CH_4 in the carbothermic reduction.

Table 2.2 Sample characteristics and physical properties of UN, $U_{0.4}Zr_{0.6}N$ and UN+60mol%TiN

Compound		UN	$U_{0.4}Zr_{0.6}N$	UN+60mol%TiN
Structure type		NaCl	NaCl	NaCl
Theoretical density	g/cm^3	14.32	10.51	7.28
Molecular Weight	–	252	163.9	105.2
Mass density	g/cm^3	13.21	9.12	6.77
Relative density	% T.D.	92.2	86.8	92.8
Lattice parameter	nm	0.4889	0.4697	0.4890 (UN), 0.4243 (TiN)
Arithmetic roughness	nm	2.8	1.0	2.2
Average grain size	μm	10.4	5.2	3.6 (UN), 4.4 (TiN)
Maximum grain size	μm	1.1	0.7	0.4 (UN), 0.5 (TiN)
Minimum grain size	μm	22.5	7.2	5.3 (UN), 6.5 (TiN)
N/M ^{a)}	–	0.97	1.06	1.02
O ₂ content	wt. %	0.246	0.873	0.207
C content	wt. %	0.094	0.238	0.082

a) Ratio of nitrogen for metal (U, Ti and Zr)

Table 2.3 Sample characteristics and physical properties of UN, $U_{0.4}Zr_{0.6}N$ and UN+60mol%TiN

Compounds		ZrN			TiN				
SPS temperature	K	1773	1873	2073	1648	1788	1873	1973	2073
Structure type	–	NaCl			NaCl				
Theoretical density	g/cm^3	7.28			5.44				
Molecular Weight	–	105.2			61.89				
N/M	–	0.935			0.96				
Mass density	g/cm^3	6.01	6.597	6.81	3.89	4.58	4.89	4.76	5.11
Relative density	% T.D.	82.5	90.5	93.5	71.6	84.1	89.8	87.5	94
Lattice parameter	nm	0.4580	0.4580	0.4579	0.4242	0.4242	0.4242	0.4242	0.4243
Arithmetic roughness	nm	–	–	2.0	–	–	–	–	2.4
Average grain size	μm	9.3	8.8	9.0	13.8	14.5	14.1	12.9	13.3
Maximum grain size	μm	1.1	0.9	1	1.7	1.9	1.5	1.8	2.3
Minimum grain size	μm	23.5	20.8	22.6	20.2	20.8	21.4	22.5	20.5

Table 2.4 Result of ultrasonic pulse-echo method of UN, $U_{0.4}Zr_{0.6}N$ and UN+60mol%TiN

Compounds		UN		$U_{0.4}Zr_{0.6}N$		UN+60mol%TiN	
Porosity, P		0.079	0	0.133	0	0.069	0
Longitudinal sound velocity, V_L	m/sec	4378	4802	5642	6600	6063	6582
Shear sound velocity, V_S	m/sec	2507	2750	3219	3766	3524	3825
Young's modulus, E	GPa	208	273	238	375	286	362
Shear modulus, G	GPa	83.0	109	94.4	149	115	145
Poisson's ratio, ν		0.256	0.256	0.259	0.259	0.245	0.245
Bulk modulus, B	GPa	142	187	164	259	187	237
Debye temperature, θ_D	K	339	373	453	531	–	–

In this table, the data at $P=0$ are the estimated data.

Table 2.5 Results of the ultrasonic pulse echo method of ZrN

Compounds		Zr			
Porosity, P	–	0.175	0.089	0.065	0
Longitudinal sound velocity, V_L	m/sec	5561	7126	7196	8559
Shear sound velocity, V_S	m/sec	3333	4066	4135	4919
Young's modulus, E	GPa	162	275	288	442
Shear modulus, G	GPa	66.4	109	115	176
Poisson's ratio, ν	–	0.220	0.259	0.253	0.253
Bulk modulus, B	GPa	96.3	189.6	194.9	299
Debye temperature, θ_D	K	479	587	597	711

In this table, the data at $P=0$ are the estimated data.

Table 2.6 Results of the ultrasonic pulse echo method of TiN

Compounds		TiN				
Porosity, P	–	0.284	0.125	0.102	0.060	0
Longitudinal sound velocity, V_L	m/sec	7201	9090	9597	9851	10990
Shear sound velocity, V_s	m/sec	4326	5285	5800	5984	6581
Young's modulus, E	GPa	178	331	399	442	575
Shear modulus, G	GPa	72.9	133	164	183	236
Poisson's ratio, ν	–	0.218	0.244	0.212	0.207	0.221
Bulk modulus, B	GPa	105	216	231	252	343
Debye temperature, θ_D	K	574	703	770	793	1022

In this table, the data at $P=0$ are the estimated data.

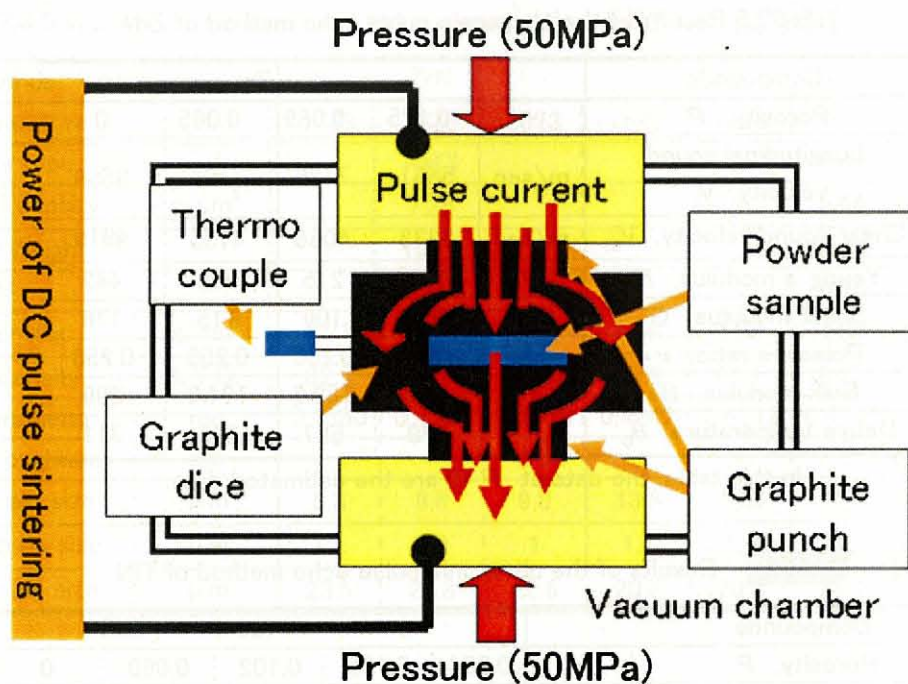


Fig. 2.1 Schematic of the SPS

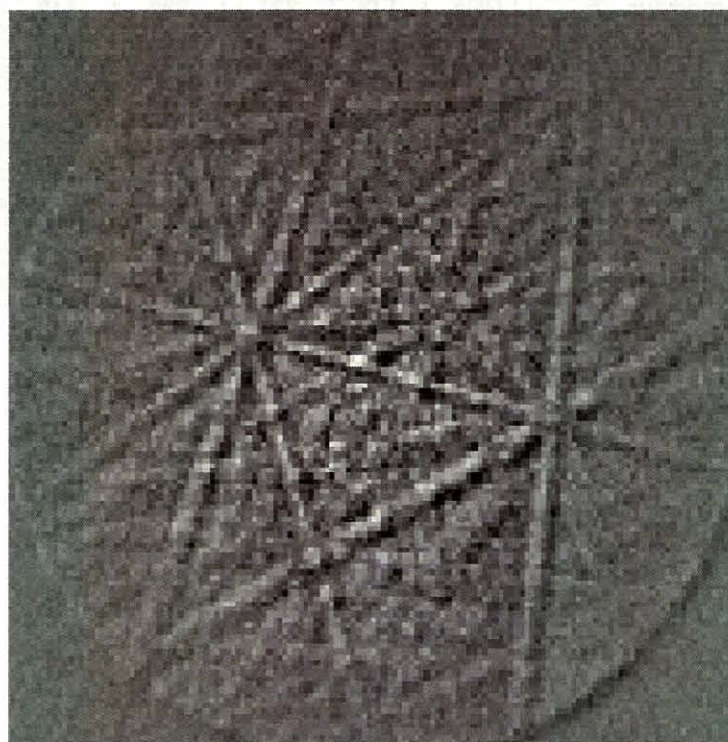


Fig. 2.2 Kikuchi pattern of ZrN

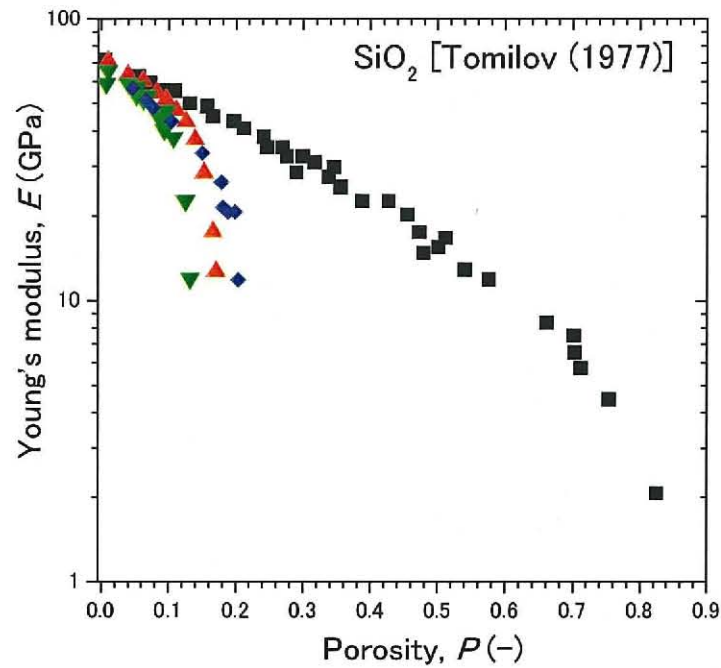


Fig. 2.3 Porosity dependence of Young's modulus of fused silica referred from Ref. 11

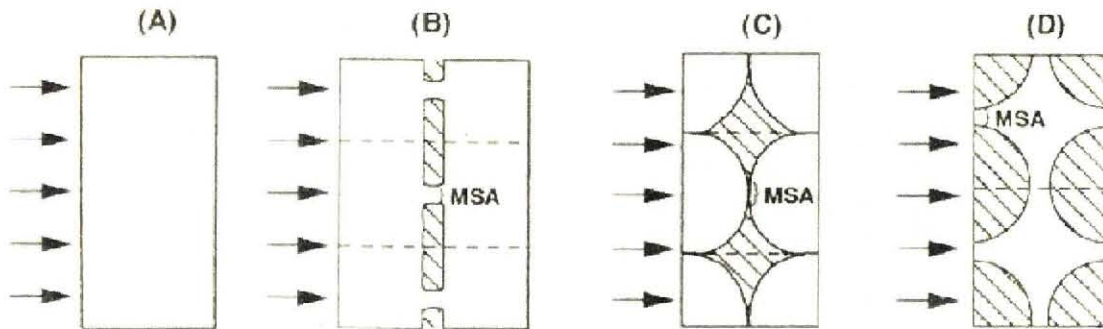


Fig. 2.4 Schematic of the MSA model concept (cross-hatched area = pores) referred from Ref. 10

For a homogeneous solid (A) the minimum and average solid cross sections are the same. However, it is clear that flux or stress transmission in (B) must be dominated by the MSA normal to the direction of the stress or flux (dashed lines delineate cell structure). Corresponding definitions of the MSA for pores between spherical particles (C) and spherical pores (D).

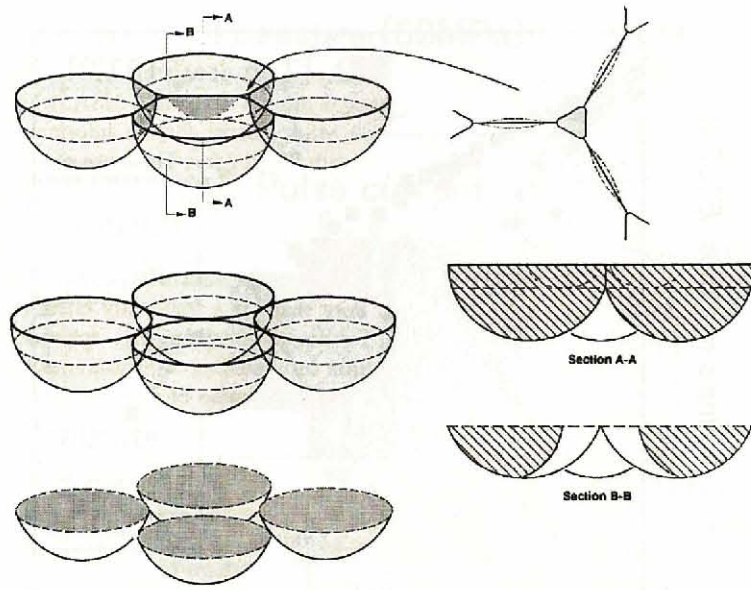


Fig. 2.5 Shape of pores in the sample with the single grain stacking referred from Ref. 10

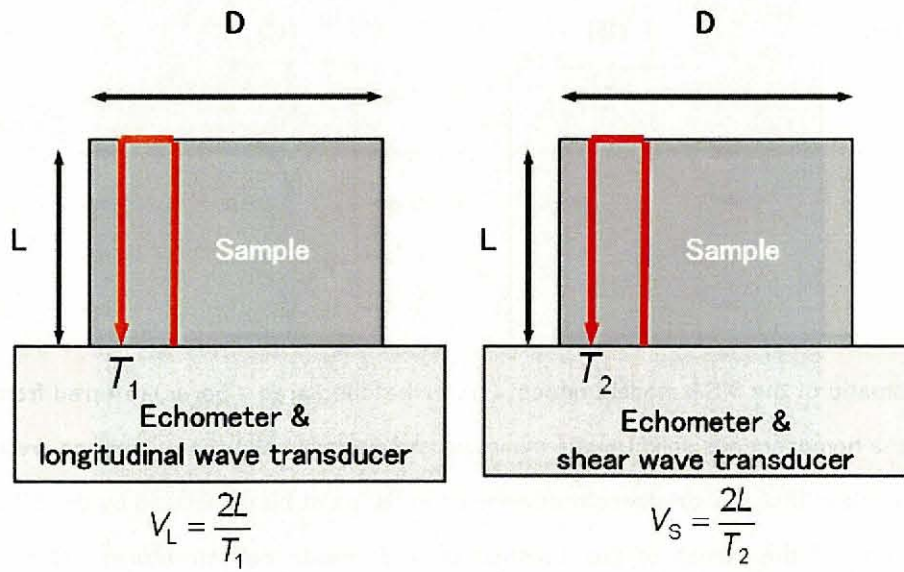


Fig. 2.6 Schematic view of ultrasonic pulse echo measurement

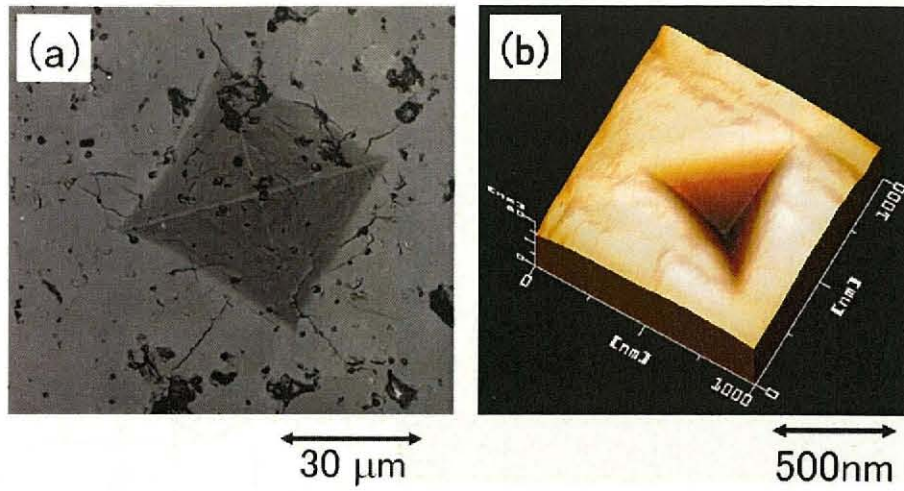


Fig. 2.7 Impression image of UN

(a) Vickers hardness test at the load of 9800 mN (SLM image)

(b) Indentation test at the load of 4.0 mN (AFM image)

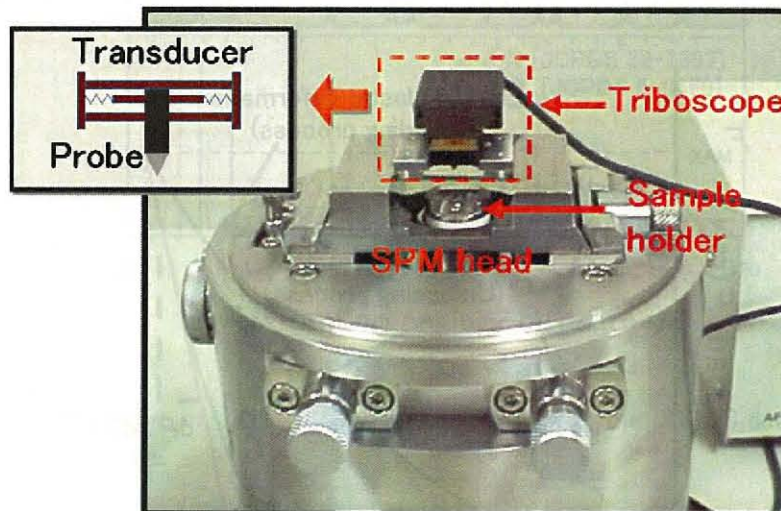


Fig. 2.8 Appearance of the indentation system.

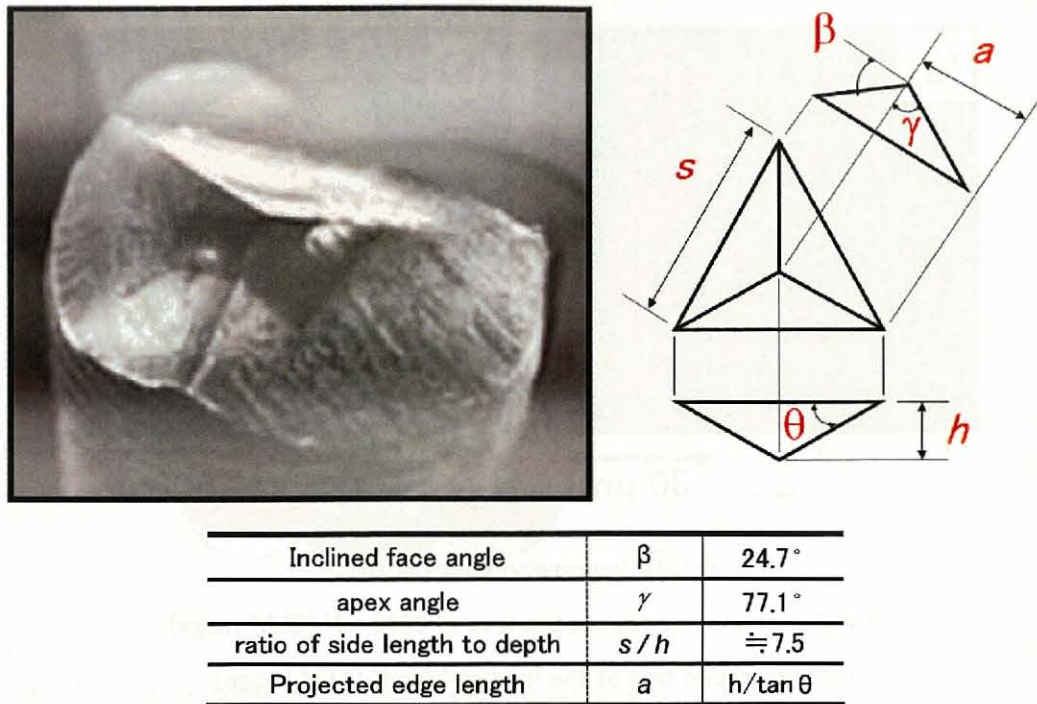


Fig. 2.9 SEM image and characteristics of the Berkovich type diamond indenter

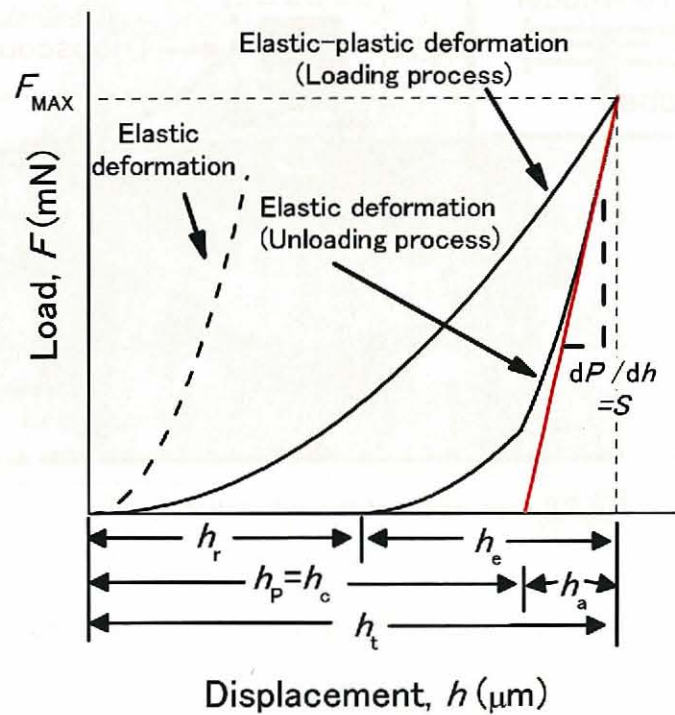


Fig. 2.10 Load-displacement curve in indentation test

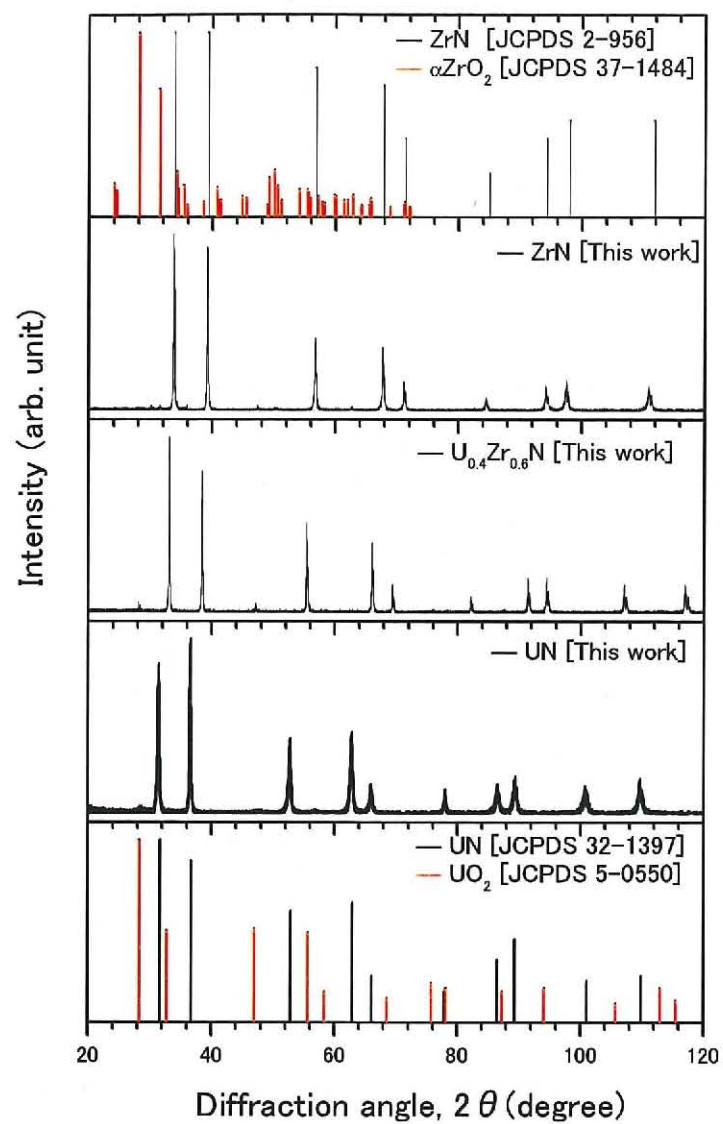


Fig. 2.11 XRD pattern of UN, $U_{0.4}Zr_{0.6}N$, ZrN, together with the JCPDS data [28-31]

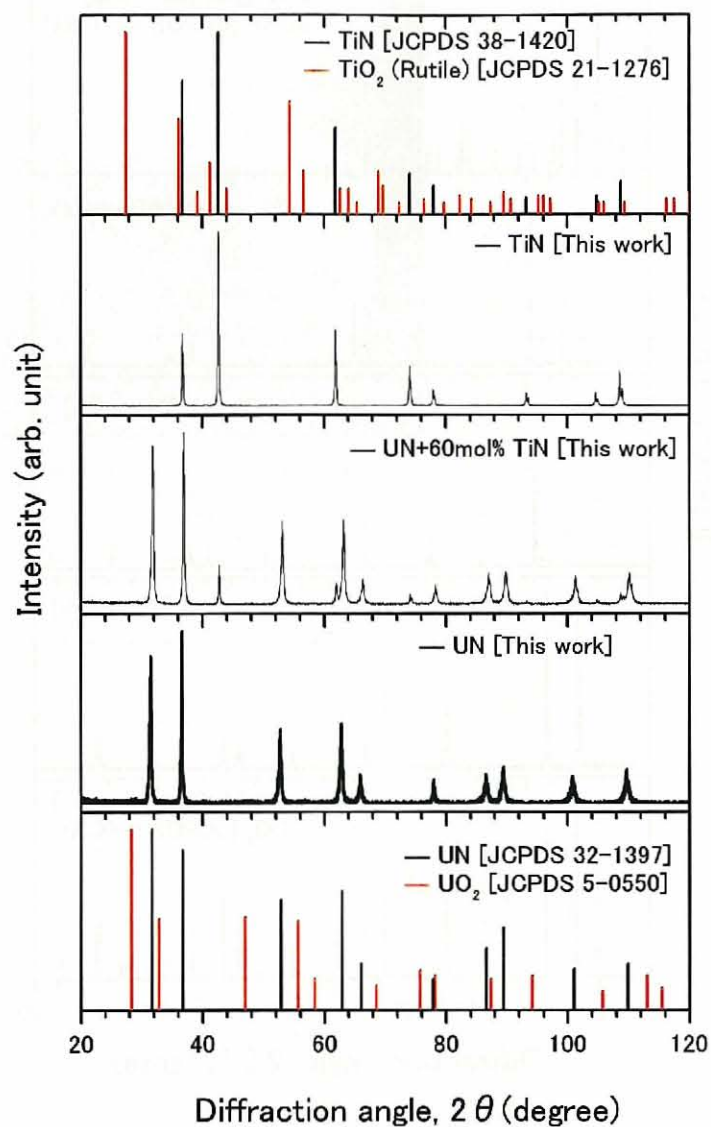


Fig. 2.12 XRD pattern of UN UN+60mol%TiN and TiN, together with the JCPDS data [28, 29, 32, 33]

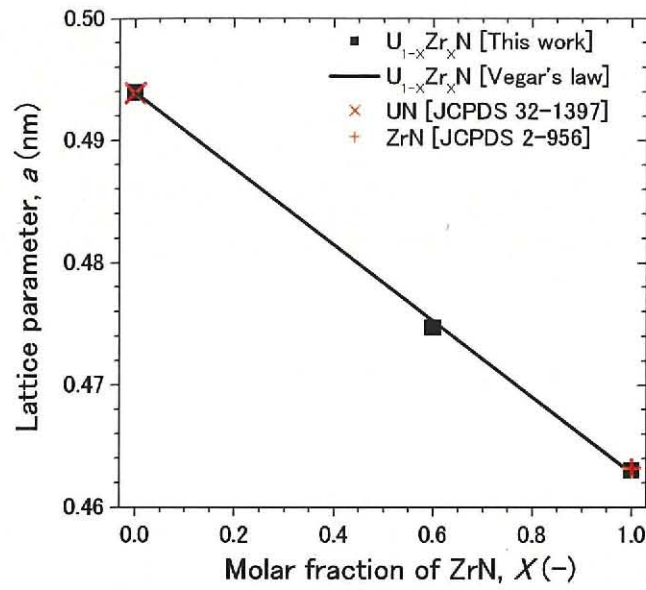


Fig. 2.13 Zr content dependence of lattice parameter of UN, $U_{0.4}Zr_{0.6}N$ and ZrN, together with literature data [25, 27]

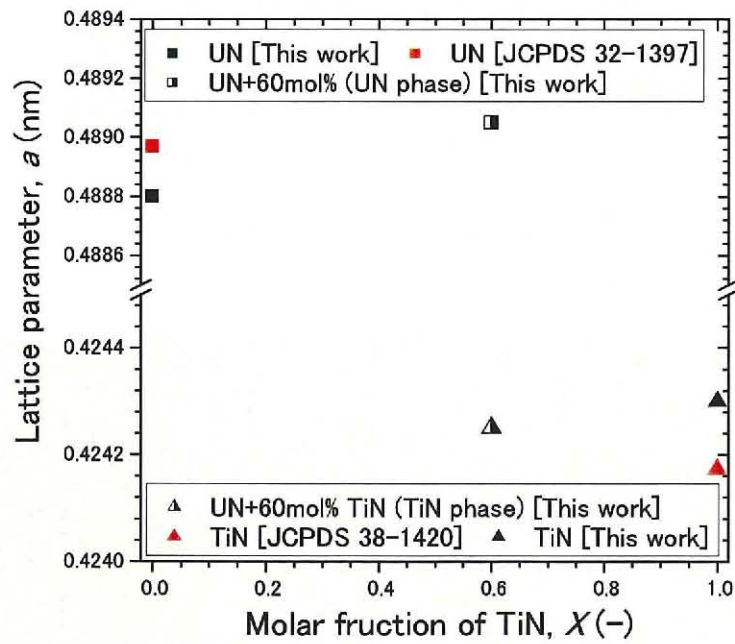


Fig. 2.14 Ti content dependence of lattice parameter of UN, UN+60mol%TiN and TiN, together with literature data [25, 29]

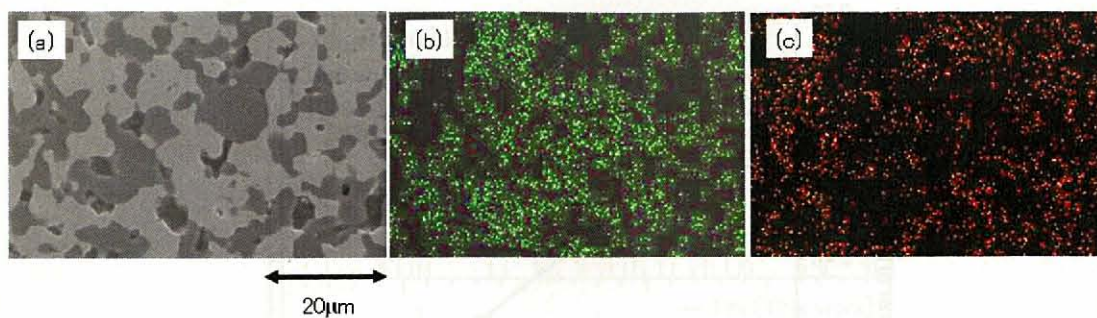


Fig. 2.15 SEM-EDX analysis of UN+60mol%TiN (a) SEM image (b) Ti element (c) U element

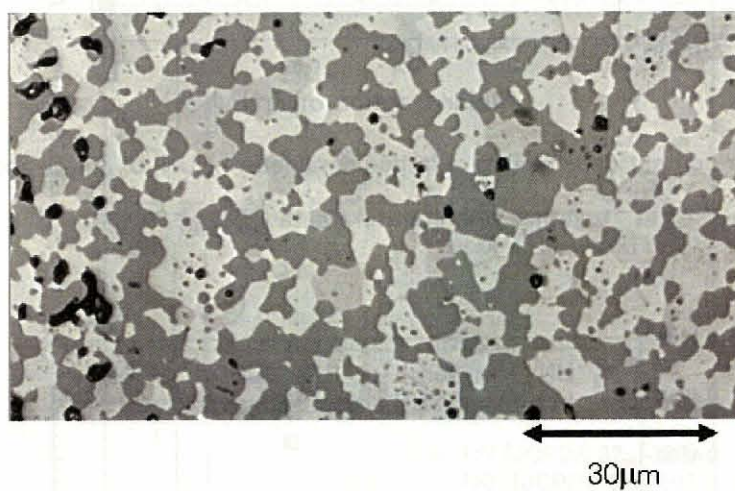


Fig. 2.16 SLM image of UN+60mol%TiN

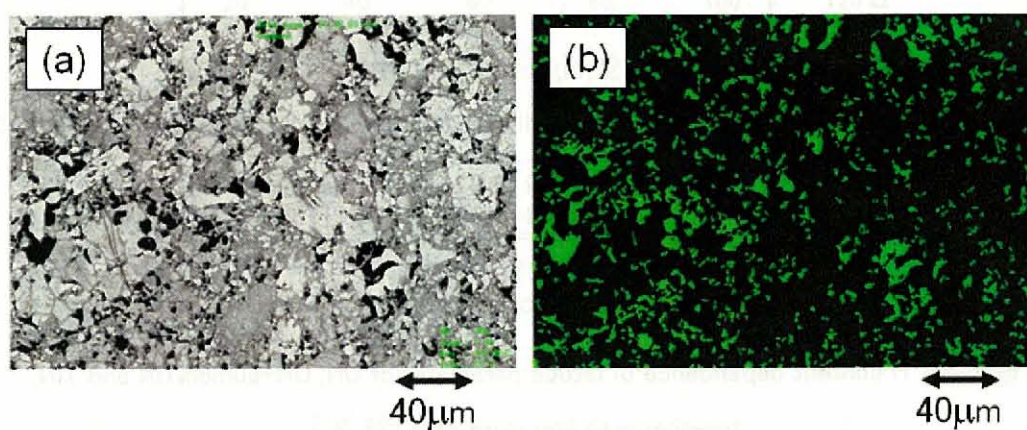


Fig. 2.17 ZrN 91.1%T.D. (a) SLM image (b) MSA image (=Black zone)

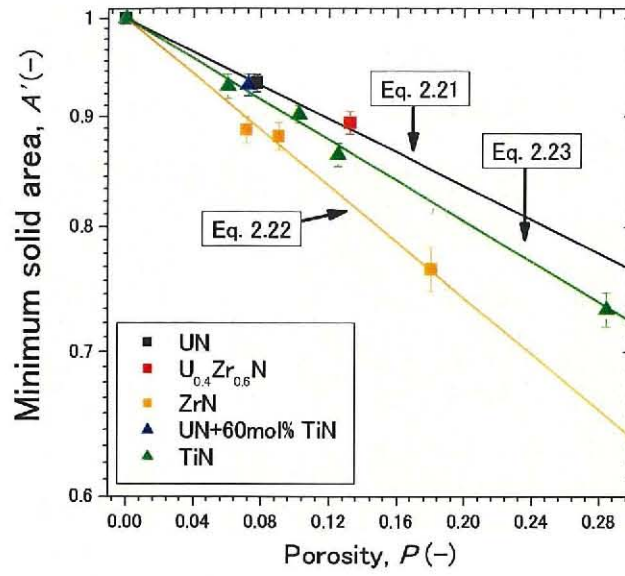


Fig. 2.18 Porosity dependence of MSA of UN, $U_{0.4}Zr_{0.6}N$, UN+60mol%, ZrN and TiN

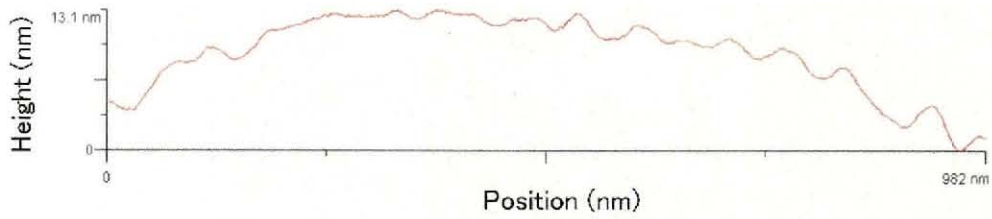


Fig. 2.19 Surface roughness of UN

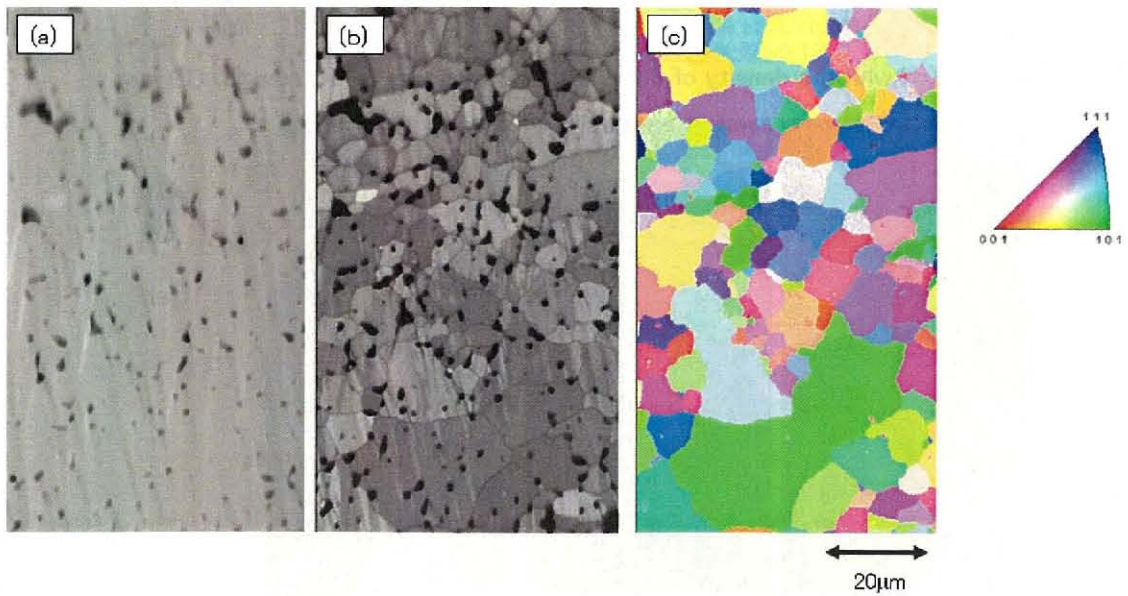


Fig. 2.20 UN (a) SEM image (b) IQ map (c) CD map

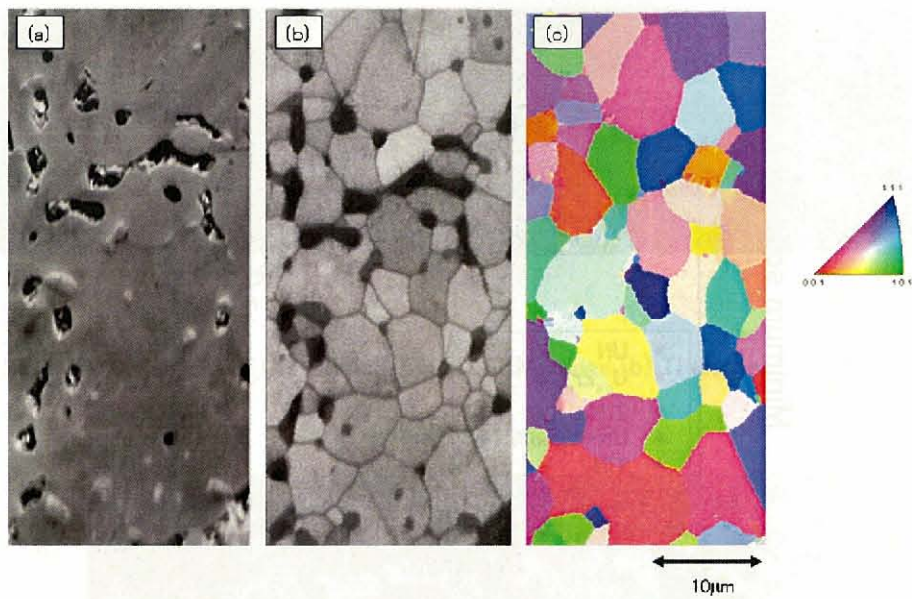


Fig. 2.21 $U_{0.4}Zr_{0.6}N$ (a) SEM image (b) IQ map (c) CD map

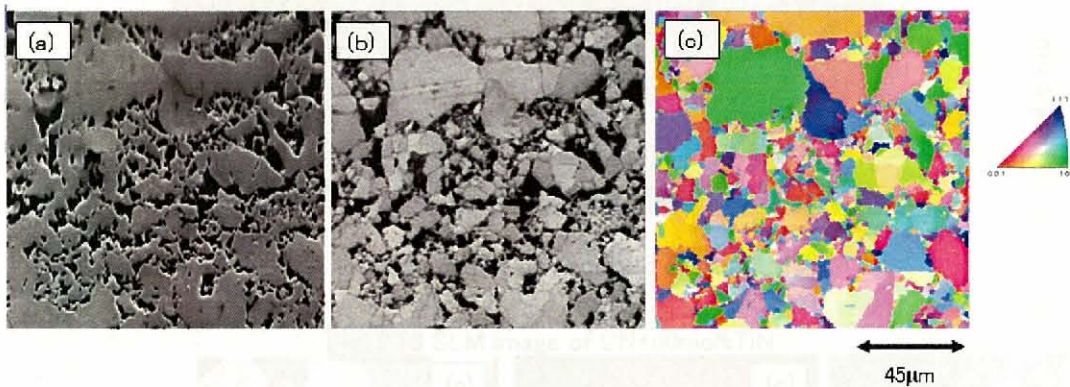


Fig. 2.22 ZrN with the density of 93.5%T.D (a) SEM image (b) IQ map (c) CD map

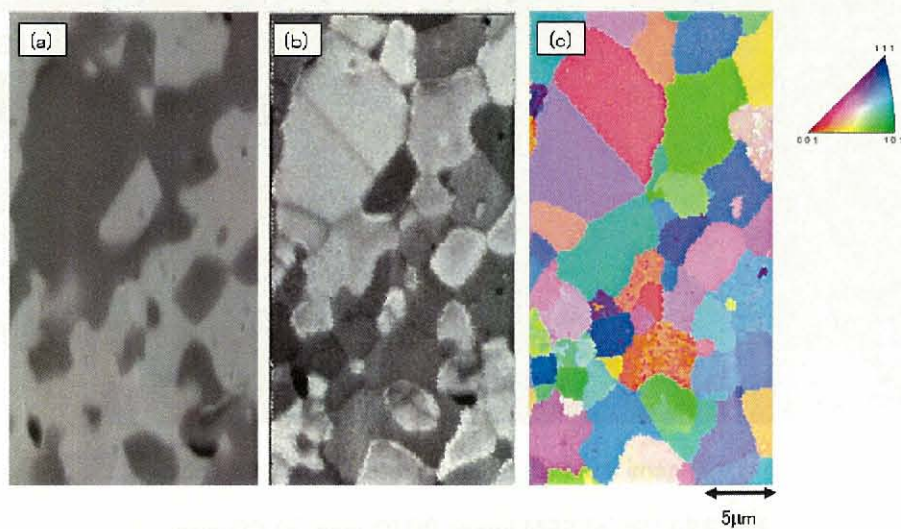


Fig. 2.23 UN+60mol%TiN (a) SEM image (b) IQ map (c) CD map

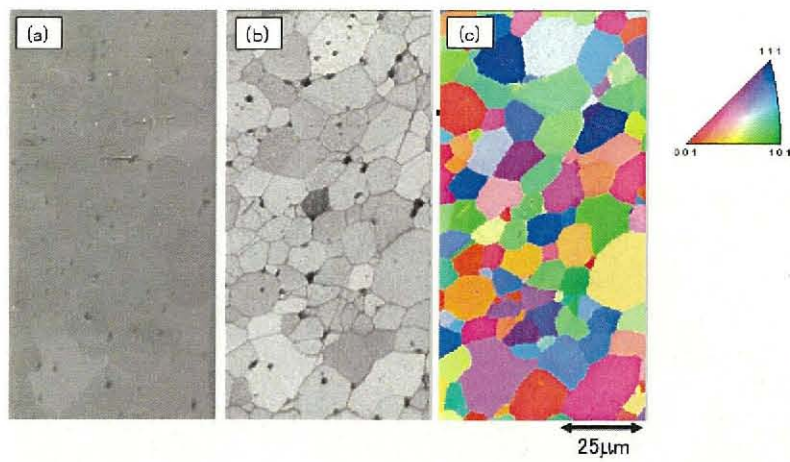


Fig. 2.24 TiN with the density of 94.0%T.D. (a) SEM image (b) IQ map (c) CD map of

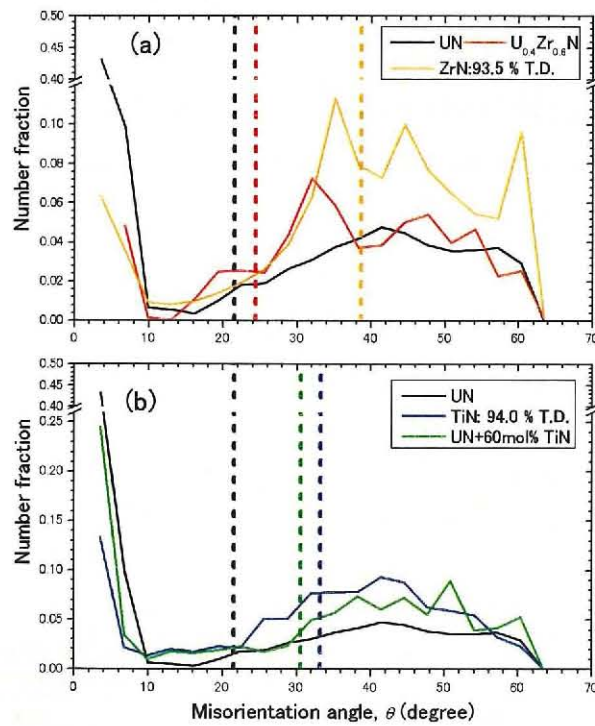


Fig. 2.25 Number fraction of misorientation angle

(a) UN, $U_{0.4}Zr_{0.6}N$ and ZrN (b) UN, UN+60mol%TiN and TiN

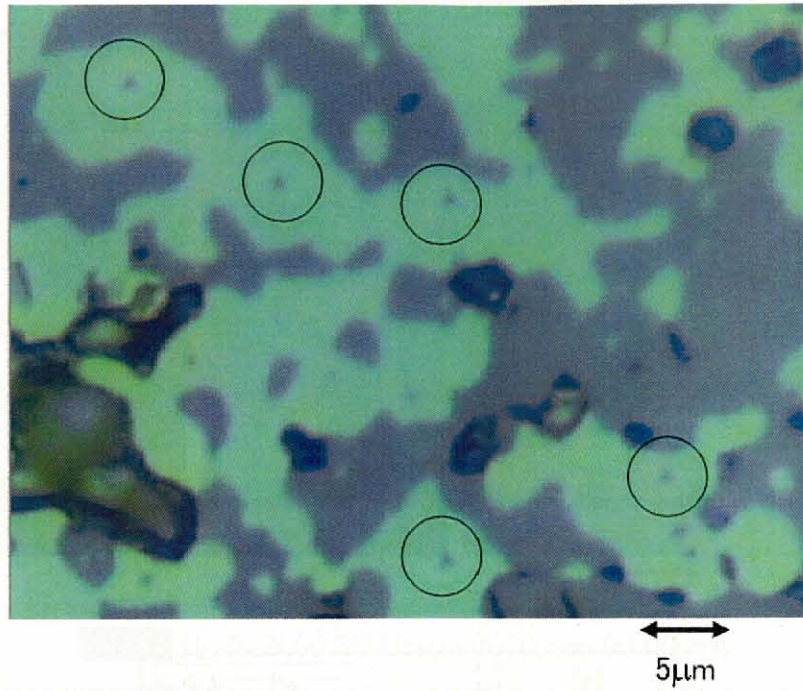


Fig. 2.26 Metallographic picture of UN+60mol%TiN

The impressions of the indentation tests remain in the center of the circle.

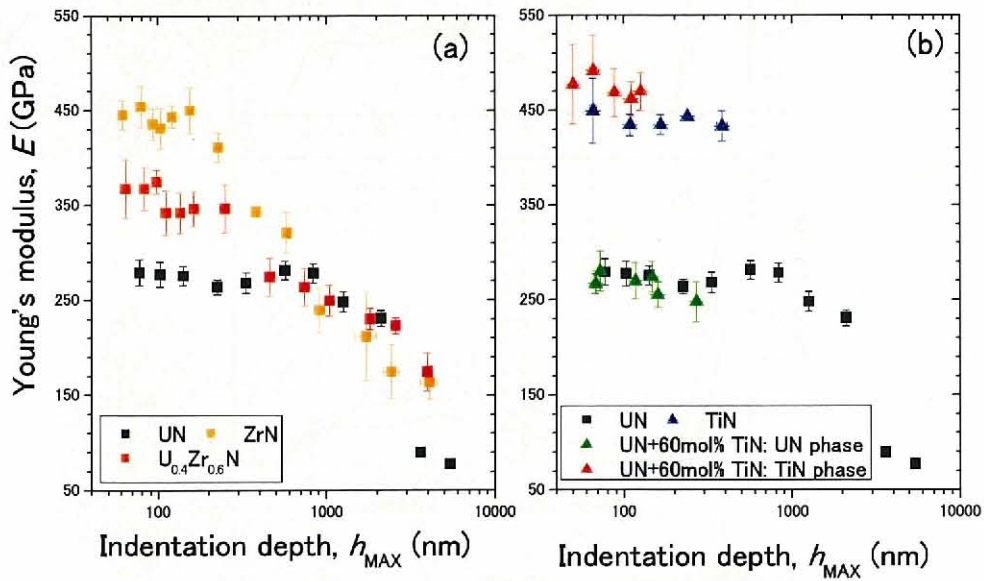


Fig. 2.27 Depth dependence of Young's modulus

(a) UN, $U_{0.4}Zr_{0.6}N$ and ZrN (b) UN, UN+60mol%TiN and TiN

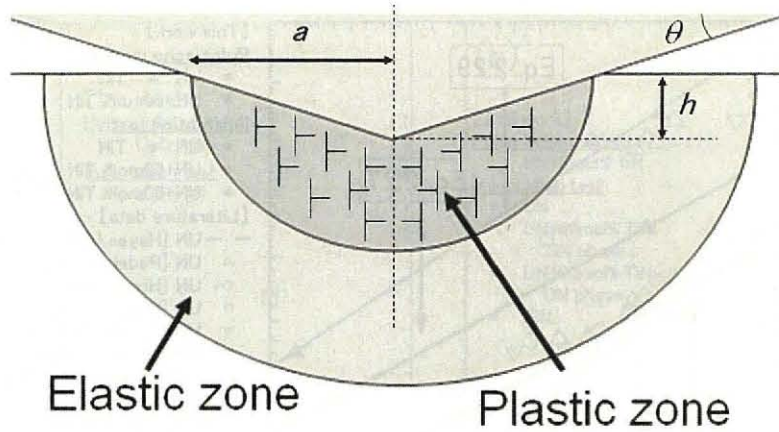


Fig. 2.28 Schematic of elastic and plastic deformation zone on indentation test referred from Ref. 21

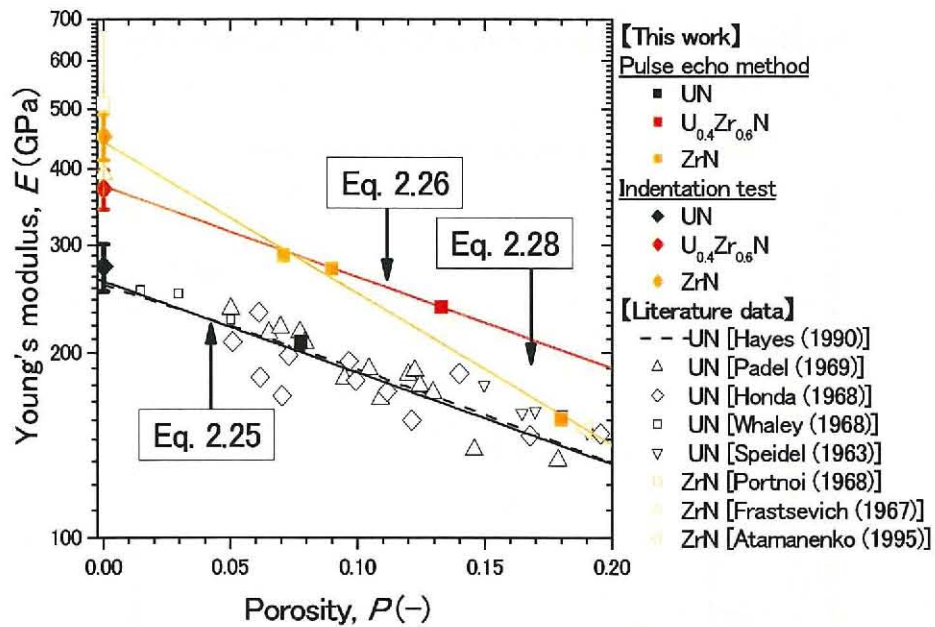


Fig. 2.29 Porosity dependence of Young's modulus of UN, $U_{0.4}Zr_{0.6}N$ and ZrN, together with the literature data of UN [24, 35-41]

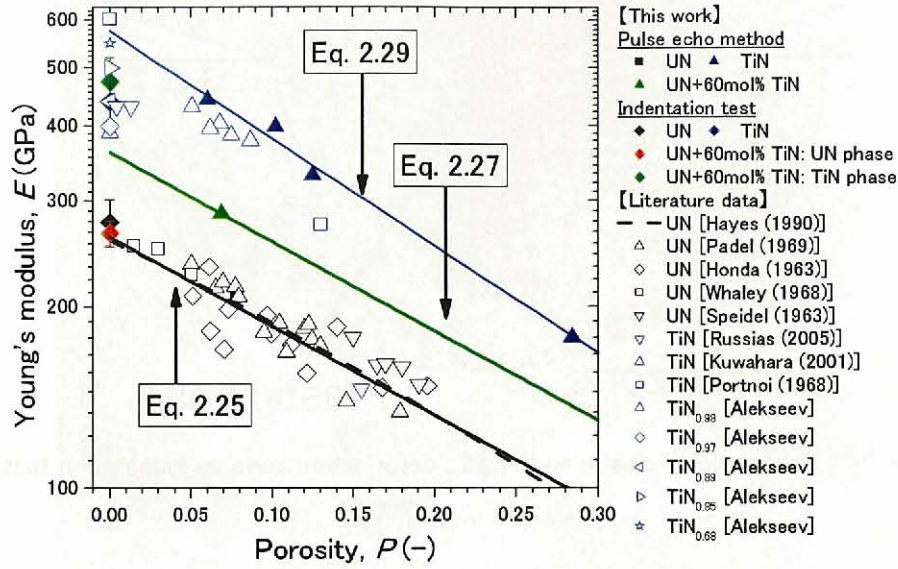


Fig. 2.30 Porosity dependence of Young's modulus of UN, UN+60mol%TiN and TiN, together with the literature data of UN [21, 35–38, 40, 42–44]

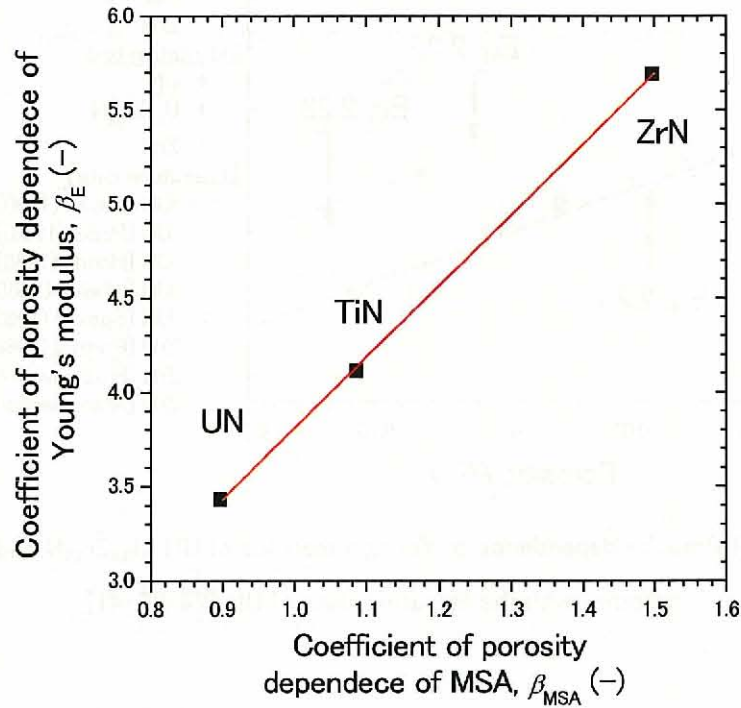


Fig. 2.31 Coefficient of porosity dependence of MSA vs. Coefficient of porosity dependence of Young's modulus

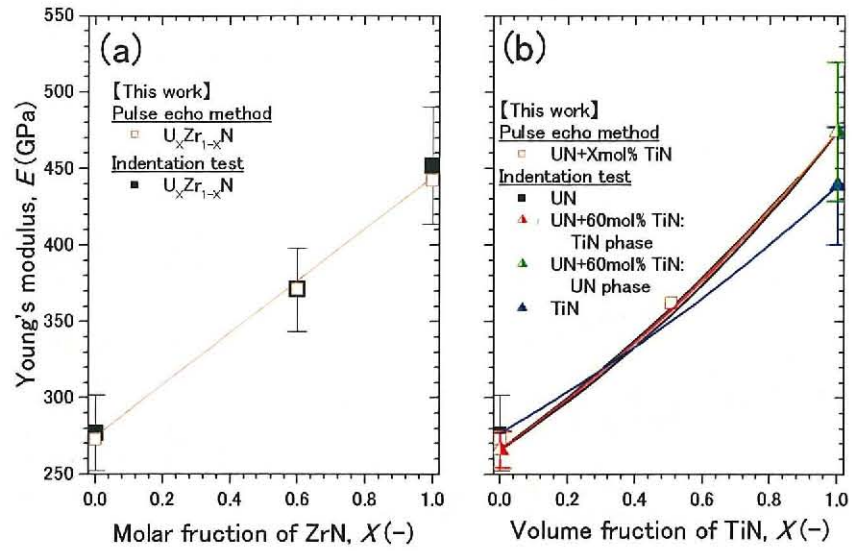


Fig. 2.32 Young's modulus vs. ZrN or TiN content

(a) UN, $U_{0.4}Zr_{0.6}N$ and ZrN (b) UN, UN+60mol%TiN and TiN

In Fig. 2.32(b), the red and black line represent the data estimated from Young's modulus of UN phase and TiN phase in UN+60mol%TiN pellet using Fan's equation (Eq. 2.31) and Hashin's equation (Eq. 2.43 and 2.44). The blue line represent the data estimated from Young's modulus of UN pellet and TiN pellet using Fan's equation (Eq. 2.31).

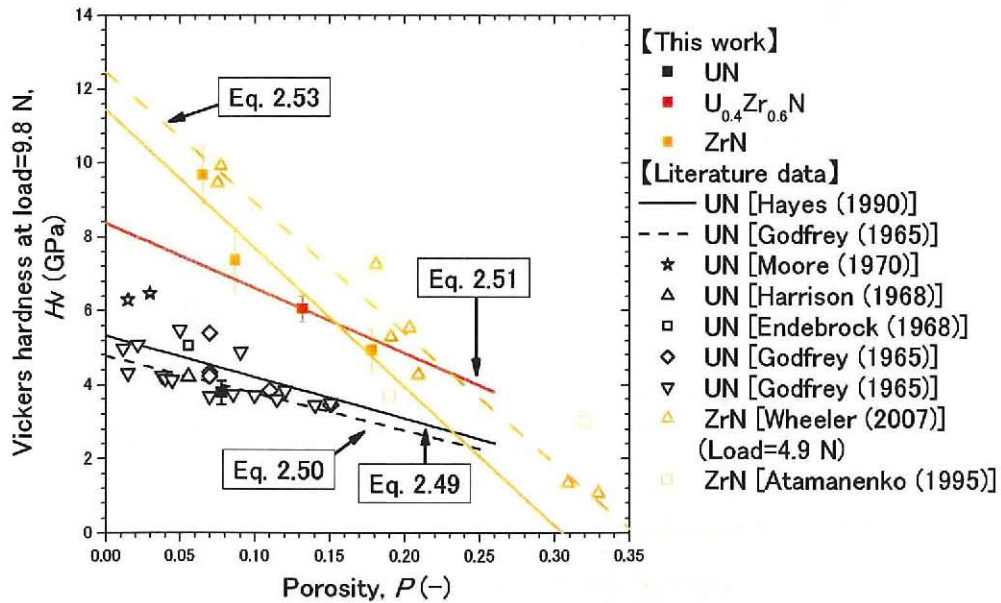


Fig. 2.33 Porosity dependence of Vickers hardness of UN, $U_{0.4}Zr_{0.6}N$ and ZrN, together with the literature data of UN [24, 39, 48–53]

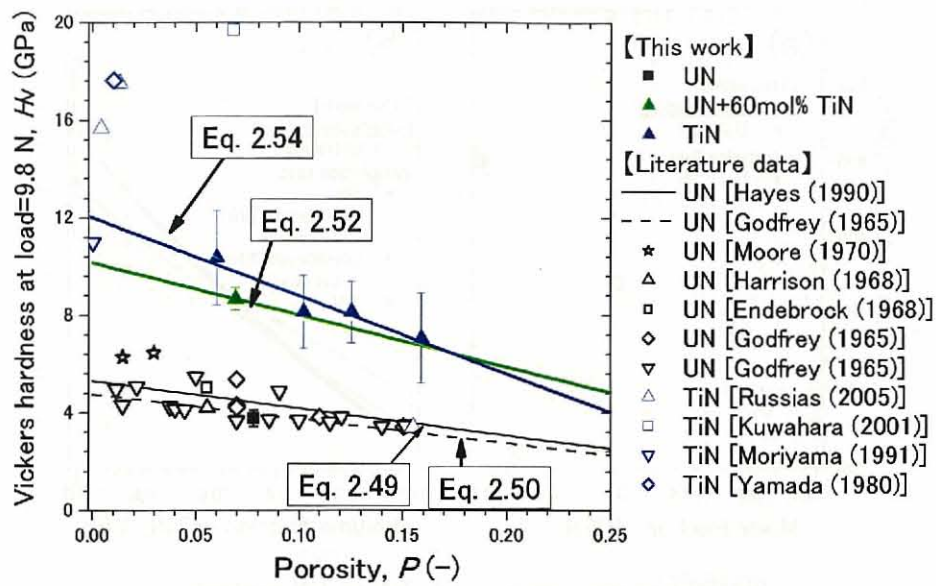


Fig. 2.34 Porosity dependence of Vickers hardness of UN, UN+60mol%TiN and TiN, together with the literature data [24, 43, 44, 48–52, 54, 55]

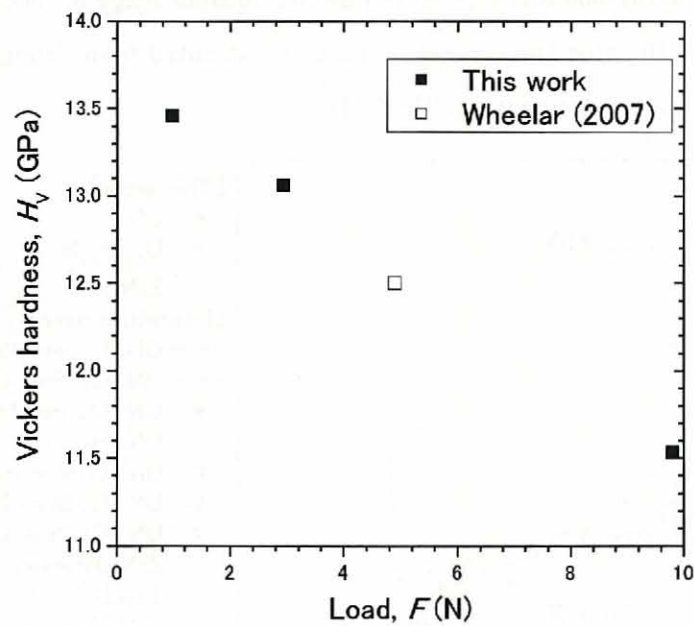


Fig. 2.35 Load dependence of Vickers hardness of porosity-free ZrN, together with the literature data [53]

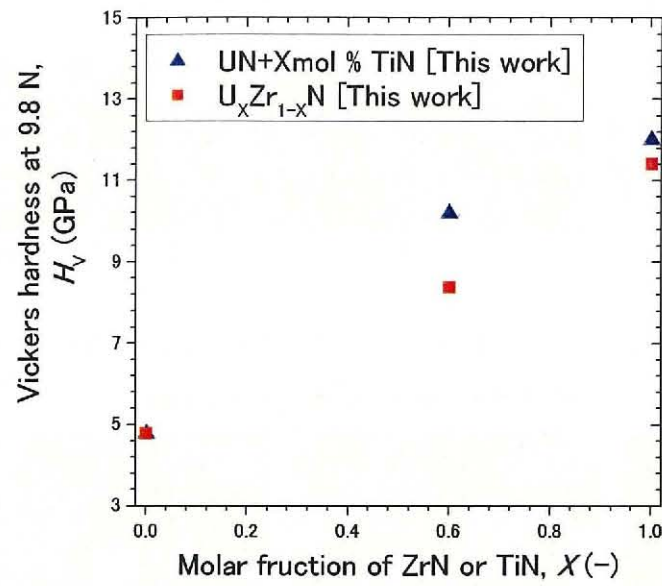


Fig. 2.36 Vickers hardness as the function of ZrN or TiN content

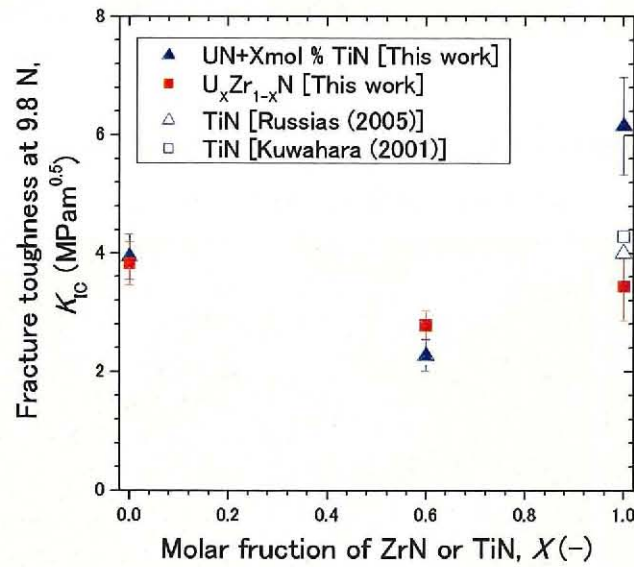


Fig. 2.37 Fracture toughness as the function of ZrN or TiN content, together with the literature data [42, 43]



Fig. 2.38 The crack generating from the vertex of the Vickers impression of UN

(a) SEM image (b) IQ map (c) CD map

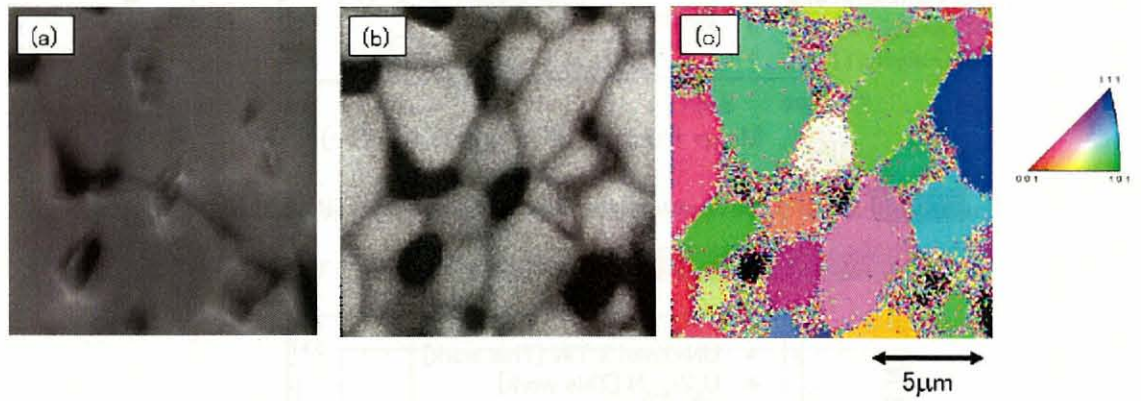


Fig. 2.39 The crack generating from the vertex of the Vickers impression of $U_{0.4}Zr_{0.6}N$

(a) SEM image (b) IQ map (c) CD map

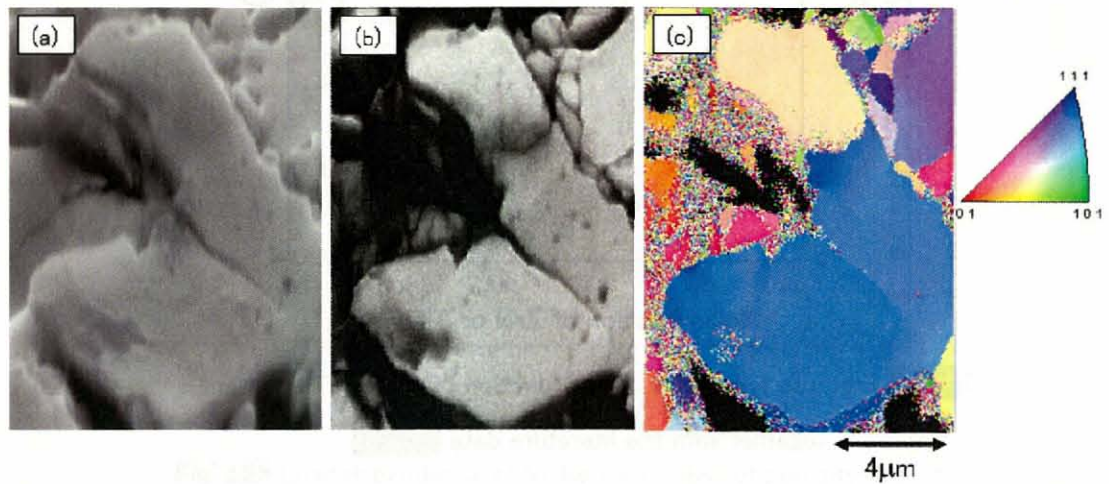


Fig. 2.40 The crack generating from the vertex of the Vickers impression of ZrN

(a) SEM image (b) IQ map (c) CD map

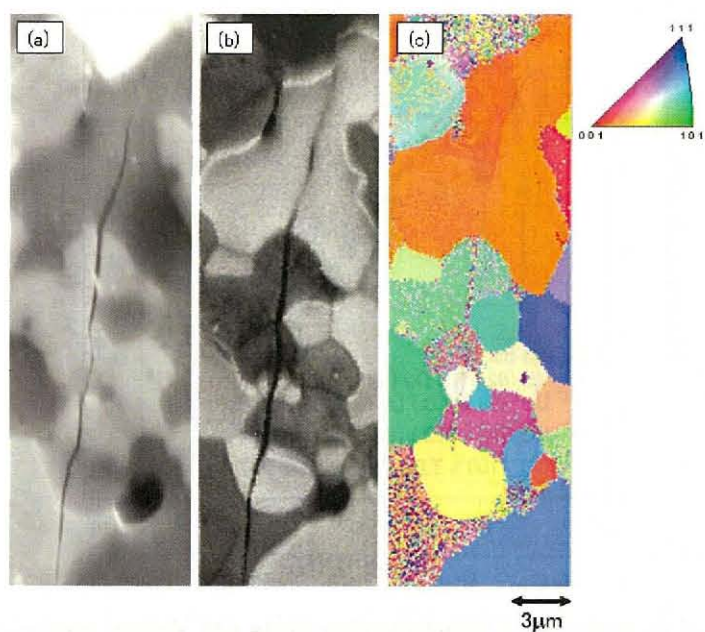


Fig. 2.41 The crack generating from the vertex of the Vickers impression of UN+60mol%TiN

(a) SEM image (b) IQ map (c) CD map

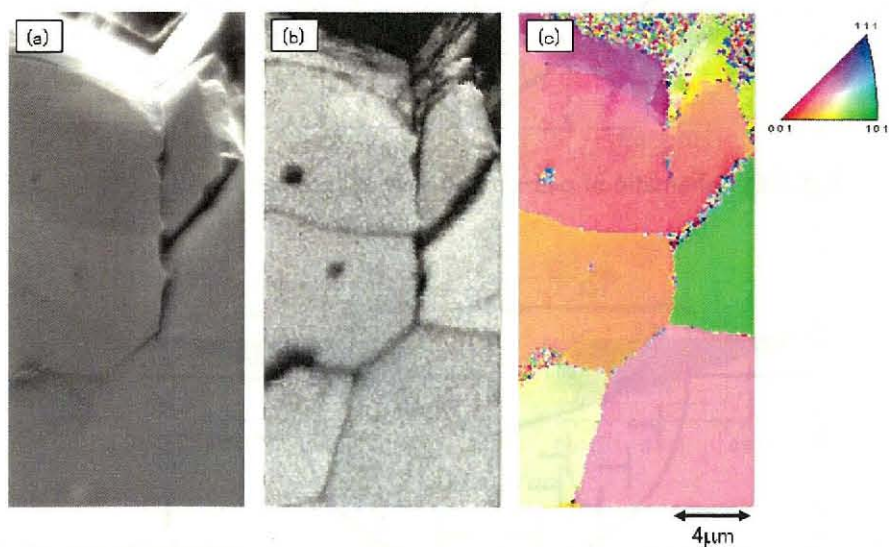


Fig. 2.42 The crack generating from the vertex of the Vickers impression of TiN

(a) SEM image (b) IQ map (c) CD map

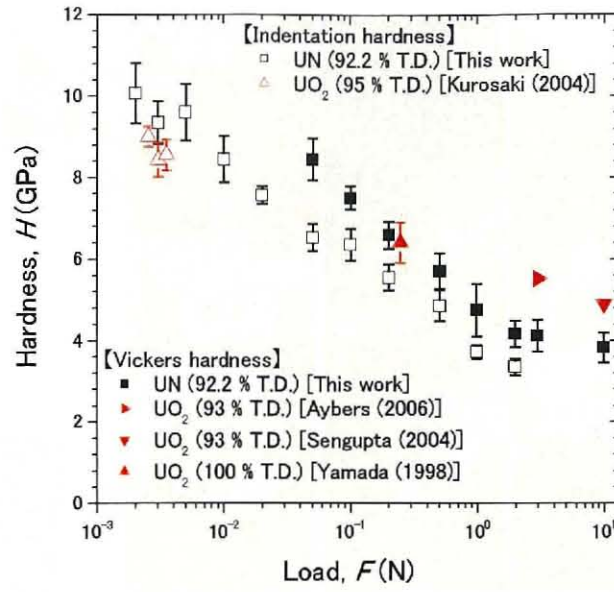


Fig. 2.43 Load dependence of indentation hardness and Vickers hardness of UN, together with the literature data of UO_2 [57–60].

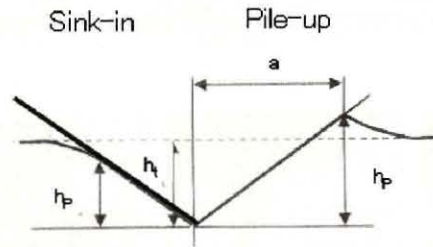


Fig. 2.44 Schematic of pile-up and sink-in referred from Ref. 21

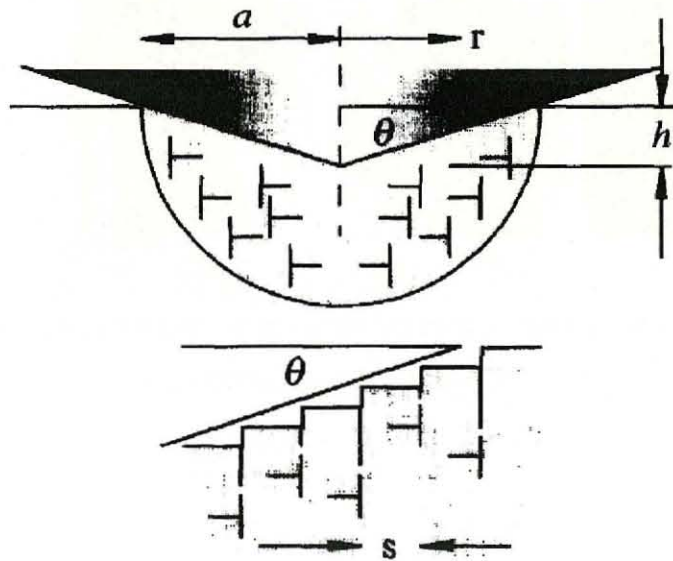


Fig. 2.45 Schematic of GNDs created by the indentation test referred from Ref. 62

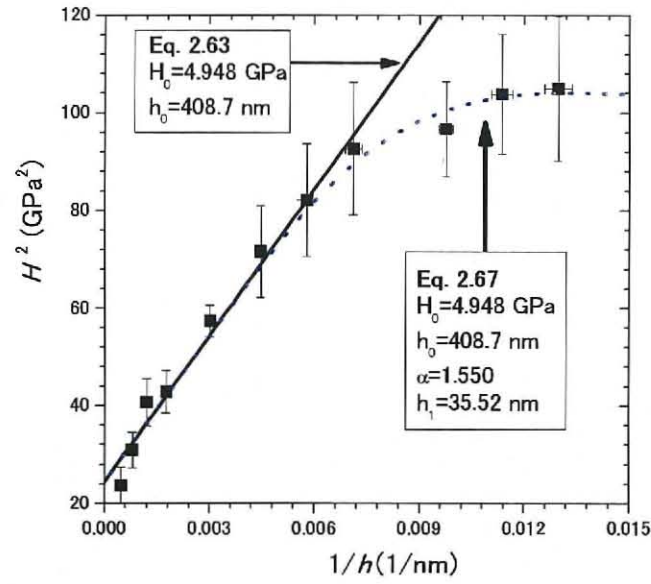


Fig. 2.46 Square of indentation hardness vs. Inverse of indentation depth (UN)

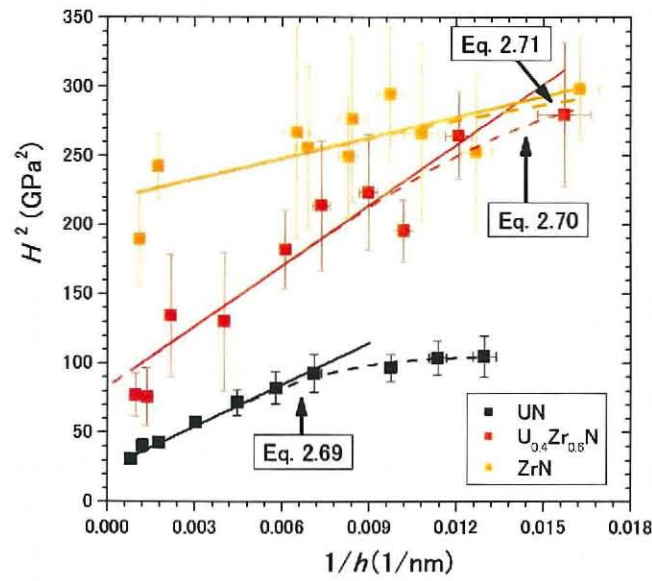


Fig. 2.47 Square of indentation hardness vs. Inverse of indentation depth (UN, $U_{0.4}Zr_{0.6}N$, ZrN)

The solid and dot lines represent the fitting results by Eq. 2.63 and Eq. 2.65.

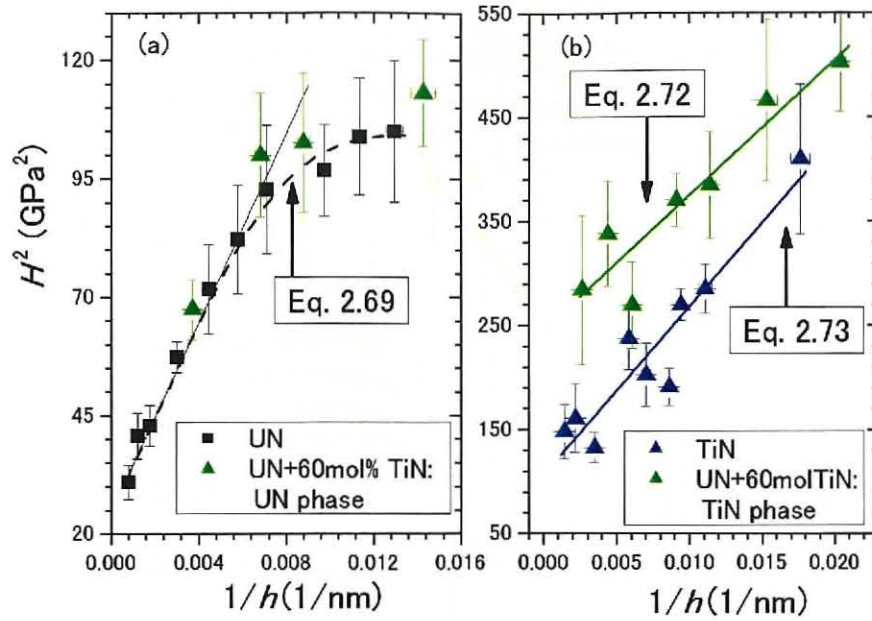


Fig. 2.48 Square of indentation hardness vs. Inverse of indentation depth

(a) UN pellet and UN phase in UN+60mol%TiN (b) TiN pellet and TiN phase in UN+60mol%TiN

The solid and dot lines represent the fitting results by Eq. 2.63 and Eq. 2.65.

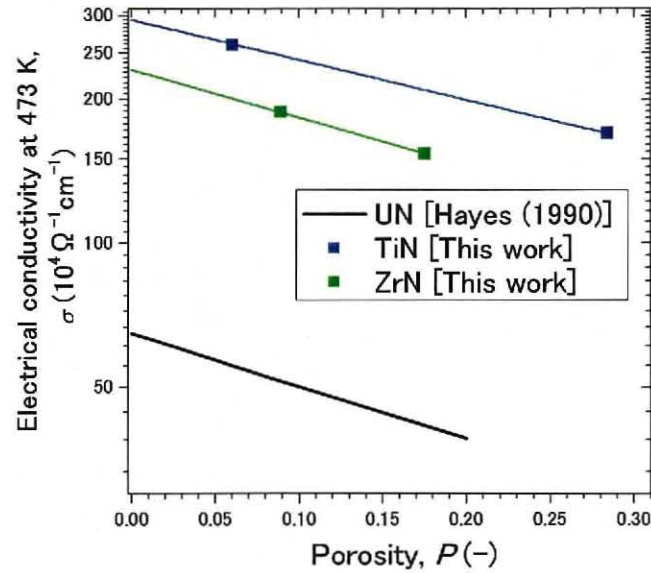


Fig. 2.49 Porosity dependence of electrical conductivity of ZrN and TiN, together with the literature data of UN [25]

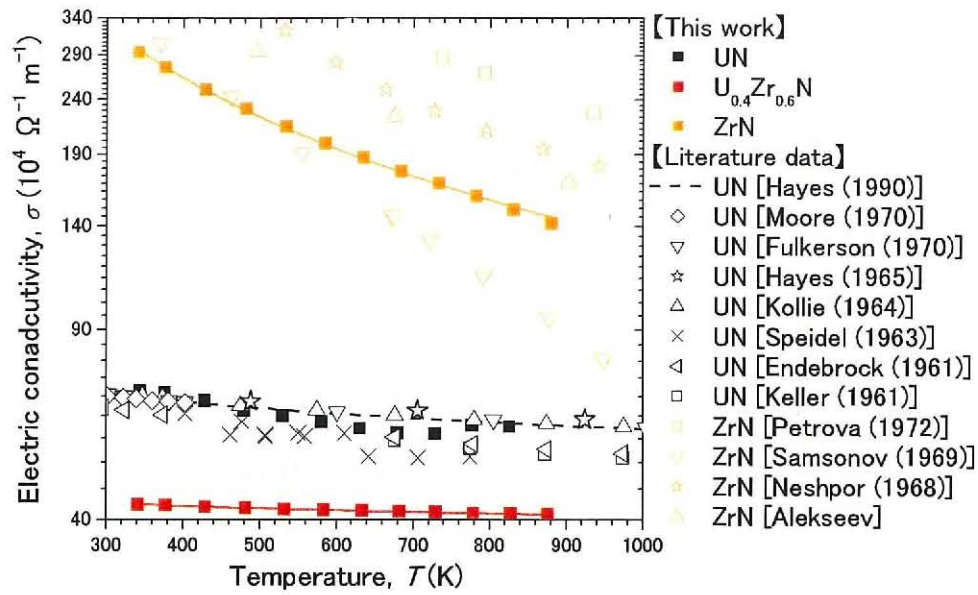


Fig. 2.50 Temperature dependence of electrical conductivity of UN, $U_{0.4}Zr_{0.6}N$ and ZrN, together with the literature data [25, 38, 44, 49, 68–75]

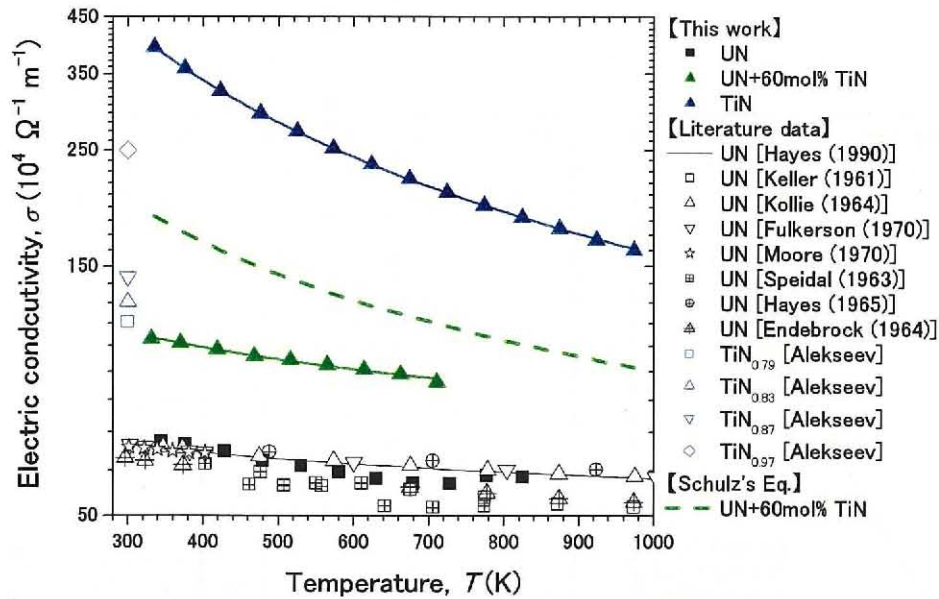


Fig. 2.51 Temperature dependence of electrical conductivity of UN, UN+60mol%TiN and TiN, together with the literature data [25, 38, 44, 49, 68–72]

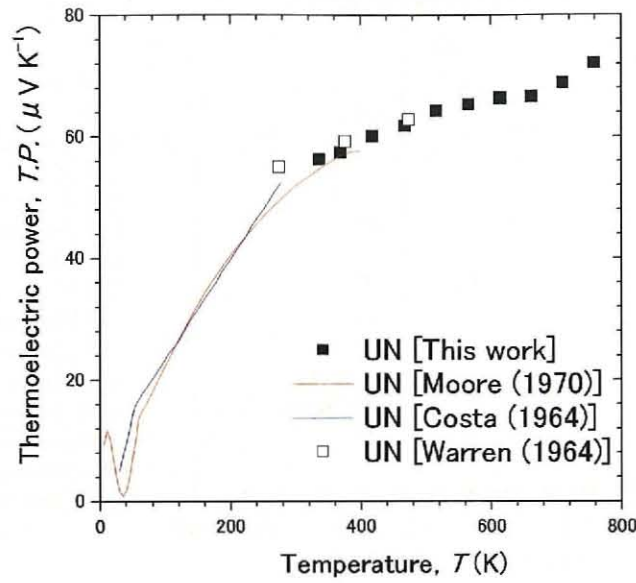


Fig. 2.52 Temperature dependence of thermoelectric power of UN, together with the literature data of UN [49, 76, 77]

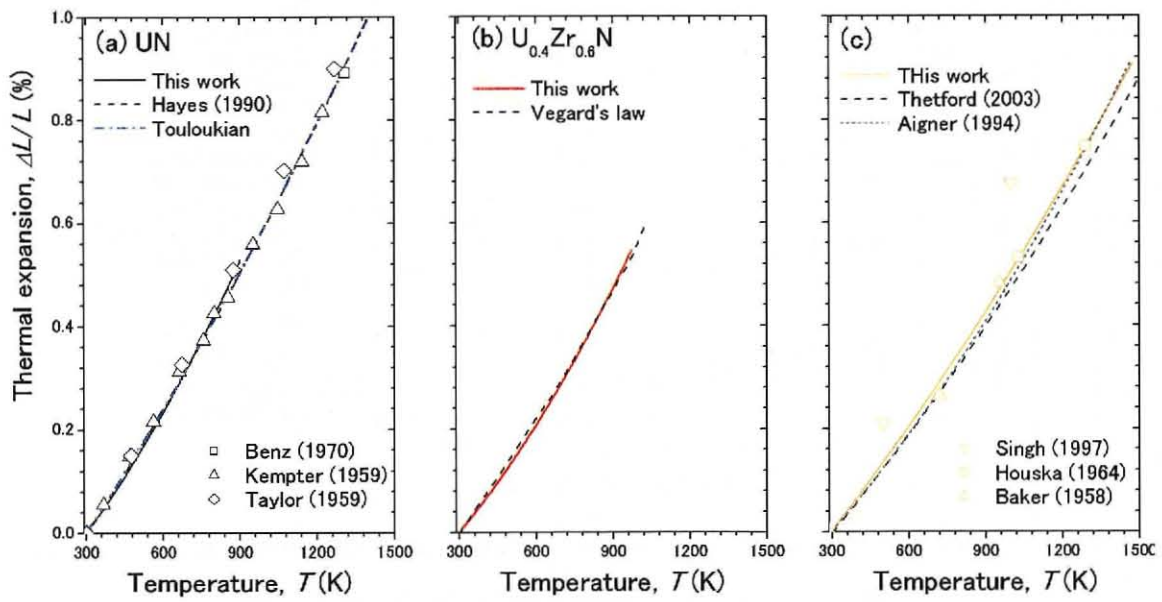


Fig. 2.53 Thermal expansion, together with the literature data [23, 79–87]

(a) UN (b) $U_{0.4}Zr_{0.6}N$ (c) ZrN

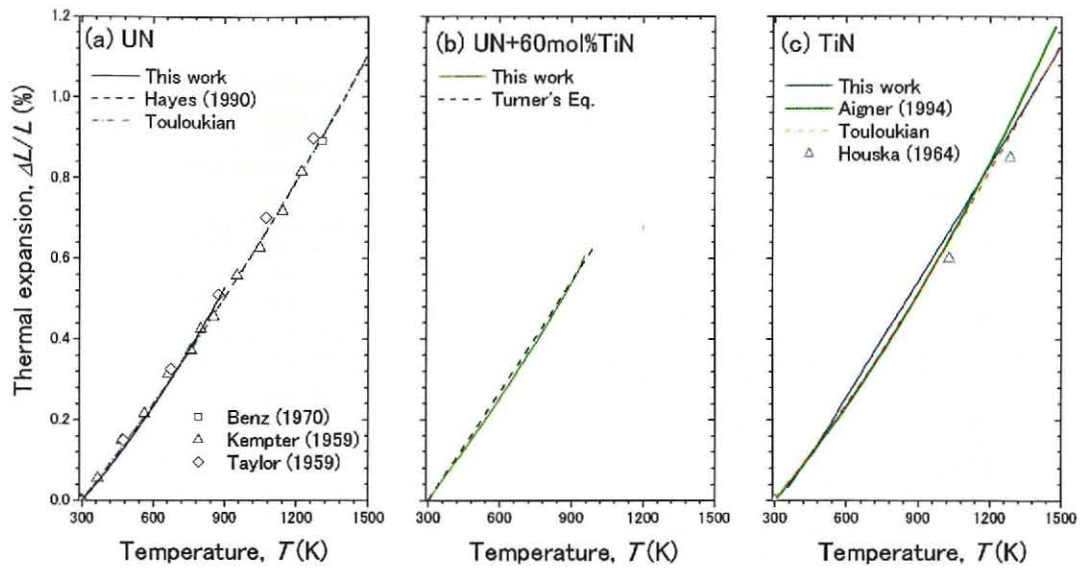


Fig. 2.54 Thermal expansion, together with the literature data [23, 79–82, 84, 86]

(a) UN (b) UN+60mol%TiN (c) TiN

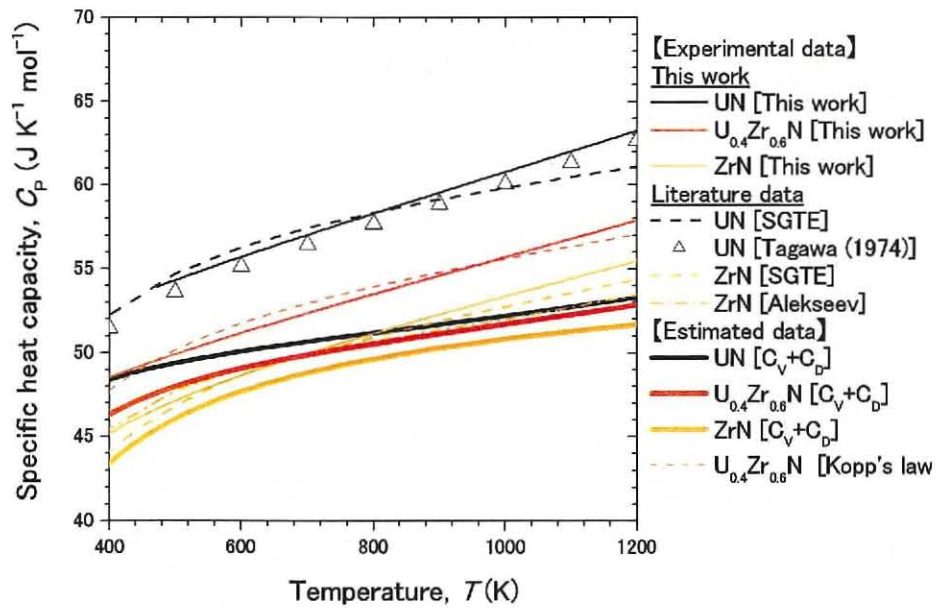


Fig. 2.55 Temperature dependences of specific heat capacity, of UN, $U_{0.4}Zr_{0.6}N$ and ZrN together with the literature data [44, 89, 90] and estimated data

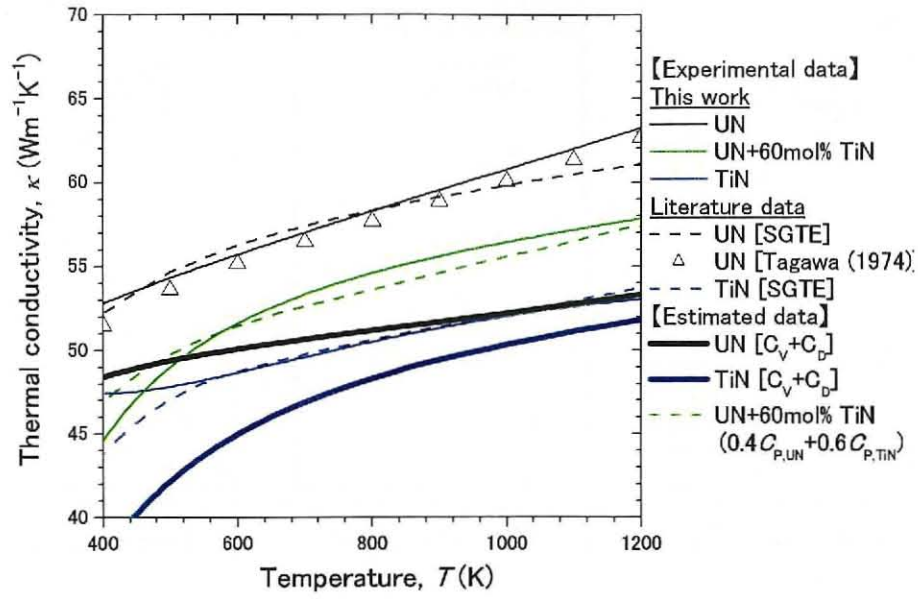


Fig. 2.56 Temperature dependences of specific heat capacity, of UN, UN+60mol%TiN and TiN together with the literature data [44, 89, 90] and estimated data

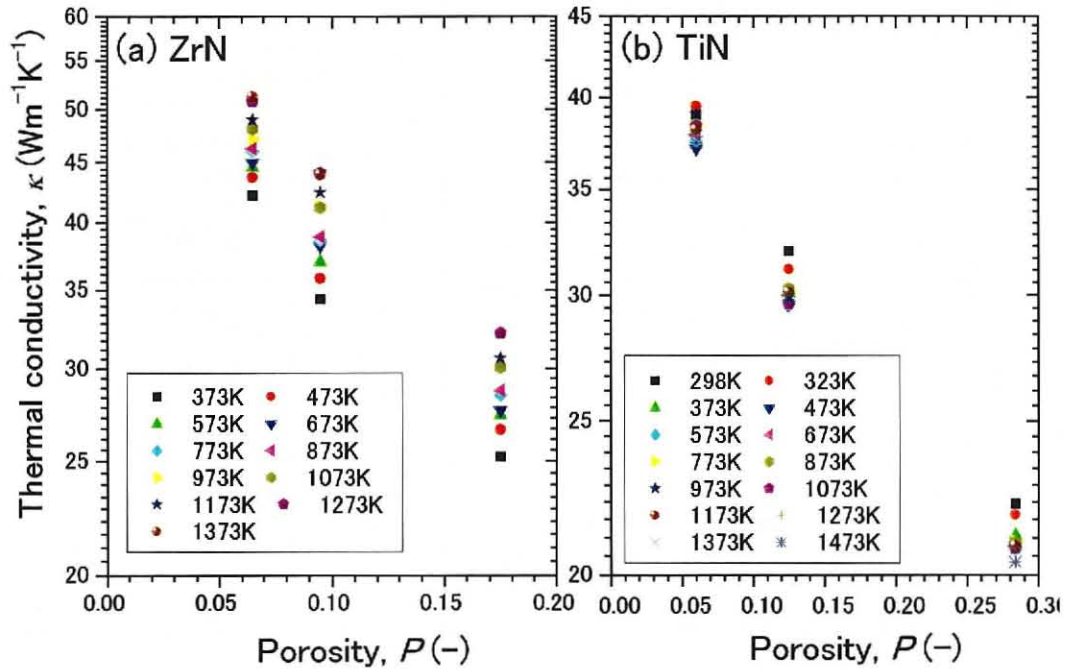


Fig. 2.57 Porosity dependence of thermal conductivity (a) ZrN (b) TiN

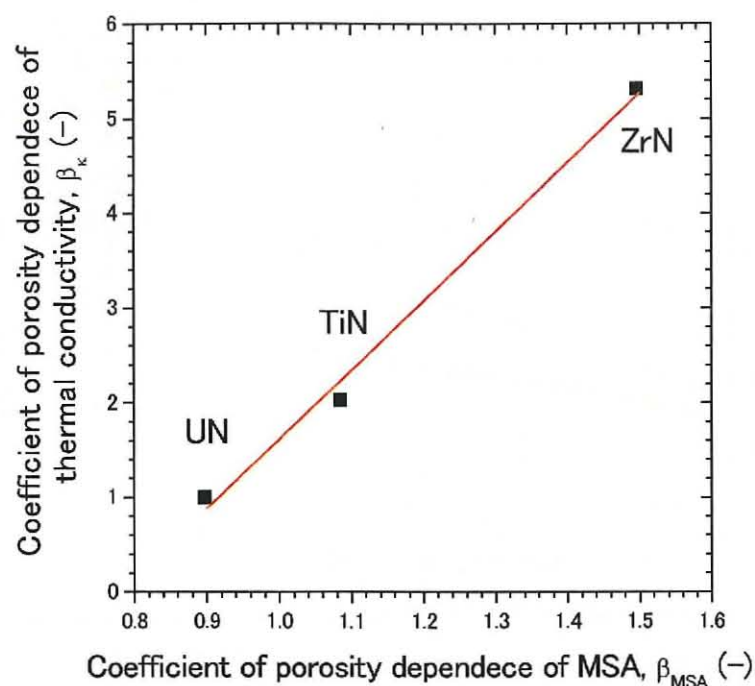


Fig. 2.58 Coefficient of porosity dependence of MSA

vs. coefficient of porosity dependence of thermal conductivity

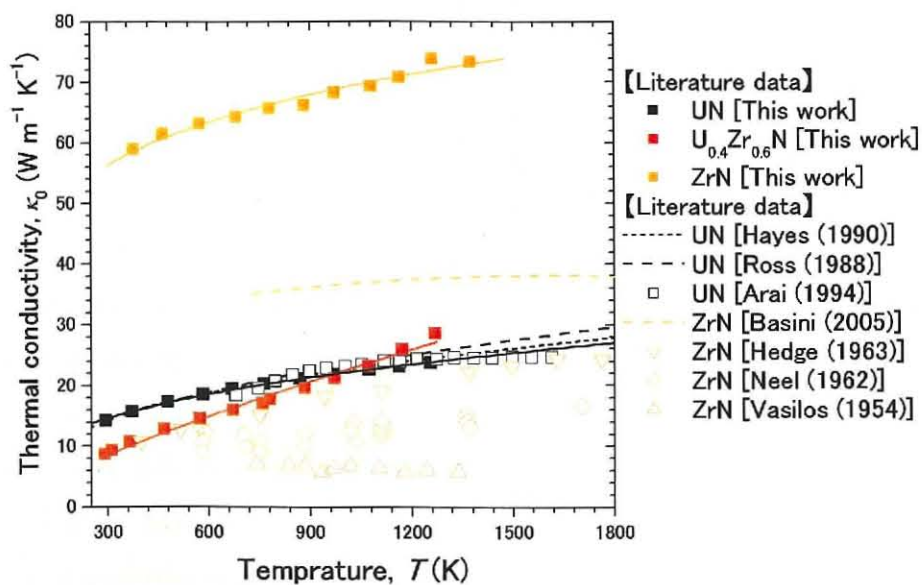


Fig. 2.59 Temperature dependence of thermal conductivity of UN, $U_{0.4}Zr_{0.6}N$ and ZrN, together with literature data [25, 27, 91–95]

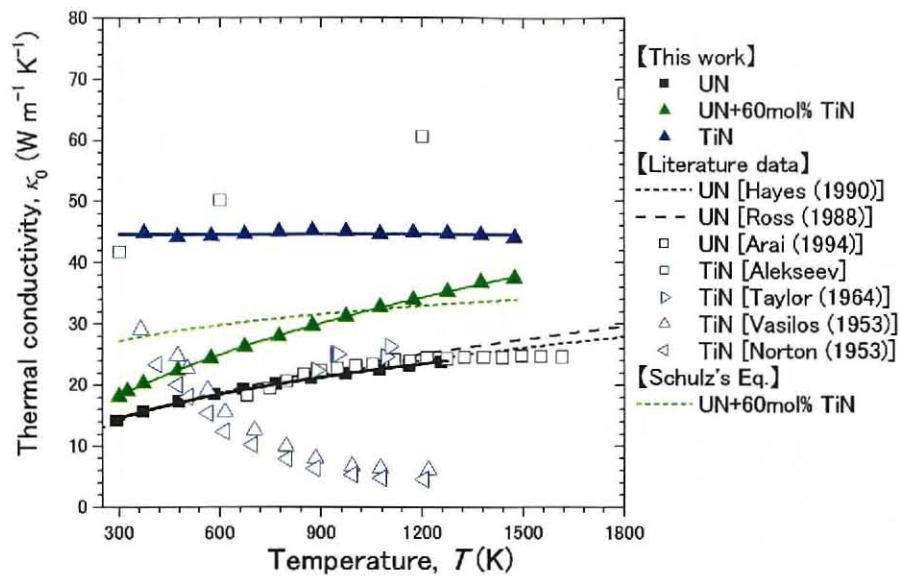


Fig. 2.60 Temperature dependence of thermal conductivity of UN, UN+60mol%TiN and TiN, together with the literature data of UN [25, 27, 44, 91, 95–97]

Chapter 3: Molecular dynamics (MD) studies of actinide nitrides, nitride, ADS target fuels, actinide dioxides and MA-containing MOX fuels

3-1 Background

MA(Minor Actinide: Np, Am and Cm)-containing MOX (Mixed OXide) fuels and nitride fuels are considered as MA loading methods into the FR (Fast Reactor) core such as FBR (Fast Breeder Reactor) and ADS (Accelerate Driven System) [1, 2]. The MA-containing MOX fuel for use as the homogeneous mode is considered the most promising candidate of FBR in Japan [3]. Nitride fuels are under consideration as advanced fuels of FBR [4] and good targets of ADS [5, 6] as described in Chapter 1. In order to develop the technologies for nuclear fuel cycle based on MA-containing MOX and nitride fuels, it is very important to understand the thermophysical properties of not only MA-containing MOX fuels ((U,Np,Pu,Am)O₂) and nitride fuels with inert matrix ((U,Np,Pu,Am)N and (Pu,Np,Am,Zr)N), but also actinide dioxide (AnO₂: UO₂, PuO₂, NpO₂, AmO₂) and actinide mononitride (AnN: ThN, UN, NpN, PuN, AmN). However, thermophysical properties of MA-containing MOX fuels and nitride fuels with inert matrix had not almost been evaluated because it is very difficult to manage and handle MA elements. In addition, even in case of PuO₂, NpO₂, AmO₂, ThN, NpN, PuN and AmN, there are few reliable data. Especially, the thermal conductivity of AmO₂ at high temperature can't be evaluated by the laser flash method and guarded hot plate method, which are the standard method to evaluate the thermal conductivity of nuclear materials. Because O/M ratio of AmO_{2-x} changes at the high vacuum and high temperature [7]. It is difficult to handle AmN due to its high vapor pressure and hydrolysis reaction [8, 9]. Thus, by the experimental method, the thermophysical properties of the oxide fuel and nitride fuel containing Am such as the MA-containing MOX and nitride fuel with the inert matrix can't be exactly evaluated. Therefore, the author applied MD (Molecular Dynamics) calculation to evaluate the thermophysical properties of such fuels. In the present study, the thermal expansion, bulk modulus, specific heat capacity and thermal conductivity have been estimated using an MD calculation in the temperature range 300–2800 K. In addition, the thermophysical properties of ZrN were also evaluated by MD method to evaluate nitride fuels with inert matrix.

3-2 Molecular dynamics techniques

A molecular dynamics simulation is an important tool for material science. It has been

used to study the equilibrium and transport properties of liquids or crystals. The procedures and principles of this method are briefly described as the followings.

1. Setting the initial position and velocity of particles
2. Defining the interaction between particles
3. Calculating the forces to particles from reciprocal arrangement
4. Solving equations of motion in according to velocity and force
5. Controlling temperature and pressure

In the present study, MXDORTO [10] was used. In MXDORTO, the non-equilibrium calculation is usually performed. The calculation time in case of the non-equilibrium calculation is shorter than that of equilibrium calculation. However, in the field of the nuclear fuel engineering, the precise data is necessary. There, the author improved the program to perform the equilibrium calculation in MXDORTO.

3-2-1 Simulation algorithm

To calculate the motion of a particle, the following equations must be solved.

$$r_i(t + \Delta t) = r_i(t) + \int_t^{t+\Delta t} v_i(\tau) d\tau \quad (3.32)$$

$$v_i(t + \Delta t) = v_i(t) + \int_t^{t+\Delta t} a_i(\tau) d\tau \quad (3.33)$$

where $r_i(t)$, $v_i(t)$ and $a_i(t)$ are position, velocity and acceleration of i th particle at time of t , respectively. However, it is impossible to express the position or velocity of particles as a simple function in a system with a lot of particles. Therefore, the motion of particles is calculated by gradually and slightly changing time in molecular dynamics calculation. As such methods, there are Verlet, velocity Verlet, leapfrog, Beeman, and Gear algorithms [11]. Velocity Verlet algorithm is more reasonable than any other algorithms in regard to stability of a system, accuracy and sways of energy so that velocity Verlet method was used in the present study.

Velocity Verlet algorithm

In this algorithm, it is assumed that acceleration during Δt is constant. The velocity of each particle is described by the following equation.

$$v_i(t) = \frac{\Delta r_i(t \rightarrow t + \Delta t) - \Delta r_i(t - \Delta t \rightarrow t)}{\Delta t} = a_i(t) \Delta t \quad (3.34)$$

$$\Delta r_i(t \rightarrow t + \Delta t) = r_i(t + \Delta t) - r_i(t) \quad (3.35)$$

Substitute Eq. 3.4 for Eq. 3.5, then

$$\Delta r_i(t) = r_i(t - \Delta t \rightarrow t) + (\Delta t)^2 \frac{F_i(t)}{m_i}, \quad (3.36)$$

$$r_i(t + \Delta t) = r_i(t) + \Delta r_i(t \rightarrow t + \Delta t) \quad (3.37)$$

This algorithm is excellent in regard to stability and conserving energy of system.

3-2-2 Quantum correction

The MD method, which was described above, purely obeys the classical mechanics. So the MD method is adequately effective under the high temperature and the system with the weak interaction, but is not usable under the low temperature and the system with strong interaction. To estimate the quantum contribution to the structural and thermodynamic properties, Wigner (1932) [12] expressed the Helmholtz free energy (F) using Plank constant (h) by Eq. 3.7;

$$F = F_{CL} + \Delta F(h^2) + \Delta F(h^4) \dots \quad (3.38)$$

The kinetic energy (E_k) of a system with the quantum correction is expressed as

$$E_k = \frac{3}{2} N k_B T + \frac{h^2}{96 \pi^2 k_B T} \left\langle \sum_i \frac{\Delta U}{m_i} \right\rangle + O(h^4), \quad (3.39)$$

where Δ is the Laplacian with respect to the coordinates of the i th ion. In these calculations, the first non-vanishing term having the order h^2 is only included as the quantum correction term and all higher-order terms is neglected.

3-2-3 Calculations of properties

In present study, thermal expansion, bulk modulus, specific heat capacity and thermal conductivity of the cubic crystal are evaluated by MD calculation. They were calculated as follows.

Linear thermal expansion coefficient

The linear thermal expansion coefficient (LTEC: α_{lin}) was calculated by the following equation;

$$\alpha_{lin} = \frac{1}{a(298)} \left(\frac{a(T) - a(298)}{T - 298} \right)_{P:const}, \quad (3.40)$$

where T is absolute temperature and $a(T)$ is the lattice parameter of the unit cell at T .

Bulk modulus

The bulk modulus (B) was calculated by the following equation;

$$\frac{1}{B} = -\frac{3}{a(P_0)} \left(\frac{\partial a(P)}{\partial P} \right)_{T, \text{const}}, \quad (3.41)$$

where P is the pressure and P_0 is atmospheric pressure.

Specific heat capacity

Generally speaking, the specific heat capacity at constant pressure (C_p) is evaluated as the sum of the contribution of lattice vibration (C_v), lattice dilation (C_D), electron (C_{EL}) and the other (C_{OTHER}) such as generation of the lattice defect. However, in case of MD calculation, only C_v and C_D can be calculated. So in the present study, C_p is evaluated as the sum of C_v and C_D . C_v is equal to the specific heat capacity at constant volume. C_v and C_D are able to calculate using the following equations;

$$C_v = \left(\frac{\partial E(T)}{\partial T} \right)_{V, \text{const}}, \quad (3.42)$$

$$C_D = (3\alpha_{lin}(T))^2 V_m(T) B(T) T. \quad (3.43)$$

In Eq. 3.11 and 3.12, $E(T)$ and $V_m(T)$ are internal energy and molar volume at T K.

Thermal conductivity

Thermal conductivity (κ) has been calculated with Green-Kubo formula [13] using autocorrelation function of the energy current of a system $\langle S(t) \cdot S(0) \rangle$ as shown in Fig. 3.1(a),

$$\kappa = \frac{V_m}{3k_B T^2} \int_0^\infty \langle S(t) \cdot S(0) \rangle dt. \quad (3.44)$$

In this equation, S is the energy current given by the following equation;

$$S(t) = \frac{1}{V_m} \left[\sum_j \mathbf{e}_j \mathbf{v}_j + \frac{1}{2} \sum_j \sum_{i \neq j} r_{ij} f_{ij} \mathbf{v}_j \right], \quad (3.45)$$

where \mathbf{e}_j is the surplus energy of j th particle expressed as the following equation;

$$\mathbf{e}_j = \left\{ \frac{1}{2} m_j \mathbf{v}_j^2 + \frac{1}{2} \sum_{i \neq j} U(r_{ij}) \right\} - \mathbf{e}_{ave}. \quad (3.46)$$

\mathbf{e}_{ave} : Average energy of particles in a given system.

From Eq. 3.13, we could obtain the thermal conductivity as shown in Fig. 3.1(b). In the present study, the author assumed that the average of the convergence region equals to the thermal conductivity. So, the thermal conductivity calculated by MD simulation has a margin of error.

3-2-4 Decision of ionic model

There are two ionic models in MD simulation. One is the FIM (Fully Ionic Model) and another is the PIM (Partially Ionic Model). In FIM, the both crystals are fully ionic bonding with 100% of the ion valence. For example, uranium, plutonium and oxygen ions have +4, +4 and -2 electrical charge in FIM. In PIM, the ratio of the ionic bonding in the crystal is not 100%. The ratio (P_{M-O}) is roughly estimated by Pauling equation (Eq. 3.16) [14], which is the empirical equation;

$$P_{M-O} = 1 - \exp\{-(\chi_M - \chi_O)^2/4\}, \quad (3.47)$$

where χ is the electronegativity and the subscript of M and O represent the metal and oxygen. In the present study, the ionic bonding of 60 % was assumed for actinide dioxides in PIM. There are two reasons for the ionicity of 60 %. One is that this value is favorable for ceria-based materials [10]. Another reason is that an oxide material cannot generally be clearly categorized into the ionic or covalent crystal. Arima (2005) [15] was evaluated which potential model is the best for UO₂ and PuO₂. Fig. 3.2 referred from Ref. [15] shows the temperature dependences of the lattice parameter of UO₂ and PuO₂, with the experimental data [16-18]. From this figure, it was found that the PIM was more suitable than the FIM in case of UO₂ and PuO₂. Therefore, in the present study, the PIM was used. Recently, Konashi (2007) [19] reported using the first principle calculation that the ionicity of UO₂ is 59%. This value is very close to the ionicity assumed in the present study (=60%).

3-2-5 Potential function

As the potential function used in MD calculation, Morse type potential with Busing-Ida term (Eq. 3.17) was used in the present study.

$$U(r_{ij}) = f_1 \frac{z_i z_j e^2}{r_{ij}} + f_2 (b_i + b_j) \exp\left(\frac{a_i + a_j - r_{ij}}{b_i + b_j}\right) - f_2 \frac{c_i c_j}{r_{ij}^6} + f_2 D_{ij} \left\{ \exp[-2\beta_{ij}(r_{ij} - r_{ij}^*)] - 2\exp[-\beta_{ij}(r_{ij} - r_{ij}^*)] \right\} \quad (3.48)$$

where r_{ij} is the distance between i th and j th ions, z_i is the electric charge of i th. f_1 and f_2 are adjustable parameters and equal to 10^8 and $(4.18 \times 10^{10})/(6.02 \times 10^{23})$ when the units of $U(r_{ij})$ and r_{ij} are erg and Å. a_i , a_j , b_i , b_j , c_i , c_j , D_{ij} , β_{ij} and r_{ij}^* are potential parameters. In this model, the first, second, third and fourth terms of the right side represent Coulomb force, short range force, interatomic force, and covalent bond interactions, respectively.

These parameters were semi-empirically changed and determined until the thermal expansion and bulk modulus calculated by MD simulation corresponded to the experimental data.

3-2-6 Conditions of Calculations

The calculation conditions in the present study are shown in Table 3.1. 5000 steps computing of scaling method was carried out as initial relaxation. The calculations were performed at constant pressure-temperature (NPT) and constant volume-temperature (NVT), using the extended system method by Nose (1984) [20] and Andersen (1980) [21]. The basic cluster was $4 \times 4 \times 4$ cluster for nitrides and dioxides as shown in Fig. 3.3 and 3.4. It was confirmed that the results obtained from $4 \times 4 \times 4$ cluster adequately agreed with those obtained from $5 \times 5 \times 5$ cluster.

3-3 Results and discussion of actinide nitrides and nitride ADS target fuels

3-3-1 Potential parameter

The potential parameters for ThN, NpN, PuN and AmN were semi-empirically determined by fitting the experimental data of the thermal expansion [22-27, Chapter 2]. The Bulk moduli of UN and ZrN were evaluated by Hayes (1990) [28], Portnoi (1968) [29] and Chapter 2. So, the potential parameters for UN and ZrN were semi-empirically determined by fitting the experimental data of the thermal expansion and bulk modulus. These parameters are summarized in Table 3.2 and allow the author to calculate the solid solution formed from AnN and ZrN. Therefore, the author evaluated the thermal properties of not only AnN and ZrN, but also $U_{0.4}Zr_{0.6}N$, $Pu_{0.4}Zr_{0.6}N$, $Pu_{0.2}Np_{0.2}Zr_{0.6}N$ and $Pu_{0.2}Am_{0.2}Zr_{0.6}N$. The author chose these solid solutions by the following reasons. The thermophysical properties of $U_{0.4}Zr_{0.6}N$ were experimentally evaluated in Chapter 2. After evaluation of the differences between the experimental data and MD results of $U_{0.4}Zr_{0.6}N$, the differences between $Pu_{0.4}Zr_{0.6}N$ and $U_{0.4}Zr_{0.6}N$ were evaluated. To evaluate the influences of Np and Am, $Pu_{0.2}Np_{0.2}Zr_{0.6}N$ and $Pu_{0.2}Am_{0.2}Zr_{0.6}N$ were evaluated and their component was close to the candidate of the nitride fuels with the inert matrix suggested in FUTURIX-FTA project [5].

3-3-2 Thermal expansion

The temperature dependences of the lattice parameters of AnN (ThN, UN, NpN, PuN and AmN), ZrN, $U_{0.4}Zr_{0.6}N$, $Pu_{0.4}Zr_{0.6}N$, $Pu_{0.2}Np_{0.2}Zr_{0.6}N$ and $Pu_{0.2}Am_{0.2}Zr_{0.6}N$ were calculated by MD method from room temperature to 2800 K. Fig. 3.5-8 show the temperature dependences of the

lattice parameters, together with the experimental data [22–27, 30–35]. In the same way, their temperature dependences of the LTEC were shown in Fig. 3.9–12 [22–27, 30–36].

MD results of AnN and ZrN corresponded to the experimental values. Although the temperature range of the experimental data were limited for ThN, NpN, PuN, AmN and ZrN, the high temperature data could be obtained from MD calculation. And there are no data of the temperature dependences of the lattice parameter and LTEC of U_{0.4}Zr_{0.6}N, Pu_{0.4}Zr_{0.6}N, Pu_{0.2}Np_{0.2}Zr_{0.6}N and Pu_{0.2}Am_{0.2}Zr_{0.6}N but the author estimated them by MD calculation. In Fig. 3.5, the lattice parameters of UN, NpN and PuN were close to each other at room temperature, and those of ThN and AmN were higher than those of UN, NpN and PuN at room temperature. The reason of the large lattice parameter of ThN is probably that Th atom doesn't have the electron in 5f orbit and U, Np, Pu and Am have the electron in 5f orbit. However, the reason of the large lattice parameter of AmN is unknown. To understand this phenomenon, the attempts to evaluate the density of state and electron state by the XPS (X-ray Photoelectron Spectroscopy) and XAFS (X-ray absorption fine structure) are recently performed [37]. In case of the LTEC of AnN, the values of ThN, UN and NpN were similar to each other. That of AmN was slightly higher than those of ThN, UN and NpN and that of PuN was higher than the others. From these results, it was qualitatively thought that the melting temperature of PuN was lower than the others because the LTEC is generally proportional to the inverse of the melting point in case of the materials with the same crystal structure. In case of the lattice parameter and LTEC of U_{0.4}Zr_{0.6}N, MD result was well consistent with the experimental data of Chapter 2 and the data estimated from Vegard's law. This result proved that there was no problem to evaluate the thermophysical properties of the solid solutions formed from AnN and ZrN. In case of the lattice parameter of Pu_{0.4}Zr_{0.6}N, MD result was lower than the data estimated from Vegard's law. On the other hand, the LTEC obtained from MD calculation followed to Vegard's law. The similar trend was reported in the case of U_xPu_{1-x}N by Tennery (1971) [38] and Suzuki (1991) [39] as shown in Fig. 3.13. By Tennery (1971) [38] and Suzuki (1991) [39], the reason of the disagreement of MD result from Vegard's law was that Pu atom became to have the electron in 6d orbit by the formation of the solid solution nevertheless Pu atom didn't fundamentally have the electron in 6d orbit. The author thinks that the same phenomenon occurs in Pu_{0.4}Zr_{0.6}N. In case of Pu_{0.2}Np_{0.2}Zr_{0.6}N and Pu_{0.2}Am_{0.2}Zr_{0.6}N, such disagreements from Vegard's law were not almost observed in Fig. 3.8 due to the low content of PuN.

3-3-3 Bulk modulus

The temperature dependences of the bulk moduli of AnN, ZrN, U_{0.4}Zr_{0.6}N, Pu_{0.4}Zr_{0.6}N, Pu_{0.2}Np_{0.2}Zr_{0.6}N and Pu_{0.2}Am_{0.2}Zr_{0.6}N were calculated by MD method from room temperature to 2800 K and were shown in Fig. 3.14–17, with the experimental data [28, 29, 40, Chapter 2].

Except for UN and ZrN, there is no experimental data, but the author could obtain their bulk modulus by MD calculation. In case of UN and ZrN, MD results of UN and ZrN agreed with the experimental data [28, 29, 40, Chapter 2]. In the same way of the LTEC, the bulk modulus of ThN, UN and NpN were similar to each other, and those of PuN and AmN were lower than those of ThN, UN and NpN. The bulk modulus of U_{0.4}Zr_{0.6}N at low temperature (<1800 K) and Pu_{0.4}Zr_{0.6}N indicated the intermediate value of ZrN and UN or PuN. At high temperature (>1800K), the bulk modulus of U_{0.4}Zr_{0.6}N were similar to that of UN and ZrN because the bulk modulus of ZrN became to be close to that of UN with increasing the temperature. The bulk modulus was slightly decreased by the addition of Np and Am in Fig. 3.17. Using the LTEC and bulk modulus obtained from MD calculation, the author estimated the C_D by Eq. 3.12.

3-3-4 Specific heat capacity

The C_p was evaluated as the sum of C_v and C_D. The temperature dependences of the specific heat capacity of AnN, ZrN, U_{0.4}Zr_{0.6}N, Pu_{0.4}Zr_{0.6}N, Pu_{0.2}Np_{0.2}Zr_{0.6}N and Pu_{0.2}Am_{0.2}Zr_{0.6}N are shown in Fig. 3.18–21, together with the experimental data [41–45, Chapter 2]. The specific heat capacity of ThN at low temperature (<20K) was reported by Maurice (1979) [46]. Using the data of Maurice (1979) [46], the author calculated the C_{EL} of ThN as the following equation;

$$C_{EL} (\text{Jmol}^{-1}\text{K}^{-1}) = 3.12 \times 10^{-3} T \quad (3.49)$$

In case of ThN, the sum of MD result (C_v + C_D) and C_{EL} was also shown in Fig. 3.18, and it almost agreed with the experimental values [41]. This result indicates that other contributions such as Frenkel defect are very small in case of ThN. MD results of UN and ZrN was well consistent with C_v + C_D obtained in Chapter 2. In the specific heat capacity of UN, the experimental data of Tagawa (1974) [42] rapidly increased from about 1500K. In Ref. 42, it was suggested that the increasing is probably occurred from the anharmonic lattice vibration. The contribution of the anharmonic lattice vibration could be included in C_v obtained from MD calculation because the lattice behavior can be reproduced by MD simulation. Therefore, also in MD results, the rapid increasing of the specific heat capacity could be observed. The similar trend was observed in

case of ZrN. MD result of UN was lower than the experimental data [41, 42, Chapter 2], but MD result and $C_V + C_D$ obtained in Chapter 2 of ZrN showed the similar value with the experimental data [41, 45, Chapter 2]. The rapid increases in specific heat capacity at high temperature were not observed in case of ThN, NpN, PuN and AmN. The misalignments between MD results and the experimental data, which is mainly resulted from the C_{EL} , decreased with the atomic number from ThN to PuN. Judging from this tendency, MD result of AmN may show the similar value with the C_p , although there is no data of the C_p of AmN.

In Fig. 3.20, MD results of $U_{0.4}Zr_{0.6}N$ and $Pu_{0.4}Zr_{0.6}N$ were well consistent with the experimental data of Chapter 2 and the data estimated by Neumann-Kopp's law. These results probably indicate that the C_{EL} in $U_{0.4}Zr_{0.6}N$ and $Pu_{0.4}Zr_{0.6}N$ are small. In Fig. 3.21, the influences of the addition of Np and Am could not be almost observed. In the specific heat capacity of these solid solutions, the rapid increasing at the high temperature could be observed in the same way of ZrN.

3-3-5 Thermal conductivity

As the author explained in Chapter 2, the thermal conductivity is represented as the following equation;

$$\kappa_{TOT} = \kappa_{EL} + \kappa_{LAT} + \kappa_{OTHER} \quad (3.50)$$

where κ_{TOT} is the total value of the thermal conductivity, indeed κ_{TOT} is the experimental values, κ_{LAT} , κ_{EL} and κ_{OTHER} are the lattice, electrical and other contributions. κ_{EL} can be evaluated by Wiedemann-Franz law (Eq. 2.106) from the electrical conductivity. However, in MD calculation, we can't calculate κ_{EL} and κ_{OTHER} . MD results represent only κ_{LAT} . In case of AnN and ZrN, the main contribution in κ_{TOT} is κ_{EL} and κ_{OTHER} . Therefore, all we can do using MD simulation is only qualitative evaluation for the κ_{LAT} . The temperature dependences of the thermal conductivities of AnN, ZrN, $U_{0.4}Zr_{0.6}N$, $Pu_{0.4}Zr_{0.6}N$, $Pu_{0.2}Np_{0.2}Zr_{0.6}N$ and $Pu_{0.2}Am_{0.2}Zr_{0.6}N$ are shown in Fig. 3.22-25, together with the experimental data [47-57]. All of MD results followed to 1/T law. In Fig. 3.20 and 3.21, the black lines represent the fitting result by 1/T law. There are no remarkable differences between the thermal conductivities of ThN, UN, NpN, PuN and AmN. MD result of ZrN was higher than the experimental data by Vasilos (1953) [50] and Neel (1962) [52] at room temperature. Therefore, underestimation of the literature data [50, 52] was confirmed by not only the κ_{EL} (see Chapter 2), but also MD calculation.

It was found that MD results of U_{0.4}Zr_{0.6}N and Pu_{0.4}Zr_{0.6}N were lower than those of ZrN and UN or PuN in Fig. 3.24. It is because the center of the phonon scattering was made by formation of the solid solution of U_{0.4}Zr_{0.6}N and Pu_{0.4}Zr_{0.6}N. On the other hand, MD results of Pu_{0.2}Np_{0.2}Zr_{0.6}N and Pu_{0.2}Am_{0.2}Zr_{0.6}N were similar to that of Pu_{0.4}Zr_{0.6}N. The effect of the phonon scattering by formation of the solid solution depends on the differences on the ionic radii, effective mass and electron valence. Their differences between Pu and ZrN would be vastly larger than those between Np–Pu, and Pu–Am, although there are no data of the ionic radii of Np³⁺, Pu³⁺ and Am³⁺. This is probably the reason that the effects of the addition of Np and Am were not almost observed.

3-4 Results and Discussion of actinide dioxide and MA-containing MOX fuels

3-4-1 Potential parameter

In the same way of nitride, the potential parameters for NpO₂, PuO₂ and AmO₂, were semi-empirically determined by fitting the experimental data of the thermal expansion [16, 17, 55–57]. The Bulk moduli of UO₂ were evaluated by Browning (1983) [58]. So, the potential parameters for UO₂ were semi-empirically determined by fitting the experimental data of the thermal expansion [16–18] and bulk modulus [58]. These parameters are summarized in Table 3.3. By using these potential parameters, the thermal properties of AnO₂ (An: U, Np, Pu and Am), MOX (U_xPu_{1-x}O₂), Np-containing MOX (U_{0.7-x}Np_xPu_{0.3}O₂) and Am-containing MOX (U_{0.7-x}Pu_{0.3}Am_xO₂) were evaluated from MD simulation.

3-4-2 Thermal expansion

The temperature dependences of the lattice parameters of AnO₂ (An: U, Np, Pu and Am), U_xPu_{1-x}O₂, U_{0.7-x}Np_xPu_{0.3}O₂ and U_{0.7-x}Pu_{0.3}Am_xO₂ were calculated by MD method. Fig. 3.26 shows the temperature dependences of the lattice parameter of AnO₂, with the experimental data [16–18, 56, 57]. In these figures, MD results of AnO₂ were well consistent with the experimental data. The electron number in 5f orbit of An elements increases with increasing the atomic number nevertheless the most outer shell of An element is 7s orbit. Therefore, the ionic radius in An ion decreases with increasing the atomic number. This phenomenon is called “actinide contraction”. In case of AnO₂, their lattice parameters decrease with increasing the atomic number following to the actinide contraction because the main bond of AnO₂ is the ionic bond. This trend could be reproduced by MD calculation as shown in Fig. 3.26. On the other hand, in

case of AnN, the lattice parameters didn't follow to the actinide contraction as shown in Fig. 3.5 because the main bond is the covalent bond and metallic bond.

Fig. 3.27 and 3.28 show the lattice parameters at room temperature as the function of X in $U_{1-X}Pu_XO_2$, $U_{0.7-X}Np_XPu_{0.3}O_2$ and $U_{0.7-X}Pu_{0.3}Am_XO_2$ and include the estimated data from the experimental data of UO_2 (Martin (1988) [18]), NpO_2 (Serizawa (2001) [56]), PuO_2 (Taylor [16]), AmO_2 (Taylor [16]) using Vegard's law. In these figures, MD results were well consistent with the estimated data. So, it was found that $U_{1-X}Pu_XO_2$, $U_{0.7-X}Np_XPu_{0.3}O_2$ and $U_{0.7-X}Pu_{0.3}Am_XO_2$ are the ideal solid solution in the different way of $U_XPu_{1-X}N$ and $Pu_XZr_{1-X}N$. Fig. 3.29 shows the temperature dependences of the lattice parameters of $U_{0.7-X}Np_XPu_{0.3}O_2$ and $U_{0.7-X}Pu_{0.3}Am_XO_2$. From these figures, it was confirmed that $U_{0.7-X}Np_XPu_{0.3}O_2$ and $U_{0.7-X}Pu_{0.3}Am_XO_2$ followed to Vegard's law at high temperature. The same tendency was observed in the bulk modulus.

3-4-3 Specific heat capacity

Fig. 3.30 shows the temperature dependences of the specific heat capacities of AnO₂ (An: U, Np, Pu and Am), together with the experimental data of [17, 41, 56, 59–62] and estimated data [63]. In case of MD result of UO_2 , the peak was observed around 2200 K. Jackson (1986) [64] have shown that the cation migration is assisted by an anion diffusive transition, which phenomenon is called 'Bredig transition'. Ralph (1987) [60] suggested that Bredig transition could happen in PuO_2 , too. However, by MD calculation, Bredig transition could not be observed. For conformation of Bredig transition, the author evaluated the motion tracks of U^{4+} , Pu^{4+} , O^{2-} in UO_2 and PuO_2 crystal structure at 2500 K as shown in Fig. 3.31. In this figure, it was found that the MD cell of UO_2 reproduced Bredig transition and became the oxygen super-ionic conductor at 2500 K, as suggested by the neutron scattering experiments [65, 66]. This result indicates MD calculation using the potential parameters obtained in the present study gives a reasonable description of atomic motions in UO_2 at high temperatures. On the other hands, in case of PuO_2 , the oxygen ion didn't become to be the super-ionic conductor and the MD cell hold CaF_2 structure. In case of SGTE data [41], Bredig transition could not be observed. From these results, the author thinks that PuO_2 doesn't have Bredig transition. In MD calculation, Bredig transition could not be observed in case of NpO_2 and AmO_2 , too. Fig. 3.32 shows the mean-square displacement (MSD) obtained from 3000 steps (6 ps) calculation and the existence of the Bredig transition is confirmed in the MD cell at 2100–2500K. Ralph (1987) [60] reported that Bredig transition of UO_2 occurred at 2610 K (0.84 of melting temperature). Its temperature

was slightly higher than that calculated from MD simulation. The MD cell is the perfect crystal, which doesn't include the dislocation and defect. Probably, this is the reason of the differences between Bredig transition temperatures obtained from the experimental measurement and MD simulation.

Browning (1983) [58] pointed out that the C_p of UO₂ could be represented by the following equation;

$$C_p = C_v + C_D + C_{Sch} + C_{S.P.} + C_{Bredig}, \quad (3.20)$$

where the C_{Sch} , $C_{S.P.}$, C_{Bredig} are the contribution of the formation of Schottky, small polaron, defect and Bredig transition. However, in MD simulation, the C_{Sch} and $C_{S.P.}$ could not be evaluated. The C_{Sch} and $C_{S.P.}$ was evaluated by Browning (1983) [58] as the following equations;

$$C_{Sch} (\text{Jmol}^{-1}\text{K}^{-1}) = 2.95 \times 10^{-3} T \quad (3.21)$$

$$C_{S.P.} (\text{Jmol}^{-1}\text{K}^{-1}) = \frac{259 \times 10.79 \times 10^6}{T^2} \exp\left(-\frac{10.79 \times 10^3}{T}\right) \quad (3.22)$$

Therefore, the author estimated the C_p of UO₂ using the MD result ($C_v + C_D + C_{Bredig}$), C_{Sch} (Eq. 3.21) and $C_{S.P.}$ (Eq. 3.22). From Fig. 3.30, the sum of MD result ($C_v + C_D + C_{Bredig}$), C_{Sch} (Eq. 3.21) and $C_{S.P.}$ (Eq. 3.22) of UO₂ was well consistent with the experimental data [41, 59, 60]. In case of PuO₂, only the MD result agreed with the experimental data [40, 60]. In case of NpO₂ and AmO₂, there are some variations in the experimental data [17, 55, 61–63] and MD results were within the variation of the experimental data. From these results, it was confirmed that the specific heat capacity could be precisely evaluated by the MD results in case of AnO₂, which doesn't almost have the contribution of the electron.

Fig. 3.33 shows the temperature dependences of specific heat capacities of U_{1-x}Pu_xO₂ (X=0, 0.2, 0.3, 1.0), together with the experimental data of UO₂ and PuO₂ [41, 60] and the data of U_{0.7}Pu_{0.3}O₂ and U_{0.8}Pu_{0.2}O₂ estimated from the SGTE data [41] using Neumann-Kopp's law. From this figure, it was confirmed that MD results of U_{0.7}Pu_{0.3}O₂ and U_{0.8}Pu_{0.2}O₂ are well consistent with their estimated data. In addition, U_{0.7}Pu_{0.3}O₂ and U_{0.8}Pu_{0.2}O₂ had the peaks derived from Bredig transition, in the same way of UO₂. Fig. 3.34 shows the temperature dependences of the specific heat capacity of U_{0.7-x}Np_xPu_{0.3}O₂ and U_{0.7-x}Pu_{0.3}Am_xO₂. In this figure, Bredig transition could be observed in both U_{0.7-x}Np_xPu_{0.3}O₂ and U_{0.7-x}Pu_{0.3}Am_xO₂. The influence of the addition of Np and Am was very small.

3-4-4 Thermal conductivity

Before the author calculates the thermal conductivity of AnO₂ by MD simulation, the author had predicted that MD results of AnO₂ would agree with the experimental data in the different way of AnN because the κ_{EL} is very small and the κ_{LAT} is the main contribution in case of AnO₂. To confirm the validation of the prediction, the author showed the temperature dependences of the thermal conductivities of AnO₂ (An: U, Np, Pu and Am) in Fig. 3.35, with the experimental data [67–72]. The MD cell is the perfect crystal and there are no grain boundary and point defect. On the other hand, in the actual polycrystalline material, the thermal conductivity is decreased by the grain boundary scattering and point defect scattering. Therefore, in Fig. 3.35, at low temperature ($T < 700$ K), MD results of AnO₂ (An: U, Np, Pu, Am) were higher than the experimental data. MD results of UO₂ at middle temperature ($800 < T < 2000$ K), NpO₂ and PuO₂ at the high temperature ($800 \text{ K} < T$) was well consistent with the experimental data, because the effect of the phonon vibration became to be larger than the effect of the grain boundary and point defect at such temperature region. At high temperature ($2000 \text{ K} < T$), the small polaron generates in UO₂ crystal and this phenomenon increases the specific heat capacity and thermal conductivity. So, MD result of UO₂ was lower than the experimental data at high temperature ($2000 \text{ K} < T$). Fink (2000) [73] evaluated the small polaron contribution ($\kappa_{S.P.}$) as the following equation;

$$\kappa_{S.P.} (\text{Wm}^{-1}\text{K}^{-1}) = \frac{6400}{T^{5/2}} \left(\frac{-16.35}{T} \right) \quad (3.23)$$

The author plotted the sum of the MD result ($= \kappa_{LAT}$) and $\kappa_{S.P.}$ as the red triangle points in Fig. 3.35 and the sum of the MD result ($= \kappa_{LAT}$) and $\kappa_{S.P.}$ agreed with the experimental data at the whole temperature. MD result of AmO₂ was higher than the experimental data, nevertheless MD results of UO₂, NpO₂ and PuO₂ showed the similar value with the experimental data. In addition, the experimental data of UO₂, NpO₂ and PuO₂ were close to each other. On the other hand, only the experimental data of AmO₂ was quite lower than those of UO₂, NpO₂ and PuO₂. There are some reasons of this phenomenon. First reason is that the thermal conductivity is decreased by the point defect scattering because AmO₂ is reduced and O/Am changes during the measurement of the thermal conductivity. Second reason is the self-irradiation damage. Third reason is the density change by He bubble generated from the alpha decay of Am. Judging from these reasons, the experimental data underestimates the thermal conductivity of AmO₂. Therefore, the author thinks that MD result of AmO₂ represents the intrinsic thermal conductivity of AmO₂. From MD

calculation, it was found that there is no large deviation between the thermal conductivity of AnO_2 (An: U, Np, Pu and Am).

Fig. 3.36 and 3.37 show the temperature and Pu content dependences of the thermal conductivity of $\text{U}_{1-x}\text{Pu}_x\text{O}_2$, with the experimental data [67, 70, 74–76]. MD result of $\text{U}_{0.8}\text{Pu}_{0.2}\text{O}_2$ was within the variation of the experimental data [70, 74, 75]. Fig. 3.37 was convex downward and this is the typical behavior of the thermal conductivity derived from the formation of the center of the phonon scattering. By MD simulation based on only the thermal expansion data of UO_2 and PuO_2 , the author could precisely evaluate the thermal conductivity of $\text{U}_{1-x}\text{Pu}_x\text{O}_2$. From this result, it was thought that MD results of $\text{U}_{0.7-x}\text{Np}_x\text{Pu}_{0.3}\text{O}_2$ and $\text{U}_{0.7-x}\text{Pu}_{0.3}\text{Am}_x\text{O}_2$ would indicate the similar value with the experimental data.

Fig. 3.38 shows the temperature dependences of the thermal conductivities of $\text{U}_{0.7-x}\text{Np}_x\text{Pu}_{0.3}\text{O}_2$ and $\text{U}_{0.7-x}\text{Pu}_{0.3}\text{Am}_x\text{O}_2$, with the experimental data [70, 75–77]. From this figure, in the same way of UO_2 , PuO_2 and MOX, MD results of $\text{U}_{0.7-x}\text{Np}_x\text{Pu}_{0.3}\text{O}_2$ and $\text{U}_{0.7-x}\text{Pu}_{0.3}\text{Am}_x\text{O}_2$ decreased with increasing the temperature following to $1/T$ law and indicated the similar value with the experimental data of $\text{U}_{0.7}\text{Pu}_{0.3}\text{O}_2$ and $\text{U}_{0.8}\text{Pu}_{0.2}\text{O}_2$. Fig. 3.39 shows Np or Am content dependences of the thermal conductivities of $\text{U}_{0.7-x}\text{Np}_x\text{Pu}_{0.3}\text{O}_2$ and $\text{U}_{0.7-x}\text{Pu}_{0.3}\text{Am}_x\text{O}_2$, with the experimental data [76, 77]. In both case of $\text{U}_{0.7-x}\text{Np}_x\text{Pu}_{0.3}\text{O}_2$ and $\text{U}_{0.7-x}\text{Pu}_{0.3}\text{Am}_x\text{O}_2$, the MD results were well consistent with the experimental data. From this figure, it was found that the thermal conductivities of $\text{U}_{0.7-x}\text{Np}_x\text{Pu}_{0.3}\text{O}_2$ and $\text{U}_{0.7-x}\text{Pu}_{0.3}\text{Am}_x\text{O}_2$ didn't almost depend on Np or Am content. The phonon-impurity scattering can be described by both mass and size distortion effects. In case of $\text{U}_{0.7-x}\text{Np}_x\text{Pu}_{0.3}\text{O}_2$ and $\text{U}_{0.7-x}\text{Pu}_{0.3}\text{Am}_x\text{O}_2$, the mass and size differences between U^{4+} , Np^{4+} , Am^{4+} have to be considered, because U^{4+} is substituted by Np^{4+} or Am^{4+} . The atomic mass of U, Np and Am is 238, 238 and 241. The tetravalent eight-coordinate ionic radius of U^{4+} , Np^{4+} or Am^{4+} are 0.10, 0.098 and 0.095 nm, respectively [78]. Therefore, it was thought that the distortion effect by addition of Np and Am was small in $\text{U}_{0.7-x}\text{Np}_x\text{Pu}_{0.3}\text{O}_2$ and $\text{U}_{0.7-x}\text{Pu}_{0.3}\text{Am}_x\text{O}_2$. This would be one of the reasons that the thermal conductivities of $\text{U}_{0.7-x}\text{Np}_x\text{Pu}_{0.3}\text{O}_2$ and $\text{U}_{0.7-x}\text{Pu}_{0.3}\text{Am}_x\text{O}_2$ were scarcely influenced by addition of Np and Am. Another reason would be that the decreasing of the thermal conductivity by the phonon-impurity scattering is almost saturated by the solution of Pu.

3-5 Summary

By fitting the limited experimental data of the thermal expansion and bulk modulus, the

potential parameters for nitrides (ThN, UN, NpN, PuN, AmN and ZrN) and actinide dioxides (UO₂, NpO₂, PuO₂ and AmO₂) were semi-empirically determined. Using these parameters, the author evaluated the thermal expansion, bulk modulus, specific heat capacity and thermal conductivity of not only AnO₂, AnN and ZrN, but also MOX [U_{1-x}Pu_xO₂ (X=0.2, 0.3)], MA-containing MOX [U_{1-x}Np_xPu_{0.3}O₂ (X=0, 0.05, 0.10, 0.15, 0.12, 0.15), U_{1-x}Pu_{0.3}Am_xO₂ (X=0, 0.016, 0.03, 0.05, 0.10, 0.15)] and nitride fuels with the inert matrix (U_{0.4}Zr_{0.6}N, Pu_{0.4}Zr_{0.6}N, Pu_{0.2}Np_{0.2}Zr_{0.6}N and Pu_{0.2}Am_{0.2}Zr_{0.6}N).

Lattice parameter and thermal expansion

The lattice parameters as the function of temperature and LTEC of AnO₂, AnN and ZrN calculated by MD simulation were well consistent with the experimental data. MD result of U_{0.4}Zr_{0.6}N agreed with the experimental data obtained in Chapter 2 and Vegard's law. On the other hand, the lattice parameter of Pu_{0.4}Zr_{0.6}N calculated by MD simulation was lower than Vegard's law in the same way of the experimental data of U_{1-x}Pu_xN. MOX, MA-containing MOX, Pu_{0.2}Np_{0.2}Zr_{0.6}N and Pu_{0.2}Am_{0.2}Zr_{0.6}N followed to Vegard's law.

Specific heat capacity

The specific heat capacities of UN and ZrN calculated from MD simulation were well consistent with the $C_V + C_D$ of UN and ZrN obtained in Chapter 2, respectively. MD result of UN was lower than the experimental data of C_P , but MD result of ZrN was well consistent with the experimental data of C_P . In the same way of UN, MD result of ThN was lower than the experimental data of C_P , and the sum of MD result and C_{EL} showed the similar value with the experimental data of C_P . On the other hand, only MD result of NpN and PuN were close to the experimental data of C_P in the same way of ZrN. Judging from these tendency, MD result of AmN may show the similar value with C_P , although there are no experimental data of the C_P of AmN. MD results of U_{0.4}Zr_{0.6}N and Pu_{0.4}Zr_{0.6}N were well consistent with the experimental data of C_P in Chapter 2 and the data estimated by Neumann-Kopp's law. The influences of the addition of Np and Am could not be almost observed.

Bredig transition was observed in the specific heat capacity of UO₂ calculated by MD simulation. By the motion track evaluated by MD simulation, it was confirmed that O²⁻ in UO₂ crystal became to be the super-ionic conductor in the region of 2100 K < T, for the first time. The sum of MD result ($C_V + C_D + C_{Bredig}$), $C_{S.P.}$ and C_{Sch} of UO₂ was well consistent with the experimental data of C_P . Only MD result ($C_V + C_D$) of PuO₂ agreed with the experimental data of C_P . MD results of NpO₂ and AmO₂ were within the variations of the experimental data of C_P .

In case of the specific heat capacity of U_{0.8}Pu_{0.2}O₂ and U_{0.7}Pu_{0.3}O₂, MD results followed to Neumann-Kopp's law and Bredig transition could be observed. The specific heat capacity of U_{0.7-x}Np_xPu_{0.3}O₂ and U_{0.7-x}Pu_{0.3}Am_xO₂ obtained by MD simulation were almost independent on X and indicated the peaks derived from Bredig transition.

Thermal conductivity

By MD simulation, only the κ_{LAT} could be evaluated. In case of the nitride fuels, MD results were vastly lower than the experimental data ($=\kappa_{TOT}$), because the main contribution in the κ_{TOT} of the nitride fuel is the κ_{EL} . In case of the material with high electrical conductivity such as the actinide nitrides, we can't evaluate the thermal conductivity by MD simulation. On the other hand, in case of the material with low electrical conductivity such as the actinide dioxides, we can precisely evaluate the thermal conductivity by MD simulation.

There are no remarkable differences between MD results of ThN, UN, NpN, PuN and AmN and they were lower than that of ZrN. MD results of U_{0.4}Zr_{0.6}N and Pu_{0.4}Zr_{0.6}N were lower than those of ZrN and UN or PuN due to the phonon-impurity scattering. In case of Pu_{0.2}Np_{0.2}Zr_{0.6}N and Pu_{0.2}Am_{0.2}Zr_{0.6}N, the influences of the addition of Np or Am were not almost observed.

At low temperature ($T < 700$ K), the thermal conductivity of UO₂, NpO₂ and PuO₂ obtained from MD simulation were higher than the experimental data because the MD cell is the perfect crystal and there are no effects of grain boundary, point defect and so on. At the high temperature, MD results of UO₂, NpO₂ and PuO₂ showed the close value with the experimental data. MD result of AmO₂ was higher than the experimental data at whole temperature, because the experimental data would underestimate due to the reduction, self-irradiation damage and He bubble of AmO₂. So, it is thought that MD result of AmO₂ indicates the intrinsic thermal conductivity. From MD calculation, it was found that there is no large deviation between the thermal conductivity of AnO₂ (An: U, Np, Pu and Am). MD results of U_{0.8}Pu_{0.2}O₂ and U_{0.7}Pu_{0.3}O₂ were well consistent with the experimental data. MD result of U_{1-x}Pu_xO₂ as the function of Pu content showed the convex downward relationship due to the phonon-impurity scattering. MD results of U_{0.7-x}Np_xPu_{0.3}O₂ and U_{0.7-x}Pu_{0.3}Am_xO₂ didn't almost depend on Np or Am content.

From these results, it was found that the thermophysical properties of MA-containing MOX fuels are very close to those of MOX fuels. Therefore, it is thought that the fuel behavior of

MA-containing MOX fuel in the reactor core could be predicted by the code, which had been used to predict the fuel behavior of MOX fuel. In the present study, it was confirmed that MD simulation is very useful when we evaluate the thermophysical properties of the fuels with the complex component such as MA-containing MOX fuels.

In the present study, it is confirmed that the thermophysical properties of the non-irradiated oxide fuels could be precisely evaluated by MD simulation. In MD simulation, it is possible to insert the point defect, dislocation and lattice strain in the simulation cell in order to reproduce the irradiated fuel. In this case, the electron valence of a part ion of U, Pu and MAs would change. However, it is difficult to determine the potential parameters of actinide ions such as U⁵⁺ and Pu⁵⁺ because there is no material consisted from only U⁵⁺ and Pu⁵⁺. Therefore, MD calculation used in the present study could not evaluate the irradiated fuels. On the other hand, their potential parameters would be able to be theoretically determined by the first principle calculation. In the future, it will become to be important to evaluate the thermal properties of the irradiated oxide fuel by the combination of MD simulation and first principle calculation.

References

- [99] J. Rouault, J. C. Garnier, N. Cahuvin, S. Pillon, Proc. Int. Conf. GLOBAL2001, Paris, France, Sept. 9–13, 2001, pp.133.
- [100] N. Chauvin, R.J.M. Konings, H.J. Matzke, “Optimisation of inert matrix fuel concepts for americium transmutation,” J. Nucl. Mater. 274 (1999) 105–111.
- [101] T. Namekawa, K. Kawaguchi, K. Koike, S. Haraguchi, S. Ishii, “Conceptual design study and evaluation of advanced fuel fabrication systems in the feasibility study on commercialized FR fuel cycle in Japan,” Proc. Int. Conf. GLOBAL2005, Tsukuba, Japan, Oct. 9–13, 2005, paper No. 424.
- [102] H. Matzke, “Science of Advanced LMFBR Fuels: solid state physics, chemistry, and technology of carbides, nitrides, and carbonitrides of uranium and plutonium,” Elsevier Science Pub. Co. Amsterdam, North-Holland, 1986.
- [103] L. Donnet, F. Jorion, N. Drin, S. L. Hayes, J. R. Kennedy, K. Pasamehmetoglu, S. L. Voit, D. Haas, A. Fernandez, “The FUTURIX-FTA experiment in PHENIX: Status of fuel fabrication,” Proc. Int. Conf. GLOBAL2005, Tsukuba, Japan, Oct. 9–13, 2005, Paper No. 258.
- [104] K. Minato, M. Akabori, M. Takano, Y. Arai, K. Nakajima, A. Itoh, T. Ogawa, “Fabrication of nitride fuels for transmutation of minor actinides,” J. Nucl. Mater. 320 (2003) 18–24.
- [105] T. Nishi, M. Takano, A. Itoh, M. Akabori, Y. Arai, K. Minato, M. Numata, “Thermal conductivity of AmO_{2-x},” J. Nucl. Mater. In Press.
- [106] T. Ogawa, T. Ohmichi, A. Maeda, Y. Arai, Y. Suzuki, “Vaporization behavior of (Pu,Am)N,” J. Alloys Compd. 224 (1995) 55–59
- [107] M. Takano, A. Itoh, M. Akabori, K. Minato, “Hydrolysis reactions of rare-earth and americium mononitrides,” J. Phys. Chem. Solids 66 (2005) 697–700.
- [108] 平野 一之, 河村 雄行, “パソコンによる材料設計,” 裳華房, 東京, 1994.
- [109] L. Verlet, “Computer “Experiments” on Classical Fluids. I. Thermodynamical properties of Lennard-Jones Molecules,” Phys. Rev. 159 (1967) 98–103.
- [110] E. Wigner, “On the quantum correction for thermodynamic equilibrium,” Phys. Rev. 40 (1932) 749–759.
- [111] D. Forster, “Hydrodynamics and correlation functions in ordered systems: Nematic liquid crystals,” Ann. Phys. 84[1–2] (1974) 505–534.
- [112] L. Pauling, “The Nature of the Chemical Bond, 3rd ed.,” Cornell University Press, New York, U.S.A., 1960.
- [113] T. Arima, S. Yamasaki, Y. Inagaki, K. Idemitsu, “Evaluation of thermal properties of UO₂ and

PuO₂ by equilibrium molecular dynamics simulations from 300 to 2000K," J. Alloys Compd. 400 (2005) 43–50.

[114] D. Taylor, "Thermal expansion data: II. Binary oxides with the fluorite and retille structures, MO₂, and the antiferroite structure, M₂O," Br. Ceram. Trans. J. 83 (1984) 32–37.

[115] T. Yamashita, N. Nitani, T. Tsuji, H. Inagaki, "Thermal expansions of NpO₂ and some other actinide dioxides," J. Nucl. Mater. 245 (1997) 72–78.

[116] D.G. Martin, "The thermal expansion of solid UO₂ and (U, Pu) mixed oxides — a review and recommendations," J. Nucl. Mater. 152 (1988) 94–101.

[117] 小無 健司, 加藤 正人, 神戸 振作, 源 聡, "MOX-TRU 燃料に関する計算科学研究の現状," Abstract of fall meeting of Atomic Energy Society of Japan, 2007, pp. 995 (TD12).

[118] S. Nose, "A unified formulation of the constant-temperature molecular-dynamics methods," J. Chem. Phys. 81 (1984) 511–519.

[119] H.C. Andersen, "Molecular dynamics simulations at constant pressure and/or temperature," J. Chem. Phys. 72 (1980) 2384–2393.

[120] S. Aronson, E. Cisney, K.A. Gingerich, "Thermal expansion of some cubic refractory compounds of thorium," J. Am. Ceram. Soc. 50[5] (1967) 248–252.

[121] S.L. Hayes, J.K. Thomas, K.L. Peddicord, "Material property correlations for uranium mononitride; I. Physical properties," J. Nuclear Mater. 171 (1990) 262–270.

[122] A.T. Ardred, B.D. Dunlap, A.R. Harvey, D.J.G.H. Lander, M.H. Mueller, "Magnetic properties of the neptunium mononitrides," Phys. Rev. B 9[9] (1974) 3766–3779.

[123] D.F. Carroll, "Thermal Expansion of Plutonium Nitride," J. Am. Ceram. Soc. 46 (1963) 406–406.

[124] K. Minato, M. Takano, T. Nishi, A. Itoh, M. Akabori, "Properties of minor actinide compounds relevant to nuclear fuel technology," Recent advances in actinide science, Royal society of chemistry, Cambridge, U.S.A., 2006, pp. 317–322.

[125] C.R. Houska, "Thermal expansion and atomic vibration amplitudes for TiC, TiN, ZrC, ZrN, and pure tungsten," Phy. Chem. Solids 25[4] (1964) 359–366.

[126] S.L. Hayes, J.K. Thomas, K.L. Peddicord, "Material property correlations for uranium mononitride; II Mechanical properties," J. Nucl. Mater. 171 (1990) 271–288.

[127] K.I. Portnoi, A.A. Mulaseev, V.N. Gribkov, Yu.V. Levinskii, "Modulus of normal elasticity of porosity-free titanium and zirconium nitride," Soviet Powder Metallurgy and Metal Ceramics 8[5] (1968) 406–409.

- [128] R. Benz, G. Balog, B.H. Baca, "Uranium-uranium dioxide-uranium nitride (UN₂) phase diagram," High Temp. Sci. 2[3] (1970) 221-251.
- [129] K.M. Taylor, P.A. Smudski, L.N. Halley, T.J. Keaty, "Synthesis and fabrication of refractory uranium compounds," U.S.At. Energy Comm. ORO-248 (1959) 21.
- [130] C.P. Kempter, R.O. Elliott, "Thermal expansion of UN, UO₂, (U,Th)O₂, and ThO₂," J. Chem. Phys. 30 (1959) 1524-1526.
- [131] C.A. Alexander, R.B. Clark, O.L. Krugar, J.L. Robins, "Fabrication and high-temperature thermodynamic and transport properties," Plutonium and other Actinides 1975, Proc. Int. Conf., 5th, 1976, pp. 277-286.
- [132] K. Aigner, W. Lengauer, D. Rafaja, P. Ettmayer, "Lattice parameters and thermal expansion of Ti(C_xN_{1-x}), Zr(C_xN_{1-x}), Hf(C_xN_{1-x}) and TiN_{1-x} from 298 to 1473 K as investigated by high-temperature X-ray diffraction," J. Alloys Compd. 215 (1994) 121-126.
- [133] M. Singh, H. Wiedemeier, "Estimation of thermal expansion behavior of some refractory carbides and nitrides," J. Mater. Sci. 32 (1997) 5749-5751.
- [134] E.O. Speidel, D.L. Keller, "Fabrication and properties of hot-pressed uranium mononitride," U.S. At. Energy Comm. BMI-1633 (1963) 65.
- [135] T. Nishi, M. Takano, M. Akabori, K. Minato, Private connection.
- [136] V.J. Tennery, E.S. Bomar, "Lattice parameters of (U,Pu)N solid solutions," J. Am. Ceram. Soc. 54[5] (1971) 247-249.
- [137] Y. Suzuki, Y. Arai, "Lattice parameter of UN-PuN solid solutions," J. Nucl. Sci. Tech. 28[7] (1991) 689-691.
- [138] A. Padel, C. De Novion, "Constantes elastiques des carbures, nitrures et oxydes d'uranium et de plutonium," J. Nucl. Mater. 33 (1969) 40-51.
- [139] The SGTE Pure Substance and Solution databases, GTT-DATA SERVICES, 1996.
- [140] H. Tagawa, "Phase relations and thermodynamic properties of the uranium-nitrogen system," J. Nucl. Mater. 51[1] (1974) 78-89.
- [141] K. Nakajima, Y. Arai, "Heat capacity of neptunium mononitride," J. Nucl. Sci. Tech. Suppl.-3 (2002) 620-623.
- [142] F.L. Oetting, "The chemical thermodynamic properties of nuclear materials III. Plutonium mononitride," J. Chem. Thermodyn. 10[10] (1978) 941-948.
- [143] A.G. Alekseev, "高融点化合物物性便覧," 日ソ通信社, 和歌山, 1994.
- [144] V. Maurice, J.L. Boutard, D. Abbe, "Low temperature specific heat of rocksalt thorium

compounds," J. de Physique, Colloque C4 (1979) 140–141.

[145] S.L. Hayes, J.K. Thomas, K.L. Peddicord, "Material property correlations for uranium mononitride; III Transport properties," J. Nucl. Mater. 171 (1990) 289–299.

[146] S.B. Ross, M.S. El-Genk, R.B. Matthews, "Thermal conductivity correlation for uranium nitride fuel between 10 and 1923 K," J. Nucl. Mater. 151 (1988) 313–317.

[147] Y. Arai, Y. Suzuki, T. Iwai, T. Ohmichi, "Dependence of the thermal conductivity of (U,Pu)N on porosity and plutonium content," J. Nucl. Mater. 195[1–2] (1992) 37–43.

[148] Y. Arai, Y. Okamoto, Y. Suzuki, "Thermal conductivity of neptunium mononitride from 740 to 1600 K," J. Nucl. Mater. 211[3] (1994) 248–250.

[149] T. Nishi, M. Takano, A. Itoh, M. Akabori, K. Minato, M. Kizaki, "Thermal diffusivity of Americium mononitride from 373 to 1473 K," J. Nucl. Mater. 355 (2006) 114–118.

[150] V. Basini, J.P. Ottaviani, J.C. Risharud, M. Streit, F. Ingold, "Experimental assessment of thermophysical properties of (Pu,Zr)N," J. Nucl. Mater. 344[1–3] (2005) 186–190.

[151] T. Vasilos, W.D. Kingery, "Thermal conductivity. XI. Conductivity of some refractory carbides and nitrides," J. Am. Ceram. Soc. 37 (1954) 409–414.

[152] J.C. Hedge, J.W. Kopeck, C. Kostenko, J.L. Lang, "Thermal properties of refractory alloys," U.S. At. Energy Comm. ASD-TDR-63-597 (1963) 128.

[153] D.S. Neel, C.D. Pears, S. Oglesby Jr., "The thermal properties of thirteen solid materials to 5000° F or their destruction temperatures," NASA Doc. N62-12987 (1962) 216.

[154] H. Serizawa, Y. Arai, K. Nakajima, "The estimation of the heat capacity of NpO₂," J. Chem. Thermodyn. 33 (2001) 615.

[155] J.A. Fahey, R.P. Turcotte, T.D. Chikalla, "Thermal expansion of the actinide dioxides," Inorg. Nucl. Chem. Lett. 10 (1974) 459.

[156] P. Browning, G.J. Hyland, J. Ralph, "Origin of the specific heat anomaly in solid urania," High Temp.-High Press. 15[2] (1983) 169–178.

[157] Thermodynamic data base for personal computer MALT2, Japan thermal measurement of society, 1992.

[158] J. Ralph, "Specific heat of UO₂, ThO₂, PuO₂ and the mixed oxides (Th_xU_{1-x})O₂ and (Pu_{0.2}U_{0.8})O_{1.97} by enthalpy data analysis," J. Chem. Soc. Faraday Trans. 83 [2] (1987) 1253–1262.

[159] V.A. Arkhipov, E.A. Gutina, V. N. Dobretsov, "Enthalpy and heat capacity of neptunium dioxide in the temperature range of 300–1100 K," Radiokhimiya 16 (1974) 122.

[160] M.A. Mignanelli, R. Thetford, The Second Workshop Proceedings of the International

Conference on Advanced Reactors with Innovative Fuels (ARWIF-2001), Chester, UK, 2001.

- [161] C. Thiriet, R.J.M. Konings, "Chemical thermodynamic representation of AmO_{2-x}," J. Nucl. Mater. 320 (2003) 292-298.
- [162] R.A. Jackson, A.D. Murray, J.H. Harding, C.R.A. Catlow, "The calculation of defect parameters in uranium dioxide," Philos. Mag. A 53(11986) 27-50.
- [163] K. Clausen, W. Hayes, J.E. MacDonald, R. Osborn, M.T. Hutchings, "Observation of oxygen Frenkel disorder in uranium dioxide above 2000 K by use of neutron-scattering techniques," Phys. Rev. Lett. 52[14] (1984) 1253-1241.
- [164] J. Ralph, G.J. Hyland, "Empirical confirmation of a Bredig transition in UO₂," J. Nucl. Mater. 132[1] (1985) 76-79.
- [165] D. L. Hargman, G.A. Reymann, "MATPRO-Version 11: A handbook of materials properties for use in the analysis of light water reactor fuel rod behavior," NUREG/CR-0497, TREE-1280, Rev. 3, 1979.
- [166] J.H. Harding, D.G. Martin, "A recommendation for the thermal conductivity of uranium dioxide," J. Nucl. Mater. 166[3] (1989) 223-226.
- [167] T. Nishi, M. Takano, A. Itoh, M. Akabori, K. Minato, T. Tomita, M. Numata, "Thermal conductivity of neptunium dioxide," Abstract of spring meeting of Atomic Energy Society of Japan, 2007, pp. 558 (L22).
- [168] R.L. Gibby, "Effect of plutonium content on the thermal conductivity of (U, Pu)O₂ solid solutions," J. Nucl. Mater. 38[2] (1971) 163-177.
- [169] S.E. Lemehov, V. Sobolev, P. Van Uffelen, "Modelling thermal conductivity and self-irradiation effects in mixed oxide fuels," J. Nucl. Mater. 320[1-2] (2003) 66-76.
- [170] T. Nishi, M. Takano, A. Itoh, M. Akabori, Y. Arai, K. Minato, M. Numata, "Thermal conductivity of AmO_{2-x}," J. Nucl. Mater. In Press.
- [171] J.K. Fink, "Thermophysical properties of uranium dioxide," J. Nucl. Mater. 279 (2000) 1-18.
- [172] C.A. Olsen, G.A. Reymann, "MATPRO-Version09, A handbook of Materials properties of use in the analysis of light water reactor fuel rod behavior," USNRC TREE NUREG-1005, 1976.
- [173] Y. Philippneau, "Thermal conductivity of (U, Pu)O_{2-x} mixed oxide fuel," J. Nucl. Mater. 188 (1992) 194.
- [174] K. Morimoto, M. Kato, A. Komeno, M. Kashimura, M. Ogasawara, "Thermal conductivity of (U_{0.7-x}Np_xPu_{0.3})O₂," Abstract of fall meeting of Atomic Energy Society of Japan, 2007, pp. 934 (P53).

- [175] K. Morimoto, M. Kato, A. Komeno, M. Kashimura, T. Abe, M. Ogasawara, T. Sunaoshi, H. Uno, T. Tamura, "Thermal physical properties of MOX fuels II – Thermal diffusivity measurement of (U,Pu,Am)O_{2.00} –, " Abstract of fall meeting of Atomic Energy Society of Japan, 2006, pp. 401 (H24).
- [176] R.D. Shannon, "Revised effective ionic radii and systematic studies of interatomic distances in halides and chalcogenides," *Acta Crystallogr. A* 32(5) (1976) 751–767.

Table 3.7 Calculation condition

System	Particles	Nitrides: 512 particles (N ³⁻ :256, An ³⁺ :256, 4 × 4 × 4 cluster)			
	Structure	Oxides: 768 ((O ²⁻ :512, An ⁴⁺ :256, 4 × 4 × 4 cluster))			
	Boundary	NaCl type (nitrides) or CaF ₂ type (oxides)			
Control	Temperature	Scaling	Scaling	Nose	Nose
	Pressure	Scaling	Scaling	No control	Andersen
	Time per a step	2f sec	2f sec	2f sec	2f sec
Number of steps		20,000	20,000	40,000	1,000,000

Table 3.8 Interatomic potential function parameters for ThN, UN, NpN, PuN, AmN and ZrN

Ions	z	a	b	c	Ion pair	D _{ij}	β _{ij}	r _{ij} [*]
N ³⁻	-1.450	1.797	0.080	20				
Th ³⁺	1.450	1.358	0.080	2.5	Th ³⁺ -N ³⁻	9.10	2.50	2.500
U ³⁺	1.450	1.228	0.080	0	U ³⁺ -N ³⁻	7.00	1.25	2.364
Np ³⁺	1.450	1.248	0.080	1.0	Np ³⁺ -N ³⁻	9.56	1.25	2.364
Pu ³⁺	1.450	1.196	0.080	0	Pu ³⁺ -N ³⁻	0.10	0.80	2.453
Am ³⁺	1.450	1.2705	0.080	25	Am ³⁺ -N ³⁻	0.70	2.20	2.510
Zr ³⁺	1.450	1.019	0.080	2.35	Zr ³⁺ -N ³⁻	6.50	4.51	2.27

Table 3.9 Interatomic potential function parameters for UO₂, NpO₂, PuO₂ and AmO₂

Ions	z	a	b	c	Ion pair	D _{ij}	β _{ij}	r _{ij} [*]
O ²⁻	-1.2	1.926	0.106	20				
U ⁴⁺	+2.4	1.659	0.106	0	U ⁴⁺ -O ²⁻	18	1.25	2.369
Np ⁴⁺	+2.4	1.190	0.080	0	Np ⁴⁺ -O ²⁻	10.5	3.27	2.339
Pu ⁴⁺	+2.4	1.229	0.080	0	Pu ⁴⁺ -O ²⁻	13	1.56	2.339
Am ⁴⁺	+2.4	1.052	0.080	0	Am ⁴⁺ -O ²⁻	8.6	3.98	2.339

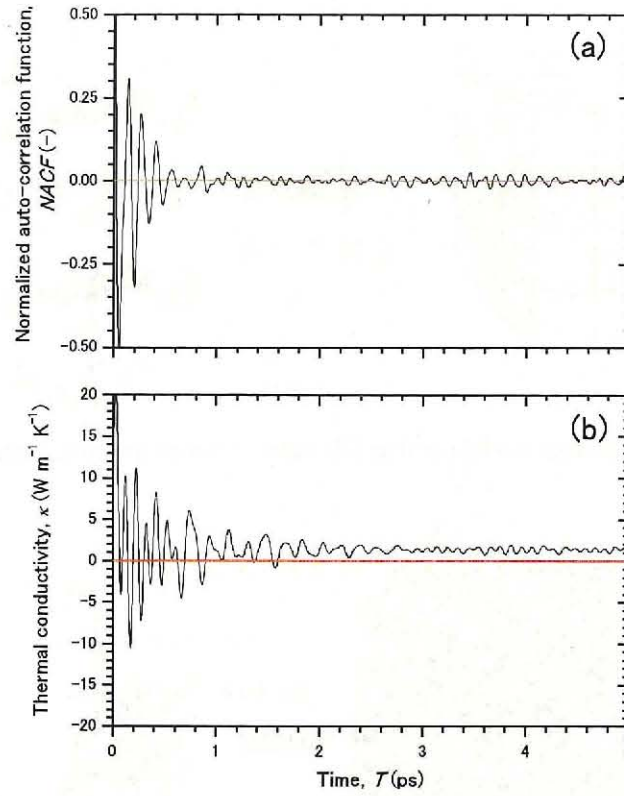


Fig. 3.61 (a) normalized auto-correlation function (b) thermal conductivity as function of time of UO₂ at 1300 K

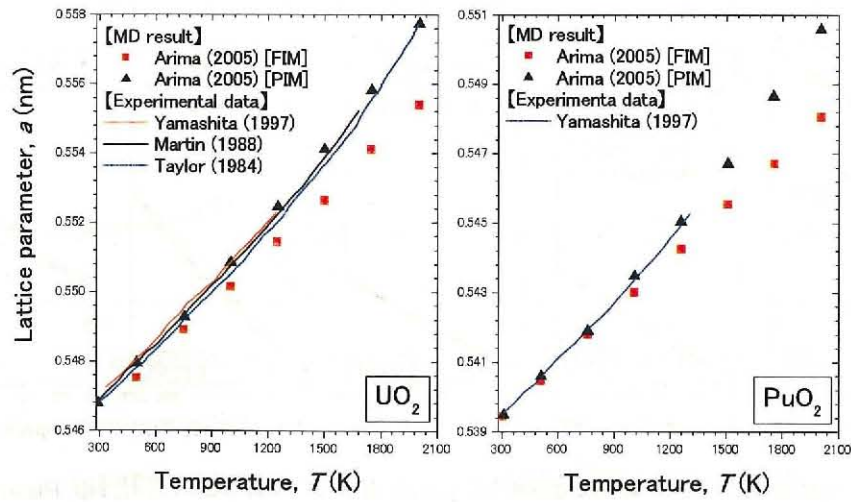


Fig. 3.62 Temperature dependence of lattice parameter referred of UO₂ and PuO₂ from Ref 15, together with the experimental data [16-18]

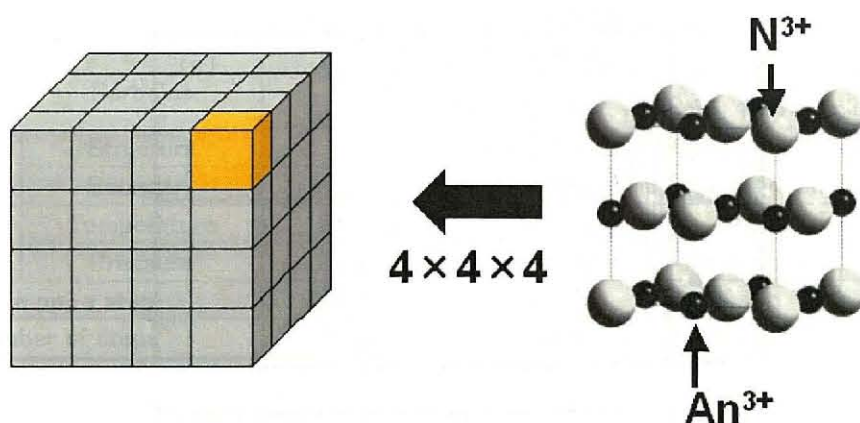


Fig. 3.63 Cluster model used in MD calculation of the metal nitrides

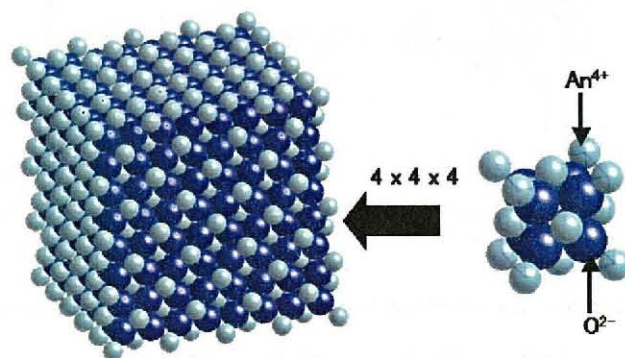


Fig. 3.64 Cluster model used in MD calculation of the metal dioxides

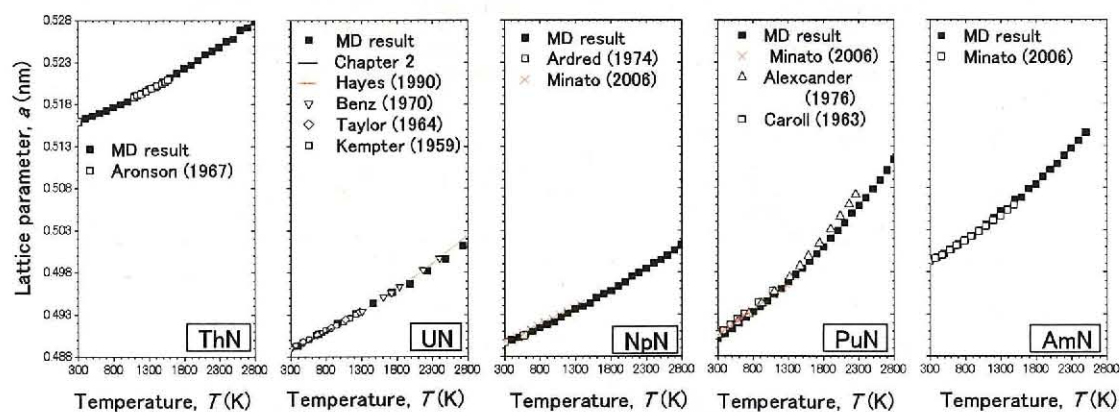


Fig. 3.65 Temperature dependence of lattice parameter of AnN (An: Th, U, Np, Pu and Am), together with the experimental data [22–26, 30–33, Chapter 2]

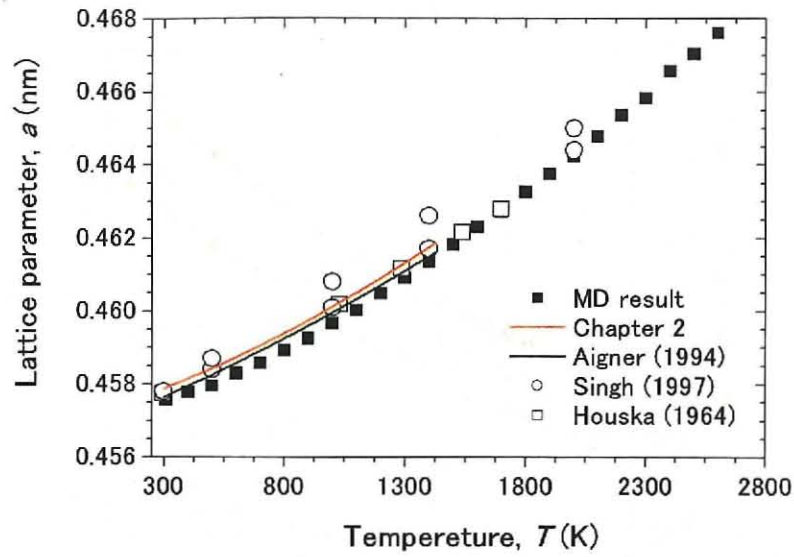


Fig. 3.66 Temperature dependence of the lattice parameter of ZrN, together with the experimental data [27, 34, 35, Chapter 2]

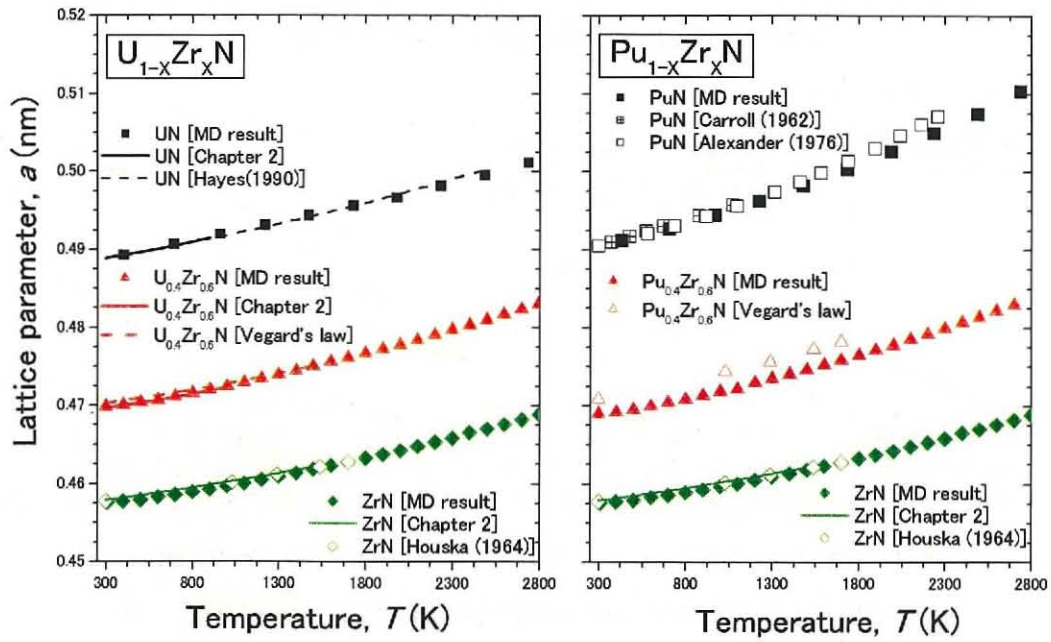


Fig. 3.67 Temperature dependence of lattice parameter $U_{1-x}Zr_xN$ and $Pu_{1-x}Zr_xN$ ($x=0, 0.6, 1$), together with the experimental data [23, 25, 27, 33, Chapter 2]

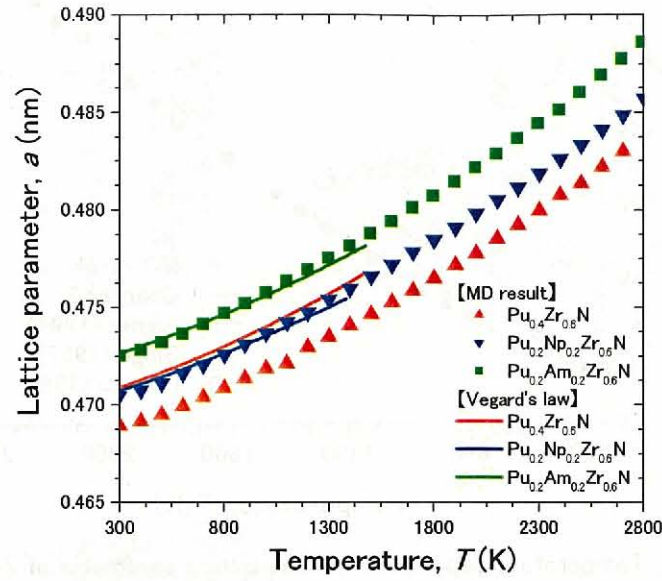


Fig. 3.68 Temperature dependence of lattice parameter of $\text{Pu}_{0.4-x}\text{Np}_x\text{Zr}_{0.6}\text{N}$ and $\text{Pu}_{0.4-x}\text{Am}_x\text{Zr}_{0.6}\text{N}$ ($x=0, 0.2$)

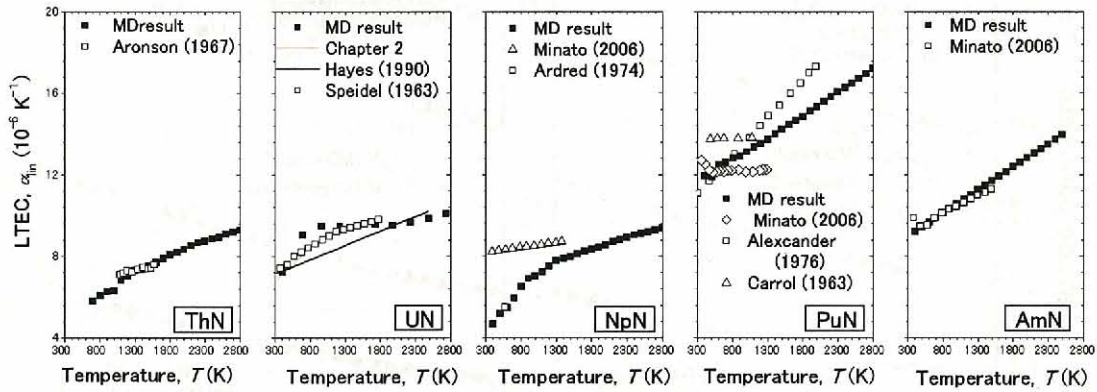


Fig. 3.69 Temperature dependence of LTEC of AnN (An: Th, U, Np, Pu and Am), together with the experimental data [22–26, 33, 36, Chapter 2]

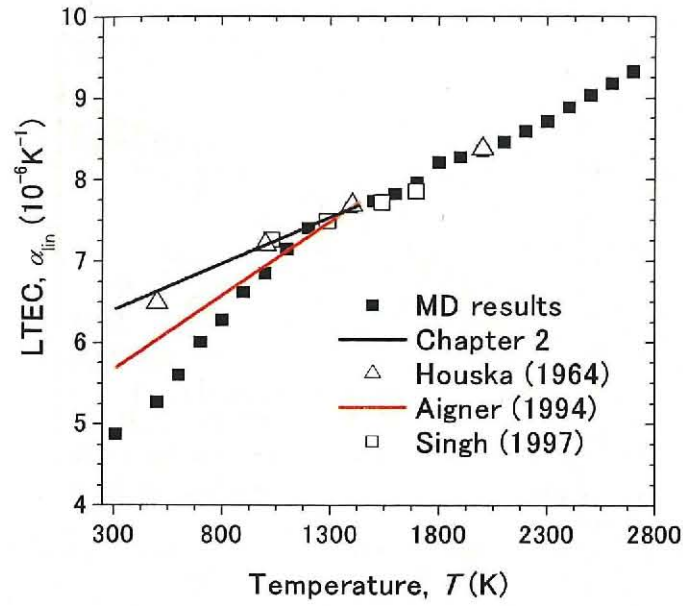


Fig. 3.70 Temperature dependence of LTEC of ZrN, together with the experimental data [22, 28, 29, Chapter 2].

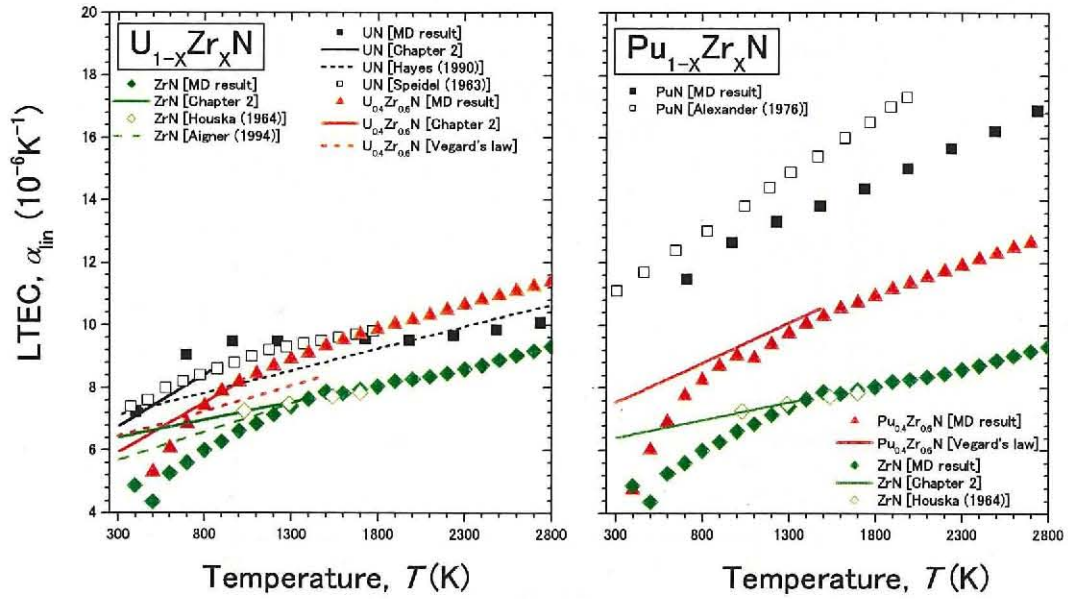


Fig. 3.71 Temperature dependences of LTEC of U_{1-x}Zr_xN and Pu_{1-x}Zr_xN (X=0, 0.6, 1), together with the experimental data [23, 27, 33, 34, 36 Chapter 2]

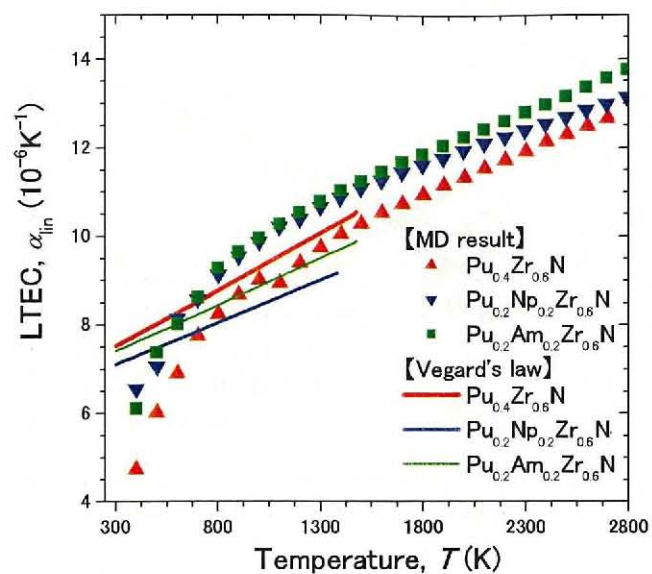


Fig. 3.72 Temperature dependences of LTEC of $Pu_{0.4-x}Np_xZr_{0.6}N$ and $Pu_{0.4-x}Am_xZr_{0.6}N$ ($X=0, 0.2$)

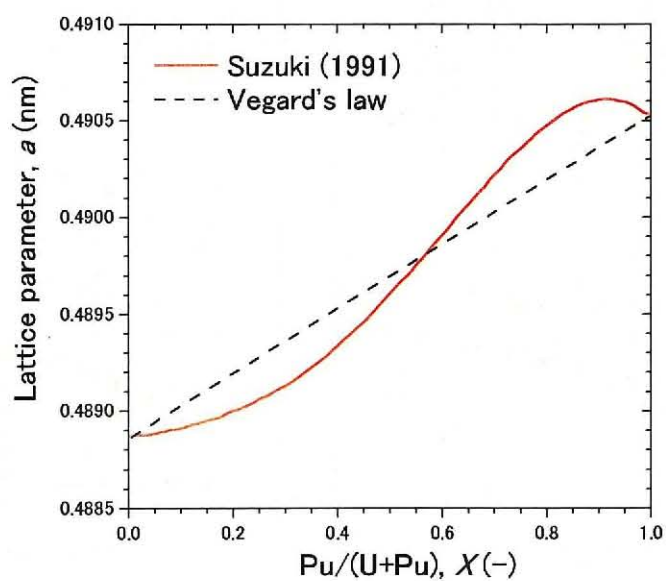


Fig. 3.73 Pu content dependence of lattice parameter of $U_{1-x}Pu_xN$ referred from Ref. 39

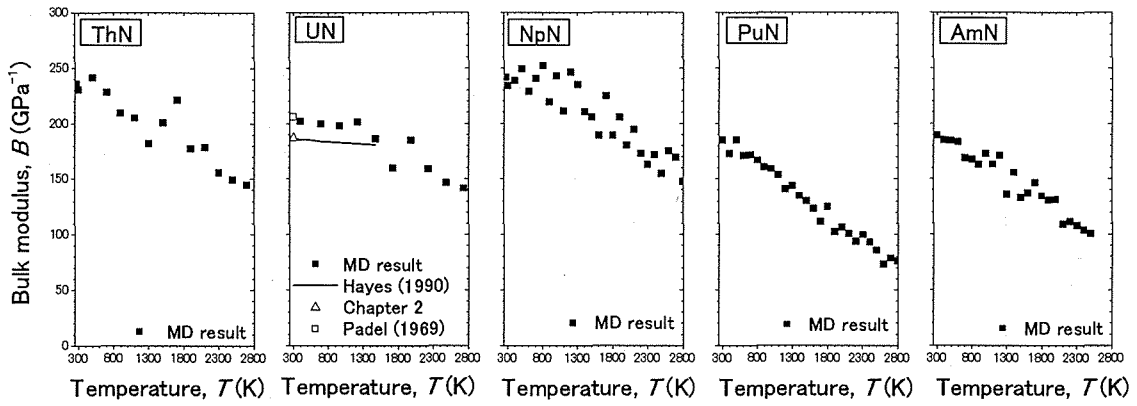


Fig. 3.74 Temperature dependence of bulk modulus of AnN (An: Th, U, Np, Pu and Am), together with the experimental data [28, 40, Chapter 2]

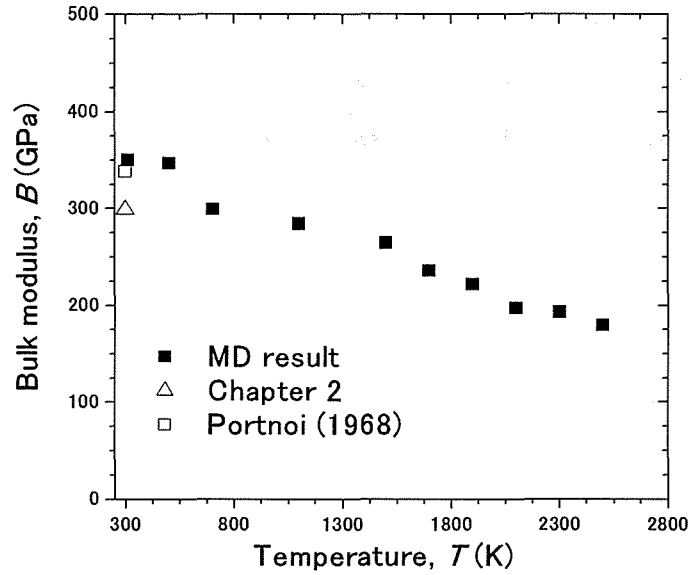


Fig. 3.75 Temperature dependence of bulk modulus of ZrN, together with the experimental data [29, Chapter 2]

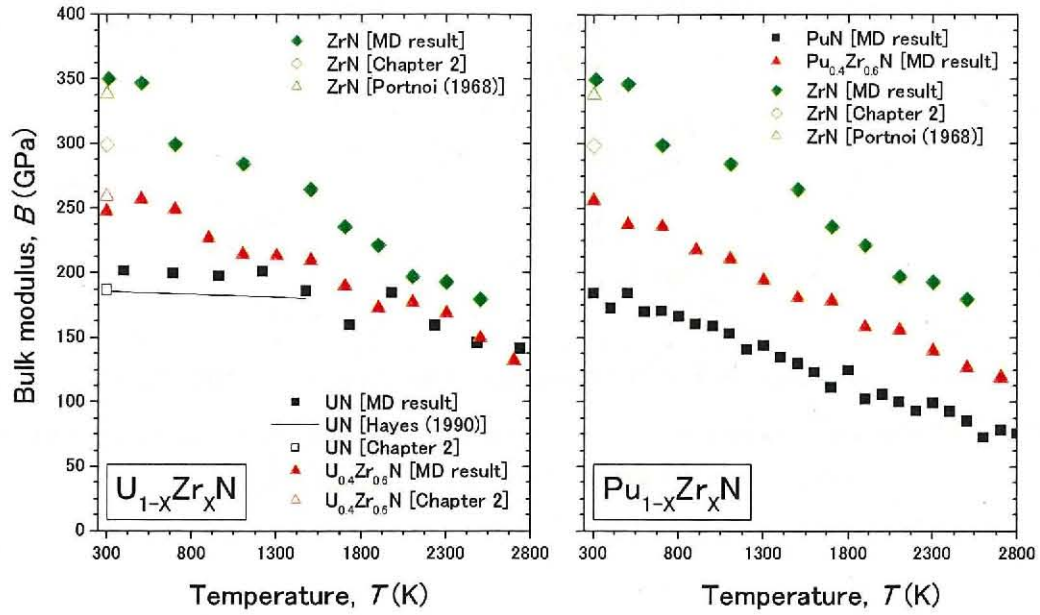


Fig. 3.76 Temperature dependence of bulk modulus of $U_xZr_{1-x}N$ and $Pu_xZr_{1-x}N$ ($x=0, 0.4, 1$), together with the experimental data of [28, 29, Chapter 2]

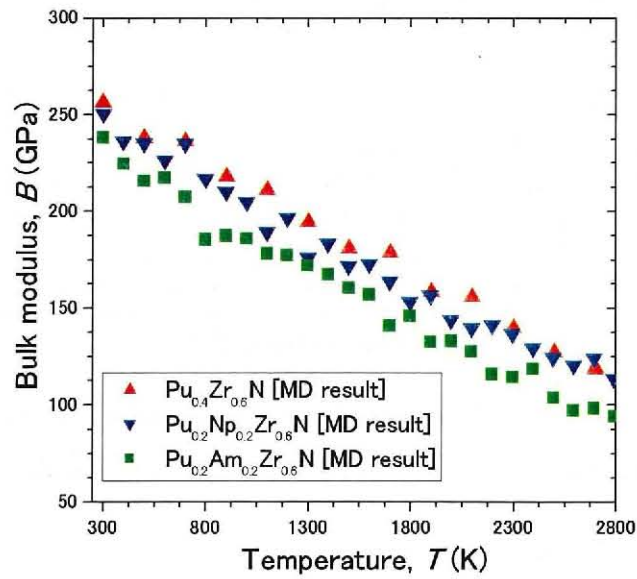


Fig. 3.77 Temperature dependence of bulk modulus of $Pu_{0.4-x}Np_xZr_{0.6}N$ and $Pu_{0.4-x}Am_xZr_{0.6}N$ ($x=0, 0.2$)

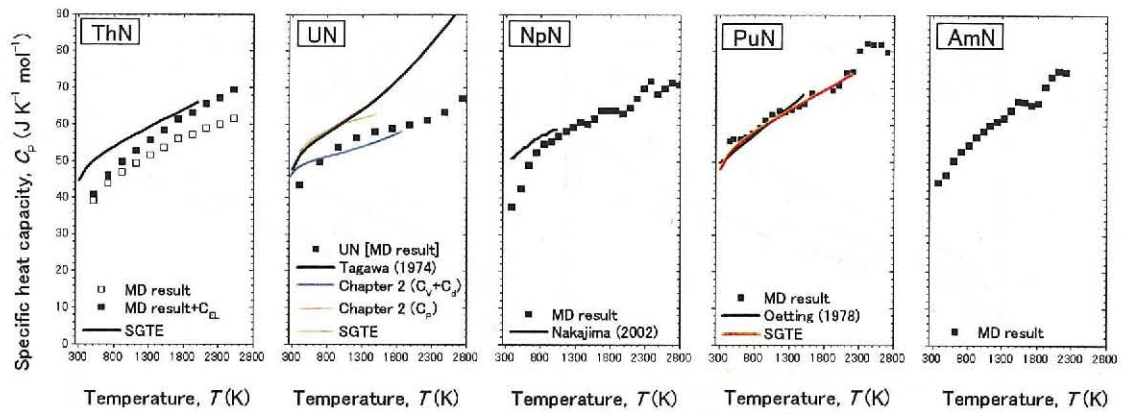


Fig. 3.78 Temperature dependence of specific heat capacity of AnN (An: Th, U, Np and Pu), together with the experimental data [41–44, Chapter 2]

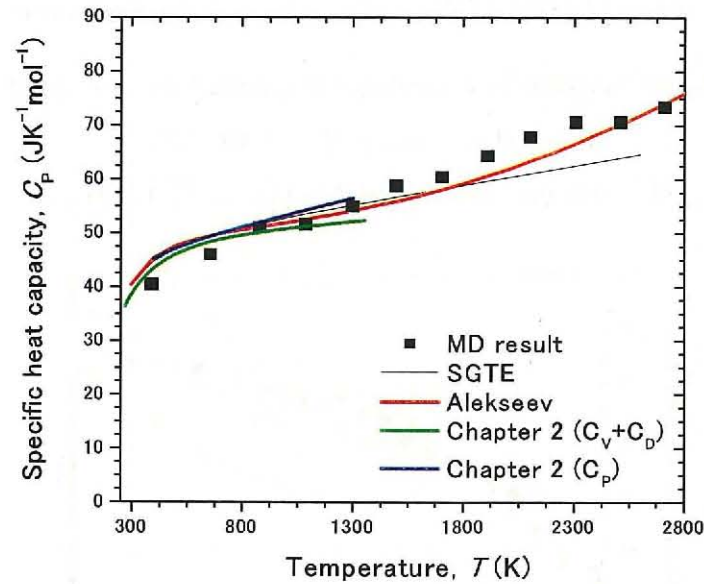


Fig. 3.79 Temperature dependence of specific heat capacity of ZrN, together with the experimental data [41, 45, Chapter 2]

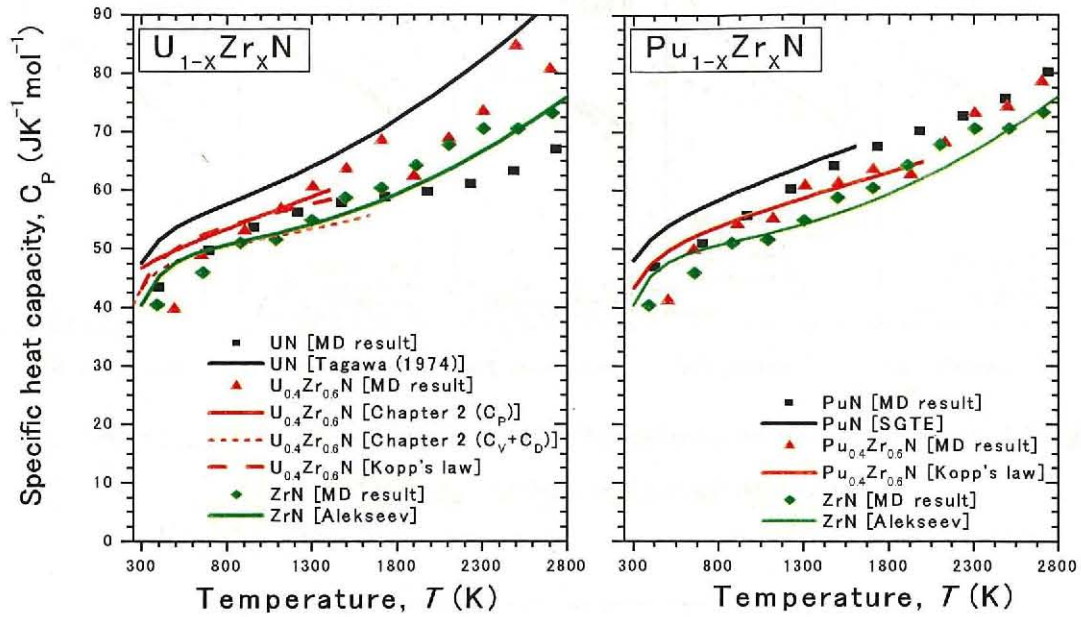


Fig. 3.80 Temperature dependence of specific heat capacity of $U_xZr_{1-x}N$ and $Pu_xZr_{1-x}N$ ($X=0, 0.6, 1.0$), together with the experimental data [41, 42, 45, Chapter 2]

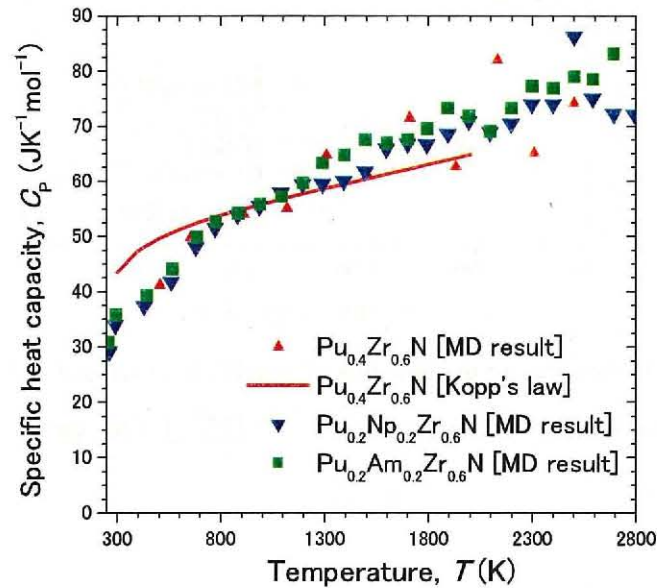


Fig. 3.81 Temperature dependence of specific heat capacity of $Pu_{0.4-x}Np_xZr_{0.6}N$ and $Pu_{0.4-x}Am_xZr_{0.6}N$ ($X=0, 0.2$)

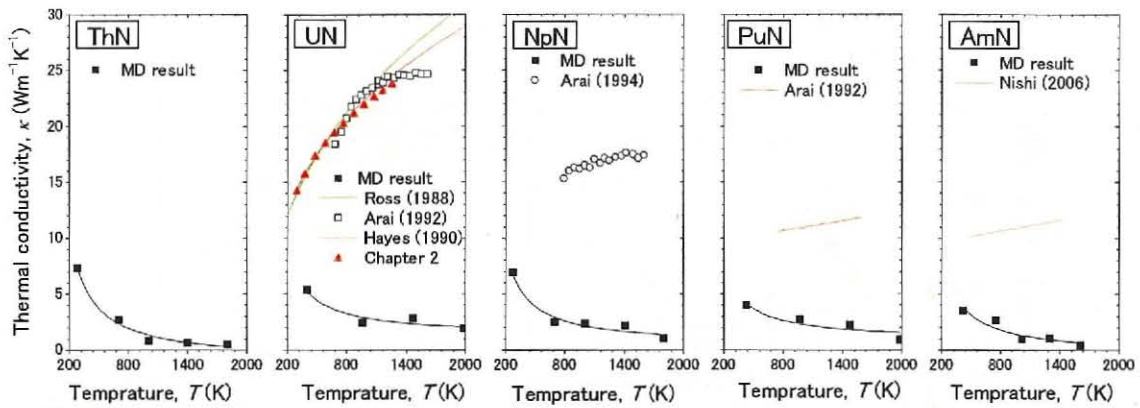


Fig. 3.82 Temperature dependence of thermal conductivity of AnN (An: Th, U, Np and Pu), together with the experimental data [47–51, Chapter 2]

The black lines represent the fitting results by 1/T law.

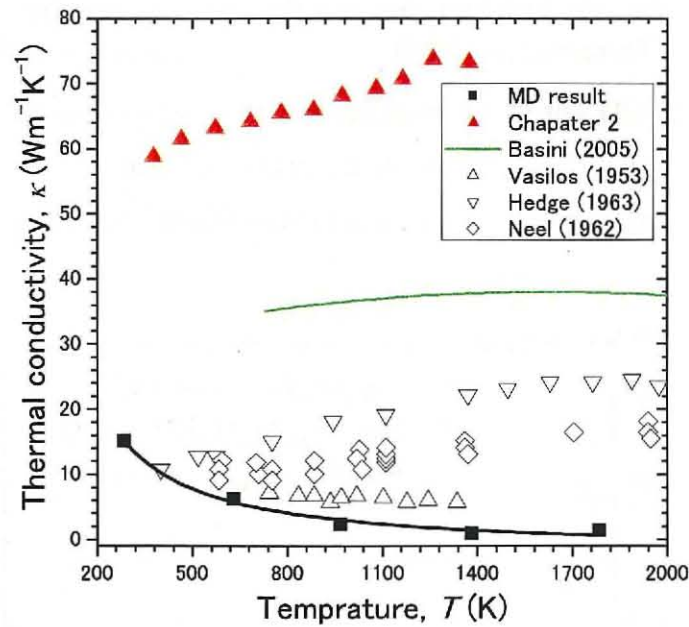


Fig. 3.83 Temperature dependence of thermal conductivity of ZrN together with the experimental data [52–55, Chapter 2]

The black lines represent the fitting results by 1/T law.

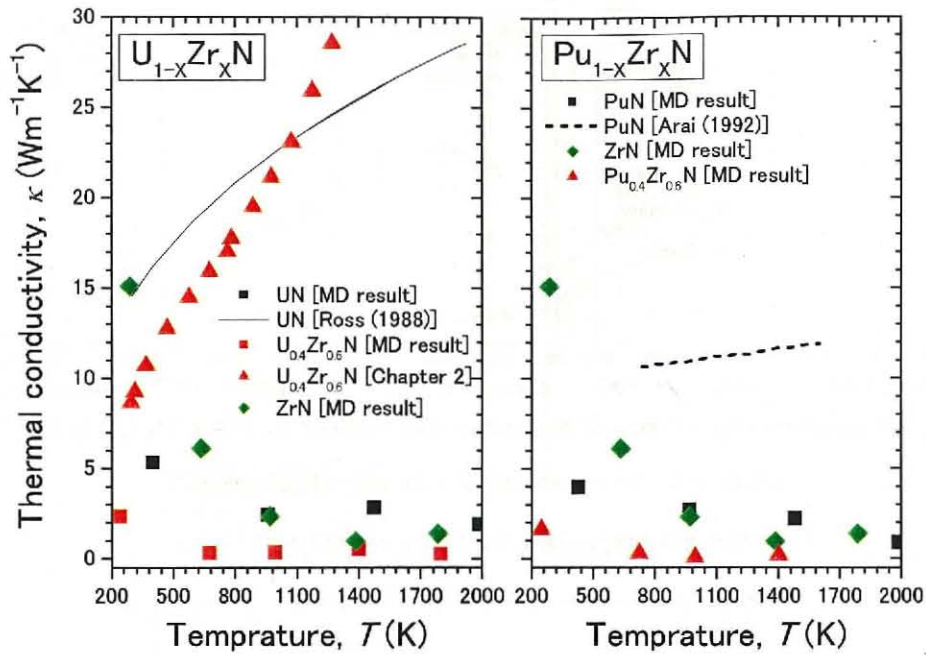


Fig. 3.84 Temperature dependence of thermal conductivity of $U_xZr_{1-x}N$ and $Pu_xZr_{1-x}N$ (X=0, 0.6, 1.0), together with the experimental data [48, 49, Chapter 2]

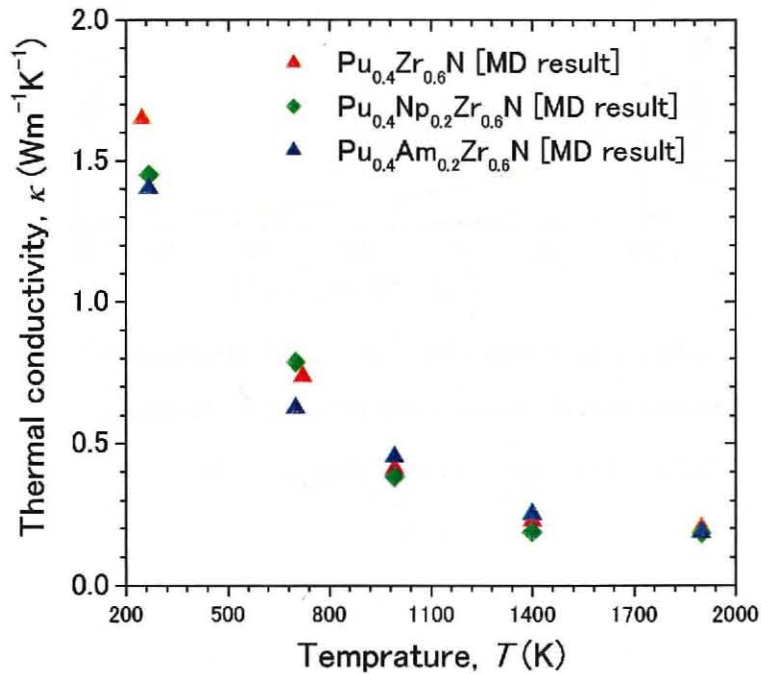


Fig. 3.85 Temperature dependence of thermal conductivity of $Pu_{0.4-x}Np_{0.2}Zr_{0.6}N$ and $Pu_{0.4-x}Am_{0.2}Zr_{0.6}N$ (X=0, 0.2)

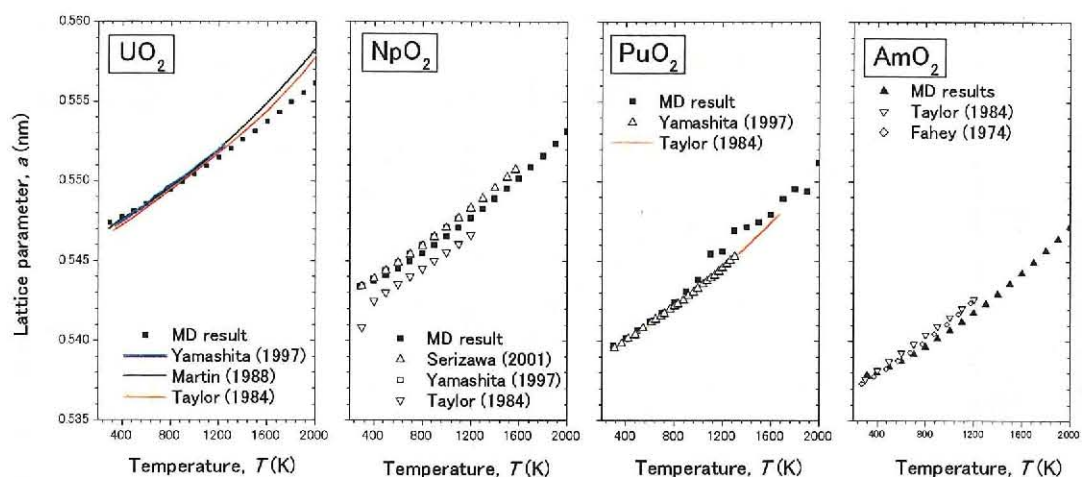


Fig. 3.86 Temperature dependence of lattice parameter of AnO₂ (An: U, Np, Pu and Am), together with the experimental data of [16–18, 56, 57]

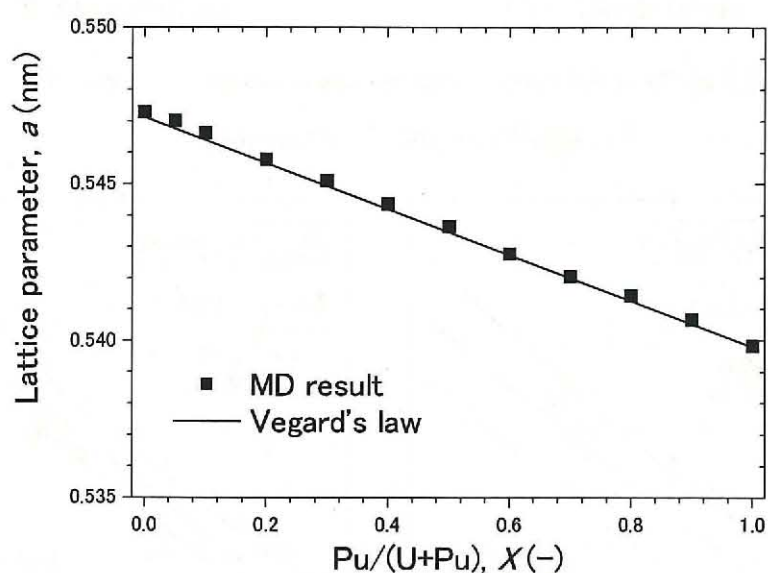


Fig. 3.87 Pu content dependence of lattice parameter at room temperature of $\text{U}_{1-x}\text{Pu}_x\text{O}_2$

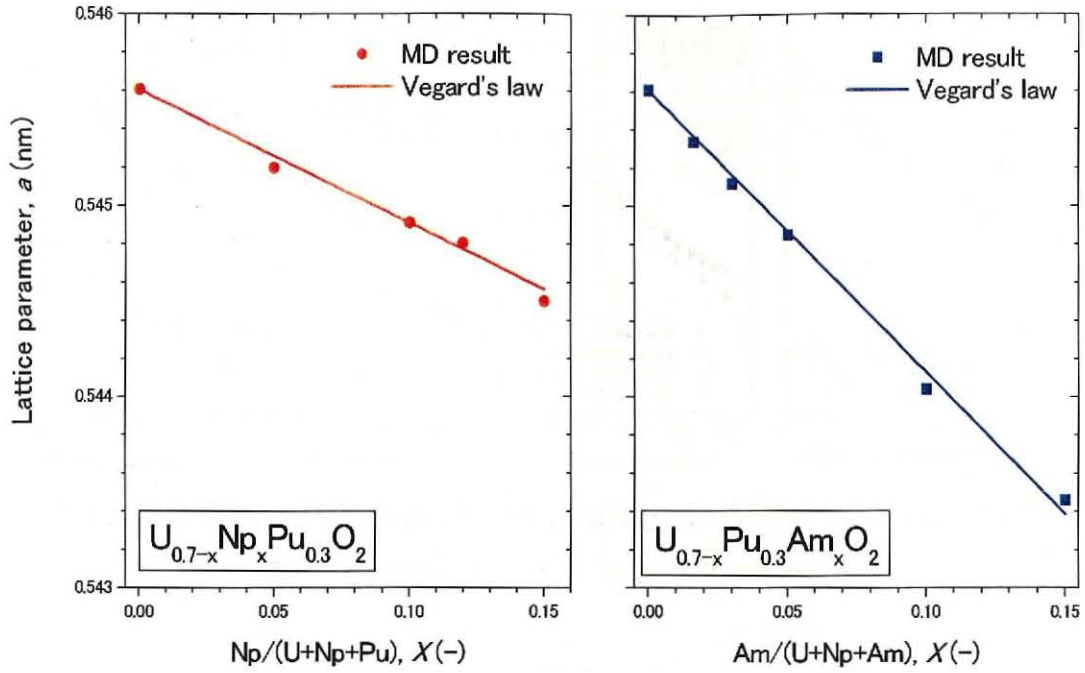


Fig. 3.88 Np or Am content dependence of lattice parameter of

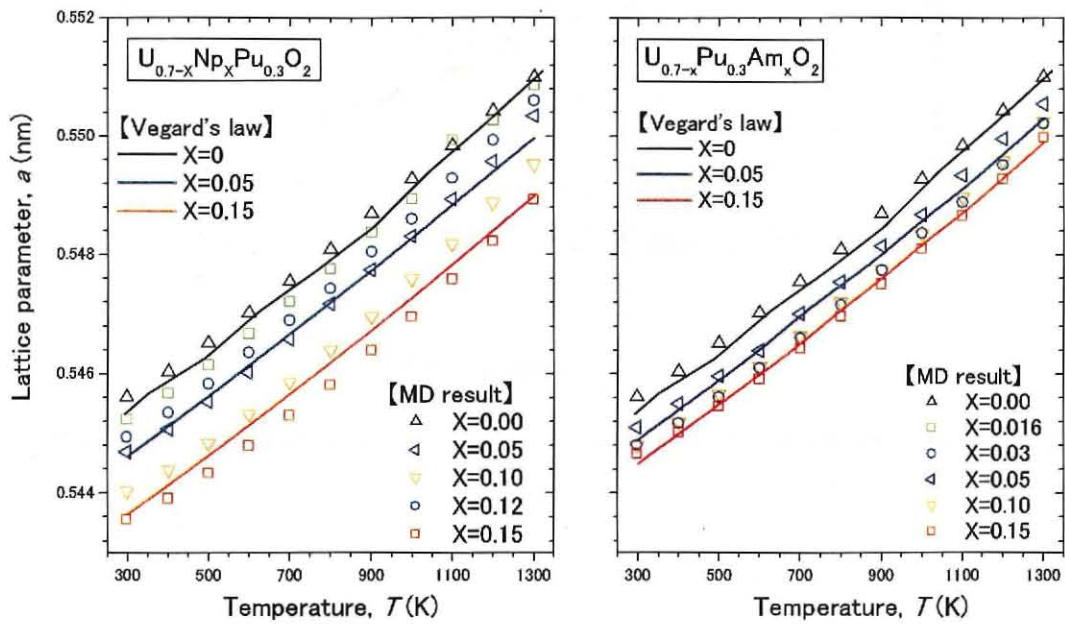
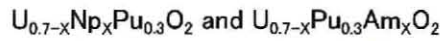
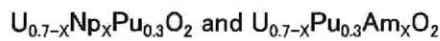


Fig. 3.89 Temperature dependence of lattice parameter of



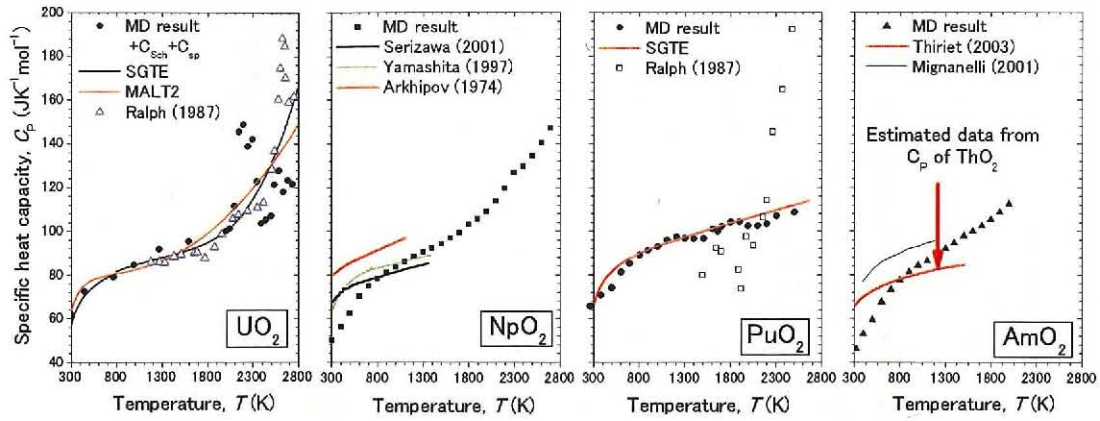


Fig. 3.90 Temperature dependence of specific heat capacity of AnO₂ (An: U, Np, Pu and Am), together with the experimental data [17, 41, 56, 59–62] and estimated data [63]

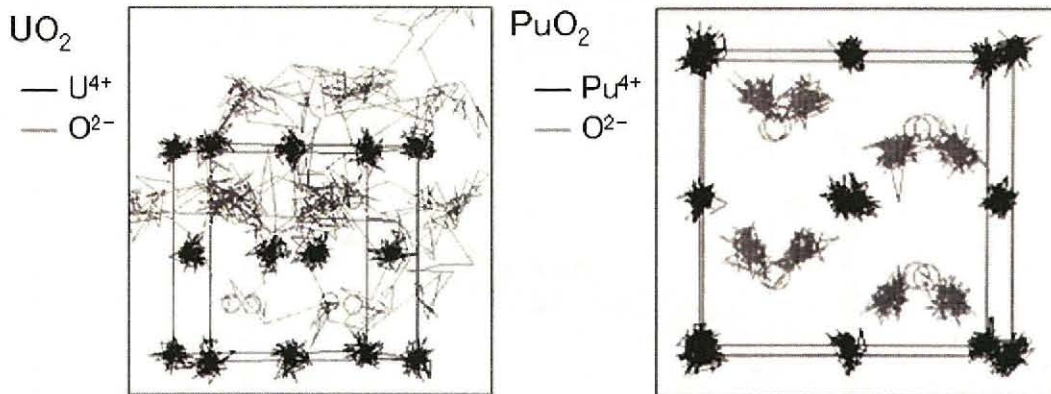


Fig. 3.91 Motion track of each ion at 2500 K

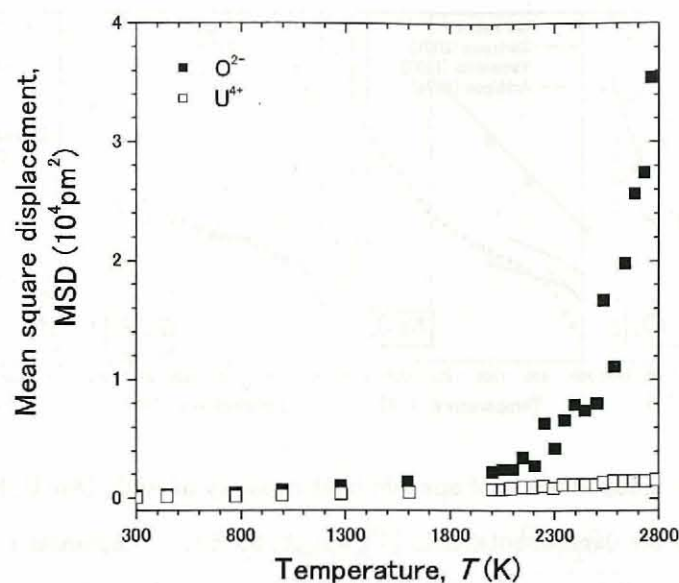


Fig. 3.92 Temperature dependence of mean square displacement of U⁴⁺ and O²⁻ in UO₂ crystal

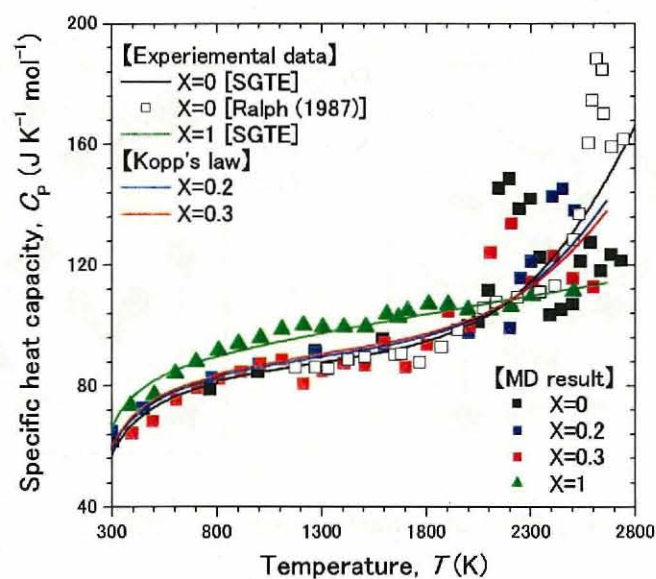


Fig. 3.93 Temperature dependence of specific heat capacity of U_{1-x}Pu_xO₂ (X=0, 0.2, 0.3, 1.0), together with the literature data [41, 60]

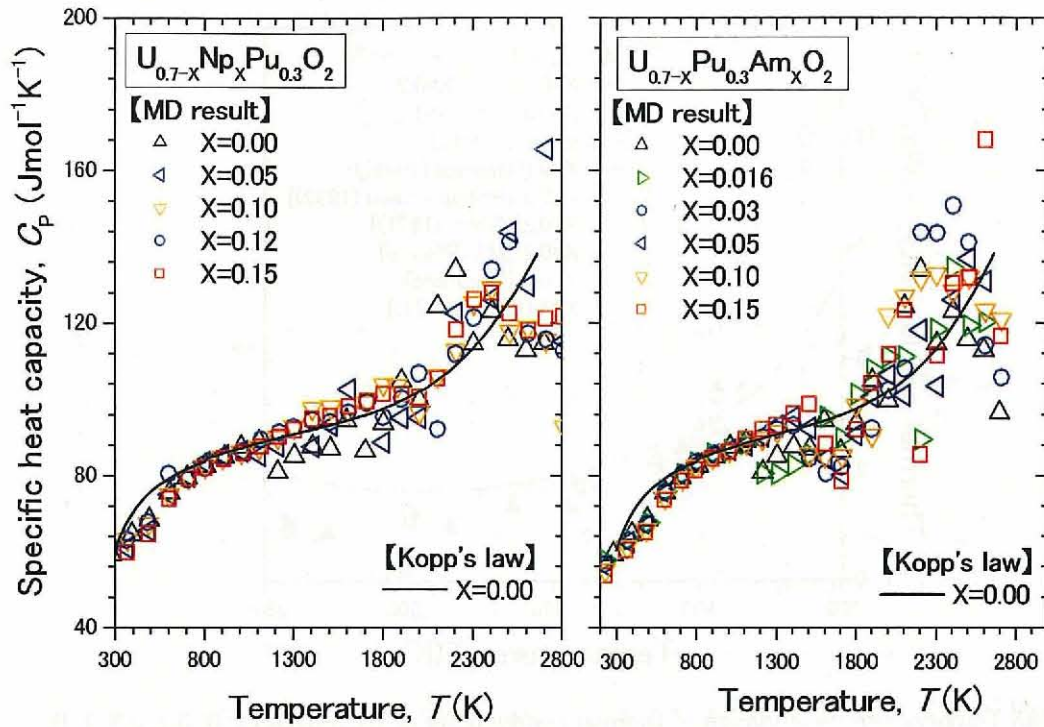


Fig. 3.94 Temperature dependence of specific heat capacity of

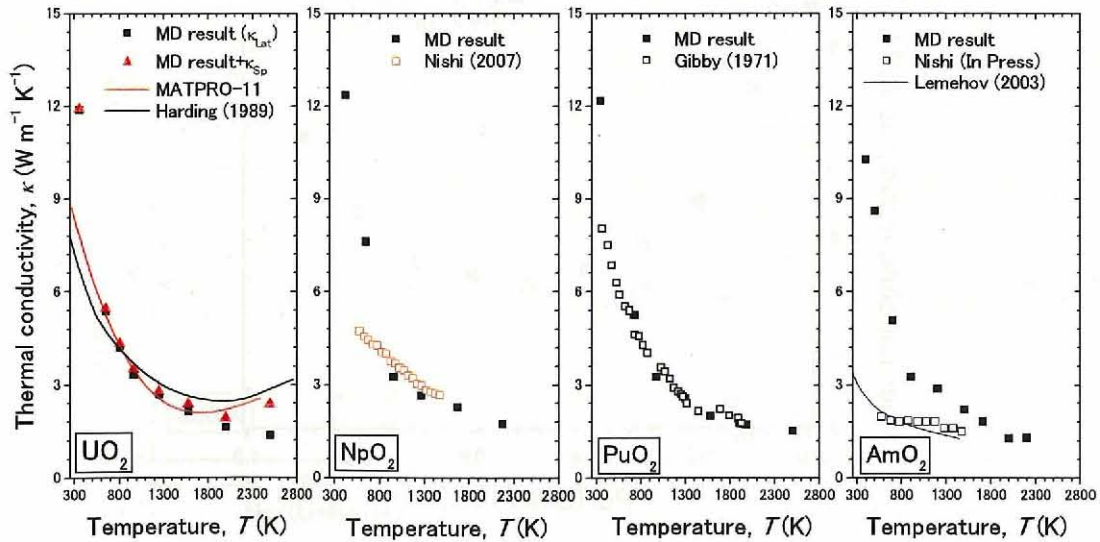
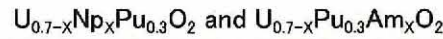


Fig. 3.95 Temperature dependence of thermal conductivity of AnO₂ (An: U, Np, Pu and Am), together with the experimental data [67–72]

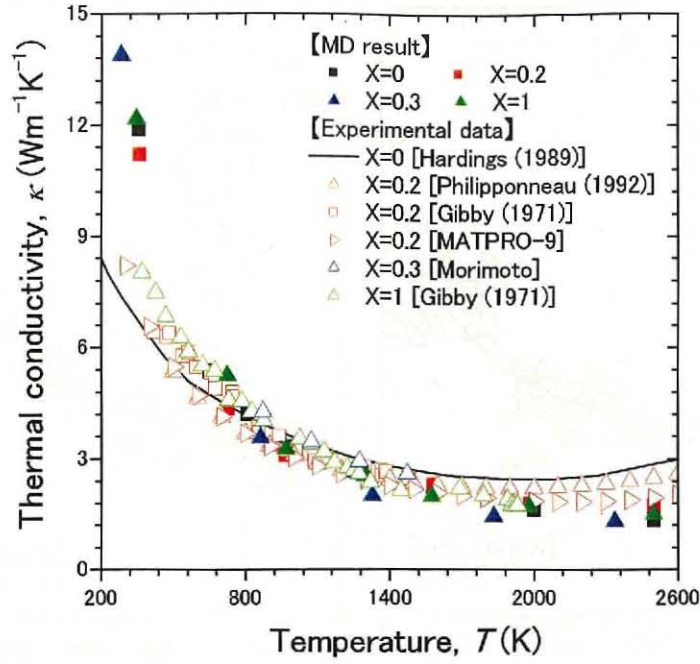


Fig. 3.96 Temperature dependence of thermal conductivity of $U_{1-x}Pu_xO_2$ (X=0, 0.2, 0.3, 1.0), together with the experimental data [68, 70, 74–76]

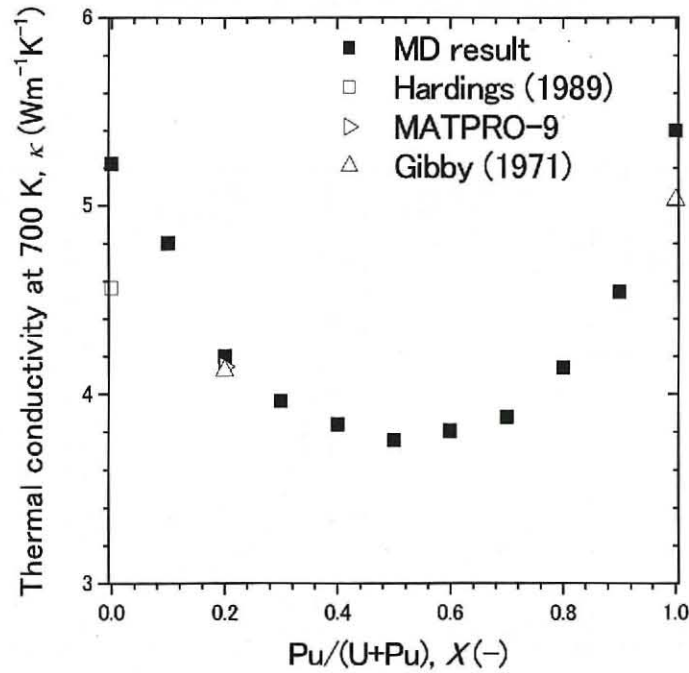


Fig. 3.97 Pu content dependence of thermal conductivity of $U_{1-x}Pu_xO_2$ at 700K together with the experimental data [68, 70, 74]

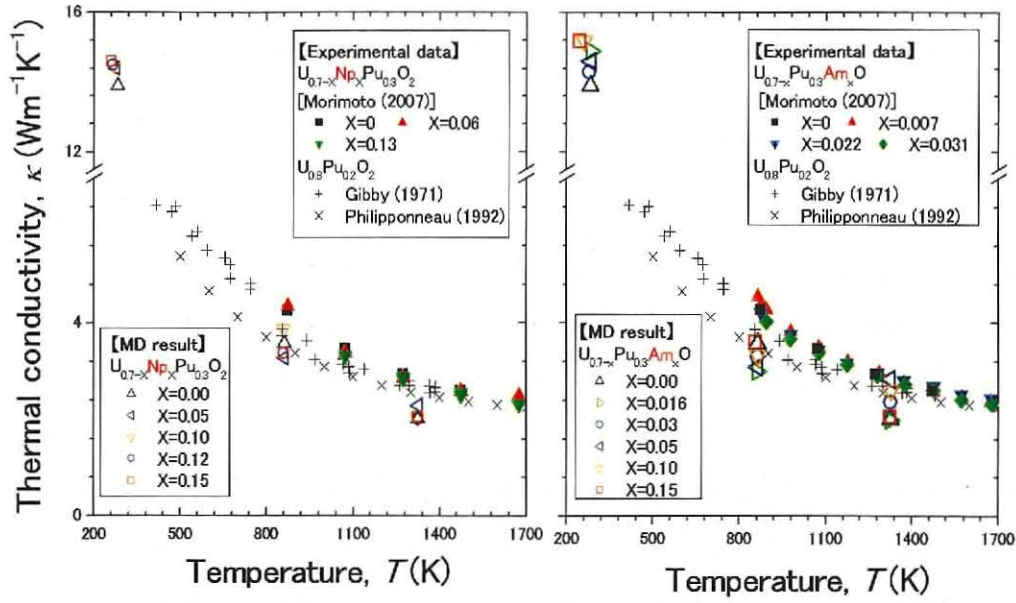


Fig. 3.98 Temperature dependence of thermal conductivity of $U_{0.7-x}Np_xPu_{0.3}O_2$ and $U_{0.7-x}Pu_{0.3}Am_xO_2$, with the experimental data [70, 75–77]

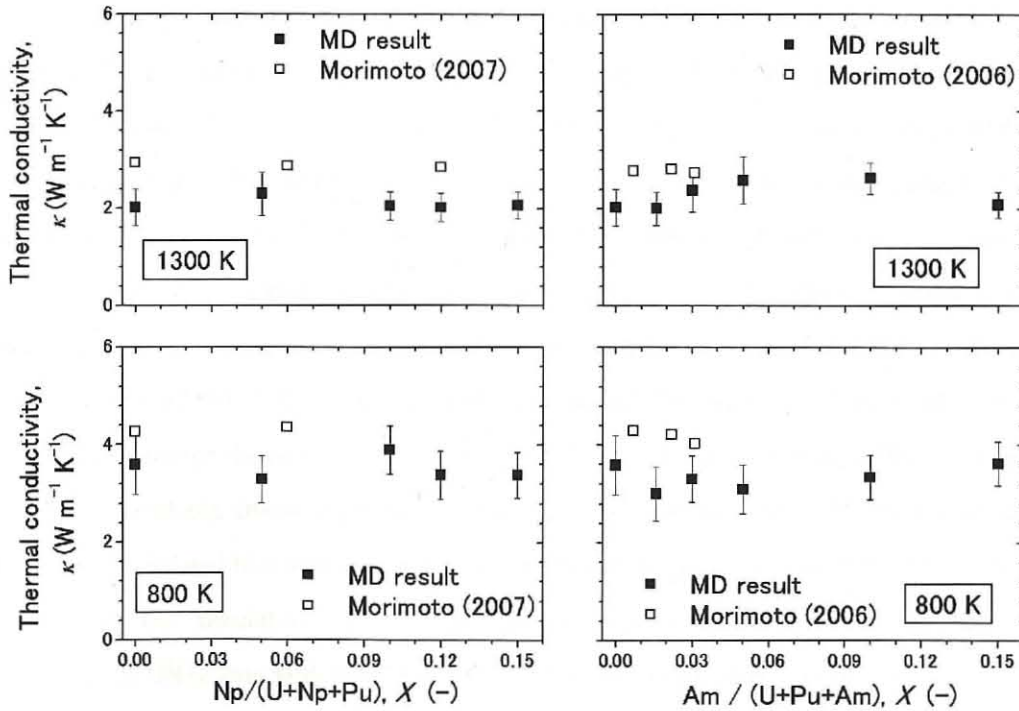


Fig. 3.99 Np or Am content dependence of thermal conductivity of $U_{0.7-x}Np_xPu_{0.3}O_2$ and $U_{0.7-x}Pu_{0.3}Am_xO_2$, with the experimental data [76, 77]

Chapter 4: FPs (Pd, Mo and Nd) effects on thermophysical properties of simulated high-burnup nitride fuels

4-1 Background

As the author described at the previous chapter, the nitride fuel is a good candidate of the advanced fuel for FBR [1] and ADS [2-3]. It is necessary to evaluate the thermophysical properties of nitride fuels under high-burnup because the thermophysical properties of the high-burnup nitride fuel are not almost known. However, the researches of the actual irradiated fuels take a lot of time and cost. So, when the thermophysical properties of the high-burnup oxide fuels are evaluated, the simulated high-burnup fuel (SIMFUEL) [4-10] has been often used. SIMFUEL is UO_2 pellet including the non-radioactive isotope elements of FP elements such as ^{129}Nd and ^{14}C . The thermophysical properties of the non-radioactive isotope element are almost same to those of the radioactive isotope element. Therefore, we can predict the thermophysical properties of the high-burnup fuels from those of SIMFUEL. However, in case of the nitride fuels, the SIMFUEL studies have not been performed. Whereat, the author applied the concept of SIMFUEL to the nitride fuel. In the present study, the author chose Pd, Nd and Mo as the typical FP elements. The reasons that Pd, Nd and Mo were chosen are described in the following sentences. The solid FP elements in the nitride fuels can be roughly divided into three groups: first is the element which forms the intermetallic compounds with uranium element and precipitates, second is the element which resolve in the nitride fuel, and third is the element which precipitates as the pure metal and doesn't react with uranium element. Pd, Nd and Mo are the typical elements of the first, second and third group of FP elements, respectively. It is the reason that the author chose Pd, Nd and Mo. In addition, the author prepared UN pellet including Nd and Mo, to evaluate the interaction between the FP elements. The additive amount of each FP element (Pd, Nd and Mo) was determined to be the burnup of 50 and 200 GWd/tU. Briefly, the eight kinds of the simulated high-burnup fuels were prepared in the present study, which components are $\text{UN}+2.2\text{mol}\%\text{Pd}$, $\text{UN}+11.7\text{mol}\%\text{Pd}$, $\text{UN}+2.7\text{mol}\%\text{Nd}$, $\text{UN}+12.2\text{mol}\%\text{Nd}$, $\text{UN}+1.6\text{mol}\%\text{Mo}$, $\text{UN}+7.1\text{mol}\%\text{Mo}$, $\text{U}_{0.973}\text{Nd}_{0.027}\text{N}+1.5\text{mol}\%\text{Mo}$, $\text{U}_{0.891}\text{Nd}_{0.119}\text{N}+7.1\text{mol}\%\text{Mo}$. Pd reacted with U and precipitates in the grain boundary as UPd_3 , Nd formed the solid solution with UN, and Mo precipitated as metal Mo. The details would be explained later. There are a lot of data of the thermophysical properties of Mo. On the other hand, there are few data of UPd_3 and NdN . In

addition to the SIMFUEL, the author experimentally evaluated the mechanical properties of UPd_3 and thermophysical properties of NdN . In case of pure NdN , the thermal properties were also evaluated by MD calculation because it is difficult to handle NdN due to the extremely low oxidation resistivity. In case of UPd_3 , only XRD pattern and mechanical properties were evaluated in the present study because the thermal properties and elastic properties of UPd_3 were evaluated in our previous work [11, 12].

4-2 Experimental procedure

4-2-1 Sample preparation

Simulated high-burnup fuel

Basically, the preparation methods of $\text{UN}+\text{Pd}$, $(\text{U,Nd})\text{N}$, $\text{UN}+\text{Mo}$ and $(\text{U,Nd})\text{N}+\text{Mo}$ pellets are fundamentally same to that of UN . In case of $\text{UN}+\text{Pd}$, $\text{UN}+\text{Mo}$ and $(\text{U,Nd})\text{N}+\text{Mo}$ pellets, Pd (99.95%) and Mo (99.9%) powders were added to UN powder after the conversion from UO_2 to UN . In case of $(\text{U,Nd})\text{N}$ and $(\text{U,Nd})\text{N}+\text{Mo}$ pellets, Nd_2O_3 powder was added to UO_2 powder before the conversion. After the conversion process, the solid solution $((\text{U,Nd})\text{N})$ was obtained. The small different points in the preparation conditions of UN , $\text{UN}+\text{Pd}$, $\text{UN}+\text{NdN}$, $\text{UN}+\text{Mo}$ and $(\text{U,Nd})\text{N}+\text{Mo}$ pellets are summarized in Table 4.1. By these methods, the eight samples, which are $\text{UN}+2.2\text{mol}\%\text{Pd}$, $\text{UN}+11.7\text{mol}\%\text{Pd}$, $\text{U}_{0.973}\text{Nd}_{0.027}\text{N}$, $\text{U}_{0.878}\text{Nd}_{0.122}\text{N}$, $\text{UN}+1.6\text{mol}\%\text{Mo}$, $\text{UN}+7.1\text{mol}\%\text{Mo}$, $\text{U}_{0.974}\text{Nd}_{0.026}\text{N}+1.5\text{mol}\%\text{Mo}$ and $\text{U}_{0.881}\text{Nd}_{0.119}\text{N}+7.1\text{mol}\%\text{Mo}$, were prepared. In the present study, $\text{UN}+2.2\text{mol}\%\text{Pd}$, $\text{UN}+11.7\text{mol}\%\text{Pd}$, $\text{U}_{0.973}\text{Nd}_{0.027}\text{N}$, $\text{U}_{0.878}\text{Nd}_{0.122}\text{N}$, $\text{UN}+1.6\text{mol}\%\text{Mo}$, $\text{UN}+7.1\text{mol}\%\text{Mo}$, $\text{U}_{0.974}\text{Nd}_{0.026}\text{N}+1.5\text{mol}\%\text{Mo}$ and $\text{U}_{0.881}\text{Nd}_{0.119}\text{N}+7.1\text{mol}\%\text{Mo}$ are named as $\text{UN}+\text{Pd-L}$, $\text{UN}+\text{Pd-H}$, $(\text{U,Nd})\text{N-L}$, $(\text{U,Nd})\text{N-H}$, $\text{UN}+\text{Mo-L}$, $\text{UN}+\text{Mo-H}$, $(\text{U,Nd})\text{N}+\text{Mo-L}$ and $(\text{U,Nd})\text{N}+\text{Mo-H}$. The simulated burnup of the pellets with low FP content ($\text{UN}+\text{Pd-L}$, $(\text{U,Nd})\text{N-L}$, $\text{UN}+\text{Mo-L}$ and $(\text{U,Nd})\text{N}+\text{Mo-L}$) is 50 GWd/tU and that of the pellets with high FP content ($\text{UN}+\text{Pd-H}$, $(\text{U,Nd})\text{N-H}$, $\text{UN}+\text{Mo-H}$ and $(\text{U,Nd})\text{N}+\text{Mo-H}$) is 200 GWd/tU.

NdN

The oxidation resistivity of NdN is very low. So, in case of the atmospheric pressureless sintering, most of NdN pellets were oxidized because the sintering time was long. The high-density and high-purity samples of NdN could be obtained by the SPS because the sintering time of SPS (≈ 5 min) is vastly shorter than that of the atmospheric pressure sintering ($>10\text{hr}$).

NdN (99.9%) powder was supplied from Furuuchi Chemical Co. Ltd. In the SPS process,

the author used two graphite dices ($T2\text{mm} \times \phi 20\text{mm}$ and $T4\text{mm} \times \phi 10\text{mm}$) to minimize the time of the polish and cut of the bulk sample. The disk samples ($T2\text{mm} \times \phi 20$) of NdN were used in the measurements of the thermal properties such as the thermal expansion, specific heat capacity and thermal diffusivity, and the column samples ($T4\text{mm} \times \phi 10\text{mm}$) were used to evaluate the elastic properties and hardness.

UPd₃

The button-shaped sample of UPd₃ was prepared by high vacuum induction melting. The purities of starting materials (metal U and Pd) are above 99.9%. The prepared buttons were annealed at 1073 K for 10 hr in a vacuum below 10^{-5} Pa.

4-2-2. Sample characterization and crystallographic, mechanical, electrical and thermal properties

The experimental procedures of polishing, sample characterization, crystallographic properties, mechanical properties, electrical properties and thermal properties used in this chapter were same with those used in Chapter 2.

4-3. Results and discussion

4-3-1. Crystallographic properties

Sample preparation

From the carbothermic reduction and atmospheric pressure sintering, the high-density bulk samples (>85%T.D.) of UN, UN+Pd, (U,Nd)N, UN+Mo and (U,Nd)N+Mo could be obtained. Their impurity oxygen, carbon content and N/M ratio were summarized in Table 4.2. From Table 4.2, it was found that there are no sample including the high impurity oxygen and carbon, compared with UN pellet, in the different way of $U_{0.4}Zr_{0.6}N$ pellet. The highest density of NdN samples prepared by the SPS was 88.2 %T.D. In Chapter 2, the maximum SPS temperature of TiN and ZrN was 2073 K. On the other hand, that of NdN was 1873. It was because the powder sample was melted in the SPS process due to the diremption of the nitrogen from NdN from about 1923 K. The sample characteristics of NdN were summarized in Table 4.3. The density of UPd₃ prepared by high vacuum induction melting method was 95.0 %T.D.

In the same way of $U_{0.4}Zr_{0.6}N$ and UN+60mol%TiN, the author assumed that the coefficients (β) of the porosity dependences of the thermophysical properties of UN+Pd, (U,Nd)N, UN+Mo and (U,Nd)N+Mo are same to that of UN. The β of NdN was determined in the present study by evaluation of the thermophysical properties of the sample with various porosities in the

same way of ZrN and TiN.

XRD

XRD patterns of UN, UN+Pd-L, UN+Pd-H, (U,Nd)N-L, (U,Nd)N-H, UN+Mo-L, UN+Mo-H, (U,Nd)N+Mo-L, (U,Nd)N+Mo-H, NdN and UPd₃ are shown in Fig 4.1-4.4, together with the literature data [11, 13-18].

In Fig. 4.1, most of peaks of UN, UN+Pd-L and UN+Pd-H agreed with the JCPDS data of UN [13] and the experimental data of UPd₃ agreed with the literature data of UPd₃ [11]. In UN+Pd-L and UN+Pd-H, the peaks of the precipitation were observed at about 43°. By Uno (1997) [19] and Akabori (1998) [20], Pd reacts with UN and forms UPd₃ under the equilibrium state. So, it is thought that the precipitation in UN+Pd is Pd or UPd₃. Both Pd and UPd₃ have the main peak at about 43° and the other main peak of UPd₃ laps over the peak of UN. Therefore, from Fig. 4.1, we cannot judge what the precipitation is. When the XRD pattern between 60 and 80° is upsized as shown in Fig. 4.5, the third peak of UPd₃ was confirmed and the second peak of Pd could not be confirmed. From these results, it was found that Pd reacts with UN and forms UPd₃. The lattice parameters of UN phase of UN+Pd-L pellet (0.4886nm) and UN+Pd-H pellet (0.4889nm) were well consistent with that of UN pellet (0.4889nm) and that of UPd₃ phase could not be evaluated because the peaks of UPd₃ phase are very unclear and small. From these results, it was found that Pd didn't resolve in UN phase. The lattice parameter of pure UPd₃ were (a=0.5778 nm, c=0.9721 nm).

In Fig. 4.2, (U,Nd)N-L, (U,Nd)N-H and NdN were single phase. By using these XRD patterns, their lattice parameters were estimated and the lattice parameters as NdN content were showed in Fig. 4.6, together with the literature data [13, 16, 21, 22]. Judging from Fig. 4.6, it was found that the lattice parameter of NdN was within the variation of the literature data [16, 21, 22] and those of U_{1-x}Nd_xN followed to Vegard's law. From these results, it was confirmed that NdN resolved in UN.

In Fig. 4.3, most of peaks of UN+Mo-L and UN+Mo-H agreed with the JCPDS data of UN [13]. Except for the peak corresponding to the JCPDS data of UN, the peaks were observed at about 40° and 73° and these peaks are consistent with the JPCDS data of Mo [18]. The lattice parameters of UN phase in UN+Mo-L pellet (=0.4889 nm) and UN+Mo-H pellet (=0.4889nm) were perfectly agreed with that of UN pellet (=0.4889nm). The lattice parameters of Mo phase in UN+Mo-H (=0.3115nm) were roughly consistent with that of the JCPDS data of Mo (=0.3147 nm) [18]. From these results, it was confirmed that UN didn't react with Mo and pure metal Mo

precipitated in UN phase.

From these results, it is predicted that NdN resolves and Mo precipitate as the pure metal in (U,Nd)N+Mo pellets. Following this prediction, in Fig. 4.4, the peaks of (U,Nd)N and Mo were observed. The lattice parameters of (U,Nd)N phase in (U,Nd)N+Mo-L pellet ($=0.4897$ nm) and (U,Nd)+Mo-H pellet ($=0.4910$ nm) were well consistent with those of (U,Nd)N-L ($=0.4896$ nm) and (U,Nd)N-H ($=0.4911$ nm), and that of Mo phase in (U,Nd)N+Mo-H ($=0.3105$ nm) was roughly consistent with the JCPDS data of Mo [18] ($=0.3147$ nm). The lattice parameters obtained in the present study were summarized in Table 4.2 and 4.3.

Surface observation and MSA (Minimum Solid Area)

In the LSM, SEM and EDX analysis, the segregations of particular elements and precipitation could not be observed in case of UN, (U,Nd)N-L, (U,Nd)N-H, NdN and UPd₃. In case of the other samples, the precipitations were clearly observed as shown in Fig. 4.7-9. In case of UN+Pd, Pd concentrated along the grain boundary of UN. The Pd/U ratio at the precipitation was about 3.0. In case of UN+Mo and (U,Nd)N+Mo pellets, Mo precipitated as the sphere particle, and U and Nd didn't exist the particle of Mo.

By the LSM observation, the MSA of UN+Pd, (U,Nd)N, UN+Mo and (U,Nd)N+Mo were evaluated. Their MSA were almost consistent with Eq. 2.21, which represents the porosity dependences of the MSA of UN, U_{0.4}Zr_{0.6}N, UN+TiN. Therefore, the author assumed that the porosity dependences of the thermophysical properties of UN+Pd, (U,Nd)N, UN+Mo and (U,Nd)N+Mo equal to those of UN.

From the AFM observation, the arithmetic average surface roughness of each sample was summarized in Table 4.2. Their values were lower than 4 nm and adequately lower than the indentation depth (>50 nm).

Crystallographic properties

The grain size and misorientation angle of UN, UN+Pd-L, UN+Pd-H, (U,Nd)N-L, (U,Nd)N-H, UN+Mo-L, UN+Mo-H, (U,Nd)N+Mo-L and (U,Nd)N+Mo-H obtained from the EBSP analysis are summarized in Table 4.2. The grain size of UN, (U,Nd)N-L, (U,Nd)N-H, UN+Mo-L, UN+Mo-H, (U,Nd)N+Mo-L and (U,Nd)N+Mo-H indicated the similar value with each other. So, it was found that the addition of Nd and Mo don't almost influence the sintering properties of the nitride fuel. On the other hand, the grain sizes of UN+Pd-L and UN+Pd-H were about four times of that of UN. It is well known that Pd is the excellent sintering aids because Pd plays as a role of the catalyst to decrease the surface energy of the matrix grain [23]. So, it was thought that the

grain in UN+Pd becomes to be large due to the sintering aids effect of Pd. By the same reason, the average misorientation angles of UN+Pd-L and UN+Pd-H were lower than those of other samples.

Fig. 4.10–13 show the SEM image, IQ map, CD map of UN+Pd-L, UN+Pd-H, UN+Mo-H, (U,Nd)N+Mo-H. As shown Fig. 4.10 and 4.11, UPd₃ phases in UN+Pd pellet orientated for the direction from (10 $\bar{1}0$) to (10 $\bar{1}1$). The author performed the EBSP measurement for some points of UN+Pd-L and UN+Pd-H. In all cases, the orientation of UPd₃ phase could be observed. This orientation of UPd₃ phase would influence various thermophysical properties. On the other hand, the orientation of Mo phase in UN+Mo and (U,Nd)N+Mo could not be observed as shown in Fig. 4.12 and 4.13.

4-3-2 Mechanical properties

Elastic properties

The elastic properties of all pellets at macroscale were obtained by the ultrasonic pulse echo method, and the elastic properties of the matrix (UN, (U,Nd)N) and precipitation (Mo, UPd₃) were evaluated by the indentation test. In the same way of Fig. 2.26, the Young's moduli of the simulated high-burnup nitride fuels obtained from the indentation test took the constant value at the low depth and decreased with increasing the depth at the high depth. In case of NdN, the indentation test could not be performed due to the low oxidation resistivity of NdN because the indentation test is performed in air and the measurement time is long.

Fig. 4.14 shows the porosity dependences of Young's modulus of UN, UN+Pd-L, UN+Pd, (U,Nd)N, NdN, UN+Mo and (U,Nd)N+Mo obtained from the ultrasonic pulse echo method, together with the literature data [11, 24–29]. Young's modulus of UN+Pd-L, UN+Pd, (U,Nd)N, UN+Mo and (U,Nd)N+Mo at $P=0$ were estimated from Fig. 4.14 using the same correction factor of the porosity dependence of UN (Eq. 2.25). On the other hand, Young's modulus of NdN at $P=0$ were evaluated from the data of the samples with the various porosities as the following equation;

$$\text{NdN: } E_p (\text{GPa}) = 261 \exp(-3.90P) \quad (0 < P < 0.16), \quad (4.107)$$

The Young's modulus of NdN at $P=0$ was 261 GPa and very similar to that of UN (262 GPa). The estimated Young's modulus at $P=0$ of the simulated high-burnup nitride fuels and NdN were summarized in Table. 4.4–4.8.

Fig. 4.15–4.17 shows Young's modulus as the function of UPd₃, NdN or Mo content, with the literature data [11, 23, 28]. These figures include the data estimated from Fan's equation (Eq.

2.30) [29] and Hashin equation (Eq. 2.42 and 2.43) [30]. Young's modulus of UPd_3 obtained from the indentation test ($=168 \pm 10$ GPa) was well consistent with the literature data (Yamanaka (1998) [11]) (161 GPa), which was evaluated by the ultrasonic pulse echo method. The Young's modulus of UN obtained from the indentation tests agreed with those of UN phases in UN+Pd-L and UN+Pd-H. On the other hand, those of UPd_3 phase in UN+Pd-L and UN+Pd-H were higher than that of pure UPd_3 . In the indentation test, the load-displacement curves shows only the elastic deformation in the loading process when the indentation load is extremely low. When the load-displacement curve at loading process changes from the elastic deformation to the elastic-plastic deformation, the load-displacement curve shows the discontinuous curves. This phenomenon is called "pop-in". By Setoyama (2005) [32], the Young's modulus before pop-in depends on the crystal orientation, but the Young's modulus after pop-in doesn't almost depend on the crystal direction. In the present study, the author confirmed that the loading processes of all indentation tests were the elastic-plastic deformation. By Chen (2001) [33], the crystal direction dependence of the Young's modulus of the hexagonal crystal structure is generally small. The author described that UPd_3 phase in UN+Pd orientates for the face from $(10\bar{1}0)$ to $(10\bar{1}1)$ in 4.3.1. Judging from the reports of Setoyama (2005) [29] and Chen (2001) [30], the crystal orientation of UPd_3 phase in UN+Pd would not almost influence the Young's modulus. Therefore, the difference between the Young's modulus of UPd_3 phase in UN+Pd and pure UPd_3 was probably resulted from the strain-hardening, which is occurred from the formation of the composite. On the other hand, Young's moduli of Mo phases in UN+Mo and (U,Nd)N+Mo pellets agreed with that of pure Mo [29].

In Fig. 4.15, the Young's moduli of UN+Pd-L and UN+Pd-H obtained from the ultrasonic pulse echo method was consistent with that estimated from Fan's equation using Young's modulus of UN [Chapter 2] and UPd_3 [11]. In Fig. 4.16, the Young's moduli of (U,Nd)N-L and (U,Nd)N-H obtained from the indentation tests were well consistent with those of the ultrasonic pulse echo method. The Young's modulus of (U,Nd)N-L and (U,Nd)N-H were similar to those of UN and NdN. In Fig. 4.17, the Young's moduli of UN phase and Mo phase in UN+Mo pellets obtained from the indentation tests agreed with those of pure UN and Mo. The results of UN+Mo-L and UN+Mo-H obtained from the ultrasonic pulse echo method were similar to the estimated data from Fan's equation and using Young's modulus of UN [Chapter 2] and Mo [29]. From these results, the interaction between UN phase and Mo phase in UN+Mo pellets is small in the different way of UN+Pd pellets. In case of (U,Nd)N+Mo pellets, the Young's modulus of UN

phase obtained from the indentation tests were close to those of UN and (U,Nd)N pellets and those of Mo phase were similar to those of pure Mo and Mo phase in UN+Mo pellets. From these results, the interaction between Nd and Mo was very small. The influences of Pd, Nd and Mo for Young's modulus of the nitride fuels were very small.

Vickers hardness and fracture toughness

Fig. 4.18 shows Vickers hardness of UN, UN+Pd, UPd₃, (U,Nd)N, NdN, UN+Mo, (U,Nd)N+Mo and Mo, together with the literature data [23, 28, 33–37]. From this figure, the porosity dependence of Vickers hardness of NdN was evaluated by the following equation;

$$\text{NdN: } H_V = 7.5(1 - 3.7P) \quad (0 < P < 0.16). \quad (4.108)$$

Using the data in Fig. 4.18, the Vickers hardness of UN+Pd, (U,Nd)N, UN+Mo and (U,Nd)N+Mo at $P = 0$ were evaluated from the correction factor in Eq. 2.50, which was suggested by Godfrey (1965) [34] and represented the porosity dependences of the Vickers hardness of UN. The Vickers hardness of UN+Pd, (U,Nd)N, UN+Mo, (U,Nd)N+Mo at $P = 0$ and $F = 9.8\text{N}$ were shown as the function of UPd₃, NdN and Mo content in Fig. 4.19. In this figure, the straight lines represent the addition match of UN and UPd₃, NdN or Mo. In case of UN+Pd and UN+Mo, the influence of Pd and Mo could not almost be observed. The reason is probably that UN is predominant for the Vickers hardness of UN+Pd and UN+Mo because the Vickers hardness of Mo and UPd₃ are lower than that of UN and the Vickers hardness means the resistivity of the plastic deformation and the recovery by the surface tensile force. On the other hand, the Vickers hardness of (U,Nd)N increased with increasing the NdN content. The Vickers hardness of (U,Nd)N+Mo-L (4.91 GPa) and (U,Nd)N+Mo-H (5.19 GPa) were similar to those of (U,Nd)N-L (=4.72 GPa) and (U,Nd)N-H (5.29 GPa). From these results, it was found that the interaction between NdN and Mo is vanishingly small.

The fracture toughness of UPd₃ could not be measured by the IF method because the crack didn't generate at the vertex of the Vickers impression. Fig. 4.20 shows UPd₃, NdN or Mo content dependences of the fracture toughness of UN+Pd, (U,Nd)N and UN+Mo. The fracture toughness of (U,Nd)N and UN+Mo were very similar to that of UN. On the other hand, those of UN+Pd-L and UN+Pd-H were higher than that of UN. The difference could not be explained from the Vickers hardness and Young's modulus. To explain the differences between UN+Pd and UN, the author performed the EBSP measurements. The SEM, IQ map and CD map of UN+Pd, (U,Nd)N and UN+Mo around the crack generating from the vertex of the Vickers impression were shown in Fig. 4.21–4.23.

In the same way of UN, $U_{0.4}Zr_{0.6}N$ and UN+60mol%TiN (Fig. 2.38, 2.39 and 2.40), the crack in (U,Nd)N progresses without stopping at the grain boundary. In case of UN+Mo, the crack goes the long way to avoid Mo particle when the crack contacts with Mo particle, and progresses without stopping at the grain boundary. On the other hand, the crack in UN+Pd pellets stopped at the grain boundary because UPd_3 distributed like the spider net along the grain boundary of UN and the fracture toughness of UPd_3 is high. From these results, it was found that Mo precipitation in UN+Mo pellets didn't almost influence the crack propagation and UPd_3 precipitation along the grain boundary in UN+Pd pellets disturbed the crack propagation.

Indentation hardness

In the same way of Chapter 2, the indentation size effects were observed in case of UN+Pd, (U,Nd)N, UN+Mo, (U,Nd)N+Mo and UPd_3 , too. To evaluate the indentation hardness, the author used Nix and Gao model (Eq. 2.61) [38] and Fig. 4.24–27 show the square of the indentation hardness of UN+Pd, UPd_3 , (U,Nd)N, UN+Mo and (U,Nd)N+Mo as the function of the inverse of the indentation depth. In Fig. 4.24, Nix and Gao model overestimated the indentation hardness of UPd_3 at the low depth ($h < 200$ nm). Therefore, the author used Eq. 2.65, to evaluate the depth dependence of the indentation hardness of UPd_3 . The depth dependence of the indentation hardness of UPd_3 was evaluated as the following equation;

$$UPd_3: \left(\frac{H(\text{GPa})}{3.786} \right)^2 = 1 + [1 + 1.465 \exp(-h / 21.51)]^{-3} \frac{629.9}{h} \quad (90 < h < 950 \text{ nm}). \quad (4.109)$$

From this equation, the indentation hardness at the infinite load (H_0) of UPd_3 was 3.8 GPa and this value was very close to the Vickers hardness at the load of 9.8 N. In Fig. 4.24–27, the indentation harnesses of the matrix (=UN phase or (U,Nd)N phase) in the simulated high-burnup nitride fuels were well consistent with that of UN. In the same way of UN, it is thought that Nix and Gao model overestimated the indentation hardness at the low load. The indentation hardness of UPd_3 phases in UN+Pd-L and UN+Pd-H were higher than that of pure UPd_3 (Eq. 4.3). This tendency corresponds to the case of Young's modulus of UN+Pd and indicates that the strain concentrates in UPd_3 phase. The indentation hardness of Mo phase in UN+Mo and (U,Nd)N+Mo showed the similar value, each other. From these results, it was found that the FP elements didn't almost influence the indentation hardness of the matrix phase.

4-3-3 Electrical property

The electrical resistivity of NdN was too high to be measured. Fig. 4.26 shows the

temperature dependences of the electrical conductivities of UN, UN+Pd, (U,Nd)N, UN+Mo and (U,Nd)N+Mo, together with the literature data [28, 29, 35, 40–45]. The experimental data of UN+Mo–L and UN+Mo–H were well consistent with the data estimated from the literature data of UN [40] and Mo [29] using Schulz's equation [46] (Eq. 2.79) and the electrical conductivity of UN+Mo increased with increasing the Mo content. From this result, it was found that there is no interaction between UN and Mo. On the other hand, in case of UN+Pd, (U,Nd)N and (U,Nd)N+Mo, the electrical conductivity decreased with increasing the FP content. The main reason in case of (U,Nd)N is probably that the free electron in (U,Nd)N pellets decreased due to the high electrical resistivity of NdN. The reason in case of UN+Pd is not obvious because there is no data of the electrical conductivity of UPd₃. However, it is probably one of the reasons that the grain boundary scattering of the electron is increased by UPd₃, which distributes like the spider net along the grain boundary of UN. The electrical conductivities of (U,Nd)N+Mo pellets increased by the addition of Mo when the author compared the electrical conductivity of (U,Nd)N+Mo with that of (U,Nd)N.

4-3-4 Thermal property

Thermal expansion

The thermal expansions of UN, UN+Pd, (U,Nd)N, NdN, and UN+Mo were shown in Fig. 4.28–31, together with the literature data [11, 19, 47–51]. In the present study, the thermal expansion of NdN was measured for the first time as Eq. 4.4:

$$\text{NdN: } \Delta L / L(\%) = 7.297 \times 10^{-4} (T - 298) + 2.665 \times 10^{-7} (T - 298)^2 \quad (298 < T < 900 \text{ K}) \quad (4.110)$$

Using the thermal expansion (Fig. 4.29) and bulk modulus (Table 4.8) of NdN, the potential parameters of NdN in MD calculation were determined and summarized in Table 4.9. The thermal expansion of NdN, (U,Nd)–L and (U,Nd)–H obtained from MD calculation were also shown in Fig. 4.29.

Fig. 4.28 includes the thermal expansion of UN+Pd–L and UN+Pd–H estimated from Turner's equation (Eq. 2.83). When the author estimated the thermal expansion from Turner's equation, the author used the thermal expansion and bulk modulus of polycrystalline UN and UPd₃ evaluated by Hayes (1990) [47] and Yamanaka (1998) [11]. In both case of UN+Pd–L and UN+Pd–H, the experimental data didn't agree with the data evaluated from Turner's equation using the thermophysical properties of polycrystalline sample. This difference is resulted from only the bulk modulus and thermal expansion because the thermal expansion of the composite

material is independent of the shape and size of the precipitation and matrix [52]. From the indentation tests, it was found that the Young's modulus of UPd₃ phase in UN+Pd pellets was higher than that of UPd₃ pellet. The author assumed that Poisson's ratio of UPd₃ phase in UN+Pd pellets is same to that of pure UPd₃ (=0.340), and calculated the bulk modulus of UPd₃ phase. Ref. [11] reported the volume thermal expansion coefficient of UPd₃ and didn't report the LTEC for a axis ($\alpha_{lin,a}$) and c axis ($\alpha_{lin,c}$). There is no data of $\alpha_{lin,a}$ and $\alpha_{lin,c}$ of UPd₃ above room temperature, but $\alpha_{lin,c}$ from 0 K to 300 K was reported by Takeuchi (2000) [53] ($=16.2 \times 10^{-6} \text{ K}^{-1}$ at room temperature). So, the author assumed that the ratio between $\alpha_{lin,a}$ and $\alpha_{lin,c}$ of UPd₃ at room temperature equals to that at high temperature and calculated $\alpha_{lin,a}$ and $\alpha_{lin,c}$ of UPd₃ from the volume thermal expansion coefficient [11] and $\alpha_{lin,c}$ at room temperature [53]. The author estimated the LTEC for (10 $\bar{1}$ 0) of UPd₃. Using these calculated data of UPd₃, the author re-estimated the thermal expansion of UN+Pd by Turner's equation (Eq. 2.83). The re-estimated data was well consistent with the experimental data. This method based on the indentation test and EBSD measurements, would allow us to estimate the thermal expansion of the high-burnup fuel from the minimum specimen of the high-burnup (<1mm × 1mm × 1mm), nevertheless the large sample (>4mm × 2mm × 2mm) is generally necessary to evaluate the thermal expansion.

From Fig. 4.29, it was found that the thermal expansion of NdN is very close to that of UN and that of (U,Nd)N follows to Vegard's law. The thermal expansions of NdN and (U,Nd)N calculated from the MD simulation were well consistent with the experimental data. In the different way of UN+Pd pellets, the thermal expansion of UN+Mo pellets followed to Turner's equation. This result could be predicted from the results of the indentation tests of UN+Mo pellets because there was no interaction on the mechanical properties between UN phase and Mo phase. In the present study, the author established the new method to estimate the thermal expansion of the fuels including the FP precipitation from the indentation test and EBSD analysis.

Specific heat capacity

Fig. 4.32–35 show the temperature dependences of the specific heat capacity of UN, UN+Pd, (U,Nd)N, UN+Mo and (U,Nd)N+Mo, together with the literature data [54–56].

Burriel (1988) [57] and Arita (1997) [58] evaluated the specific heat capacity of UPd₃ as the following equations:

$$\text{UPd}_3 \text{ (Burriel (1988) [57]): } C_p (\text{Jmol}^{-1}\text{K}^{-1}) = 99.69 + 1.141 \times 10^{-2} T,$$

$$(350 < T < 850 \text{ K}) \quad (4.111)$$

$$\text{UPd}_3 \text{ (Arita (1997) [58]): } C_p (\text{Jmol}^{-1}\text{K}^{-1}) = 95.20 + 1.141 \times 10^{-2} T - 1.5373 \times 10^{-4} T^{-2}.$$

$$(298 < T < 1351 \text{ K}) \quad (4.112)$$

The specific heat capacities of UN+Pd-L and UN+Pd-H were estimated as the addition match of that of UPd₃ (Eq. 4.6) [58] and UN (Eq. 2.92) [Chapter 2]. The differences between the estimated data of UN+Pd and the experimental data of UN were very small.

The specific heat capacity of NdN obtained in the present study was evaluated at the following equation;

$$\text{NdN: } C_p (\text{Jmol}^{-1}\text{K}^{-1}) = 53.29 + 9.258 \times 10^{-3} T - 9.446 \times 10^{-5} T^{-2} \quad (400 < T < 1273 \text{ K}). \quad (4.113)$$

In Fig. 4.33, that of NdN was very close to that of NdN in Ref. 56 and the experimental data of UN [54–56]. In the same way of Chapter 2, the sum of C_v and C_D of NdN was calculated from the thermal expansion (Eq. 4.4), bulk modulus (Table 4.8) and Debye temperature (Table 4.8) using Eq. 2.92 and 2.93. In both the data estimated from the Debye function and MD calculation, the data of NdN were very close to those of UN. In the present study, it was found that NdN was similar to UN on the elastic moduli, thermal expansion and specific heat capacity. So, the author thought that the influence of Nd in the nitride pellets is very small on the thermodynamics properties such as the specific heat capacity and Gibbs free energy. As expected, the differences between the experimental data of the specific capacity of (U,Nd)N and UN was very small.

In Fig. 4.33 and 4.34, the specific heat capacities of UN+Mo and (U,Nd)N+Mo decreased with increasing the Mo content and this trend was consistent with the sum of the specific heat capacity of UN (Eq. 2.94), NdN (Eq. 4.7) and Mo (Eq. 4.8) [55].

$$\text{Mo: } C_p (\text{Jmol}^{-1}\text{K}^{-1}) = 25.43 + 3.393 \times 10^{-3} T - 5.871 \times 10^{-7} T^2 - 2.154 \times 10^5 T^{-2}$$

$$(298 < T < 1000 \text{ K}),$$

$$C_p (\text{Jmol}^{-1}\text{K}^{-1}) = 16.96 + 6.929 \times 10^{-3} T - 1.142 \times 10^{-6} T^2 - 2.995 \times 10^6 T^{-2}$$

$$(1000 < T < 2100 \text{ K}),$$

$$C_p (\text{Jmol}^{-1}\text{K}^{-1}) = 7.616 \times 10^2 - 0.4510 T - 8.047 \times 10^{-5} T^2 - 5.827 \times 10^8 T^{-2}$$

$$(2100 < T < 2500 \text{ K}),$$

$$C_p (\text{Jmol}^{-1}\text{K}^{-1}) = -3.509 \times 10^2 - 0.1585 T - 1.359 \times 10^{-5} T^2 + 5.213 \times 10^8 T^{-2}$$

$$(2500 < T < 2892 \text{ K}). \quad (4.114)$$

Thermal conductivity

Fig. 4.36–39 show the temperature dependences of the thermal conductivities of UN, UN+Pd, (U,Nd)N, NdN, UN+Mo and (U,Nd)N+Mo at $P=0$, together with the literature data [12, 29, 40, 59, 60]. In these figures, the thermal conductivity of UN, UN+Pd, (U,Nd)N, UN+Mo and (U,Nd)N+Mo at $P=0$ were calculated using the same coefficient ($\beta=1$) of the porosity dependence of the thermal conductivity of UN (Eq. 2.99).

Fig. 4.36 includes the data estimated from the experimental data of UN [Chapter 2] and UPd₃ [12] using Schulz's equation (Eq. 2.79). Schulz's equation (Eq. 2.79) [46] is the model to estimate the transport properties such as the thermal conductivity and electrical conductivity of the composite material with the spherical or ellipsoidal precipitation. Therefore, it is difficult to precisely estimate the thermal conductivity of UN+Pd, which has precipitation (UPd₃) distributing like the spider net, by Schulz's equation. Therefore, the author predicted that there would be small differences between the estimated data and experimental data of the thermal conductivity of UN+Pd. In fact, the experimental data of UN+Pd-L and UN+Pd-H were quietly lower than the estimated data in Fig. 4.36. The author explained that Schulz's equation didn't take into the grain boundary scattering in Chapter 2. In UN+Pd pellets, the grain of UPd₃ exists along that of UN. So, it is thought that the contact area between UPd₃ grain and UN grain in this case is vastly larger than that in case of the composite material with the spherical precipitation. Therefore, since the effect of the grain boundary scattering becomes to be large in UN+Pd pellets, there are large differences between the estimated data and experimental data.

Fig. 4.40 shows the porosity dependence of the thermal conductivity of NdN obtained in the present study. It was confirmed that the oxidation in the measurement process doesn't effect because the thermal conductivity at the heating process agreed with that at the cooling process. In each temperature, the thermal conductivity rapidly decreased with increasing the porosity from around $P>0.21$. From this result, it was found that the P_c value exists around $P=0.21$. The P_c value represents the starting point where the thermal conductivity rapidly decreases because the MSA reaches at the percolation limit. The author estimated the thermal conductivity of NdN at $P=0$ using the data at the region of $P<0.21$, and could obtain the temperature and porosity dependences of the thermal conductivity of NdN as the following equation;

$$\text{NdN: } \kappa(P, T) = 115T^{-0.330} \frac{1-P}{1+1.96P} \quad (298 < T < 1473 \text{ K}, 0 < P < 0.2). \quad (4.115)$$

The thermal conductivity of NdN at $P=0$ was shown in Fig. 4.37 and decreased with increasing the temperature in the different way of UN. The electrical resistivity of NdN was too high to measure. Therefore, it is thought that the κ_{EL} of NdN would be very small and the κ_{LAT} is predominant in the κ_{TOT} of NdN. The κ_{LAT} generally decreases with increasing the temperature because the phonon scattering increases with increasing the temperature due to increasing of the lattice vibration. So, the temperature dependence of the thermal conductivity of NdN obtained in the present study is reasonable. The thermal conductivity of $U_{1-x}Nd_xN$ decreased with increasing the X. In Fig. 4.27, the electrical conductivities of the temperature dependence of $U_{1-x}Nd_xN$ decreased with increasing the X. Indeed, the κ_{EL} decreased by the addition of NdN. The κ_{LAT} would decreased with increasing the X because the center of the phonon scattering would form in (U,Nd)N by the addition of NdN to UN. Since both κ_{LAT} and κ_{EL} of (U,Nd)N decreased, κ_{LAT} of (U,Nd)N largely decreased with increasing the X.

Fig. 4.38 includes the thermal conductivity of UN+Mo-L and UN+Mo-H estimated from the experimental data of UN [Chapter 2] and Mo [28] using Schulz's equation (Eq. 2.79) [46]. The estimated data was well consistent to the experimental data. Their value was very close to that of UN [Chapter2]. From this result, it is thought that the influence of the generation of Mo in the high-burnup would be very small. Therefore, the thermal conductivities of (U,Nd)N-L and (U,Nd)N-H were close to those of (U,Nd)N-L and (U,Nd)N-H as shown in Fig. 4.39.

4-4 Summary

Sample preparation

The simulated high-burnup nitride fuel pellets (UN+Pd-L, UN+Pd-H, (U,Nd)N-L, (U,Nd)N-H, UN+Mo-L, UN+Mo-H, (U,Nd)N+Mo-L, (U,Nd)N+Mo-H) were prepared by the carbothermic reduction and atmospheric pressure sintering. NdN pellets with various porosities (66.3–88.2 %T.D.) and UPd₃ pellet (95.0%T.D.) were prepared by the SPS and high vacuum induction melting method.

Sample characterization and crystallographic properties

From XRD analysis, it was found that Pd precipitates as UPd₃ in UN+Pd-L and UN+Pd-H and doesn't solve in UN phase. In case of UN+Mo and (U,Nd)N+Mo, Mo precipitates as the pure metal. In case of (U,Nd)N and (U,Nd)N+Mo, it was confirmed that UN and NdN forms the solid solution because the lattice parameters of (U,Nd)N pellets follows to Vegard's law.

The surface observations were performed by the SLM, SEM-EDX and optical microscope. UPd₃ precipitated at the grain boundary of UN phase in UN+Pd pellets. Mo

precipitated as the spherical particle in UN+Mo and (U,Nd)N+Mo pellets. The MSA of UN+Pd, (U,Nd)N, UN+Mo and (U,Nd)N+Mo followed Eq. 2.21, which represents the porosity dependences of the MSA of UN. Judging from these results, the author applied the coefficient of the porosity dependences of the thermophysical properties of UN to UN+Pd, (U,Nd)N, UN+Mo, (U,Nd)N+Mo pellets.

By the EBSD measurements, it was found that the addition of NdN and Mo don't almost influence the sintering properties of nitride fuels. On the other hand, the grain sizes of UN+Pd-L and UN+Pd-H were about four times of that of UN and their misorientation angles were lower than that of UN. These results indicate that Pd accelerates the sintering of nitride fuels. UPd_3 precipitation in UN+Pd pellets orientated for the direction from $(10\bar{1}0)$ to $(10\bar{1}1)$.

Mechanical properties

(1) Young's modulus

The ultrasonic pulse echo measurement and indentation tests were performed to evaluate elastic properties at macroscale and sub-microscale, respectively. Young's modulus of porosity-free NdN was very close to that of UN. Young's moduli of porosity-free UN+Pd, (U,Nd)N, UN+Mo and (U,Nd)N+Mo obtained from the ultrasonic pulse echo method were very similar to that of UN. From these results, it is found that the influences of Pd, Nd and Mo for Young's modulus of the nitride fuels are very small. From the indentation tests, Young's moduli of UPd_3 phase in UN+Pd-L and UN+Pd-H were higher than that of UPd_3 pellet due to the strain-hardening occurred in the preparation of the pellets, and those of Mo phase in UN+Mo-L, UN+Mo-H, (U,Nd)N+Mo-L and (U,Nd)N+Mo-H were very similar to that of pure Mo.

(2) Vickers hardness and fracture toughness

Vickers hardness of porosity-free NdN estimated in the present study was higher than that of UN. So, Vickers hardness of $U_{1-x}Nd_xN$ linearly increased with x . On the other hand, Vickers hardness of porosity-free UN+Pd and UN+Mo were not almost influenced by the addition of Pd and Mo because the nitride phases have the predominant effect. Therefore, Vickers hardness of (U,Nd)N+Mo-L and (U,Nd)N+Mo-H corresponded to those of (U,Nd)N-L and (U,Nd)N-H, respectively.

From the EBSD measurements, Mo precipitation in UN+Mo pellets didn't almost influence the crack propagation and UPd_3 precipitation along the grain boundary in UN+Pd pellets disturbed the crack propagation. The crack propagation in (U,Nd)N was very similar to that of UN. Therefore, the fracture toughness of (U,Nd)N and UN+Mo agreed with that of UN and that of UN+Pd was higher than that of UN.

(3) Indentation hardness

By the indentation test, the indentation hardness of UPd_3 phase, Mo phase and matrix phases in the simulated high burnup fuels were evaluated. The indentation hardness of the matrix phase (=nitride phase) in the simulated high-burnup fuels were consistent with each other. From these results, the matrix grain was not influenced by the addition of FPs (Pd, Nd and Mo). On the other hand, the indentation hardness of UPd_3 phase in UN+Pd pellets was higher than that of UPd_3 pellets.

Electrical conductivity

The electrical conductivities of UN+Mo-L and UN+Mo-H pellets obtained in the present study were well consistent with the data estimated from Schulz's equation. The electrical conductivity of (U,Nd)N-L and (U,Nd)N-H pellets decreased with increasing the NdN content due to the high electrical resistivity of NdN. Those of UN+Pd pellets decreased with increasing the Pd content.

Thermal properties

(1) Thermal expansion

The thermal expansion was evaluated by the thermodilatometry. The experimental data of UN+Pd were not consistent with the data estimated from the volume thermal expansion coefficients and bulk modulus of UPd_3 and UN using Turner's equation. So, when the author re-estimated the thermal expansion of UN+Pd based on the data of Young's modulus of UPd_3 phase obtained from the indentation tests and crystallographic properties of UPd_3 phase obtained from the EBSD measurements, the estimated data corresponded to the experimental data. Although the large bulk sample ($>5\text{mm} \times 3\text{mm} \times 3\text{mm}$) is required in the thermodilatometry, this method based on the indentation test and EBSD measurements would allow us to estimate the thermal expansion of the high-burnup fuel from the small specimen ($<1\text{mm} \times 1\text{mm} \times 1\text{mm}$). This method was suggested in the present study for the first time. This method is very effective when we evaluate the thermal expansion of the high-burnup fuel because the large bulk sample of the high-burnup fuels could not be obtained.

The thermal expansion of NdN obtained in the present study was very close to that of UN. Using this data, the potential parameters of NdN in MD simulation were obtained. The experimental data of (U,Nd)N-L and (U,Nd)N-H were well consistent with Vegard's law and MD results.

The experimental data of UN+Mo-L and UN+Mo-H were well consistent with the data

estimated from the volume thermal expansion coefficients and bulk modulus of Mo and UN using Turner's equation.

(2) Specific heat capacity

The temperature dependences of the specific heat capacities of UN+Pd and UN+Mo slightly decreased with increasing the Pd and Mo contents. The specific heat capacity of NdN showed the close value with that of UN. So, those of (U,Nd)N-L and (U,Nd)N-H agreed with those of UN and NdN. The sum of C_V and C_D estimated from the experimental data of NdN was also similar to that of UN, and was well consistent with the data obtained from MD simulation.

(3) Thermal conductivity

The experimental data of the thermal conductivities of UN+Pd pellets were lower than the data estimated from Schulz's equation. It is probably because the grain boundary scattering increased by UPd_3 , which is the precipitation along the grain boundary of UN. The thermal conductivity of NdN decreased with increasing the temperature in the different way of UN. The addition of NdN in UN pellet decreases both κ_{LAT} and κ_{EL} . So, those of $(U_{1-x},Nd_x)N$ pellets decreased with increasing the X. In the case of UN+Mo, the experimental data were well consistent with the data estimated from Schulz's equation. The effect of the addition of Mo in UN and (U,Nd)N pellets were very small.

References

- [177] Japan Atomic Energy Research Institute: Research Group of Actinides Science, "Proceedings of the symposium on nitride fuel cycle technology," JAERI-Conf 2004-015.
- [178] L. Donnet, F. Jorion, N. Drin, S.L. Hayes, J.R. Kennedy, K. Pasamehmetoglu, S.L. Voit, D. Haas, A. Fernandez, "The FUTURIX-FTA experiment in PHENIX: Status of fuel fabrication," Proc. Int. Conf. GLOBAL2005, Tsukuba, Japan, Oct. 9-13, 2005, Paper No. 258.
- [179] K. Minato, M. Akabori, M. Takano, Y. Arai, K. Nakajima, A. Itoh, T. Ogawa, "Fabrication of nitride fuels for transmutation of minor actinides," J. Nucl. Mater. 320 (2003) 18-24.
- [180] R.A. Verrall, I.J. Hastings, P.G. Lucuta, H. Matzke, B.J.F. Palmer, "Preparation and applications of simulated high-burnup nuclear fuel," Annual Conference Proceedings 11th - Canadian Nuclear Society, 1990, 6.1-6.3.
- [181] P.G. Lucuta, R.A. Verrall, H. Matzke, B.J. Palmer, "Microstructural features of SIMFUEL - simulated high-burnup uranium dioxide-based nuclear fuel," J. Nucl. Mater. 178[1] (1991) 48-60.
- [182] P.G. Lucuta, H. Matzke, R.A. Verrall, H.A. Tasman, "Thermal conductivity of SIMFUEL," J. Nucl. Mater. 188 (1992) 198-204.
- [183] P.G. Lucuta, R.A. Verrall, H. Matzke, I.J. Hastings, "Characterization and thermal properties of hyperstoichiometric SIMFUEL," Conf. Proc. - Int. Conf. CANDU Fuel Perform. 3rd, 1992, 2-61/2-73.
- [184] P.G. Lucuta, H. Matzke, R.A. Verrall, "Modeling of UO₂-based SIMFUEL thermal conductivity. The effect of the burnup," J. Nucl. Mater. 217[3] (1994) 279-286.
- [185] P.G. Lucuta, H. Matzke, R.A. Verrall, P.G. Klemens, "Analysis of SIMFUEL thermal conductivity," Thermal Conductivity: Proceedings of the 'International Thermal Conductivity Conference' & 'International Thermal Expansion Symposium' 22 (1994) 894-903.
- [186] H. Matzke, P.G. Lucuta, R.A. Verrall, J.P. Hiernaut, "Thermophysical properties of UO₂ and SIMFUEL -simulated high-burnup fuel," Thermal Conductivity: Proceedings of the 'International Thermal Conductivity Conference' & 'International Thermal Expansion Symposium' 22 (1994) 904-12.
- [187] S. Yamanaka, K. Yamada, T. Tsuzuki, T. Iguchi, M. Katsura, Y. Hoshino, W. Saiki, "Mechanical and thermal properties of uranium intermetallic compounds," J. Alloys Compd. 271-273 (1998) 549-556.
- [188] K. Kurosaki, H. Kobayashi, M. Uno, S. Yamanaka, "Thermal conductivities of uranium intermetallic compounds," J. Nucl. Sci. Tech. Suppl. 3 (2002) 811-814.

- [189] JCPDS 32-1397 (UN).
- [190] JCPDS 5-550 (UO₂).
- [191] JCPDS 5-681 (Pd).
- [192] JCPDS 17-20 (NdN).
- [193] JCPDS 40-1282 (Nd₂O₃).
- [194] JCPDS 42-1120 (Mo).
- [195] M. Uno, K. Kurosaki, A. Nakamura, "Reactions of uranium nitride with platinum-family metals," J. Nucl. Mater. 247 (1997) 322-327.
- [196] M. Akabori, T. Ogawa, A. Itoh, H. Motohashi, H. Shiwaku, "Local structure of (U,Zr)Pd₃ by EXAFS," J. Alloys Compd. 271-273 (1998) 363-366.
- [197] P. Ettmayer, J. Waldhart, A. Vendl, G. Banik, "Über die Mischbarkeit von ThC mit LaN, CeN, PrN, NdN, SmN, GdN und ErN," Monatshefte fuer Chemie 111 (1980) 1185-1188.
- [198] P. Schobinger-Paramantellos, P. Fisher, O. Bogt, E. Kaldis, "Magnetic ordering of neodymium mononitrides determined by neutron diffraction," J. Phys. C: Solid state physics 6 (1973) 725-737.
- [199] M. Osaka, S. Tanaka, K. Tanaka, "Densification of Mo-Cermet fuel by sintering with metal additives," Abstract of fall meeting of Atomic Energy Society of Japan, 2007, pp. 924 (P43).
- [200] S.L. Hayes, J.K. Thomas, K.L. Peddicord, "Material property correlations for uranium mononitride; II Mechanical properties," J. Nucl. Mater. 171 (1990) 271-288.
- [201] A. Padel, C.D. Novion, "Constantes elastiques des carbures, nitrures et oxides d'uranium et de plutonium," J. Nucl. Mater. 33 (1969) 40-51.
- [202] T. Honda, T. Kikuchi, "Porosity dependence of elastic modulus of uranium nitride," J. Nucl. Sci. Technol. 6 (1968) 221-222.
- [203] H.L. Whaley, R.A. Potter, W. Fulerson, "Ultrasonic Velocity Measurements in UN," U.S. At. Energy Comm. Rep. ORNL-4370 (1968) 86.
- [204] E.O. Speidel, D.L. Keller, "Fabrication and Properties of Hot-pressed Uranium Mononitride," U.S. At. Energy Comm. Rep. BMI-1633 (1963) 65.
- [205] 日本金属学会 (JIM: The Japan Institute of Metals), "金属便覧," 丸善, 東京, 2000.
- [206] Z. Fan, P. Tsakiroopoulos, A.P. Miodownik, "Prediction of Young's modulus of particulate two phase composites," Mater. Sci. Tech-Lond. 8 (1992) 922-929.
- [207] Z. Hashin, S. Shtrikman, "A variational approach to the theory of the elastic behavior of polycrystals," J. Mech. Phys. Solid. 10 (1963) 343-352.

- [208] D. Setoyama, "Study on the physico-chemical properties of zirconium-oxygen-hydrogen ternary system," Doctoral thesis, 2005.
- [209] Q. Chen, B. Sundman, "Calculation of Debye temperature for crystalline structures - A case study on Ti, Zr, and Hf," *Acta. Mater.* 49 (2001) 947-961.
- [210] T.G. Godfrey, G. Hallerman, O.B. Cavin, "Microhardness Studies on Sintered UN," U.S. At. Energy Comm. ORNL/TM-1050 (1965) 142.
- [211] J.P. Moore, W. Fulkerson, D.L. McElroy, "Thermal conductivity, electrical resistivity, and Seebeck coefficient of uranium mononitride," *J. Am. Ceram. Soc.* 53 (1970) 76-82.
- [212] J.D.L. Harrison, "The hot-hardness of Uranium Carbonitrides," U.S. At. Energy Comm. ORNL-4330 (1968) 28.
- [213] R.W. Endeck, E.L. Foster, D.L. Keller, "Preparation and Properties of Cast UN," U.S. At. Energy Comm. BMI-1690 (1968) 22.
- [214] T.G. Godfrey, G. Hallerman, "Microhardness Studies on Sintered UN," U.S. At. Energy Comm. ORNL-3870 (1965) 66.
- [215] W.D. Nix, H. Gao, "Indentation size effects in crystalline materials: a law for strain gradient plasticity," *J. Mech. Phys. Solids* 46 (1998) 411-425.
- [216] S.L. Hayes, J.K. Thomas, K.L. Peddicord, "Material property correlations for uranium mononitride; III. Transport properties," *J. Nucl. Mater.* 171 (1990) 289-299.
- [217] W. Fulkerson, T.G. Kollie, S.C. Weaver, J.P. Moore, R.K. Williams, *Proc. 4th Int. Conf. On Plutonium and Other actinides*, AIME, Santa Fe, U.S.A., 1970, p.374.
- [218] B.A. Hayes, M.A. DeCrescente, "Thermal conductivity and electrical resistivity of uranium mononitride," U.S. At. Energy Comm. PWAC-481 (1965) 28.
- [219] T.G. Kollie, J.P. Moore, "Metals and ceramics division annual progress report," U.S. At. Energy Comm. ORNL-3670 (1964) 317.
- [220] R.W. Endeck, E.L. Foster, D.L. Keller, "Preparation and Properties of Cast UN," U.S. At. Energy Comm. BMI-1690 (1961) 22.
- [221] D.L. Keller, "Development of uranium mononitride," U.S. At. Energy Comm. BMI-X-178 (1961) 11.
- [222] B. Schulz, "Thermal conductivity of porous and highly porous materials," *High Temp.-High Press.* 13 (1981) 649-660.
- [223] Y.S. Touloukian, R.K. Kirby, R.E. Taylor, T.Y.R. Lee, "Thermal expansion: Nonmetallic solids," IFI/Plenum, New York, U.S.A., 1977.

- [224] S.L. Hayes, J.K. Thomas, K.L. Peddicord, "Material property correlations for uranium mononitride; I. Physical properties," J. Nucl. Mater. 171 (1990) 262-270.
- [225] K.M. Taylor, P.A. Smudski, L.N. Halley, T.J. Keaty, "Synthesis and fabrication of refractory uranium compounds," U.S.At. Energy Comm. ORO-248 (1959) 21.
- [226] C.P. Kempter, R.O. Elliott, "Thermal expansion of UN, UO₂, (U,Th)O₂, and ThO₂," J. Chem. Phy. 30 (1959) 1524-1526.
- [227] R. Benz, G. Balog, B. H. Baca, "Uranium-uranium dioxide-uranium nitride (UN₂) phase diagram," High Temp. Sci. 2[3] (1970) 221-251.
- [228] R.W. Rice, "Porosity of ceramics," Marcel Dekker Inc., New York, U.S.A., 1999.
- [229] T. Takeuchi, Y. Tokiwa, R. Settai, Y. Haga, E. Yamamoto, T. Honma, Y. Onuki, "Thermal expansion and magnetostriction of UPd₃," Phys. B 281-282 (2000) 602-603.
- [230] H. Tagawa, "Phase relations and thermodynamic properties of the uranium-nitrogen system," J. Nucl. Mater. 51 (1974) 78.
- [231] The SGTE Pure Substance and Solution databases, GTT-DATA SERVICES, 1996.
- [232] A.G. Alekseev, "高融点化合物物性便覧," 日ソ通信社, 和歌山, 1994.
- [233] R. Burriel, M.W.K. To, H. Zainel, E.F. Westrum Jr., E.H.P. Cordfunke, R.P. Mauris, G. Wiibenga, "Thermodynamics of uranium intermetallic compounds II, Heat capacity of UPd₃ from 8 to 850 K," J. Chem. Thermodyn. 20 (1988) 815-823.
- [234] Y. Arita, N. Sasajima, T. Matsui, "Thermodynamics study on UPd₃ and U(Pd_{0.85}Rh_{0.15})₃," J. Nucl. Mater. 247 (1997) 232-234.
- [235] S.B. Ross, M.S. El-Genk, R.B. Matthews, "Thermal conductivity correlation for uranium nitride fuel between 10 and 1923 K," J. Nucl. Mater. 151 (1988) 313-317.
- [236] Y. Arai, Y. Suzuki, T. Iwai, T. Ohmichi, "Dependence of the thermal conductivity of (U,Pu)N on porosity and plutonium content," J. Nucl. Mater. 195[1-2] (1992) 37-43.

Table 4.10 Different points in the preparation conditions of the bulk sample of

UN, UN+Pd, (U,Nd)N, UN+Mo and (U,Nd)N+Mo

		UN	UN+Pd	(U,Nd)N	UN+Mo	(U,Nd)N+Mo
Specific surface area of UO_2	m^2/g	8.0	8.0	8.2	8.0	8.2
O/M of UO_2 powder	–	2.14	2.14	2.08	2.14	2.08
Holding temperature in the sintering process	K	2073	2073	2073	2073	2073
Holding time in the sintering process	hr	4	8	4	15	10

Table 4.11(a) Sample characteristics and crystallographic properties of

UN, UN+Pd-L, UN+Pd-H, UN+Mo-L and UN+Mo-H

Sample name		UN	UN+Pd-L	UN+Pd-H	UN+Mo-L	UN+Mo-H
Additional material		–	Pd	Pd	Mo	Mo
Burnup	GWD/tU	0	50	200	50	200
Additional quantity	mol.%	–	2.2	11.2	1.6	7.1
Molecular Weight		252.0	248.8	235.7	250.7	245.9
Theoretical density	g/cm^3	14.32	14.29	14.21	14.27	14.16
Mass density	g/cm^3	13.21	12.19	12.71	13.11	12.78
Relative density	% T.D.	92.2	85.2	89.4	91.8	90.3
Lattice parameter of nitride phase	nm	0.4889	0.4886	0.4889	0.4889	0.4889
Average grain size of nitride phase	μm	10.4	41.4	34.8	6.8	6.1
Maximum grain size of nitride phase	μm	22.5	49.7	52.8	18.2	12.3
Minimum grain size of nitride phase	μm	1.1	2.3	3.7	1.2	0.7
Average misorientation angle of nitride phase	degree	21.4	8.3	9.6	20.4	18.1
Grain size of Mo phase	μm	–	–	–	3–10	5–20
Arithmetic surface roughness	nm	2.8	3.9	1.20	2.7	0.8
N/U or N/(U+Nd)		0.97	1.04	1.07	0.99	1.0
O_2 content	wt.%	0.246	0.327	0.424	0.327	0.424
C content	wt.%	0.094	0.151	0.130	0.151	0.130

Table 4.2(b) Sample characteristics and crystallographic properties of

UN, (U,Nd)N-L, (U,Nd)N-H, (U,Nd)N+Mo-L and (U,Nd)N+Mo-H

Sample name		UN	(U,Nd)N-L	(U,Nd)N-H	(U,Nd)N+Mo-L	(U,Nd)N+Mo-H
Additional material		–	Nd	Nd	Nd, Mo	Nd, Mo
Burnup	GWD/tU	0	50	200	50	200
Additional quantity	mol.%	–	2.7	12.2	Nd: 2.6 Mo: 1.5	Nd: 11.9 Mo: 7.1
Molecular Weight		252.0	249.5	240.6	248.2	244.2
Theoretical density	g/cm ³	14.32	14.14	13.53	14.11	13.42
Mass density	g/cm ³	13.21	13.26	12.90	12.94	12.78
Relative density	% T.D.	92.2	93.8	95.3	91.8	96.0
Lattice parameter of nitride phase	nm	0.4889	0.4896	0.4911	0.4897	0.4910
Average grain size of nitride phase	μm	10.4	6.7	8.8	9.8	14.5
Maximum grain size of nitride phase	μm	22.5	15.5	17.9	25.1	29.6
Minimum grain size of nitride phase	μm	1.1	11	1.4	1.4	1.5
Average misorientation angle of nitride phase	degree	21.4	21.7	20.9	20.1	15.3
Grain size of Mo phase	μm	–	–	–	3–10	5–20
Arithmetic surface roughness	nm	2.8	1.4	2.7	1.5	2.2
N/U or N/(U+Nd)		0.97	0.98	1.01	1.02	1.00
O ₂ content	wt.%	0.246	0.370	0.439	0.223	0.251
C content	wt.%	0.094	0.115	0.189	0.078	0.065

Table 4.12 Sample characteristics and crystallographic properties of NdN prepared by SPS

Molecular Weight		158.2									
Theoretical density	g/cm ³	7.879									
Purpose		Measurements of mechanical properties					Measurements of thermal properties				
SPS temperature	K	1473	1573	1673	1673	1773	1473	1673	1673	1773	1873
Heating rate at SPS process	K/min	100	100	100	50	50	100	100	50	50	50
Mass density	g/cm ³	5.224	6.047	6.938	6.304	6.942	5.603	6.330	6.708	6.682	6.906
Relative density	% T.D.	66.3	76.8	88.1	80.1	88.2	71.5	80.4	86.1	84.9	87.7
Lattice parameter	nm	–	–	–	–	0.5114	–	–	–	–	–
Grain size	μm	10–30	10–30	10–30	10–30	10–30	10–30	10–30	10–30	10–30	10–30

Table 4.13 Results of ultrasonic pulls echo method of UN+Pd-L and UN+Pd-H

		UN		UN+Pd-L		UN+Pd-H	
Porosity, P	—	0.079	0	0.147	0	0.109	0
Longitudinal sound velocity, V_L	m/sec	4378	4802	3967	4716	4190	4769
Shear velocity, V_S	m/sec	2507	2750	2301	2736	2384	2713
Young's modulus, E	GPa	208	273	161	267	181	264
Shear modulus, G	GPa	83.0	109	64.5	107	71.9	105
Poisson's ratio, ν		0.256	0.256	0.246	0.246	0.261	0.261
Bulk modulus, B	GPa	142	187	106	175	126	184
Debye temperature, θ_D	K	339	373	—	—	—	—

Table 4.14 Results of ultrasonic pulls echo method of (U,Nd)N-L and (U,Nd)N-H

		UN		(U,Nd)N-L		(U,Nd)N-H	
Porosity, P	—	0.079	0	0.062	0	0.047	0
Longitudinal sound velocity, V_L	m/sec	4378	4802	4461	4782	4502	4765
Shear velocity, V_S	m/sec	2507	2750	2547	2730	2535	2683
Young's modulus, E	GPa	208	273	217	265	210	247
Shear modulus, G	GPa	83.0	109	86.4	105	82.8	97.4
Poisson's ratio, ν		0.256	0.256	0.258	0.258	0.268	0.268
Bulk modulus, B	GPa	142	187	150	183	151	177
Debye temperature, θ_D	K	339	373	344	369	342	362

Table 4.15 Results of ultrasonic pulls echo method of UN+Mo-L and UN+Mo-H

		UN		UN+Mo-L		UN+Mo-H	
Porosity, P	—	0.079	0	0.073	0	0.100	0
Longitudinal sound velocity, V_L	m/sec	4378	4802	4377	4770	4406	4952
Shear velocity, V_S	m/sec	2507	2750	2475	2698	2507	2818
Young's modulus, E	GPa	208	273	205	263	202	283
Shear modulus, G	GPa	83.0	109	81.1	104	80.2	112
Poisson's ratio, ν		0.256	0.256	0.265	0.265	0.260	0.260
Bulk modulus, B	GPa	142	187	145	186	141	198
Debye temperature, θ_D	K	339	373	—	—	—	—

Table 4.16 Results of ultrasonic pulls echo method of (U,Nd)N+Mo-L and (U,Nd)N+Mo-H

		UN		(U,Nd)N +Mo-L		(U,Nd)N +Mo-H	
Porosity, P	-	0.079	0	0.083	0	0.048	0
Longitudinal sound velocity, V_L	m/sec	4378	4802	4404	4862	4650	4924
Shear velocity, V_s	m/sec	2507	2750	2492	2751	2666	2823
Young's modulus, E	GPa	208	273	203	270	228	269
Shear modulus, G	GPa	83.0	109	80.3	107	90.8	107
Poisson's ratio, ν		0.256	0.256	0.265	0.265	0.255	0.255
Bulk modulus, B	GPa	142	187	144	191	155	183
Debye temperature, θ_D	K	339	373	-	-	-	-

Table 4.17 Results of ultrasonic pulls echo method of UN+Mo-L and UN+Mo-H

		NdN				
Porosity, P	-	0.151	0.139	0.123	0.109	0
Longitudinal sound velocity, V_L	m/sec	4566	4711	4930	4975	6186
Shear velocity, V_s	m/sec	2710	2822	2919	2946	3676
Young's modulus, E	GPa	142	153	165	168	261
Shear modulus, G	GPa	57.8	62.7	67.1	68.3	106
Poisson's ratio, ν		0.228	0.220	0.23	0.23	0.227
Bulk modulus, B	GPa	87.0	91.1	102	104	159
Debye temperature, θ_D	K	349	363	376	379	473

Table 4.18 Potential parameters of U^{3+} , Nd^{3+} and N^{3-}

Ions	z	a	b	C	D_{ij} β_{ij} r_{ij}^*			
N ³⁻	-1.450	1.797	0.080	20				
U ³⁺	1.450	1.228	0.080	0	U ³⁺ -N ³⁻	7.00	1.25	2.364
Nd ³⁺	1.450	1.393	0.100	13.0	Np ³⁺ -N ³⁻	4.50	1.50	2.680

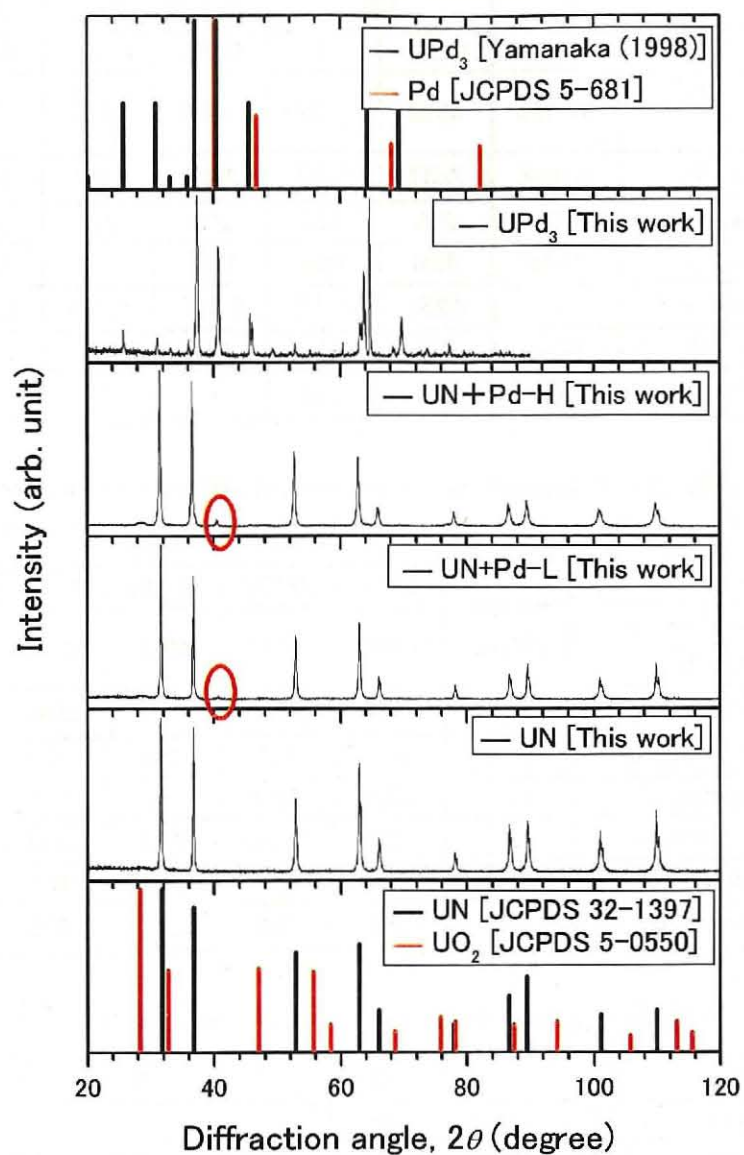


Fig. 4.100 XRD pattern of UN, UN+Pd-L, UN+Pd-H and UPd_3 , together with the literature data [11, 13-15]

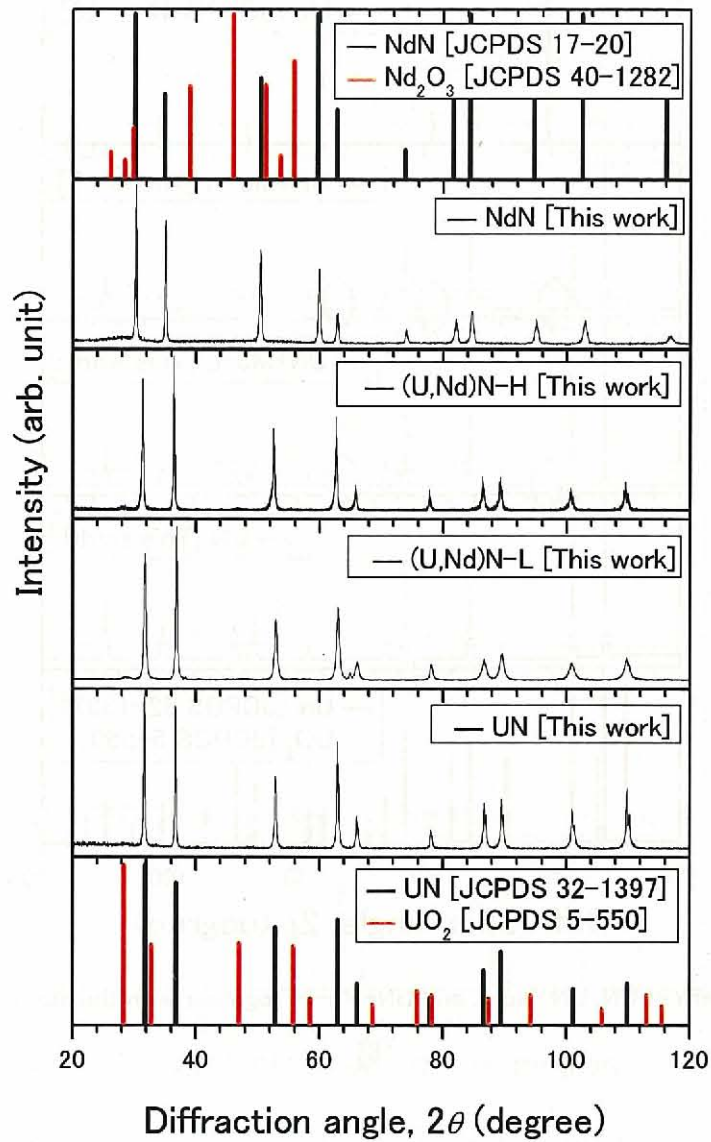


Fig. 4.101 XRD pattern of UN, (U,Nd)N-L, (U,Nd)N-H and NdN together with the literature data [13, 14, 16, 17]

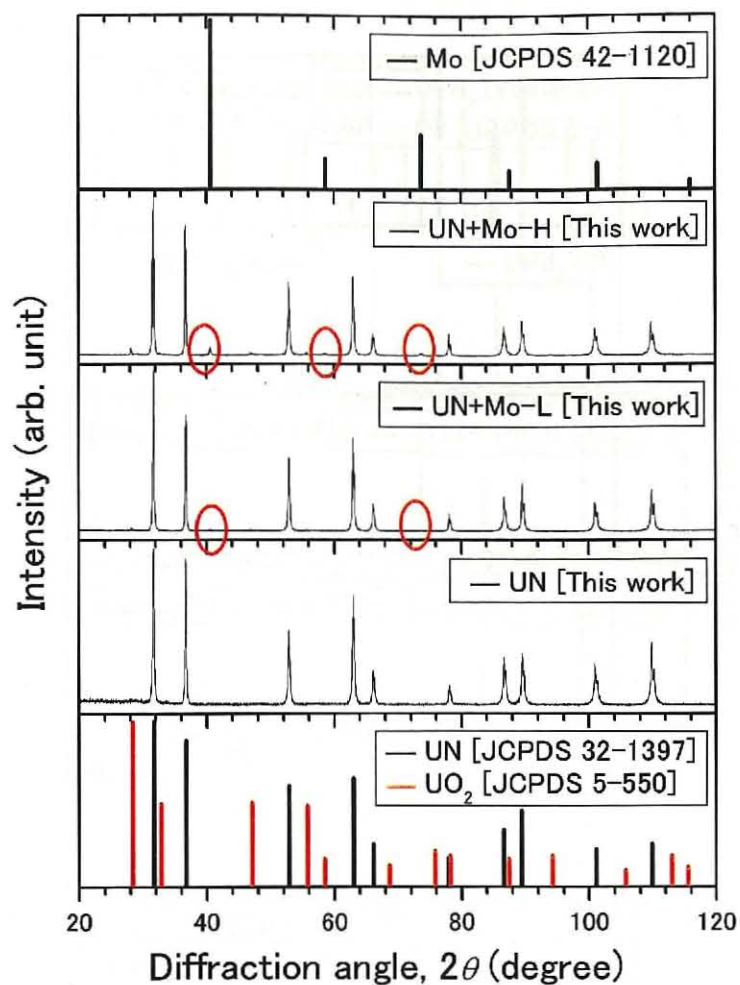


Fig. 4.102 XRD pattern of UN, UN+Mo-L and UN+Mo-H, together with the literature data [13, 14,

18]

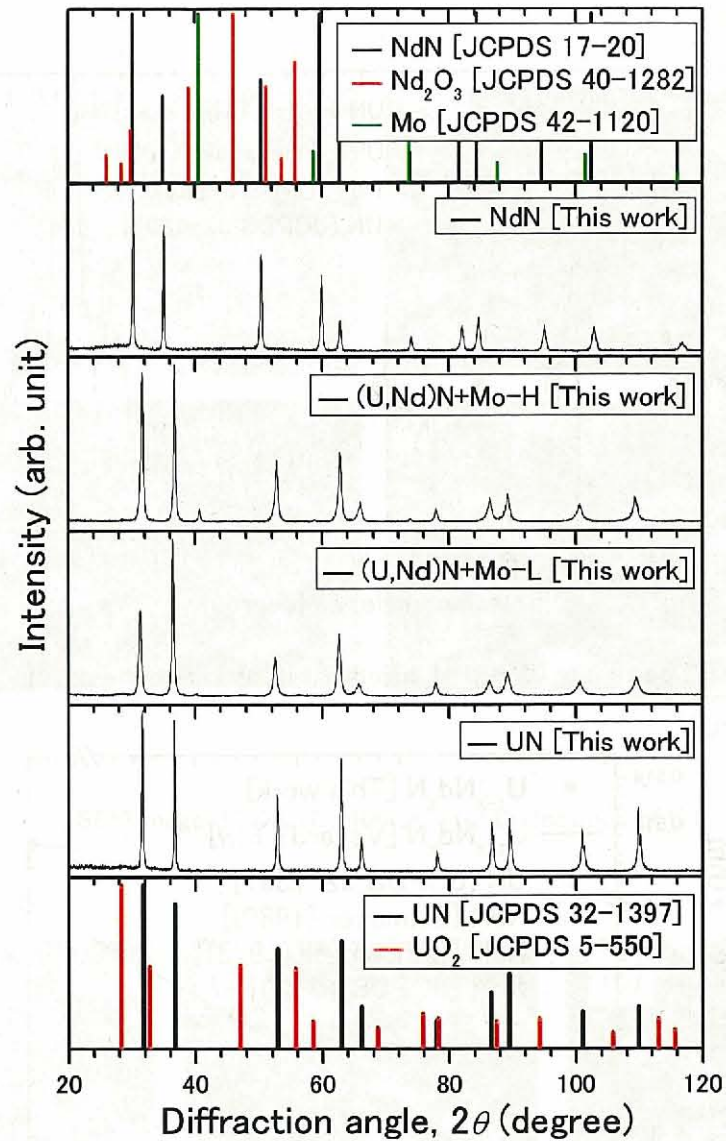


Fig. 4.103 XRD pattern of UN, (U,Nd)N+Mo-L, (U,Nd)N+Mo-H and NdN together with the literature data [13, 14, 16–18]

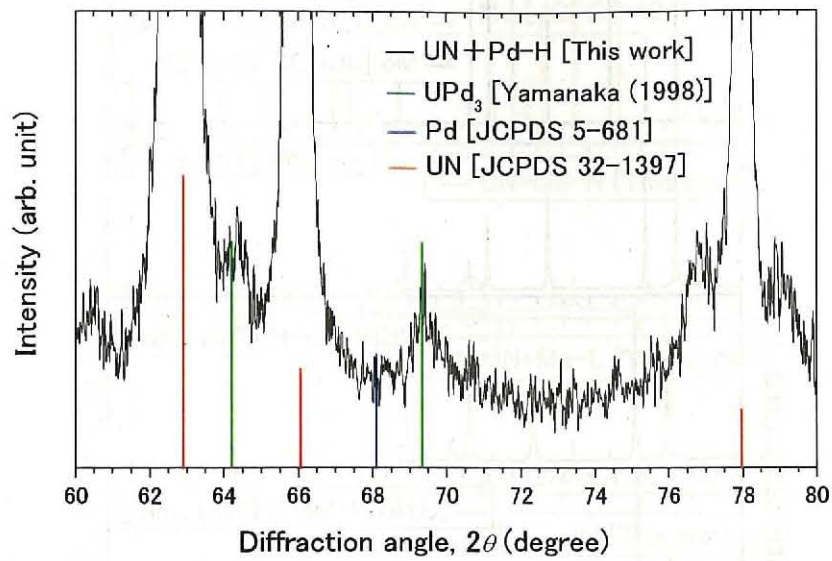


Fig. 4.104 XRD pattern of UN+Pd-H, together with the literature data [11, 13, 15]

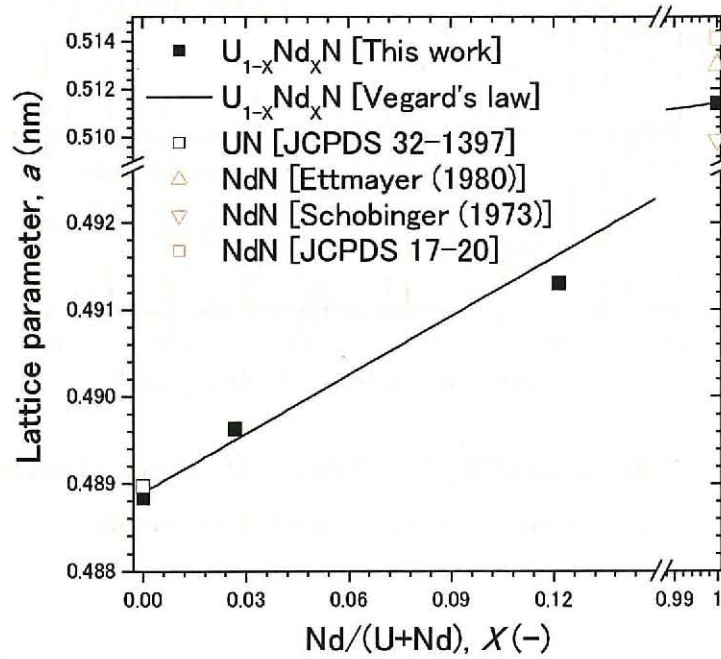


Fig. 4.105 Nd content dependence of $\text{U}_{1-x}\text{Nd}_x\text{N}$, together with the literature data [13, 16, 21, 22]

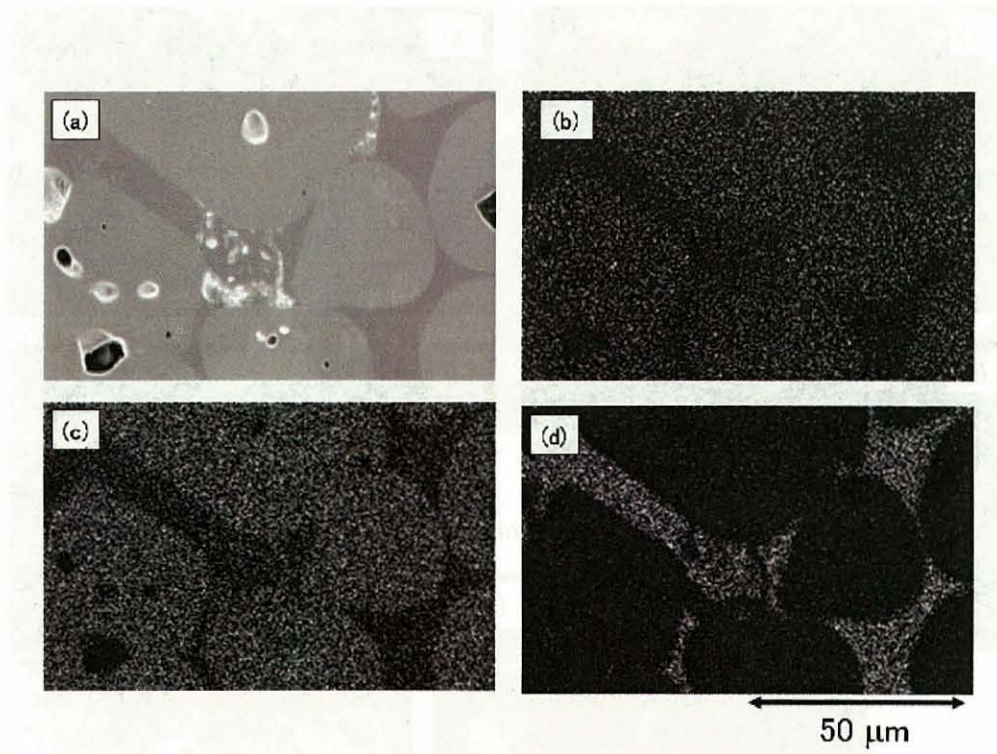


Fig. 4.106 UN+Pd-H (a) SEM image (b) Distribution of N (c) Distribution of U (d) Distribution of Pd

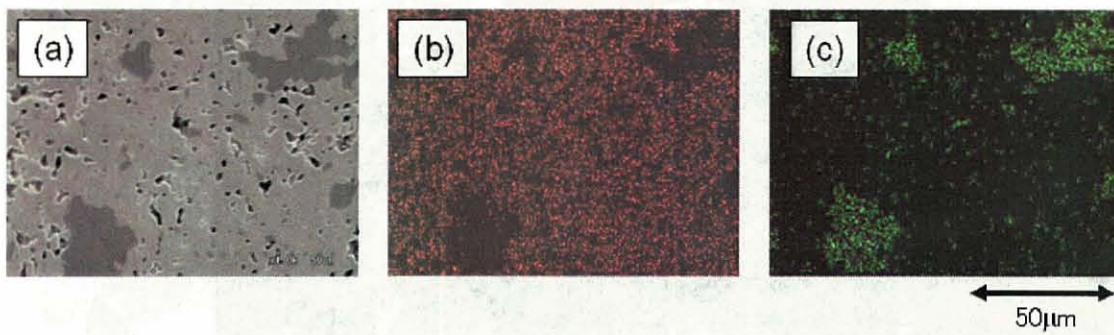


Fig. 4.107 UN+Mo-H (a) SEM image (b) Distribution of U (c) Distribution of Mo

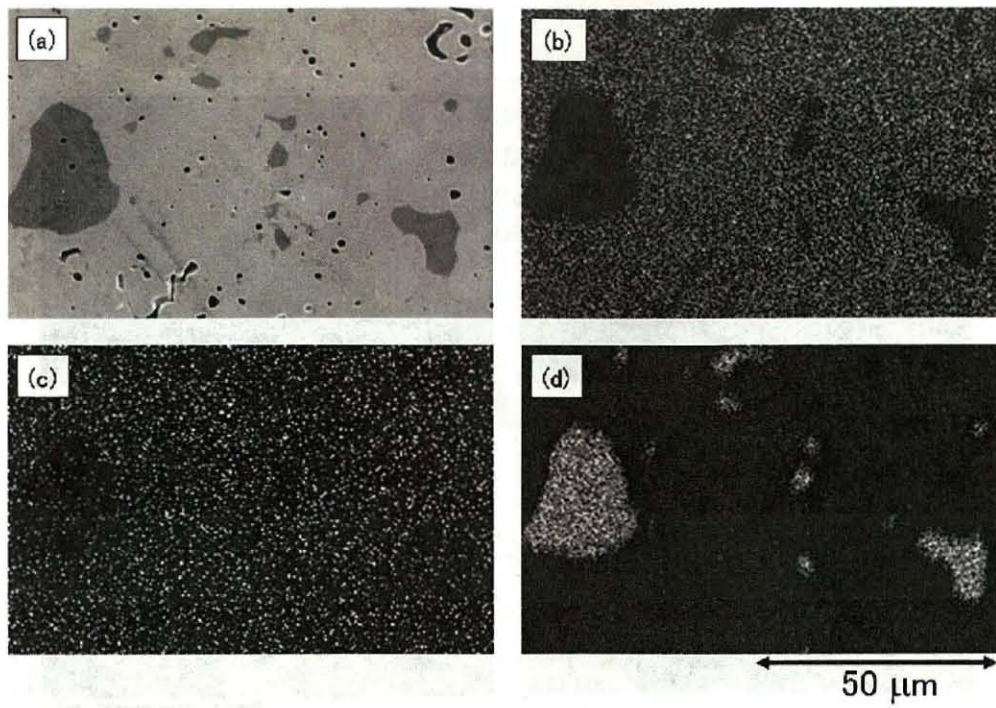


Fig. 4.108 (U,Nd)N+Mo-H

(a) SEM image (b) Distribution of U (c) Distribution of Nd (d) Distribution of Mo

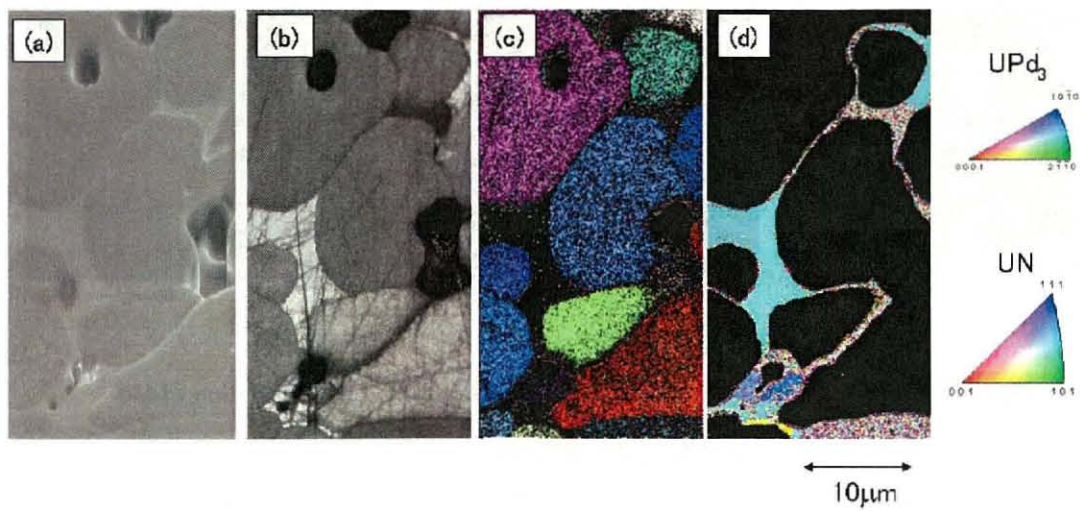


Fig. 4.109 UN+Pd-L (a) SEM image (b) IQ map (c) CD map of UN (d) CD map of UPd₃

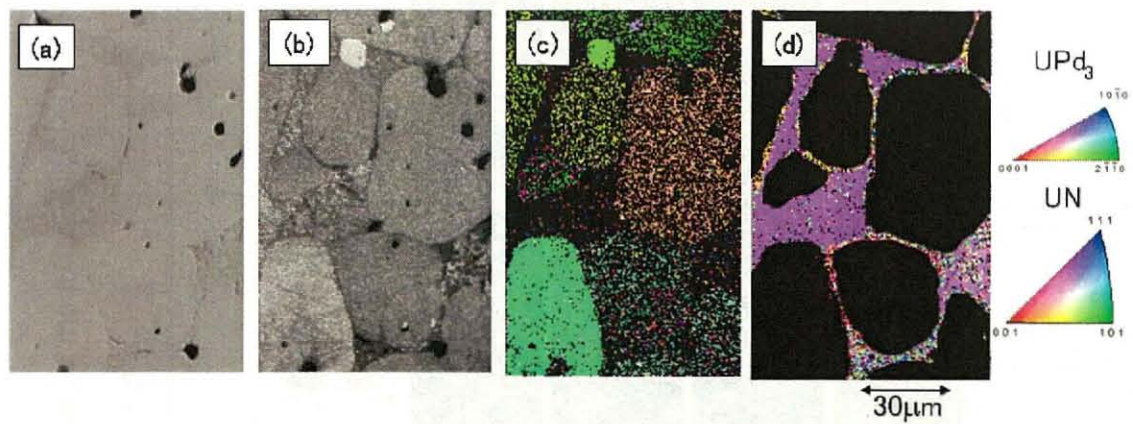


Fig. 4.110 UN+Pd-H (a) SEM image (b) IQ map (c) CD map of UN (d) CD map of UPd_3

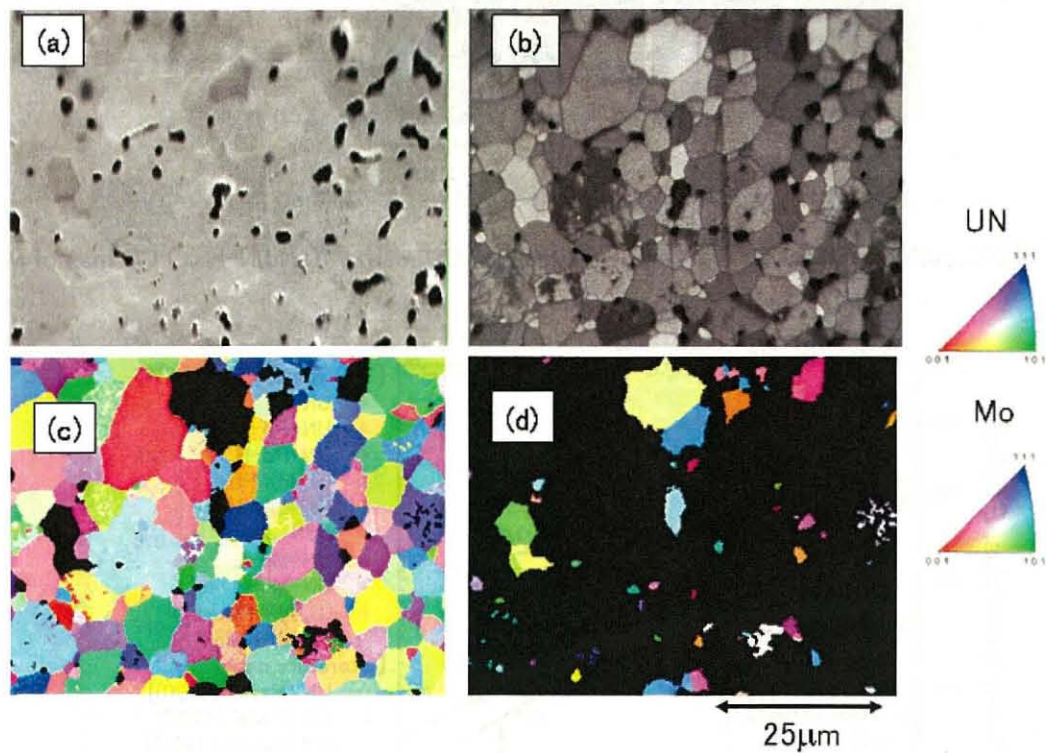


Fig. 4.111 UN+Mo-H (a) SEM image (b) IQ map (c) CD map of UN (d) CD map of Mo

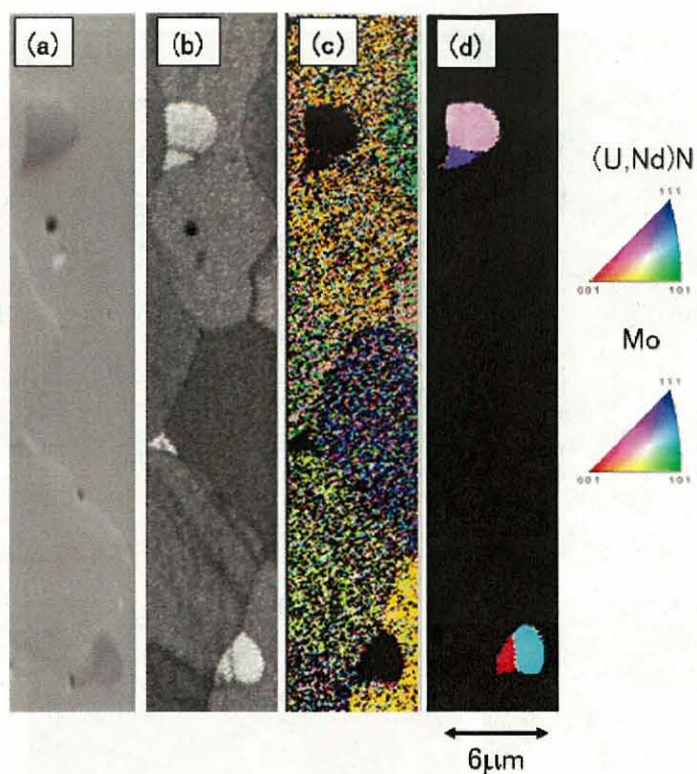


Fig. 4.112 (U,Nd)N+Mo-H (a) SEM image (b) IQ map (c) CD map of (U,Nd)N-H (d) CD map of Mo

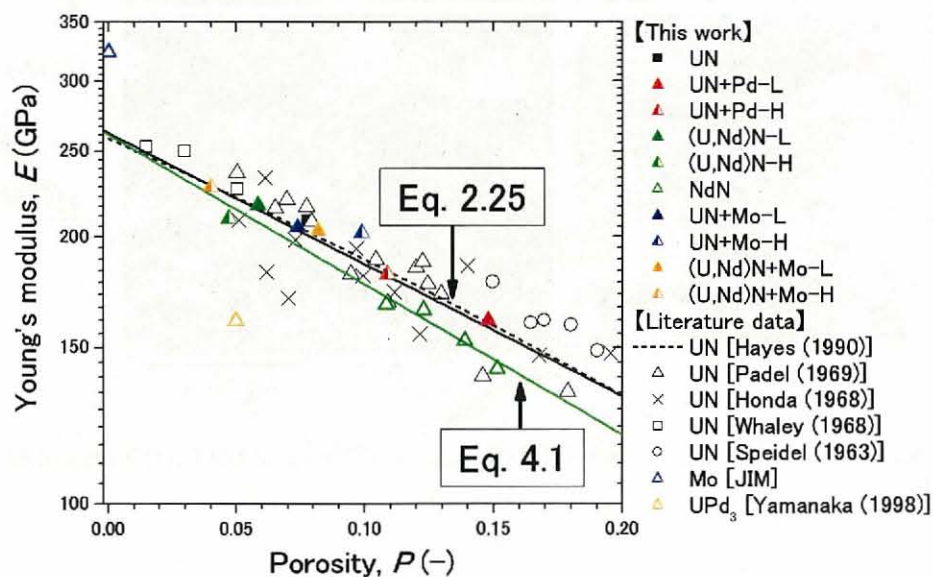


Fig. 4.113 Porosity dependences of Young's modulus of UN, UN+Pd, (U,Nd)N, UN+Mo, (U,Nd)N+Mo and NdN, together with literature data [11, 24-29]

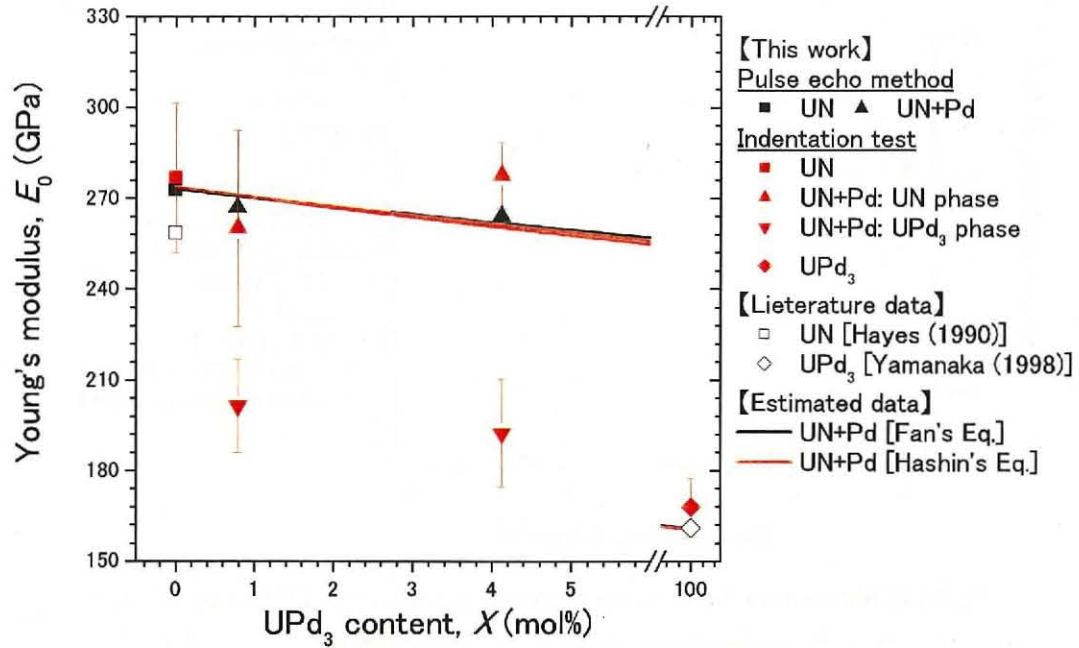


Fig. 4.114 UPd_3 content dependence of Young's modulus of UN+Pd at $P=0$, together with literature data [11, 24]

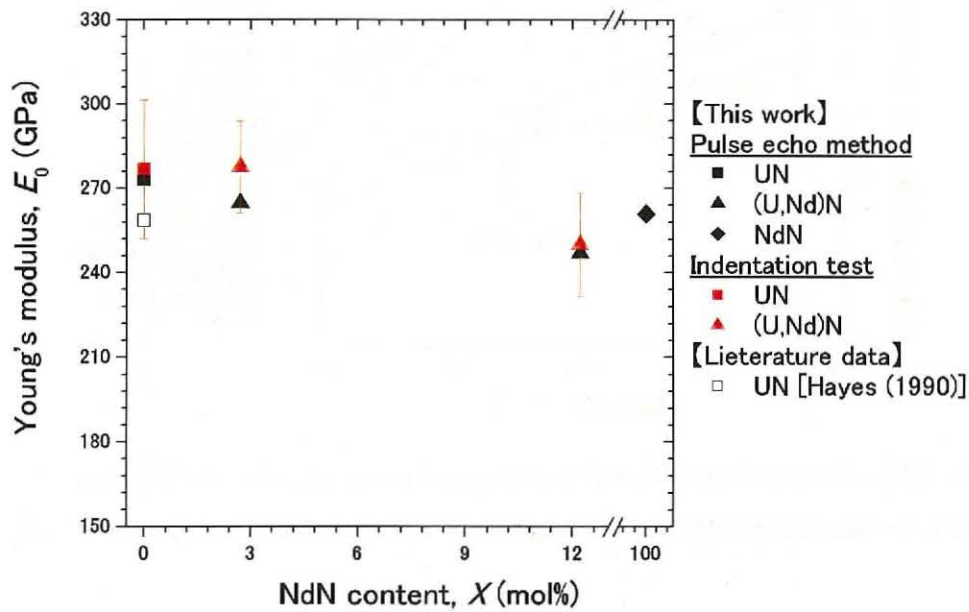


Fig. 4.115 NdN content dependence of Young's modulus of (U,Nd)N at $P=0$, together with the literature data [24]

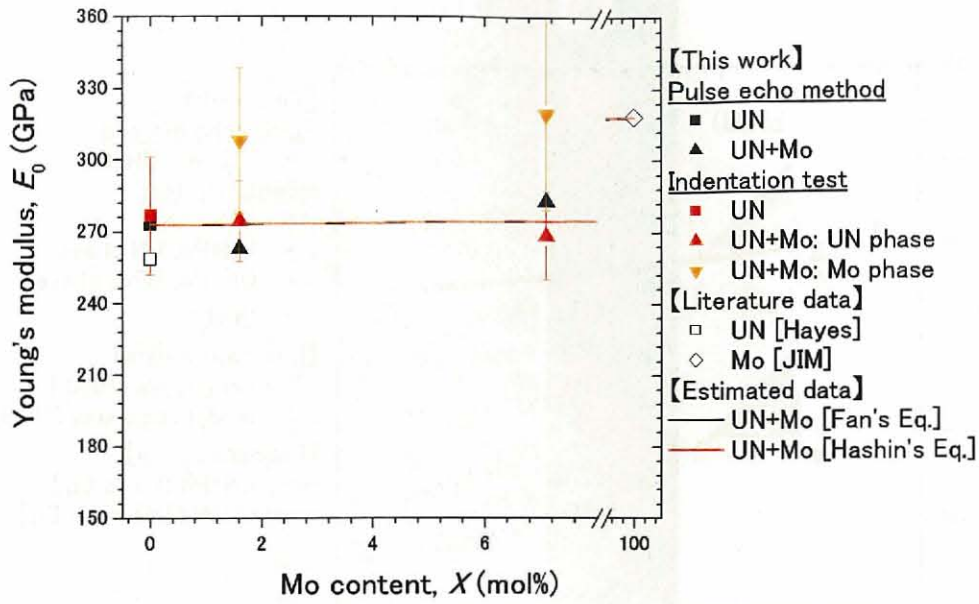


Fig. 4.116 Mo content dependence of Young's modulus of UN+Mo at $P=0$, together with the literature data [23, 29]

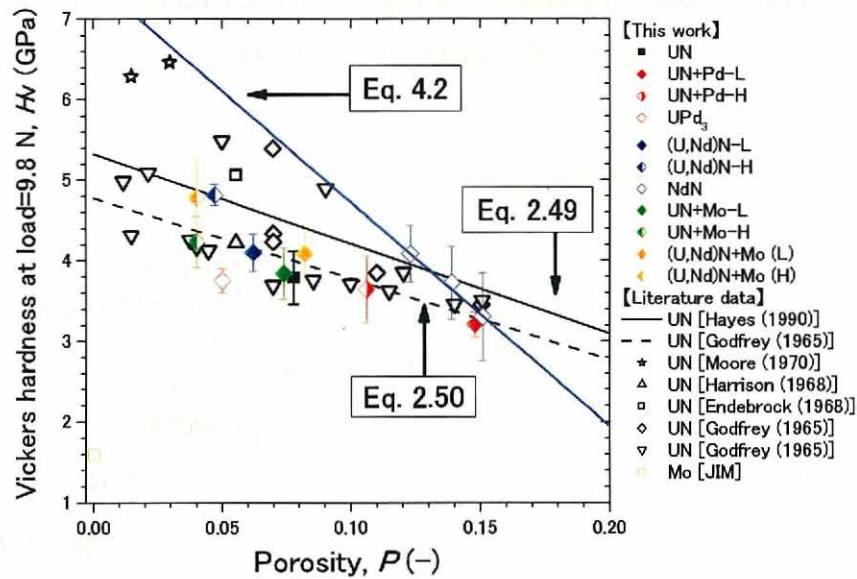


Fig. 4.117 Porosity dependence of Vickers hardness of UN, UN+Pd, UPd_3 , (U,Nd)N, NdN, UN+Mo, (U,Nd)N+Mo and Mo, together with the literature data [24, 29, 34–38]

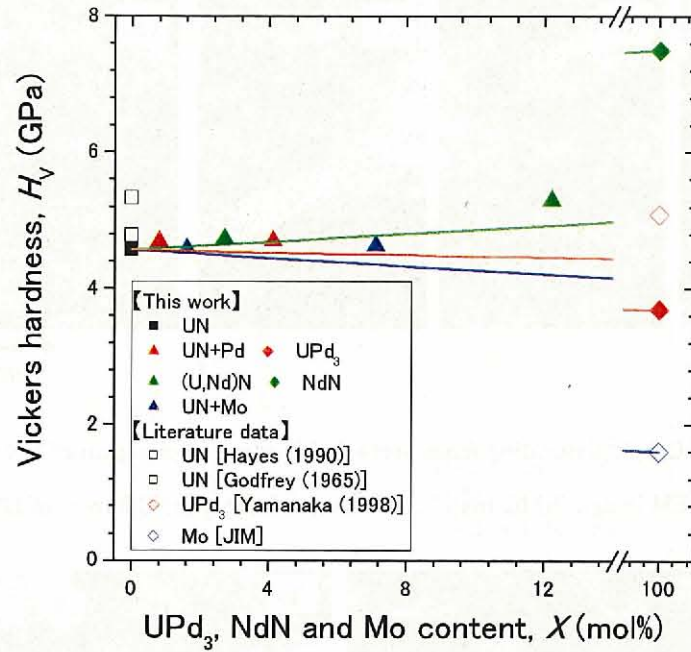


Fig. 4.118 Vickers hardness of UN+Pd, (U,Nd)N, and UN+Mo at $P=0$ and $F=9.8\text{N}$ as the function of UPd_3 , NdN and Mo content, together with the literature data [11, 24, 29, 34]

In this figure, the straight lines represent the addition match of UN and UPd_3 , NdN or Mo.

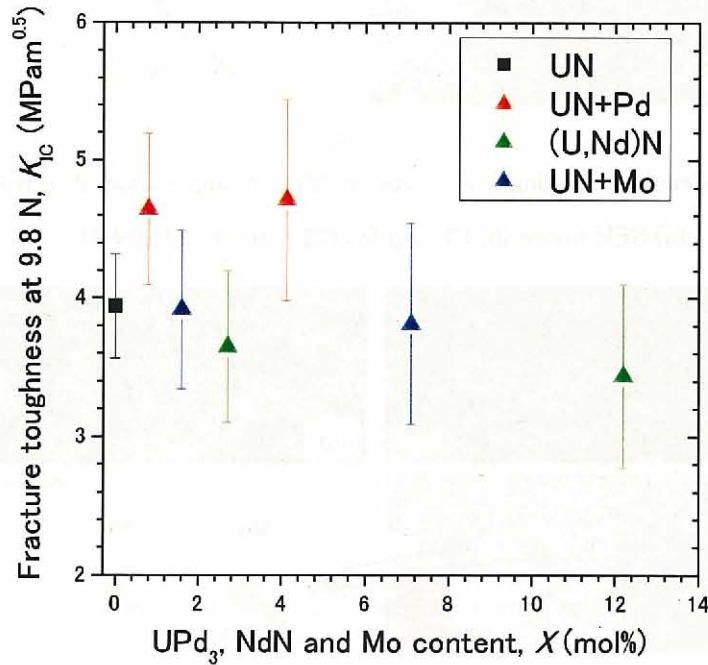


Fig. 4.119 Fracture toughness of UN+Pd, (U,Nd)N, and UN+Mo as the function of UPd_3 , NdN and Mo content

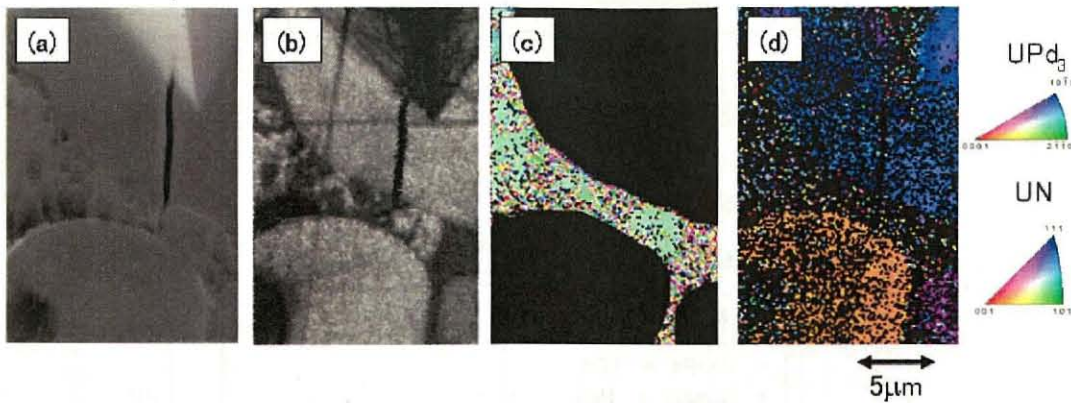


Fig. 4.120 Crack generating from vertex of Vickers impression of UN+Pd-H

(a) SEM image (b) IQ map (c) CD map of UPd_3 (d) CD map of UN

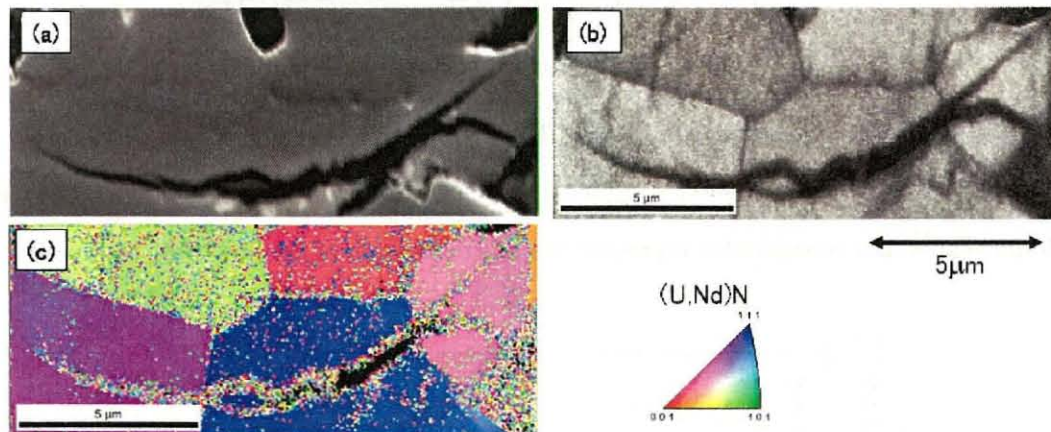


Fig. 4.121 Crack generating from vertex of Vickers impression of (U,Nd)N-H

(a) SEM image (b) IQ map (c) CD map of (U,Nd)N-H

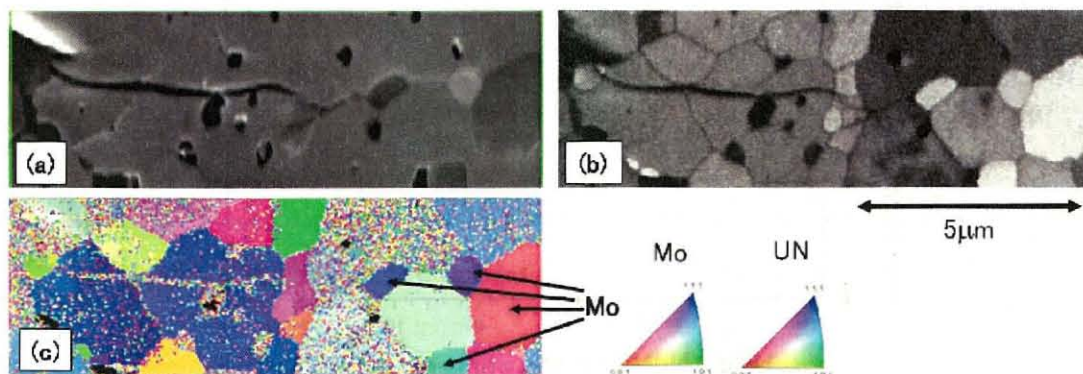


Fig. 4.122 Crack generating from vertex of Vickers impression of UN+Mo-H

(a) SEM image (b) IQ map (c) CD map of UN and Mo

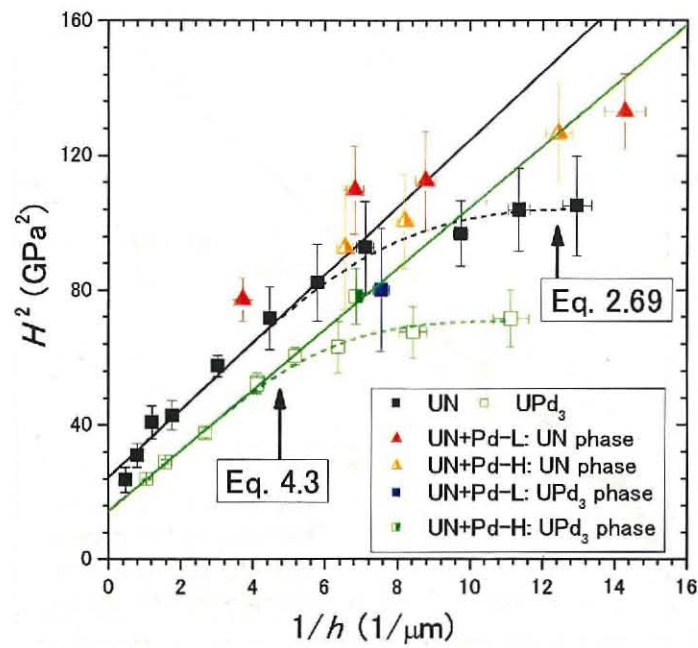


Fig. 4.123 Square of indentation hardness vs. inverse of depth (UN+Pd and UPd_3)

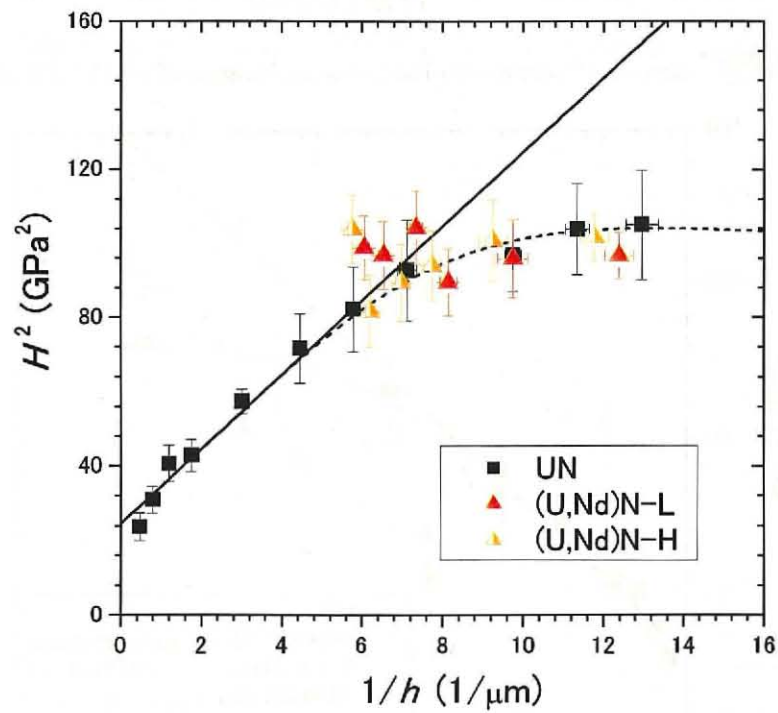


Fig. 4.124 Square of indentation hardness vs. inverse of depth ((U,Nd)N)

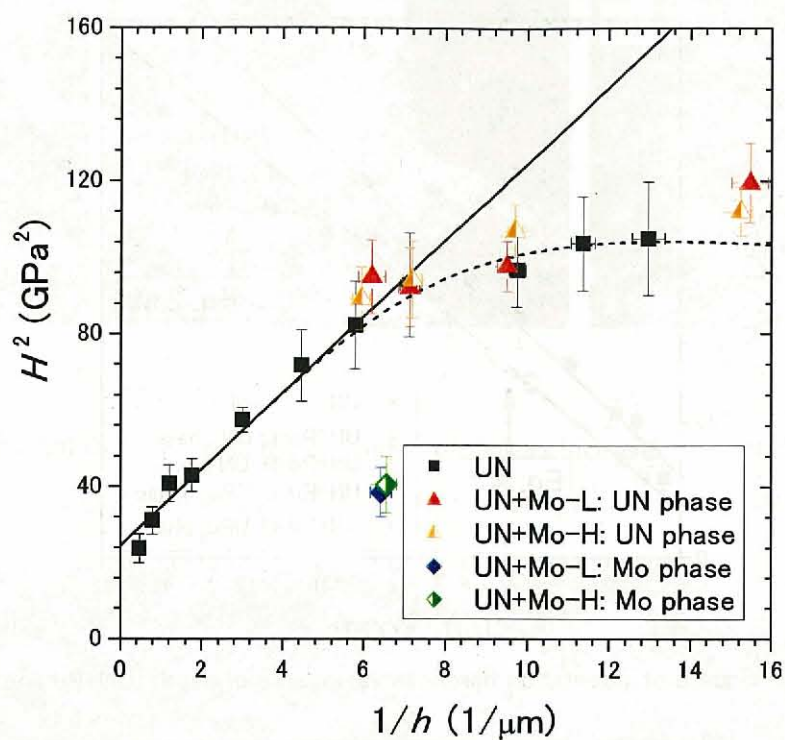


Fig. 4.125 Square of indentation hardness vs. inverse of depth (UN+Mo)

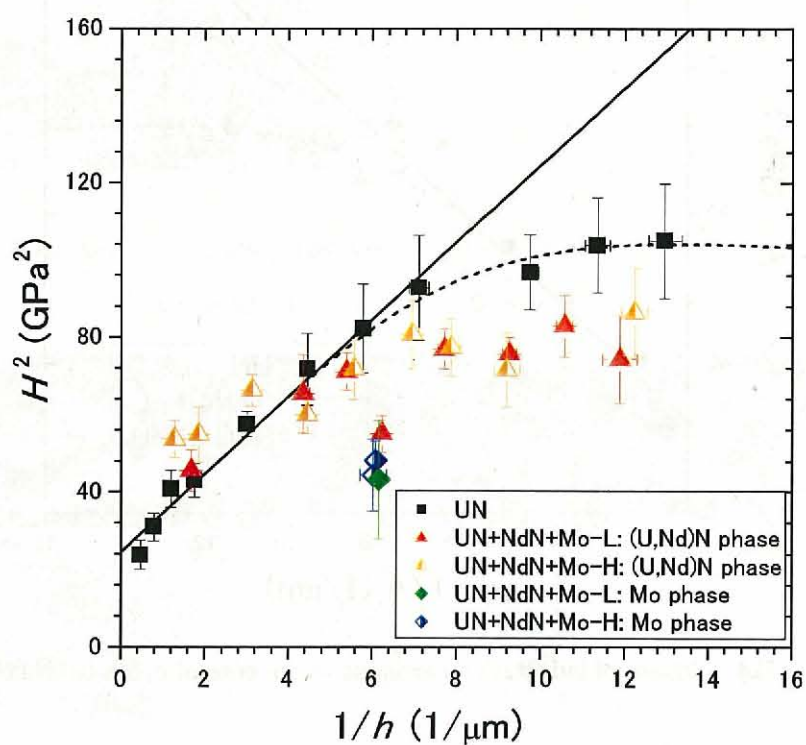


Fig. 4.126 Square of indentation hardness vs. inverse of depth ((U,Nd)N+Mo)

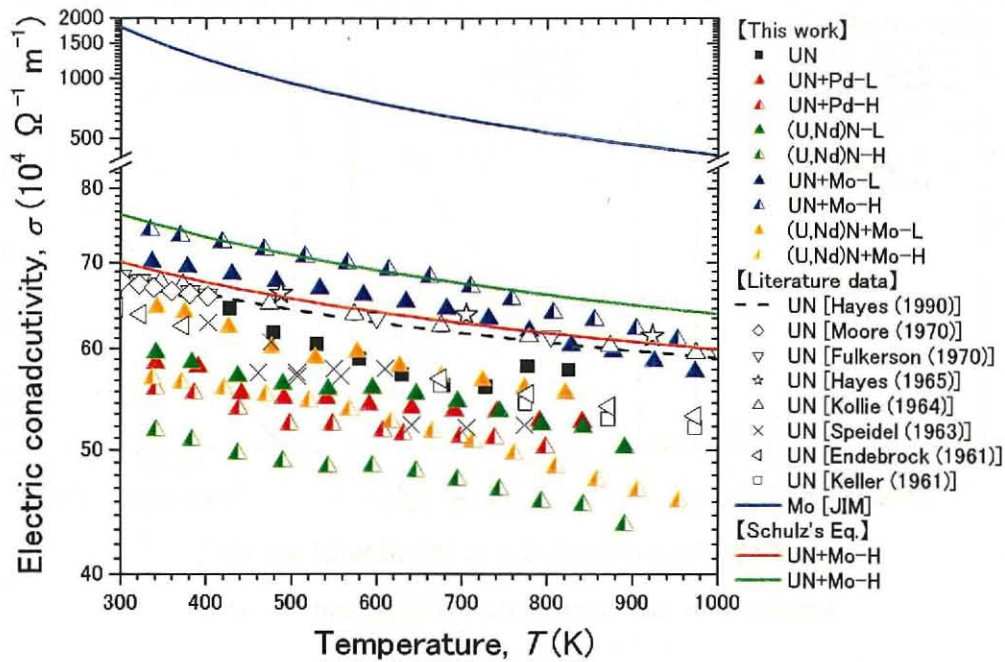


Fig. 4.127 Temperature dependence of electrical conductivity of UN, UN+Pd, (U,Nd)N, UN+Mo, (U,Nd)N+Mo, together with the literature data of UN [28, 29, 35, 40–45]

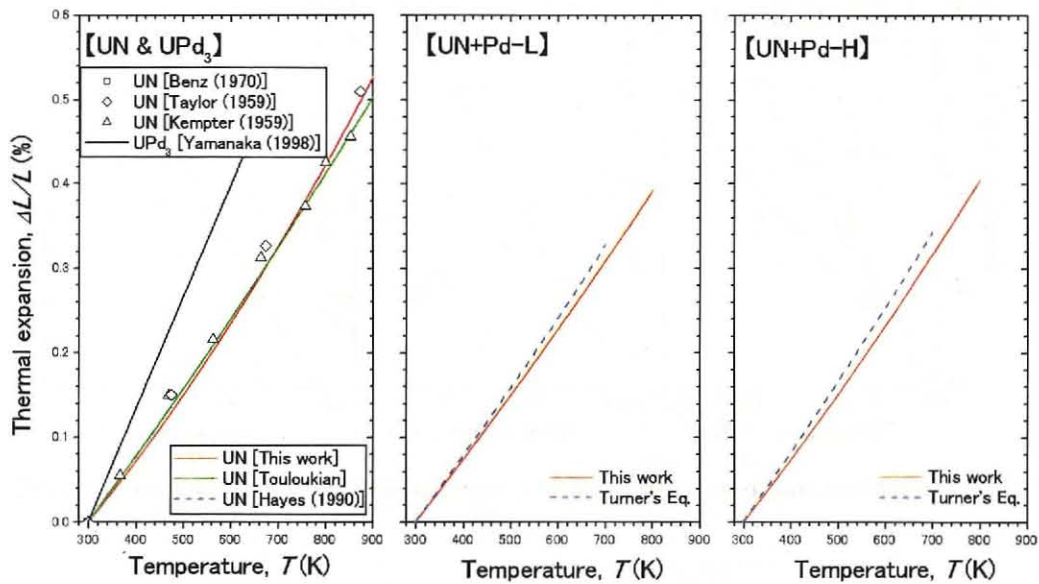


Fig. 4.128 Thermal expansion of UN, UN+Pd-L and UN+Pd-H, together with the literature data [11, 47–51]

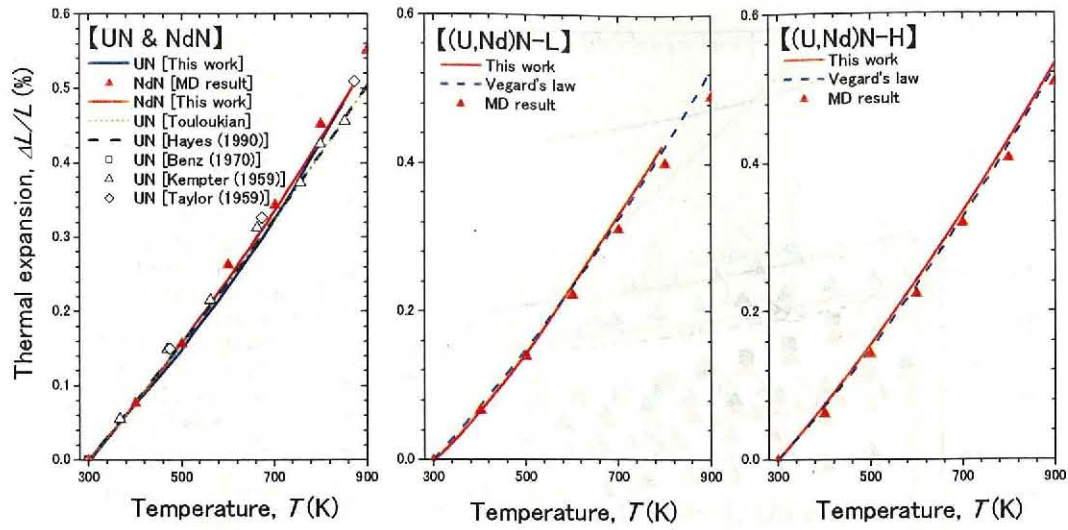


Fig. 4.129 Thermal expansion of UN, (U,Nd)N and NdN, together with the literature data [47–51] and MD result

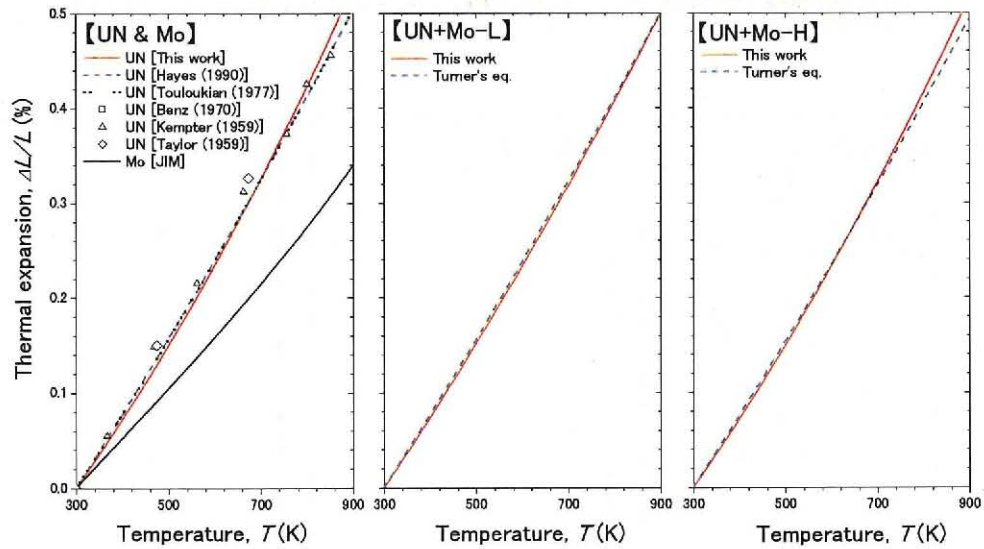


Fig. 4.130 Thermal expansion of UN and UN+Mo, together with the literature data [19, 47–51]

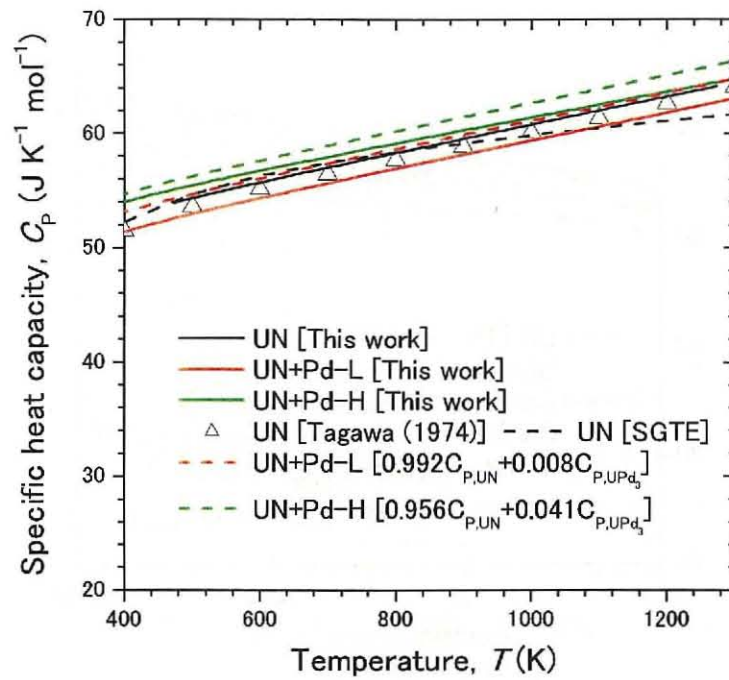


Fig. 4.131 Temperature dependence of specific heat capacity of UN and UN+Pd, together with the literature data [54, 55]

In this figure, the dot lines represent the data estimated from the experimental data of UN [Chapter 2] and UPd₃ [57].

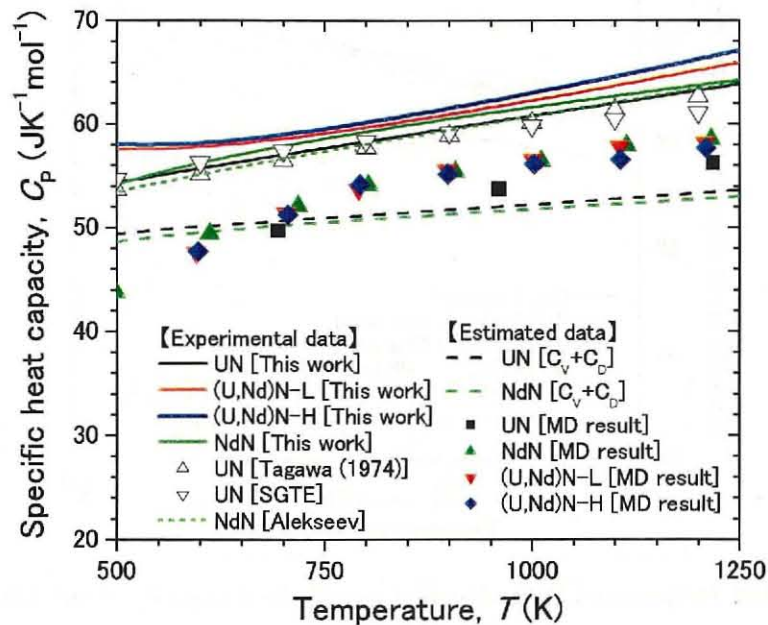


Fig. 4.132 Temperature dependence of specific heat capacity of UN, (U,Nd)N and NdN, together with the literature data [54–56]

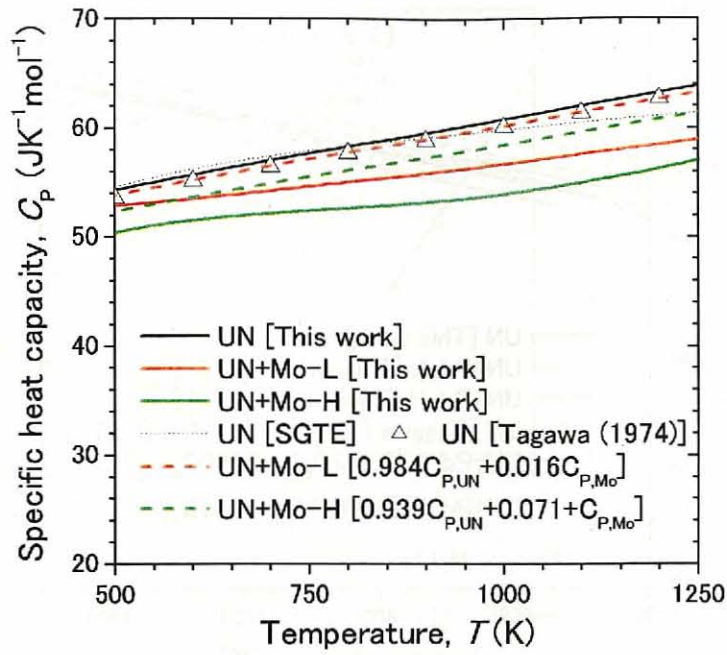


Fig. 4.133 Temperature dependence of specific heat capacity of UN, UN+Mo together with the literature data [54, 55]

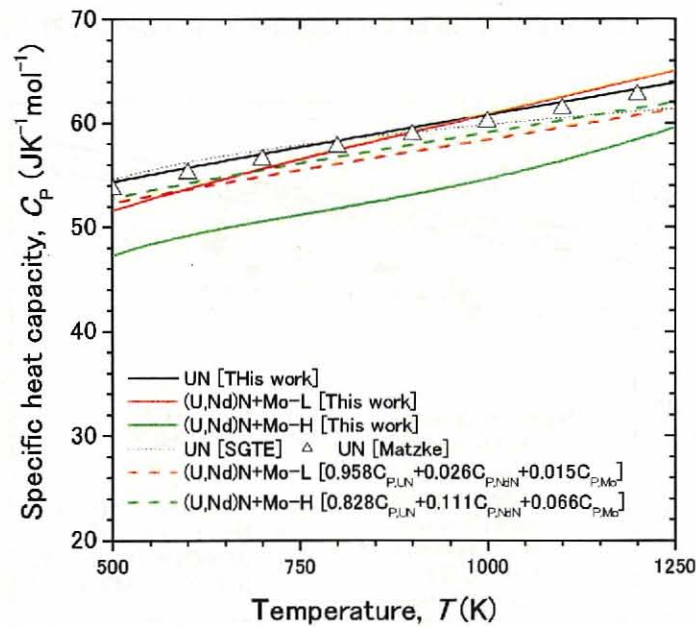


Fig. 4.134 Temperature dependence of specific heat capacity of UN, UN+Mo together with the literature data [54, 55]

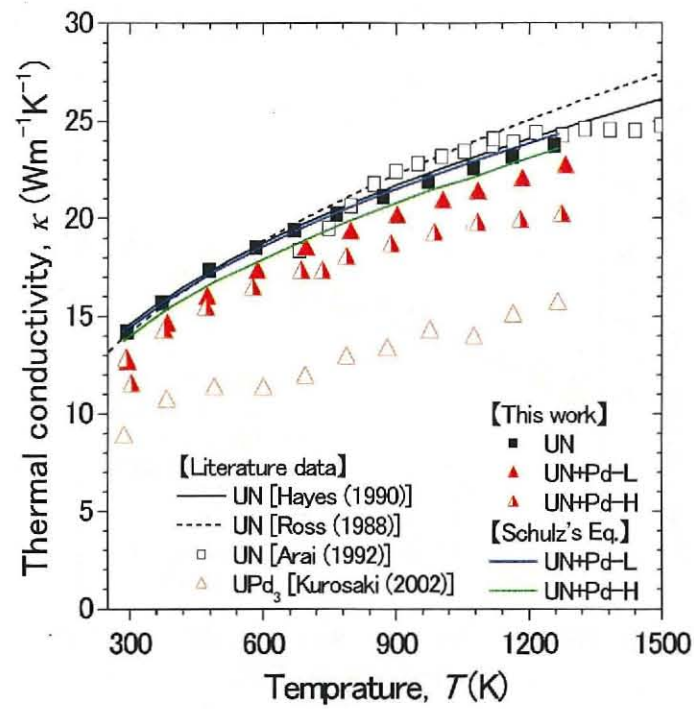


Fig. 4.135 Temperature dependence of thermal conductivity of UN, UN+Pd together with the literature data [12, 40, 59, 60]

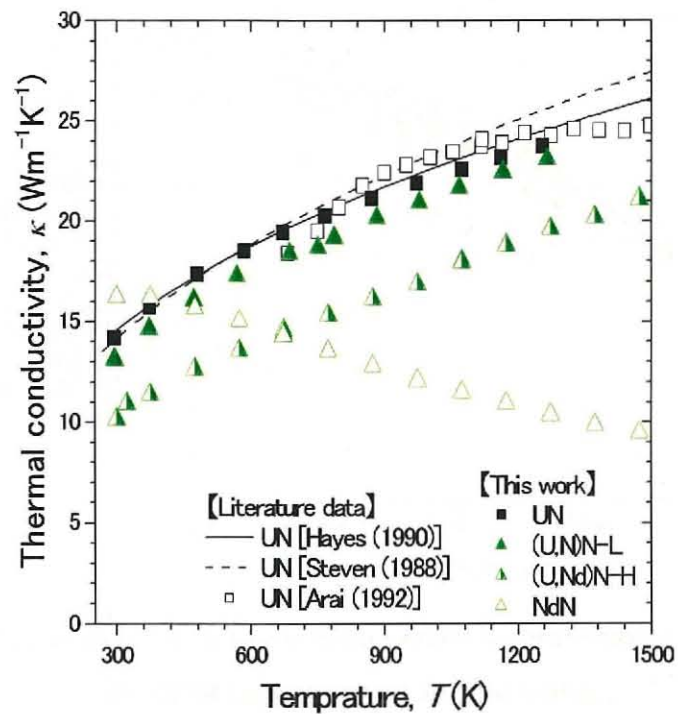


Fig. 4.136 Temperature dependence of thermal conductivity of UN, (U,Nd)N, NdN, together with the literature data [40, 59, 60]

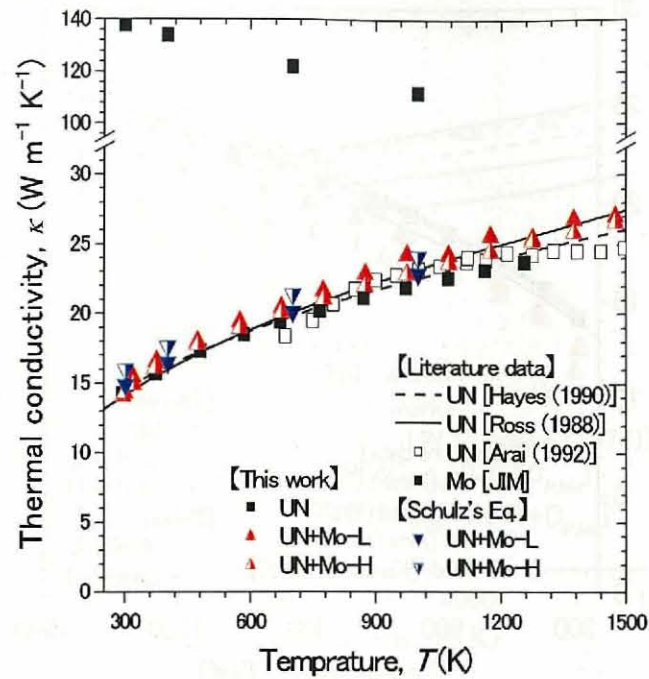


Fig. 4.137 Temperature dependence of thermal conductivity of UN, UN+Mo, together with the literature data [29, 40, 59, 60]

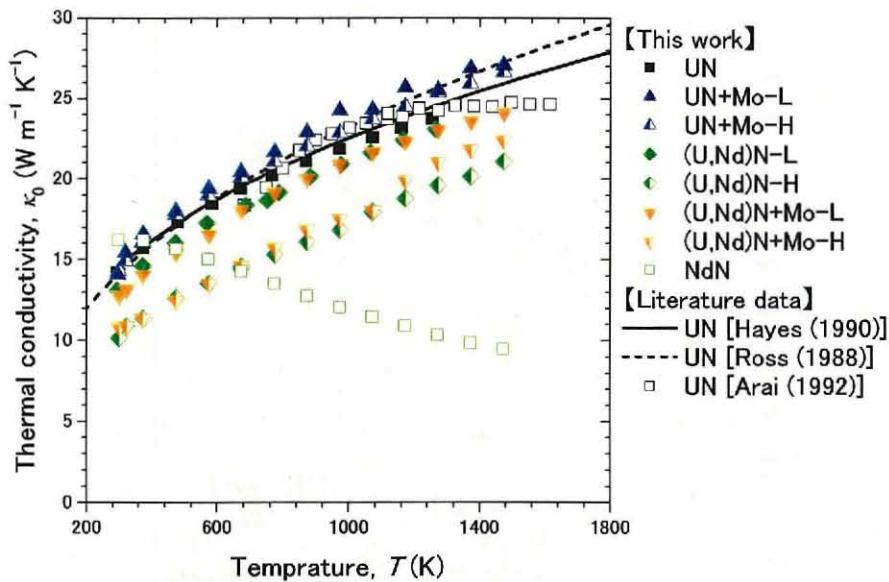


Fig. 4.138 Temperature dependence of thermal conductivity of UN, (U,Nd)N, UN+Mo, (U,Nd)N+Mo, together with the literature data [40, 59, 60]

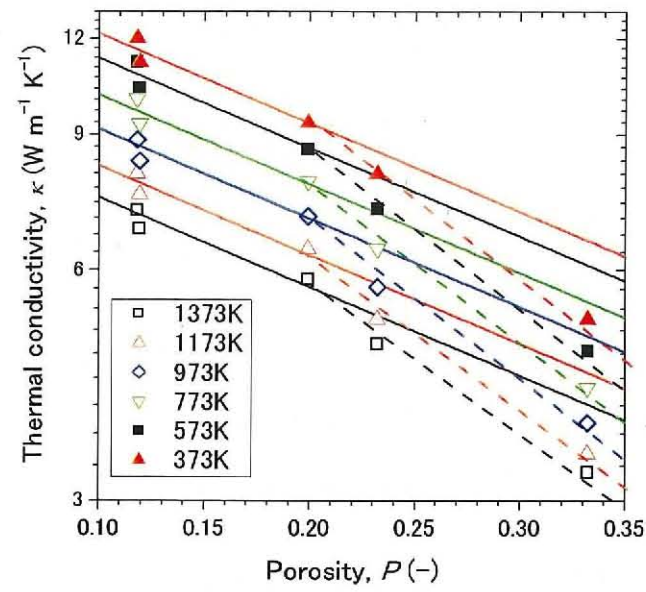


Fig. 4.139 Porosity dependence of thermal conductivity of NdN

Chapter 5: Thermodynamics modeling of U-N and Pu-N binary system

5-1 Background

When we evaluate the integrity of the advanced nuclear fuels, it is important to know the chemistry state of nuclear fuels in the reactor core. In particular, it is remarkable in case of the nitride fuel because it was written in Ref. 1 that it is necessary to understand the FCI and thermal dissociation at the meltdown. Therefore, we must evaluate the phase diagram of U-Pu-N ternary system. The phase diagrams of U-N, Pu-N and U-Pu binary system have been experimentally obtained, but it is necessary to storage the information as the thermodynamics data (Gibbs energy) of each phase. In fact, ACTINET constructed by ITU at German, CEA at France, KTH at Sweden, C. Thermo at Sweden and so on is promoting FUELBASE project [2], in which a thermodynamic database for advanced nuclear fuels is constructed. In FUELBASE project, the binary systems of metal-nitrogen, metal-carbon and so on are just now being modeled. The binary systems modeling in FUELBASE project are summarized in Table 5.1. In addition to the binary systems, they are modeling the ternary systems such as C-N-Ti, C-Si-Ti, C-Mo-Ti, C-Mo-Si, U-Pu-C, U-O-C, Pu-O-C, U-Ti-C, U-Zr-C and U-Si-C. In the present study, the phase diagrams of U-N and Pu-N binary system were calculated by CALPHAD (CALculation of PHase Diagram) method, which connects the experimental thermodynamics information with the phase diagram.

5-2 Thermodynamics modeling

The principle of CALPHAD is based on that the phase in a system appear so as to minimize the sum of the Gibbs energy of each phase [3]. The CALPHAD method has been used well at various companies and academies. The thermodynamic parameters are assessed taking into account all the existing experimental results, such as phase diagram information or chemical potential results. In the present study, Thermo-Calc [4], which had been developed by the Royal Institute of Technology of Sweden, was used as the thermodynamics equilibrium calculation program based on the CALPHAD method. The phases, which exist in U-N and Pu-N binary systems, are summarized in Table 5.2 and 5.3. The Gibbs energy of U-N system was basically modeled by Chevalier (2000) [5]. In the present study, the author modeled the Gibbs energy of each phase in Pu-N binary system and improved the Gibbs energy of each phase in U-N binary system, which was modeled by Chevalier (2000) [5]. The details of the determination of various compounds are described in the follows.

Pure element

The Gibbs energy (G) for an element A at the absolute temperature of T K, a pressure of P and a phase of Φ is expressed using the enthalpy (H) and entropy (S) as follows:

$$G_A^{\circ\Phi}(T) - H_A^{\circ\text{SER}}(298.15\text{K}) = H_A^{\circ\Phi}(T) - H_A^{\circ\text{SER}}(298.15\text{K}) - T[S_A^{\circ\Phi}(T) - S_A^{\circ\text{SER}}(298.15\text{K})] \quad (5.116)$$

where $H_A^{\circ\text{SER}}(298.15\text{K})$ and $S_A^{\circ\text{SER}}(298.15\text{K})$ are the enthalpy and entropy of the element as the 'stable element reference'. The enthalpy and entropy are estimated from the specific heat capacity (C_p) by Eq. 5.2.

$$H_A^{\circ\Phi}(T) - H_A^{\circ\text{SER}}(298.15\text{K}) = \int_{298.15}^T C_p dT \quad (5.117)$$

$$S_A^{\circ\Phi}(T) - S_A^{\circ\text{SER}}(298.15\text{K}) = \int_{298.15}^T \left(\frac{C_p}{T} \right) dT \quad (5.118)$$

The specific heat is generally given the empirical following equation;

$$C_p = a + bT + cT^2 + dT^{-2} \quad (5.119)$$

where a , b , c and d are the constants. Therefore, the molar Gibbs energy is given by the following equation.

$$\begin{aligned} G_A^{\circ\Phi}(T) - H_A^{\circ\text{SER}}(298.15\text{K}) &= \int_{298.15}^T C_p dT - T \int_{298.15}^T \left(\frac{C_p}{T} \right) dT \\ &= \left[aT + \frac{b}{2}T^2 + \frac{c}{3}T^3 - \frac{d}{T} \right]_{298.15}^T - T \left[a \ln T + bT + \frac{c}{2}T^2 - \frac{d}{2T^2} \right]_{298.15}^T \\ &= a' + b'T + c' \ln T + d'T^2 + e'T^3 + f'T^{-1} \end{aligned} \quad (5.120)$$

where a' , b' , c' , d' , e' and f' are the constants estimated from a , b , c and d .

Stoichiometric compound

For a compound C with the chemical formula of $A_{x_A} B_{x_B}$, the molar Gibbs energy is expressed as follows;

$$G_{m,C}(T) = (x_A G_A^{\circ\text{SER}}(T) + x_B G_B^{\circ\text{SER}}(T)) + a' + b'T + c' \ln T + d'T^2 + e'T^3 + f'T^{-1} \quad (5.121)$$

where $G_A^{\circ, \text{SER}}(T)$ and $G_B^{\circ, \text{SER}}(T)$ are the Gibbs energies defined by Eq. 5.1, and the coefficients χ_A and χ_B are the stoichiometric ratio of A and B in the compound C , respectively. These coefficients have the following relation;

$$\chi_A + \chi_B = 1. \quad (5.122)$$

Solid Solution

The solid solution is categorized into the substitutional and the interstitial solution group. Since all of the solid solutions in the present study are in the interstitial solution group, only the model for the interstitial solution is discussed. A sub-lattice model [6] expresses a phase which is impossible to be described as a simple ideal solution. This model gives the divided several lattices, and the interactions in the identical lattice are expressed as the regular solution and those between the different lattices are expressed as a function of temperature. For example, when a phase consists of the matrix element A and interstitial B , this phase is expressed as $[A]_a[B, Va]_b$, where Va denotes the vacancy and the ratio of b/a is defined by the crystal structure. Since the elements B locate different sub-lattices, these elements do not occupy the same interstices. The sub-lattices for UN and α -U₂N₃ are hypothesized as $[N, Va]_1[U]_1$ and $[N]_3[U, Va]_2$, respectively, based on the sub-lattices by Chevalier (2000) [5]. Then the molar Gibbs energies of these phases are expressed as the sum of the three terms;

$$G_m^\Phi(T) - \sum_{i=A,B} \chi_i^\Phi H_i^{\circ, \text{SER}}(298.15 \text{ K}) = G^{\text{mix}, \Phi} + G^{\text{id}, \Phi} + G^{\text{ex}, \Phi}. \quad (5.123)$$

The left side in Eq. 5.4 is the Gibbs energy for the phase Φ with the references of the enthalpies consisted from the pure elements. The first term of the right side in Eq. 5.8 is expressed as follows;

$$G^{\text{mix}, \Phi} = \frac{1}{a + by_B^\text{II}} [y_{Va}^\text{II} (G_{A:Va}^{\circ, \Phi}(T) - aH_A^{\circ, \text{SER}}(298.15 \text{ K})) + y_B^\text{II} (G_{A,B}^{\circ, \Phi}(T) - aH_A^{\circ, \text{SER}}(298.15 \text{ K}) - bH_B^{\circ, \text{SER}}(298.15 \text{ K}))]. \quad (5.124)$$

This term is the simple mixture of the Gibbs energies for the components of $[A]_a[B, Va]_b$. The y_i^N is the site fraction of the element i in the sub-lattice N. The second term is expressed as follows;

$$G^{\text{id}, \Phi} = \frac{1}{a + by_B^\text{II}} \left[b \sum_{i=B, Va} y_i^\text{II} \ln y_i^\text{II} \right].$$

(5.125)

This term is the contribution of entropy of mixture between vacancies and interstices. The third term is required when this phase is the regular solution, and is expressed as follows;

$$G^{\text{ex},\Phi} = \frac{1}{a + by_B^{\text{II}}} (y_B^{\text{II}} y_{\text{Va}}^{\text{II}} L_{\text{A:B,Va}}^{\Phi}),$$

(5.126)

where L is called as the interaction parameter and expressed as Muggianu's Redlich–Kister [7].

$$L_{\text{A:B,Va}}^{\Phi} = \sum_n^n L_{\text{A:B,Va}}^{\Phi} [y_B^{\text{II}} - y_{\text{Va}}^{\text{II}}]^n,$$

(5.127)

$$L_{\text{A:Va,Va}}^{\Phi} = \sum_n^n L_{\text{A:Va,Va}}^{\Phi} [y_B^{\text{II}} - y_{\text{Va}}^{\text{II}}]^n.$$

(5.128)

The Gibbs energies for these phases are also expressed by Eq. 5.10 and 5.11, the Gibbs energy parameters of condensed pure elements and stoichiometric compounds in the N–U and Pu–N binary systems are summarized in Table 5.4 and 5.5. Table 5.6 shows the Gibbs energy parameters of condensed solutions in the U–N binary system.

5-3 Assessment method

Using the Scientific Group Thermodata Europe (SGTE) database [9], the author calculated the Gibbs free energy of α U, β U, γ U, liquid phase and gas phase in U–N binary system, and all phases in Pu–N binary system.

The phase diagrams of U–N and Pu–N binary systems were reported in a compilation work by Massalski (1990) [9] and Okamoto (1997) [10]. Hansen (1958) [11] reported that the nitrogen could not be found in pure U (<100 ppm or 0.01 wt.% over the entire range 823–1173 K).

The melting point of UN was determined as 2923 ± 100 K by Chiotti (1952) [12], 2753 ± 50 K by Newkirk (1959) [13], 3123 ± 30 K by Bugl (1964) [14], 3078 K by Okamoto (1997) [10].

The U–N partial phase diagram was determined by Benz (1966) [15] using XRD, metallographic, chemical and thermal analyses of phases equilibrated with N_2 (up to 5atm), at temperatures up to 3123 K. The uranium-rich side is of eutectic type (composition near pure U). The phase boundaries of UN were measured as (N/U=0.96 \pm 0.02, T=1773 K), (N/U=0.92 \pm 0.02, T=2073 K) and (N/U=1.04 \pm 0.02, T=1873 K). However, Benz (1970) [16] corrected this data as

(N/U=0.991, T=1973 K) and (N/U=0.997±0.006, T=3073 K). In the present study, the author adjusted the Gibbs free energy of UN until the calculated result reproduced the data of Benz (1970) [16]. In the adjusting process, the author assumed that the lattice stability of $[U]_{0.5}[Va]_{0.5}$, which is the fictive pure U metal with NaCl type structure, was 50000 J. The author reformed the entropy at room temperature ($S^{\circ}f_{298.15K}$) (62.42528 Jmol⁻¹K⁻¹) and specific heat capacity (Eq. 5.14) evaluated by Tagawa (1974) [17].

$$UN [17]: C_p = 54.15 + 22.81 \times 10^{-4} T + 4.372 \times 10^{-6} T^2 - 6.813 \times 10^5 T^{-2} \quad (5.129)$$

The heat of formation ($H^{\circ}f_{298.15K}$) of UN evaluated by Gross (1962) [18] was referred in the present study.

The phase relations of αU_2N_3 and βU_2N_3 were experimentally studied by Bugl (1964) [14], Tagawa (1971) [19], Lapat (1964) [20], Nauomidis (1967) [21], Katsura (1993) [22], Serizawa (1996) [23], Nishimaki (1998) [24] and Nakagawa (1998) [25]. In these literatures, the transition temperature from αU_2N_3 to βU_2N_3 was 1393 K and βU_2N_3 decomposed to UN and N₂ gas at 1623 K. The mean value content of αU_2N_3 and βU_2N_3 were 1.645 and 1.425. The non-stoichiometry range of αU_2N_3 was UN_{1.54–1.75} and βU_2N_3 was near the line compound. The author referred the $S^{\circ}f_{298.15K}$ (64.76832 Jmol⁻¹K⁻¹), specific heat capacity (Eq. 5.15) and $H^{\circ}f_{298.15K}$ (24509.034 Jmol⁻¹) evaluated by Councill (1966) [26], Tagawa (1974) [17] and Johnson (1981) [27].

$$\alpha U_2N_3 [17]: C_p = 26.11 + 0.75873 \times 10^{-2} T - 6.61746 \times 10^5 T^{-2} \quad (5.130)$$

The compound existing in Pu–N binary system is only PuN. In the same way of U–N binary system, the nitrogen doesn't resolve in pure Pu. Fee (1975) [28] suggested that PuN was the non-stoichiometric compound at high temperature. However, in the present study, the author handled PuN as the stoichiometric compound due to the shortage of the data for the non-stoichiometry of PuN. There is no data of the melting heat of PuN. So, the author determined the melting heat of PuN by fitting between the calculated results and experimental data of the melting curves.

In both case of U–N and Pu–N binary systems, the author assumed that the liquid phase is the ideal solution, because there is no data of the liquid phase.

5-4 Optimization results

Fig. 5.1 and 5.2 show the phase diagram of U–N and Pu–N binary systems, together with the experimental data [9, 14–16, 20, 21, 23, 28, 29]. From these figures, it was confirmed that the overall agreement is quite satisfactory. The calculated phase diagram compared to the experimental data. Fig. 5.3 shows the partial phase diagram of U–N binary system, together with the experimental data [14–16, 29], focuses on the non-stoichiometry part of UN. From this figure, it was found that the calculated phase boundary of UN faithfully reproduced the experimental data by Benz (1970) [16]. In addition, the transition temperature from α U_2N_3 to β U_2N_3 and decomposition temperature of β U_2N_3 calculated by CALPHAD method was well consistent with the experimental data edited by Shunk (1969) [29].

The calculated specific heat capacity of the stoichiometric compound UN and PuN are shown in comparison with the experimental data [8, 17, 30–34] in Fig. 5.4. From this figure, the calculated results are within the variation of the experimental data [8, 17, 30–34]. From these results, it is thought that we can reproduce the thermodynamics properties of U–N and Pu–N binary systems using the database modeled in the present study.

5-5 Summary

In the present study, U–N and Pu–N binary systems were assessed thermodynamically from the criticism of the available experimental data on both phase diagram and thermodynamics properties.

The liquid phase was described by an ideal associate model, UN and α U_2N_3 by a non-ideal two-sublattice model. PuN and β U_2N_3 was considered as a stoichiometric compound.

A consistent set of Gibbs energy parameters for the various phases was obtained. The agreement between the experimental and calculated phase diagram of thermodynamic properties is quite satisfactory.

Ternary compound doesn't exist in U–Pu–N ternary system as shown in Fig. 5.5. From only the Gibbs free energy data of U–N and Pu–N binary systems obtained in the present study and U–Pu binary system evaluated by Kurata (2000) [35], we would model U–Pu–N ternary system. However, Kurata (2007) [36] reported that the experimental phase diagram of U–Pu binary system used in Ref. 35 is not strictly correct. So, his group re-evaluates the phase diagram of U–Pu binary system. The author is going to assessment the U–Pu–N ternary system after Kurata re-evaluates the U–Pu binary system.

Like this way, if we model the thermodynamics database such as the Gibbs free energy of the binary systems based on CALPHAD method, the database of the binary systems allows us to evaluate the thermodynamic database for complex calculations in multi-component systems.

References

- [237] 核燃料サイクル開発機構, 日本原子力発電株式会社, “高速増殖炉サイクルの実用化戦略調査研究: フェーズ I 報告書,” JNC TN 1400 2001-006 (2001).
- [238] C. Guéneau, S. Chatain, S. Gossé, J.-C. Dumas, J.-P. Piron, J. Lechelle, Y. Pontillon, G. Ducros, C. Rado, F. Defoort, K. Froment, N. Dupin, B. Sundman, H. Noël, R. Konings, H. Kinoshita k, C. Utton, “FEULBASE: a thermodynamic database for advanced nuclear fuels,” International Information Exchange Meeting on Thermodynamics of Nuclear Fuels, 27th Nov–1st Dec, 2006, CEA Saclay, France.
- [239] N. Saunders, A. P. Miodownik, “CALPHAD (CALculation of Phase Diagrams): A Comprehensive Guide,” Pergamon press, Tokyo, Japan, 1998.
- [240] B. Sundman, “Thermo-Calc User’s Guide,” Royal Institute of Technology, Sweden, 1995.
- [241] P.-Y. Chevalier, E. Fischer, B. Cheynet, “Thermodynamics modelling of the U-N system,” J. Nuc. Mater. 280[2] (2000) 136–150.
- [242] M. Hillert, L.I. Staffanson, Acta Chem. Scand. 24 (1970) 3618.
- [243] O. Redlich, A. Kister, Ind. Eng. Chem. 40 (1948) 345.
- [244] The SGTE Pure Substance and Solution databases, GTT-DATA SERVICES, (1996).
- [245] T.B. Massalski, H. Okamoto, R.B. Subramanian, L. Kacprzak, “Binary alloy phase diagrams: Second edition,” American society of metals, Ohio, U.S.A., 1986
- [246] H. Okamoto, “N-U (Nitrogen-Uranium),” J. Phase Equilibria 18[1] (1997) 107
- [247] M. Hansen, K. Anderko, “Constitution of Binary Alloys,” McGraw-Hill, New York, U.S.A., 1958.
- [248] P. Chiotti, “Experimental refractory bodies of high-melting nitrides, carbides, and uranium dioxide,” J. Am. Ceram. Soc. 35 (1952) 123.
- [249] H.W. Newkirk, J.L. Bates, “The melting points of uranium dioxide, uranium monocarbide, and uranium mononitride,” US At. Energy Comm. HW-59468 (1959) 5.
- [250] J. Bugl, A.A. Bauer. “Phase relations in the system uranium-nitrogen,” J. Am. Ceram. Soc. 47[9] (1964) 425–429.
- [251] R. Benz. M.G. Bowman, “Some phase equilibriums in the uranium-nitrogen system,” J. Am. Ceram. Soc. 88[2] (1966) 264–268.
- [252] R. Benz, W.B. Hutchinson, “U+N₂ reaction layer growths,” J. Nucl. Mater. 36[2] (1970) 135–146.
- [253] H. Tagawa. “Phase relations and thermodynamic properties of the uranium-nitrogen system,” J. Nucl. Mater. 51[1] (1974) 78–89.

- [254] P. Gross, C. Hayman, H. Clayton, "Thermodynamics of Nuclear Materials," IAEA, Vienna, 1962, p. 653.
- [255] H. Tagawa, "Equilibrium nitrogen pressures and thermodynamic properties of uranium sesquinitride," J. Nucl. Mater. 41 (1971) 313-319.
- [256] P.E. Lapat, R.B. Holden. "Thermodynamics of the uranium-nitrogen system," U.S. At. Energy Comm. UNC-5060 (1963) 27.
- [257] A. Naoumidis, H.J. Stoecker. "Thermodynamic data of UN_x ($X=1.5-1.75$)" Proc. Br. Ceram. Soc. 8 (1967) 193-200.
- [258] M. Katsura, M. Miyake, H. Serizawa, "Some problems in nonstoichiometry of α -uranium sesquinitride," J. Alloys Compd. 193 (1993) 101-103.
- [259] H. Serizawa, K. Fukuda, M. Katsura, "Thermodynamic study of the dissolution of nitrogen in nitrogen-rich α - U_2N_{3+x} ," J. Alloys Compd. 232 (1996) 274-280.
- [260] K. Nishimaki, M. Hirota, T. Nagawa, T.A. Yamamoto, M. Miyake, M. Katsura, "Thermodynamics of nitrogen-rich uranium sesquinitride formation by reaction of uranium monocarbide with ammonia," J. Alloys Compd. 271-273[12] (1998) 654-657.
- [261] T. Nakagawa, K. Nishimaki, T. Urabe, M. Katsura, "Thermodynamic study on α - U_2N_{3+x} using N-rich starting material ($x>0.6$)," J. Alloys Compd. 271-273[12] (1998) 658-661.
- [262] J.F. Counsell, R.M. Dell, J.F. Martin, "Thermodynamic properties of uranium compounds. II. Low-temperature heat capacity and entropy of three uranium nitrides," Trans. Faraday Soc. 62 (1966) 1736-1747.
- [263] G.K. Johnson, E.H.P. Cordfunke, "The enthalpies of formation of uranium mononitride and α - and β -uranium sesquinitride by fluorine bomb calorimetry," J. Chem. Thermodyn. 13 (1981) 273-282.
- [264] D.C. Fee, C.E. Johnson, "Phase equilibriums and melting point data for advanced fuel systems," Nucl. Sci. 32[6] (1975) Abstr. No. 14754.
- [265] F.A. Shunk, "Constitution of binary alloys, second suppl.," McGraw-Hill, New York, 1969.
- [266] F.L. Oetting, J.M. Leitnaker, "The chemical thermodynamic properties of nuclear materials I. Uranium mononitride," J. Chem. Thermodyn. 4 (1972) 199-211.
- [267] C. Affortit, "Specific heats of uranium carbide and uranium nitride," J. Nucl. Mater. 34 (1970) 105-107.
- [268] J.B. Conway, P.N. Flagella, "Physical and Mechanical Properties of Reactor Materials," General Electric Company, GEMP-1012, 1969.

[269] T. Matsui, R.W. Ohse, "Thermodynamic properties of uranium nitride, plutonium nitride and uranium-plutonium mixed nitride," High Temp. – High Press. 19 (1987) 1–17.

[270] F.L. Oetting, "The chemical thermodynamic properties of nuclear materials. III. Plutonium mononitride," J. Chem. Thermodyn. 10[10] (1978) 941–948.

[271] M. Kurata, "Thermodynamic assessment of the Pu-U, Pu-Zr and Pu-U-Zr systems," CALPHAD 23[3–4] (2000) 305–337.

[272] M. Kurata, K. Nakamura, N. Yahagi, K. Nakajima, Y. Arai, Y. Arita, "Development of a fabrication technology of TRU alloy fuel and fuel design for TRU transmutation I. (2) Construction of thermodynamic database for actinide alloy," Abstract of spring meeting of Atomic Energy Society of Japan, 2007, pp. 905 (P24).

Table 5.19 Binary systems evaluated in FUELBASE project

	Mo	N	O	Pu	Si	Ti	U	Zr
C	Andersson (1988)	PURE SGTE	SSUB SGTE	Sundman (2005)	Grobner (1996)	Dumitrescu (1998)	Chevalier (2001)	Guillermet (1995)
	Mo	Frisk (1991)	Bygden (1985)	Dupin (2005)	Liu (2005)	Chung (1999)	Dupin (In progress)	Jerlerud (2002)
		N	PURE SGTE	Sundman (2005)	Hillert (1992)	Jonsson (1996)	Chevalier (2000)	Ma (2004)
			O	Gueneau (2006)	Hallstedt (1993)	Sundman (2005)	Gueneau (2002)	Liang (1997)
				Pu	Dupin (2005)	In progress	Leibowitz (1991)	Kurata (1999)
					Si	Seifert (2000)	Gueneau (1996)	Gueneau (1994)
						Ti	Rado (In progress)	Kumar (1994)
							U	Chevalier (2004)
								Zr

Table 5.20 Phase species in U–N binary system

Solid phase						
Phase	α U	β U	γ U	UN	α -U ₂ N ₃	β -U ₂ N ₃
Composition, at.%N	0	0	0	44–50	60–61	56
Temperature range (K)	0–941	941–1046	1046–1448	0–3078	0–1393	1326–1623
Space group	Cmcm	P4 ₂ /mm	Im $\bar{3}$ m	Fm $\bar{3}$ m	Ia $\bar{3}$	P $\bar{3}$ m1
Prototype	α U	β U	W	NaCl	Mn ₂ O ₃	La ₂ O ₃
$S^\circ f_{298.15K}$ (J/mol/K)	50.20			61.906	61.67	
$H^\circ f_{298.15K}$ (J/mol)	0	–2790	–4757	–294352	–352540	–350680
Liquid phase						
Phase	U(L)	N(L)				
$S^\circ f_{298.15K}$ (J/mol/K)	199.79	153.30				
$H^\circ f_{298.15K}$ (J/mol)	535000	472687				
Gas phase						
Phase	N ₂ (G)					
$S^\circ f_{298.15K}$ (J/mol/K)	191.61					
$H^\circ f_{298.15K}$ (J/mol)	0					

Table 5.21 Phase species in Pu–N binary system

Solid phase							
Phase	α Pu	β Pu	γ Pu	δ Pu	δ' Pu	ε Pu	PuN
Composition, at.%N	0	0	0	0	0	0	50
Temperature range (K)	0–398	398–488	488–593	593–736	736–756	756–913	0–3103
Space group	P2 ₁ /m	C2/m	Fddd	Fm $\bar{3}$ m	I4/mmm	Im $\bar{3}$ m	Fm $\bar{3}$ m
Prototype	α Pu	β Pu	γ Pu	Cu	In	W	NaCl
$S^\circ f_{298.15K}$ (J/mol/K)	54.461						72.383
$H^\circ f_{298.15K}$ (J/mol)	0	3706	478	736.4	1841	2824	–299156

Liquid phase		
Phase	Pu(L)	N(L)
$S^\circ f_{298.15K}$ (J/mol/K)	177.16	153.30
$H^\circ f_{298.15K}$ (J/mol)	348000	472687

Gas phase	
Phase	N ₂ (G)
$S^\circ f_{298.15K}$ (J/mol/K)	191.61
$H^\circ f_{298.15K}$ (J/mol)	0

Table 5.22 Gibbs energy parameters of pure elements compounds in U–N binary system.

$$G_A^{\circ, \Phi}(T) - H_A^{\circ, \text{SER}}(298.15\text{K}) = a' + b'T + c'\ln T + d'T^2 + e'T^3 + f'T^{-1} \text{ for } T_L \leq T < T_H$$

	T_L	T_H	$a' \times 10^3$	b'	c'	$d' \times 10^{-4}$	$e' \times 10^{-8}$	$f' \times 10^4$
$N_2(\text{G})$	298.15	700	-8.381	-0.7071	-28.55	6.974	-105.5	-1.879
	700	1700	-7.527	-25.48	-24.42	-54.41	43.60	
	1700	4100	-19.88	61.14	-36.21	-3.006	0.8003	251.1
	4100	7400	-68.13	193.8	-51.95	20.10	-5.677	304.5
$N_1(\text{G})$	298.15	2700	466.5	-14.04	-20.79	0.2254	-0.3883	
	2700	5100	464.3	3.505	-23.18	9.626	-6.615	12.33
αU	298.15	955	-8.408	131.0	-26.92	12.52	-442.6	3.857
	955	6000	-22.52	292.1	-48.66			
βU	298.15	941.5	-5.156	107.0	-22.84	-108.5	2.789	8.194
	941.5	6000	-14.33	244.2	-42.93			
γU	298.15	1049	-0.7528	131.5	-27.52	-83.56	96.79	20.46
	1049	6000	-4.698	202.7	-38.28			
$\beta \text{U}_2\text{N}_3$	298.15	6000	-151.9	172.9	-29.28	-8.285	-45.20	41.75
UN	298.15	6000	-313.5	314.1	-55.53	-0.7583	-77.68	38.38
$\text{U}(\text{L})-\alpha \text{U}$	298.15	6000	12.36	-10.32				
$\text{N}(\text{L})-\text{N}_2(\text{G})$	298.15	6000	29.95	59.02				
$\beta \text{U}_2\text{N}_3-\text{N}_2(\text{G})-\gamma \text{U}$	298.15	6000	-760.6	632.7	-49.45	98.86	-316.1	172.7

Table 5.23 Gibbs energy parameters of pure elements and compounds in Pu–N binary system.

$$G_A^{\circ\phi}(T) - H_A^{\circ\text{SER}}(298.15\text{K}) = a' + b'T + c'T \ln T + d'T^2 + e'T^3 + f'T^{-1} \text{ for } T_L \leq T < T_H$$

	T_L	T_H	$a' \times 10^3$	b'	c'	$d' \times 10^{-4}$	$e' \times 10^{-8}$	$f' \times 10^4$
α Pu	298.15	400	-7.396	80.30	18.13	224.1	-442.6	3.857
	400	944	-16.61	236.8	-42.42	-13.45	26.34	57.93
	944	6000	-14.46	233.0	-42.2			
β Pu	298.15	679.5	-4.874	123.2	-27.42	-65.30		
	679.5	1464	2.435	43.57	-15.74	-154.8	152.5	-86.49
	1464	6000	-13.96	228.2	-42.25			
γ Pu	298.15	487	-16.77	419.4	-77.58	816.4	-2810	57.48
	487	593.9	-2.943	88.33	-22.02	-114.8		
	593.9	1179	-9.337	160.3	-32.34	-70.38	69.29	63.06
δ Pu	298.15	990	-3.921	127.6	-28.48	-54.04		
	990	1464	3.528	41.53	-15.74	-154.8	152.5	-86.49
	1464	6000	-12.87	226.2	-42.25			
δ' Pu	298.15	736	-0.4962	54.59	-16.43	-240.1	516.7	-15.85
	736	757	-6.122	173.4	-35.56			
	757	2157	3.982	63.89	-19.76	-93.73	65.99	-111.3
	2157	6000	-15.20	228.1	-42.25			
ϵ Pu	298.15	745	-1.359	116.6	-27.09	-91.05	206.2	2.086
	745	956	-2.891	156.9	-33.72			
	956	2071	29.31	-132.8	6.921	-202.3	142.7	-446.9
	2071	6000	-15.40	227.4	-42.25			
PuN	298.15	6000	-316.5	272.8	-50.62	-53.35		26.15
Pu(L)	298.15	400	-0.7882	67.79	-18.13	-224.1		
	400	944	-9.998	224.3	-42.42	-13.45	26.34	57.93
	944	6000	-7.854	220.4	-42.25			
N(L)	298.15	950	26.20	49.57	-12.78	-17.67	0.2681	-3.237
	950	3350	22.59	76.22	-16.37	-6.511	3.010	56.31
	3350	6000	13.56	109.3	-20.47	2.398	-0.8333	459.6
N ₂ (L)	298.15	950	-3.751	-9.454	-12.78	-17.67	0.2681	-3.237
	950	3350	-7.359	17.20	-16.37	-6.511	3.010	56.31
	3350	6000	-16.39	50.26	-20.47	2.398	-0.8333	459.6

Table 5.24 Gibbs energy parameters of condensed solution in the N–U binary system

$$L_{j,kl} = \sum_n L_{j,kl}^n (y_i - y_k)^n L_{j,kl}^n = a_{j,kl}^n + b_{j,kl}^n T$$

Phase	Formula	Excess interaction parameters		
		Name	$a_{j,kl}^n$	$b_{j,kl}^n$
Liquid	$[N_i, N_i U_i, U_i]_i \langle L \rangle$	$L^0[N_i, N_i U_i]_i \langle L \rangle$	0	0
		$L^0[N_i, U_i]_i \langle L \rangle$	0	0
		$L^0[N_i, U_i, U_i]_i \langle L \rangle$	0	0
Fcc_B1	$[N_i, Va]_i [U_i]_i$	$L^0[N_i, Va]_i [U_i]_i$	26878.59	0
α -N ₃ U ₂	$[N_i]_3 [U_i, Va]_2$	$L^0[N_i]_3 [U_i, Va]_2$	-52537.9	87.72937
		$L^1[N_i]_3 [U_i, Va]_2$	128136.7	0

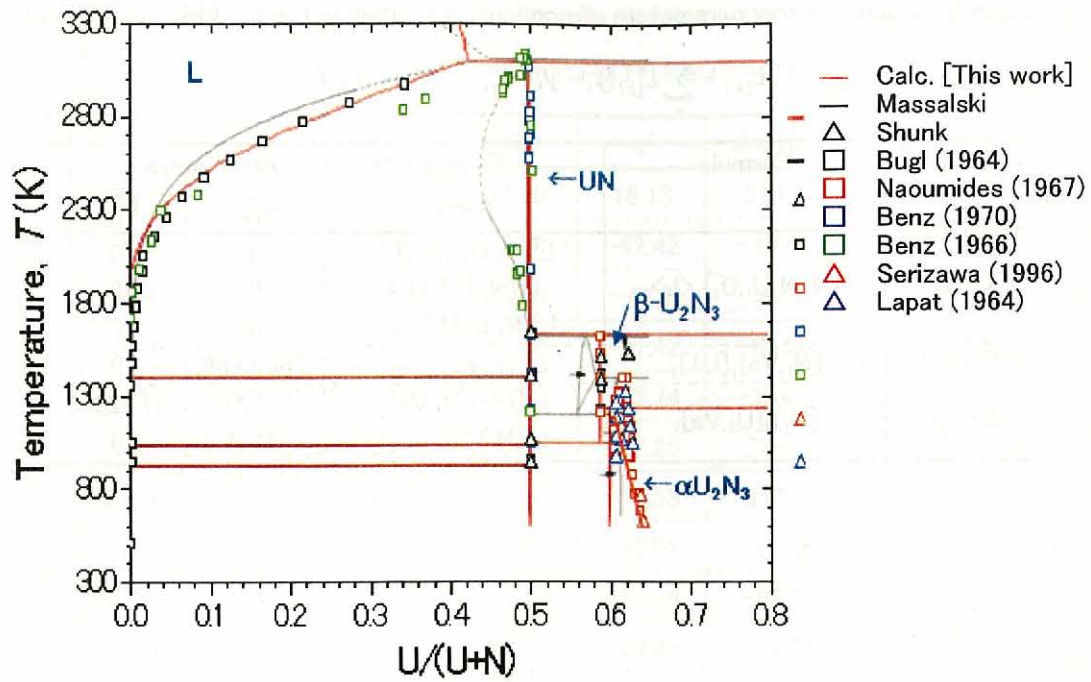


Fig. 5.140 Phase diagram of U-N binary system, with the experimental data [9, 14–16, 20, 21, 23,

29]

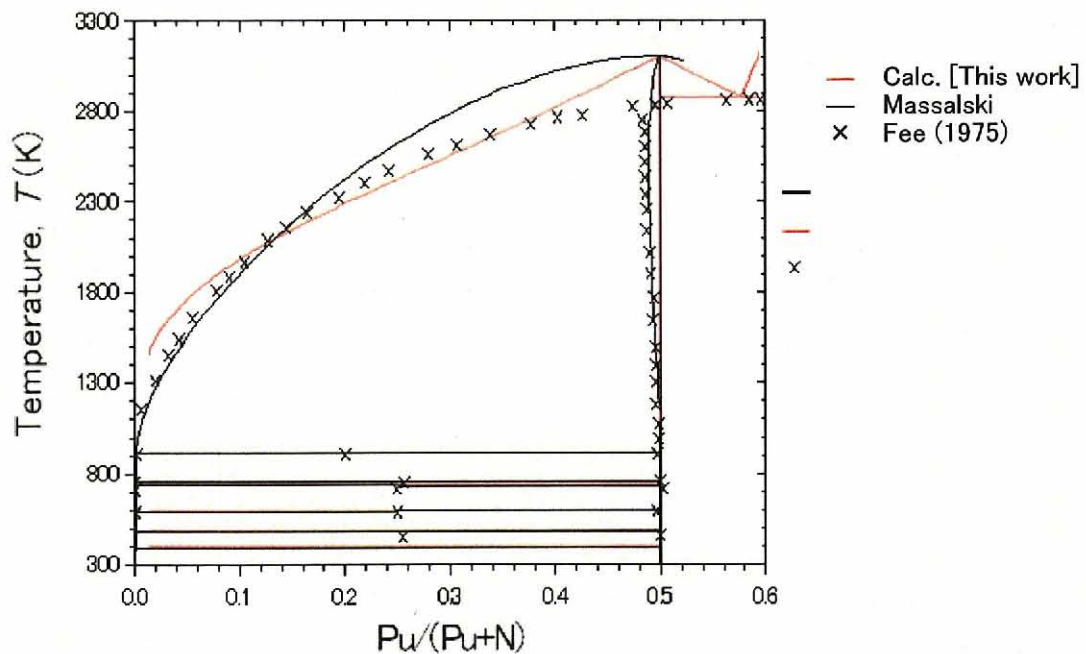


Fig. 5.141 Phase diagram of Pu-N binary system, with the experimental data [9, 28]

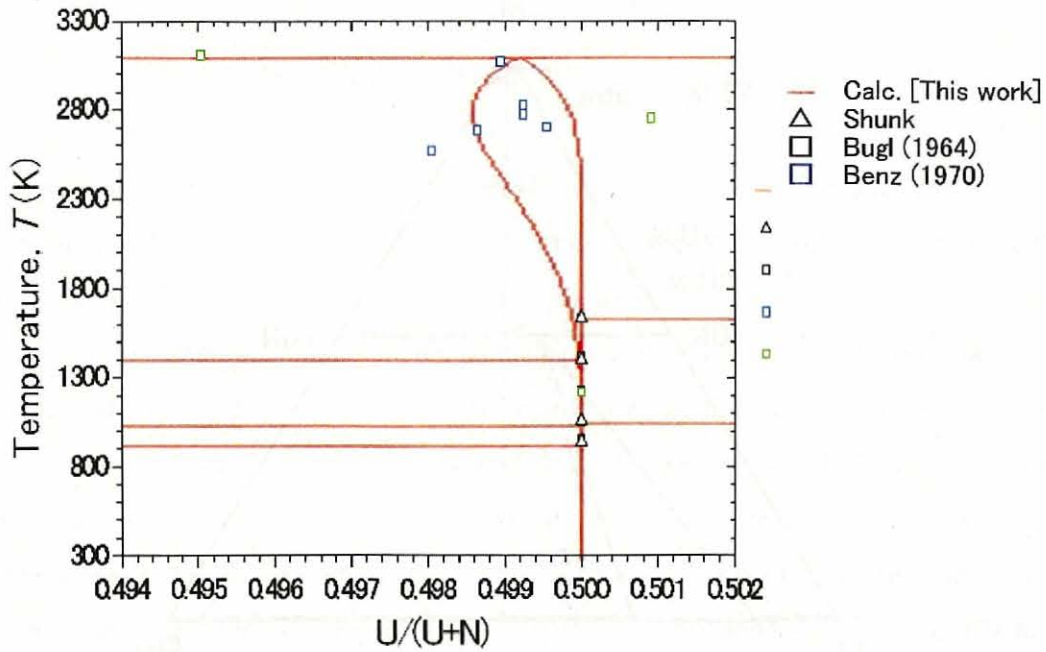


Fig. 5.142 Partial phase diagram of U-N binary system, with the experimental data [14–16, 29]

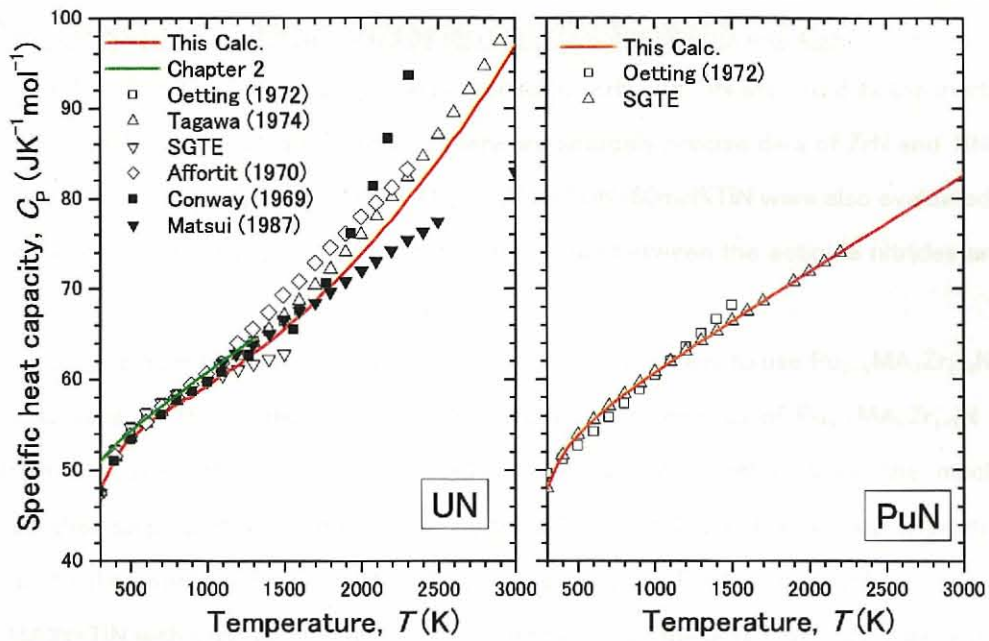


Fig. 5.143 Temperature dependence of specific heat capacity of UN and PUN, together with the literature data [8, 17, 31–36]

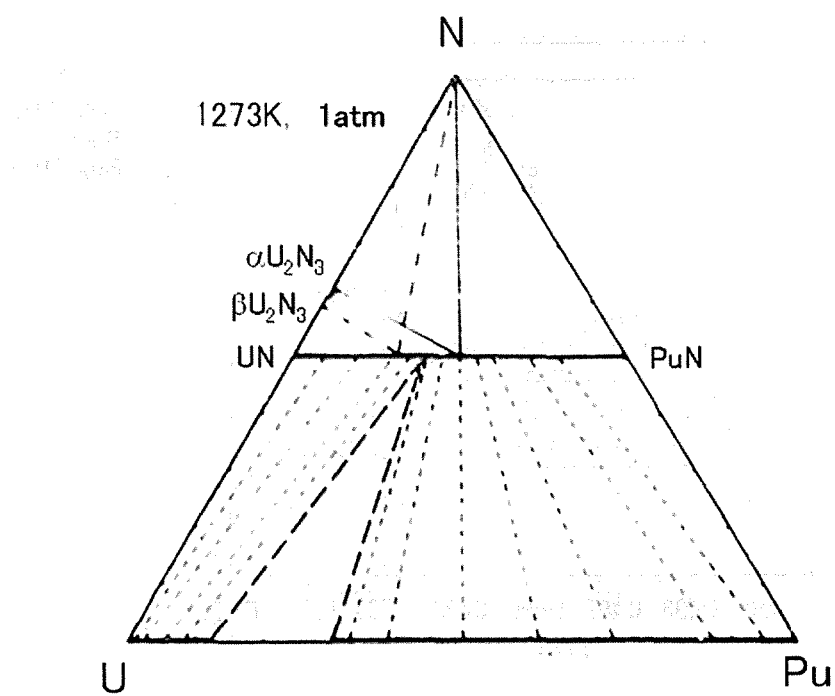


Fig. 5.144 Phase diagram of U-Pu-N ternary system referred from Ref. 28

Chapter 6: Conclusion

By partitioning and transmutation (P and T) of MAs (Minor Actinides: Np, Am and Cm) and Pu, the period that the radiotoxicity of HLW reaches to that of natural uranium is shorten from some hundred thousand years to three hundred years. The FBR (Fast Breeder Reactor) and ADS (Accelerator-Driven System) are considered as the method of transmutation of MAs and Pu. However, the nuclear fuel form to load into FR core has not been determined. The author addressed MA-containing MOX fuels and nitride fuels because there are a lot of data of MOX and oxide fuels and the nitride fuels have the superior fuel properties such as the high thermal conductivity, high melting temperature, and high chemical compatibility with the FR core materials and so on, respectively. However, there are few data of the thermophysical properties of such fuels. Therefore, in the present study, the author evaluated the thermophysical properties of nitride fuels with the inert matrix, simulated high-burnup nitride fuel and MA-containing MOX fuels by the experimental method and simulation method.

Chapter 2: Experimental evaluation of thermophysical properties of UN, simulated ADS target fuels (UN+TiN (U:Ti=4:6) and $U_{0.4}Zr_{0.6}N$) and inert matrix material (TiN and ZrN)

In Chapter 2, the thermophysical properties of ZrN and TiN expected as the inert matrix of the nitride fuels were evaluated because there are scarcely precise data of ZrN and TiN due to the high sintering resistivity. In addition, $U_{0.4}Zr_{0.6}N$ and UN+60mol%TiN were also evaluated as the simulated ADS target fuels to understand the interaction between the actinide nitrides and inert matrix.

Judging from the results of Chapter 2, it would be not easy to use $Pu_{x-y}MA_yZr_{1-x}N$ as the actual fuel because the prediction of the thermophysical properties of $Pu_{x-y}MA_yZr_{1-x}N$ is very difficult in the different way of (Pu,MA)N+TiN. In case of UN+60mol%TiN, the mechanical, electrical, thermal properties were improved by the addition of TiN and were roughly predicted by the theoretical or empirical model. Therefore, it is easy to predict the thermophysical properties of (Pu,MA)N+TiN with various component. Judging from only these results, TiN is more effective than ZrN as the inert matrix.

In case of the nitride fuels, it is a problem that the oxidation resistivity of PuN and AmN is very low, and that PuN and AmN vaporize at high temperature due to their high vapor pressure. ZrN may improve this problem because the chemical stability would be improved by the solution of ZrN to PuN and AmN. This effect could not be expected in case of (Pu,MA)N+TiN. Therefore,

evaluation of not only the thermophysical properties, but also thermodynamics properties of the nitride fuels would become to be important when we use the nitride fuels as the actual fuels.

When we predict the fuel behavior such as the fuel swelling, temperature distribution, pellet cracking, PCI, FCI and so on, it is very important to evaluate the elastic moduli, hardness, toughness creep rate, thermal properties and thermodynamic properties. In the present study, the elastic moduli, hardness and thermal properties were evaluated. If the creep rate and thermodynamics properties of the nitride fuel with inert matrix could be evaluated, we would be able to establish the model of the fuel behavior.

In the present study, the newest technique, which are SPS, EBSP and indentation test, and the new concept such as MSA were used in the field of the nuclear fuel engineering for the first time. The author succeeded to precisely evaluate the thermophysical properties of inert matrix material (ZrN and TiN) and was able to suggest the new methods to evaluate the porosity dependences of the thermophysical properties, which are extremely effective for the research of MA-containing fuels.

Chapter 3: Molecular dynamics (MD) studies of actinide nitrides, nitride ADS target fuels, actinide dioxides and MA-containing MOX fuels

By fitting the limited experimental data of the thermal expansion and bulk modulus, The potential parameters for the nitrides (ThN, UN, NpN, PuN, AmN and ZrN) and oxides (UO_2 , NpO_2 , PuO_2 and AmO_2) were semi-empirically determined. Using these parameters, the author evaluated the thermal expansion, bulk modulus, specific heat capacity and thermal conductivity of not only AnO_2 , AnN and ZrN , but also MOX, MA-containing MOX, and nitride fuels with the inert matrix.

The thermal expansion of $\text{U}_{0.4}\text{Zr}_{0.6}\text{N}$ by MD calculation agreed with the experimental data obtained in Chapter 2 and Vegard's law. On the other hand, the thermal expansion of $\text{Pu}_{0.4}\text{Zr}_{0.6}\text{N}$ calculated by MD calculation was lower than Vegard's law. MOX, MA-containing MOX, $\text{Pu}_{0.2}\text{Np}_{0.2}\text{Zr}_{0.6}\text{N}$ and $\text{Pu}_{0.2}\text{Am}_{0.2}\text{Zr}_{0.6}\text{N}$ followed to Vegard's law.

The specific heat capacity of actinide nitrides and actinide dioxides by MD calculation were similar to the experimental data. MOX, $\text{U}_{0.4}\text{Zr}_{0.6}\text{N}$ and $\text{Pu}_{0.4}\text{Zr}_{0.6}\text{N}$ followed to Neuman-Kopp's law. The influences of the addition of Np and Am could not be almost observed. In case of the oxide fuels, at high temperature, Bredig transition could be observed.

By MD simulation, only the κ_{LAT} were evaluated. In case of the nitride fuels, MD

results were vastly lower than the experimental data ($=\kappa_{TOT}$), because the main contribution in the κ_{TOT} of the nitride fuel is the κ_{EL} . In case of $Pu_{0.2}Np_{0.2}Zr_{0.6}N$ and $Pu_{0.2}Am_{0.2}Zr_{0.6}N$, the influences of the addition of Np or Am were not almost observed.

MD results of UO_2 , NpO_2 and PuO_2 showed the close value with the experimental data. MD result of AmO_2 was higher than the experimental data at whole temperature, because the experimental data would underestimate due to the reduction, self-irradiation damage and He bubble of AmO_2 . So, it is thought that MD result of AmO_2 indicates the intrinsic thermal conductivity. MD results of $U_{0.8}Pu_{0.2}O_2$ and $U_{0.7}Pu_{0.3}O_2$ were well consistent with the experimental data. MD results of $U_{0.7-x}Np_xPu_{0.3}O_2$ and $U_{0.7-x}Pu_{0.3}Am_xO_2$ didn't almost depend on Np or Am content.

From these results, it was found that the thermophysical properties MA-containing MOX fuels are very close to those of MOX fuels. Therefore, it is thought that the fuel behavior of MA-containing MOX fuel in the reactor core could be predicted by the code, which had been used to predict the fuel behavior of MOX fuel. In the present study, it was confirmed that MD simulation is very useful when we evaluate the thermophysical properties of the fuels with the complex component such as MA-containing MOX fuels and nitride fuels with the inert matrix.

In the present study, it is confirmed that the thermophysical properties of the non-irradiated oxide fuels could be precisely evaluated by MD simulation. In MD simulation, it is possible to insert the point defect, dislocation and lattice strain in the simulation cell in order to reproduce the irradiated fuel. In this case, the electron valence of a part ion of U, Pu and MAs would change. However, it is difficult to determine the potential parameters of actinide ions such as U^{5+} and Pu^{5+} because there is no material consisted from only U^{5+} and Pu^{5+} . Therefore, MD calculation used in the present study could not evaluate the irradiated fuels. On the other hand, their potential parameters would be able to be theoretically determined by the first principle calculation. In the future, it will become to be important to evaluate the thermal properties of the irradiated oxide fuel by the combination of MD simulation and first principle calculation.

Chapter 4: FPs (Pd, Mo and Nd) effects on thermophysical properties of simulated high-burnup nitride fuels

The simulated high-burnup nitride fuel pellets ($UN+Pd$, $(U,Nd)N$, $UN+Mo$, $(U,Nd)N+Mo$) were prepared by the carbothermic reduction and atmospheric pressure sintering. NdN pellets with various porosities and UPd_3 pellet were prepared by the SPS and high vacuum induction

melting method.

From the XRD and SEM-EDX analysis, it was found that Pd precipitates as UPd_3 along the grain boundary of UN, Mo precipitates as the pure metal, and Nd solves in UN phase. By the EBSP measurements, UPd_3 precipitation in UN+Pd pellets orientated for the direction from $(10\bar{1}0)$ to $(10\bar{1}1)$.

Young's modulus at macroscale obtained from the ultrasonic pulse echo method wasn't almost influenced by the FPs. From the indentation tests, it was found that Young's moduli of UPd_3 phase in UN+Pd-L and UN+Pd-H were higher than that of UPd_3 pellet. The fracture toughness improved by UPd_3 precipitation because UPd_3 precipitation stops the crack. Except for UN+Pd pellets, the remarkable change on the mechanical properties by the FPs could not be observed.

The experimental data of the thermal expansion of UN+Pd were not consistent with the data estimated from the volume thermal expansion coefficients and bulk modulus of UPd_3 and UN using Turner's equation. So, when the author re-estimated the thermal expansion of UN+Pd based on the data of Young's modulus of UPd_3 phase in UN+Pd pellets obtained from the indentation tests and crystallographic properties of UPd_3 phase obtained from the EBSP measurements. This method would allow us to evaluate the thermal conductivity of the high-burnup fuels by the small specimen. The thermal expansion of (U,Nd)N and UN+Mo, (U,Nd)N+Mo followed to Vegard's law and Turner's equation.

The experimental data of the thermal conductivity of UN+Pd were lower than the data estimated from Schulz's equation. Those of $(U_{1-x},Nd_x)N$ decreased with increasing the x . In the case of UN+Mo, the experimental data were well consistent with the data estimated from Schulz's equation. The effect of the addition of Mo in UN and (U,Nd)N pellets were very small.

In the results of chapter 2-4, the thermal conductivity and mechanical properties of the high-burnup nitride fuels and nitride fuels with the inert matrix were vastly higher than those of UO_2 and MA-containing MOX fuels. In addition, it is well known that the nuclear character and chemical compatibility with the reactor core materials of UN are superior to the oxide fuels. However, a lot of researches, which are the thermodynamics properties, irradiation tests and so on, are necessary when we take the nitride fuels into practice. Such experiment needs long term. Therefore, the author thinks that it is best to use MA-containing MOX fuels in the demonstration fast breeder reactor, which will be constructed by 2025 and the nitride fuels in the ADS and the

commercial fast breeder reactor, which will be constructed by 2050.

Chapter 5: Thermodynamics modeling of U-N and Pu-N binary system

U-N and Pu-N binary systems were assessed thermodynamically from the criticism of the available experimental data on both phase diagram and thermodynamics properties.

A consistent set of Gibbs energy parameters for the various phases was obtained. The agreement between the experimental and calculated phase diagram of thermodynamic properties is quite satisfactory.

Ternary compound doesn't exist in U-Pu-N ternary system. From only the Gibbs free energy data of U-N, Pu-N and U-Pu binary systems, we would model U-Pu-N ternary system. Like this way, if we model the thermodynamics database such as the Gibbs free energy of the binary systems based on CALPHAD method, the database of the binary systems allows us to evaluate the thermodynamic database for complex calculations in multi-component systems.

Acknowledgments

Many people have helped the author in his endeavors, and without them what has been achieved would not have been.

The author appreciates Prof. Dr. S. Yamanaka for his precious guidance, valuable discussion and everything kindly extended to the author. The author is indebted to Assoc. Prof. Dr. M. Uno for his valuable discussions and suggestions.

Prof. T. Takeda, A. Yamaguchi of Division of Sustainable Energy and Environmental Engineering, Graduate School of Engineering, Osaka University, were appreciated very much for their important and kind advices for the present study. The author also greatly appreciates Prof. T. Yamamoto of Management of Industry and Technology Graduate School of Engineering, Osaka University.

The author would like to express his greatest appreciation to Dr. K. Minato, Dr. Y. Arai, Dr. Akabori, Dr. Takano and Dr. Nishi of the Nuclear Science and Engineering Directorate, Japan Atomic Energy Agency. They taught me the basic knowledge about the nitride fuels and inert matrix. In addition, Dr. K. Minato taught me the newest trend about the research of the nuclear fuels. In the same way, the author feels grateful for Dr. M. Osaka, Dr. Ko. Tanaka and Dr. Ke. Tanaka who belong to Oarai Research and Development Center, Japan Atomic Energy Agency, for their kind advices about MA-containing MOX fuels. The author referred their data in this study and would not complete the doctoral thesis without their helps. Members of their laboratory are appreciated for their kind help.

The author expresses his great acknowledgement to Assistant Prof. Muta for his kind support to not only research-related matters but also administrative ones. Assistant Prof. Kurosaki is appreciated for his help in the laboratory. The author thanks Ms. Terasoma for her kind help in regard to administrative matter.

The author is graceful to Dr. D. Setoyama for his suggestions and helps in CALPHAD calculation and FEM calculation. The author would like to appreciate to Mr. T. Maekawa, A. Ieda and J. Matsunaga because they kindly taught me the experimental procedure. Especially, the author thanks to Mr. M. Katayama and H. Gima. They helped me as the member of the same research group. And Mr. M. Ito, S. Nishioka and H. Kitano gave me the valuable discussion and experimental method.

This paper is partially supported by Ministry of Education, Culture, Sports, Science and Technology.

Research achievements

1. List of publications

Relevant papers

- (1) J. Adachi, K. Kurosaki, M. Uno, S. Yamanaka, "A molecular dynamics study of thorium nitride," J. Alloys Compd. 394 [1-2] (2005) 312-316.
- (2) J. Adachi, K. Kurosaki, M. Uno, S. Yamanaka, "A molecular dynamics study of zirconium nitride," J. Alloys Compd. 396 [1-2] (2005) 260-263.
- (3) J. Adachi, K. Kurosaki, M. Uno, S. Yamanaka, "Thermal and electrical properties of zirconium nitride," J. Alloys Compd. 399 [1-2] (2005) 242-244.
- (4) K. Kurosaki, J. Adachi, M. Uno, S. Yamanaka, "Molecular dynamics studies of actinide nitrides," J. Nucl. Mater. 344 [1-2] (2005) 45-49.
- (5) J. Adachi, K. Kurosaki, M. Uno, S. Yamanaka, "Porosity influence on the mechanical properties of polycrystalline zirconium nitride ceramics," J. Nucl. Mater. 358 [2-3] (2006) 106-110.
- (6) J. Adachi, K. Kurosaki, M. Uno, S. Yamanaka, "Effect of porosity on thermal and electrical properties of polycrystalline ZrN prepared by spark plasma sintering," J. Alloys Compd. 432 [1-2] (2007) 7-10.
- (7) J. Adachi, K. Kurosaki, M. Uno, S. Yamanaka, "Nanoindentation Studies of Uranium Intermetallic Compounds," Recent advances in actinide science 305 (2006) 415-418.
- (8) K. Kurosaki, J. Adachi, M. Osaka, K. Tanaka, M. Uno, S. Yamanaka, "Molecular dynamics studies of uranium-plutonium mixed oxide fuel," Recent advances in actinide science 305 (2006) 409-411.
- (9) K. Kurosaki, J. Adachi, M. Katayama, M. Osaka, K. Tanaka, M. Uno, S. Yamanaka, "Molecular dynamics studies of americium-containing mixed oxide fuels," J. Nucl. Sci. Tech. 43[10] (2006) 1224-1227.
- (10) J. Adachi, M. Katayama, K. Kurosaki, M. Uno, S. Yamanaka, "Thermal properties of polycrystalline NdN bulk samples with various porosities," J. Nucl. Mater. Accepted.
- (11) J. Adachi, K. Kurosaki, M. Uno, S. Yamanaka, M. Takano, M. Akabori, K. Minato, "Mechanical properties at sub-microscale and macroscale of polycrystalline uranium mononitride," J. Nucl. Mater. Submitted
- (12) M. Katayama, J. Adachi, K. Kurosaki, M. Uno, S. Miwa, M. Osaka, K. Tanaka, S. Yamanaka, "Modeling and simulation of thermophysical properties of minor actinides-containing oxide fuels," MRS proceedings-2007 Submitted

- (13) J. Adachi, K. Kurosaki, M. Uno, S. Yamanaka, M. Takano, M. Akabori, K. Minato, "Molecular dynamics studies of nitride fuels with inert matrix [$U_{0.4}Zr_{0.6}N$, $Pu_{0.4-x}Np_xZr_xN$ and $Pu_{0.4-x}Am_xZr_{0.6}N$ ($x=0, 0.2$)],", J. Nucl. Mater. To be submitted.
- (14) J. Adachi, K. Kurosaki, M. Uno, S. Yamanaka, M. Takano, M. Akabori, K. Minato, "FPs effects on thermophysical properties of nitride fuels," J. Nucl. Sci. Tech. To be submitted.
- (15) J. Adachi, K. Kurosaki, M. Uno, S. Yamanaka, M. Takano, M. Akabori, K. Minato, "Interaction between actinide nitride and inert matrix (ZrN and TiN) on thermophysical properties," J. Nucl. Mater. To be submitted.

Other papers

- (1) K. Kurosaki, J. Adachi, T. Maekawa, S. Yamanaka, "Thermal conductivity analysis of $BaUO_3$ and $BaZrO_3$ by semi empirical molecular dynamics simulation," J. Alloys Compd. 407[1-2] (2006) 49-52.
- (2) 安達 淳, 高野 公秀, 赤堀 光雄, 荒井 康夫, 湊 和生, 宇埜 正美, 山中 伸介, "金属 Mo を不活性母材としたサーメット燃料の再処理に係る基礎研究," JAEA-Research Submitted.
- (3) M. Osaka, J. Adachi, K. Kurosaki, M. Uno, S. Yamanaka, "Molecular dynamics study on defect structure of gadolinia-doped thoria," J. Nucl. Sci. Tech. Accepted.

Article

- (1) 黒崎 健, 安達 淳, 片山 将仁, 宇埜 正美, 山中 伸介, "計算機で動く燃料中の原子の世界-分子動力学法による核燃料物質の物性評価-,", 日本原子力学会誌 10 月号

2. List of presentations

International conference and symposium (Oral presentation)

- (1) J. Adachi, K. Kurosaki, M. Uno, S. Yamanaka, "Molecular dynamics studies of actinide nitrides," 11th Symposium on Thermodynamics of Nuclear Materials (STNM-11), Karlsruhe, German, 7th September 2004.
- (2) J. Adachi, K. Kurosaki, M. Uno, S. Yamanaka, "Thermophysical properties of $U_{1-x}Zr_xN$ ($x=0, 0.6, 1.0$)," International Information Exchange Meeting on Thermodynamics of Nuclear Fuels, 30th November 2006.
- (3) J. Adachi, M. Katayama, K. Kurosaki, M. Osaka, S. Miwa, K. Tanaka, H. Muta, M. Uno, S. Yamanaka, "Molecular Dynamics Study with Interatomic Potential for Actinide Ceramics," New Cross-over Project Workshop-3, Tokyo, Japan, 13th December 2006, **Invited lecture**.

International conference and symposium (Poster presentation)

- (1) J. Adachi, K. Kurosaki, M. Uno, S. Yamanaka, "Nanoindentation studies of uranium intermetallic compounds," Actinides-2005, Manchester, England, 8th July 2005.
- (2) J. Adachi, K. Kurosaki, M. Uno, S. Yamanaka, "The nano-scale mechanical properties of metal nitrides," 4th 21st century COE international symposium, Toba, Japan, 18th November 2005.
- (3) J. Adachi, K. Kurosaki, M. Uno, S. Yamanaka, "The nano-scale mechanical properties of metal nitrides (II)," 5th 21st century COE international symposium, Awaji, Japan, 8th December 2006.

Domestic meeting (Oral presentation)

- (1) 安達 淳, 瀬戸山 大吾, 黒崎 健, 宇埜 正美, 山中 伸介, "アクチノイド元素—窒素系の熱力学・状態図解析," 日本原子力学会 2005 年 春の年会, 東海大学湘南校舎 (神奈川県), 2005 年 3 月 30 日.
- (2) 安達 淳, 黒崎 健, 宇埜 正美, 山中 伸介, "ウラン金属間化合物のナノ領域における機械的特性," 日本原子力学会 2005 年 秋の大会, 八戸工業大学 (青森県), 2005 年 9 月 14 日.
- (3) 安達 淳, 黒崎 健, 宇埜 正美, 山中 伸介, "ZrN 高密度焼結体の機械的特性の気孔率依存性," 日本原子力学会 2006 年 春の年会, 日本原子力研究開発機構大洗研究開発センター (茨城県), 2006 年 3 月 25 日.
- (4) 安達 淳, 片山 将仁, 黒崎 健, 宇埜 正美, 山中 伸介, "放電プラズマ焼結(SPS)により作成したバルク体 NdN の機械的・熱的特性," 日本原子力学会 2006 年 秋の大会, 北海道大学 (北海道), 2006 年 9 月 29 日.
- (5) 安達 淳, 片山 将仁, 黒崎 健, 宇埜 正美, 山中 伸介, "窒化物燃料用不活性マトリックス候補材料の機械的特性," 日本原子力学会 2007 年 春の年会, 名古屋大学 (愛知県), 2006 年 9 月 29 日.
- (6) 安達 淳, 黒崎 健, 宇埜 正美, 山中 伸介, "模擬 ADS ターゲット燃料 (UN+TiN(U;Ti=4:6), U_{0.4}Zr_{0.6}N) の結晶方位解析と機械的特性," 日本原子力学会 2007 年 秋の大会, 北九州国際会議場 (福岡県), 2007 年 9 月 28 日.

3. Award

- (1) 第 4 回 (平成 18 年度) 日本原子力学会関西支部賞
タイトル: 高速炉用窒化物燃料の結晶学・機械・熱・電気的性質に関する研究

4. Research grants

- (1) 平成 17 年度 産研・原子力工学専攻 21 世紀 COE 若手研究(B)

タイトル:複合型窒化物のナノ領域における機械的特性の評価

助成金額:42 万円

(2) 平成 18 年度 産研・環境エネルギー工学専攻 21 世紀 COE 若手研究(B)

タイトル:多相構造を有する窒化物のナノ領域における構造方位解析と機械的特性評価

助成金額:50 万円

(3) 平成 19 年度科学研究費補助金(特別研究員奨励費)

タイトル:窒化物燃料のナノ構造解析と特性評価および分子動力学による原子軌道解析

助成金額:90 万円

